

RAM

● ROBOTICS
AND
MECHATRONICS

3D PRINTED ELECTRONICS

H.R. (Heime) Jonkers

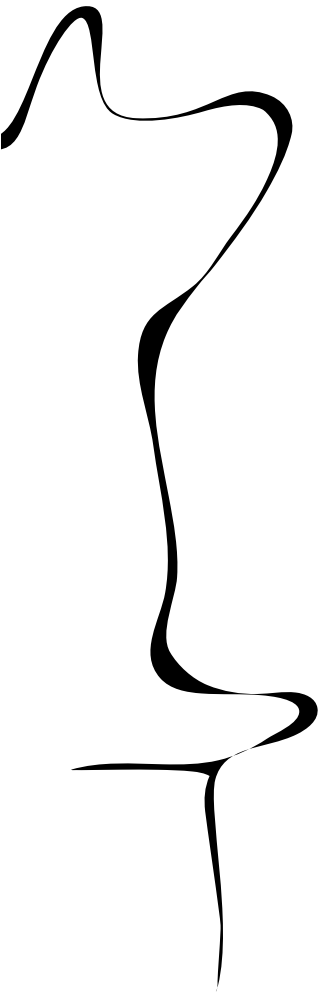
MSC ASSIGNMENT

Committee:

prof. dr. ir. G.J.M. Krijnen
ir. D. Kosmas
prof. dr. J. Schmitz

January, 2022

007RaM2022
Robotics and Mechatronics
EEMathCS
University of Twente
P.O. Box 217
7500 AE Enschede
The Netherlands



Summary

Current research into 3D printed electronics rarely focuses on integration with conventional electronics, describing either fully printed circuits or providing a characterization and design of a single circuit element. Therefore in this work, the possibility of combining conductive polymer based circuit elements with conventional electronics was studied. Characterization at typical operating conditions, interfacing with traditional substrates and potential achievable performance of printed R,C,L elements were investigated with the use of commercially available conductive filaments.

Carbon black doped conductive polymers were found to be most suitable for operation conditions commonly specified for conventional electronics. The use of a Thermoplastic Polyurethane was found to provide reliable interfacing to conventional gold contacts and sufficient adhesion to conventional substrates. Copper nanowire doped filaments were found to be most suitable for the creation of printed circuit elements due to their low resistivity, however, they were also found to incur severe degradation at the desired operation conditions.

Samenvatting

Huidig onderzoek in het 3D printen van elektronica heeft zelden focus op de integratie met traditionele elektronica, waarbij of een volledig geprint circuit beschreven wordt of de focus op het maken van enkele circuitelementen ligt. Daarom zal er in dit werk de mogelijkheid om circuitelementen gemaakt van geleidende polymeren met traditionele elektronica te integreren onderzocht worden. Karakterisatie bij normale operationele condities, de compatibiliteit met typische substraten en de prestaties van geprinte R,C,L elementen zijn onderzocht met het gebruik van commercieel verkrijgbare geleidende filamenten.

Carbon black (roet) gedoteerde geleidende polymeren bleken het meest geschikt voor operationele condities zoals die typisch zijn voor conventionele elektronica. Het gebruik van een Thermoplastische Polyurethaan bleek het meest geschikt voor elektrisch contact met gouden geleiders en voor de adhesie op conventionele substraten. Koper nano-fiber gedoteerde filamenten bleken het meest geschikt voor het creëren van circuit elementen, vanwege de lage resistiviteit, maar deze filamenten bleken echter zeer sterk te degraderen onder de vereiste operationele condities.

Preface

This master thesis is the result of work started at the beginning of March 2021 as a joint thesis project between the Robotics and Mechantronics and Integrated Devices and Systems groups at the University of Twente. Most of the work done for this thesis was completed as part of the Nature Inspired Fabrication and Transduction (NIFTy) subgroup, headed by prof.dr.ir. Gijs Krijnen, which has extensive experience in 3D printing of polymers. I found the groups members to be really helpful during bi-weekly meetings, discussing each others work and the challenges encountered, as well as being very welcoming.

From the NIFTy group I would like to thank Gijs and Dimitrios for their relaxed and at times needed critical guidance of the work performed during the (bi-)weekly meetings, commonly exceeding the reserved time due to the enjoyable discussions. I would also like to especially thank Alexander and Martijn for providing additional help when needed and a quick head start by sharing insights gained during their work as well as many pieces of great research they encountered. Lastly I would like to thank Leon for getting me excited about the field of magnetics by providing me with magnetic filaments with corresponding insights about them and for providing guidance in my consideration of a PhD towards the end of my thesis project.

From the IDS group I would like to thank Jurriaan for his guidance on the design considerations and potential pitfalls in the use of conductive polymers for the creation of circuit elements, as well as for the freedom allowed in the interpretation of the assignment on the 3D printing of electronics. Additionally I'd like to also thank Remco for his help working out the practical details of creating the experimental setups, the brainstorming sessions on how to best create the required samples and the generally dry humor associated with having Remco ("Pino") as your lab technician.

Finally I'd like to thank my family, friends and roommates for the support during the required moments of relaxation, reflection and recuperation in the form of a hike, mountainbiking or the traditional beers.

Heime Jonkers
Enschede, 30 December 2021

Acronyms

- IC** Integrated Circuit.
- PCB** Printed Circuit Board.
- CB** Carbon Black.
- CNT** Carbon Nano Tube.
- FFF** Fused Filament Fabrication.
- R** Resistor.
- C** Capacitor.
- L** Inductor.
- PLA** Poly-Lactic Acid.
- TPU** Thermoplastic Poly-Urethane.
- PVA** Poly-Vinyl Alcohol.
- PS** Poly-Styrene.
- HDDA** 1,6-HexaneDiol DiAcrylate.
- PVB** Poly-Vinyl Butyral.
- PE** Poly-Ethylene.
- HDPE** High Density Poly Ethylene.
- UV** Ultra Violet.
- DCM** DiChloroMethane.
- IPA** IsoPropyl Alcohol.
- ACF** Anisotropic Conductive Film.
- PUB** Polymer Ultrasonic on Bump.
- ENIG** Electroless Nickel Immersion Gold.
- HASL** Hot Air Solder Leveling.
- RFID** Radio-Frequency IDentification.
- GPIB** General Purpose Interface Bus.
- DC** Direct Current.
- AC** Alternating Current.
- DUT** Device Under Test.

Contents

1	Introduction	1
1.1	Project setup	1
1.2	What are 3D printed electronics?	1
1.3	Project goals	1
1.4	Research questions	2
1.5	Report structure	2
2	Background	3
2.1	Conventional electronics	3
2.2	3D printed electronics	4
2.3	Motivation for Fused Filament Fabrication	7
2.4	Discussion	12
3	Material Characteristics and Operating Conditions: Temperature and Resistivity	14
3.1	Previous work	14
3.2	Sample design	15
3.3	The experiment	17
3.4	Results	19
3.5	Discussion	24
3.6	Conclusions	27
4	Material Characteristics and Operating Conditions: Current Density	28
4.1	Previous work	28
4.2	Sample design	29
4.3	The experiment	31
4.4	Results	32
4.5	Discussion	36
4.6	Conclusions	37
5	Adhesion to Traditional Substrates: Printed Circuit Boards	39
5.1	Previous work	39
5.2	Sample design	40
5.3	The Experiment	43
5.4	Results	46
5.5	Discussion	51
5.6	Conclusions	54
6	Adhesion to Traditional Substrates: Silicon wafers	55

6.1	Previous work	55
6.2	Sample design	55
6.3	The Experiment	57
6.4	Failure point measurement	59
6.5	Results	59
6.6	Discussion	62
6.7	Conclusions	63
7	Components; Manufacturing, Performance and Prediction: Resistors	65
7.1	Previous work	65
7.2	Sample Design	65
7.3	The Characterization	68
7.4	Results	69
7.5	Discussion	69
7.6	Conclusions	71
8	Components; Manufacturing, Performance and Prediction: Capacitors	73
8.1	Previous work	73
8.2	Sample designs	73
8.3	The Characterisation	75
8.4	Results	77
8.5	Discussion	80
8.6	Conclusions	81
9	Components; Manufacturing, Performance and Prediction: Inductors	83
9.1	Previous work	83
9.2	Sample designs	83
9.3	The Characterisation	86
9.4	Results	90
9.5	Discussion	94
9.6	Conclusions	96
10	Conclusions	98
10.1	Are 3d printed electronics compatible with typical electronic operating conditions?	98
10.2	Are 3d printed components compatible with traditional substrates?	98
10.3	Are printed components performing sufficiently for typical use?	98
10.4	Are Hybrid circuits a possibility?	99
10.5	Are Fully printed circuits a possibility?	99
11	Recommendations	100
11.1	Improvements to material properties	100

11.2	Improvements to interface and adhesion	100
11.3	Improvements to component design	101
A	Long term measurements	102
A.1	Produced samples	102
A.2	Resistivity	104
A.3	Annealing	114
A.4	Temperature Coefficients	120
B	Current density experiments	125
B.1	Ninjatek Samples	125
B.2	Palmiga Samples	127
B.3	Protopasta Samples	129
C	Printed Circuit Board Experiment	133
C.1	Samples	133
C.2	LCR calibration	136
D	Silicon Wafer Experiment	143
D.1	Control Sample	143
D.2	Protopasta Sample	143
D.3	Electrifi Sample	143
D.4	Ninjatek Samples	144
D.5	Palmiga Samples	145
E	Resistors	147
E.1	0° infill orientation samples	147
E.2	15° infill orientation samples	147
E.3	30° infill orientation samples	148
E.4	45° infill orientation samples	148
E.5	60° infill orientation samples	148
E.6	75° infill orientation samples	148
E.7	90° infill orientation samples	149
F	Capacitors and Inductors	150
F1	Capacitor samples	150
F2	Inductor samples	151
F3	LCR calibration	152
	Bibliography	155
	List of Figures	164

List of Tables**164**

1 Introduction

1.1 Project setup

The following report will outline an master thesis researching the feasibility of manufacturing electronic components using 3D printing. The thesis work was performed at the University of Twente as a combined assignment of the Robotics and Mechatronics (RaM) and the Integrated Devices and Systems (IDS) groups of the faculty of Electrical Engineering, Mathematics and Computer Science (EEMCS). The assignment was performed with the help of and in association with the NIFTy subgroup of RaM, a group specialized in the creation of flexible and stiff sensors with the use of 3d printing processes, with vast experience in the usage of conductive printable materials.

The supervisory committee consisted of: prof. dr.ir. Gijs Krijnen, leader of the NIFTy team and currently specializing in the research into Transducers, Biomimetic sensors and the 3D printing of these devices; prof. dr. J. Schmitz currently specializing in above IC technologies and light-from-silicon with previous work including energy harvesting microchips, CMOS and MEMS; and ir. D. Kosmas specializing in 3d printed electro-mechanical sensors, hysteresis compensation in 3D printed sensors and capacitive force sensing.

1.2 What are 3D printed electronics?

As the term 3D printed electronics can be interpreted in many ways, a clear definition of the term 3D printed electronics is provided below for the course of this report:

"3D printed electronics are resistive (R), inductive (L) and capacitive (C) components formed by a layer by layer process wherein conductive and insulating layers are deposited to form a 3 dimensional structure."

Since the usable group of base polymer materials chosen for these components has further expanded with various research projects, the possibility of integration with commercial packaging and consumer products has been shown in multiple forms. Smart food containers [112], sensors for human interaction [49, 113], modular circuits [46] and anti-static shielding enclosures and tools [28] have been created by varying the composition of these new printable materials, showing the technology's potential.

Another advantage that can be found in these electronics is the further integration with conventional electronics, where use is made of the design freedom of 3D printing as a carrier in combination with the performance of conventionally made electronic components [50]. Wearable electronics and sensors can also easily be integrated if the printed materials are chosen to have flexible properties and making use of the material as conductor and mechanical retainer at the same time [106].

The aforementioned techniques would enable the direct addition of components in a single step process, with silicon integrated circuits (IC) and conventional printed circuit boards (PCB). This yields great potential, as it enables new options for packaging and integration, as well as savings in expensive IC die area.

1.3 Project goals

Following from the available literature on 3D printed electronics, a gap in research was noted in the challenges associated with the direct integration with conventional electronics. The majority of research was found to either describe the creation of printed circuit components with the usage of printed interconnects, as shown for example by [31], or would focus on the integration of conventional electronic components with 3d printed interconnects as shown for example by

[49, 50]. Therefore the possibility of making use of conventional circuit substrates with integrated interconnects such as PCB's and IC's for integration 3D printed components has yet to be explored.

These goals were incorporated into the research question, with three separate goals being defined. The goal being the selection of a printable material that is both suitable to provide sufficient conduction for the creation of electronics, and that is suitable to sustain these properties without degrading at typical operating conditions for conventional electronics. The second goal is to determine the possibilities for interfacing 3d printed components with traditional substrates, with a focus on direct adhesion opposed to additional interfacing materials. The third goal is to provide examples of circuit components created with these selected materials, consistent with the determined material properties. The first two goals defining the requirements for the creation of the desired interfaceable 3D printed electronics, with the third goal providing the basis for a proof of concept and validation of these electronics in operation.

1.4 Research questions

Based on these interests, the following research questions were formulated:

Q. "What are the current possibilities with respect to the implementation of 3d printing technology into conventional electronics manufacturing processes?"

To allow for a more specific answer to the three project goals stated, this main research question will be expanded by the following three sub-questions:

"Q.1 Under which kind of operating conditions can the 3d printed material perform consistently without significant degradation over time?"

"Q.2 What level of interface quality is possible between the printed material and the substrate in terms of adhesion and contact impedance?"

"Q.3 To which degree can 3d printed electronic components be produced in a repeatable, comparable and predictive manner?"

1.5 Report structure

During the course of this research report, experiments and conclusions that will provide answers to these queries will be detailed. The report will start off with a chapter of background information detailing traditional electronics construction, the processes of 3d printing and a detailed motivation for the choice of Fused Filament Fabrication for this research. This will be followed by two chapters on material properties and operating conditions describing the characterisation of the conductive materials, after which in two chapters the possibilities of adhesion to traditional substrates will be explored.

The results from the material characterisation chapters will then be used to provide reference for the analysis of resistive, capacitive and inductive components, detailed in three chapters describing their creation. Conclusions will be drawn as to the answers obtained to the posed research questions and a extensive recommendations on the basis of the research will be given.

Due to the large number of experiments performed and samples created, an appendix will be provided per experimental chapter highlighting the complete set of measurements performed, samples created and providing additional explanation of certain experiment specific concepts.

2 Background

To provide a foundation for the upcoming set of chapters describing the experiments, this chapter will begin by providing a description of the state of the art of current conventional electronics. This will be followed by a description of current 3D printing techniques based on definitions of the processes available, their suitability for printing electronics and the available materials given these techniques. In conclusion a description of the reasoning for the choice of the Fused Filament Fabrication (FFF) technique and the corresponding set of materials selected for the experiments will be given.

2.1 Conventional electronics

The electronics industry has been rapidly developing for many years leading to a continuous miniaturization of circuit components [63], substrates [82] and even the integration of these circuits onto micro and nanometer sizes on silicon dies [58, 59]. In general conventional electronics consist of several parts, all building upon one another to form a functional system.

The basis of all systems is provided by the circuit board, which provides mounting and interconnection of circuit components, traditionally these connections were formed through the use of many wires, however innovation lead to the creation of printed layers of conductors allowing for mass production [45]. With the invention the semiconductors, these printed circuit boards rapidly developed to become smaller and more integrated with the integrated circuits resulting from this invention, implementing more and more circuit components on small board mounted chips [30, 63]. Remaining components also improved by switching to mostly non-leaded surface mount packages, which are smaller and faster to place improving the manufacturing process [36].

The integrated circuits driving this miniaturization have also been developing rapidly and have evolved from purely silicon based devices. These could easily be scaled when the lithography technology afforded it [58] to multi material structures offering much smaller transistors and faster operating speeds by exploiting workarounds for limitations found to result from achieving sub 100 nm scales [59]. More recently the limits of the scaling approach has lead to the move towards the use of three dimensional stacks of IC's, offering multiple functionalities such as the integration of micro-mechanical devices, optics and different materials in a single integrated circuit [59].

A recent innovation observed in the construction of printed circuit boards is the direct integration of components and integrated circuits in the stack of interconnects and layers, fully integrating the system [82, 30]. This direct integration is also commonly found in another rising form of circuit construction: flexible circuits, where a printing process is used to create all of the parts required for a circuit whilst also providing the support as offered by PCB's [15]. Flexible electronics offer many benefits in terms of cost, durability and easy integration in comparison to traditional printed circuit board and IC technology, competing in applications where form factor is a dominant design parameter [70].

One of the key flexible electronics manufacturing techniques is the screen printing of components onto polymer films. This technique is on the edge between additive manufacturing and conventional electronics construction, offering dielectric, conductive and semiconducting materials [109]. The integration of screen printed passive resistive, capacitive and inductive components as well as screen printed batteries and diodes with IC's shows the promise offered by additive manufacturing in expanding the potential for a fully integrated electronic product [81].

2.2 3D printed electronics

Since the term of 3D printing is a umbrella for many processes, the following section will provide elaboration upon those processes as described by the ISO/ASTM 52900:2015 standard [38]. For each process a brief description will be provided along with a characterisation of the resolution, material and general abilities.

2.2.1 Processes

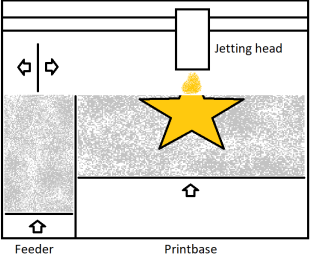
Binder Jetting	
	Resolution x,y: 200 μm -300 μm Resolution z: 35 μm -400 μm Materials: Metals (Steel, Inconel, Tungsten Carbide) Ceramics (Silica sand, Sandstone)
	Advantages: No warping since at room temperature Powder material is self supporting
	Disadvantages: Brittle nature leads to rough details Porosity affecting mechanical strength

Table 2.1: Binder Jetting characteristics [107]

Binder Jetting: Binder jetting, makes use of a material in powder form, in which droplets of a binding agent are dispensed to form the shape of the desired part. This method is commonly used for sand casting molds, colored prints and functional metal parts although the latter often requires an additional sintering process [107]. Material and machine costs are commonly quite high due to large printing volumes and the often limited reusability of remaining material [35]. In table 2.1 a illustration of the process, its abilities and its pros and cons are provided.

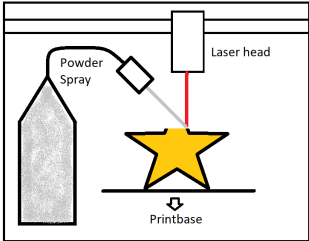
Directed Energy Deposition	
	Resolution x,y: Not specified Resolution z: 250 μm -500 μm Materials: Metals (Al,Cu,Fe,Ti,Co,Cr,Ni) Metal alloys
	Advantages: High speeds comparatively Low material wastage Ability to create large parts
	Disadvantages: Relatively low resolution Inconsistent surface finish

Table 2.2: Directed energy deposition characteristics [96]

Directed Energy Deposition: A higher energy approach to powder based fabrication is directed energy deposition, where metal is fed in either a wire or powder form, to be welded onto a formed part in a often oxygen shielded environment. Several techniques are available to provide the heating such as electron beams, lasers or plasma arcs to create a successful material weld [7]. Material costs are relatively low due to the use of only the needed quantity of material, machines are expensive due to their large build volumes, which in part is compensated by the direct nature of the process, not requiring additional processing unlike other metal capable processes [96]. Table 2.2 provides figures of the techniques abilities and a illustration of its operating principle.

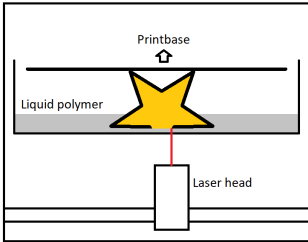
Vat Polymerisation	
	Resolution x,y: 50 μm Resolution z: 10 μm Materials: Polymers (flexible, heat resistant, Ceramic filled, conductive (in research))
	Advantages: High resolution Commonly available Smooth surface finish
	Disadvantages: Parts often brittle Small build volume

Table 2.3: Vat Polymerisation [48, 62]

Vat Polymerisation: Vat polymerisation is a very popular polymer based process where the print is commonly created bottom-up, with the use of light to harden photosensitive polymer resin. These machines make use of either laser or masked light to expose a layer of resin at a time as the build object is progressively moved up [5]. Resins are either directly cured or require UV post curing and are available at consumer prices, machines also come in at this price-point [62]. As before an illustration and characterisation of the technique is provided in table 2.3.

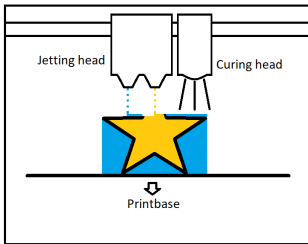
Material Jetting	
	Resolution x,y: Not specified Resolution z: 13 μm Materials: Polymers (photo-polymer, wax, silicone) Metals (silver ink, suspended) Ceramics (suspended)
	Advantages: High accuracy Multi material capability
	Disadvantages: Mechanically weak parts [6] Slow process

Table 2.4: Material Jetting characteristics [6, 1]

Material Jetting: Material Jetting is a process similar to the home inkjet printer, where small droplets are dispensed to create a layer which is skimmed afterwards to ensure a consistent buildup, forming a part step by step. Depending on the material used UV-curing or print cooling is required for the hardening of the part and support material is often required and can be made such that it can easily be dissolved [5]. In certain techniques materials can be blended to obtain desired hardness, mechanical strength and colors [6]. Machines and materials are relatively expensive compared to their build volume [1]. The techniques operation and capabilities are provided in table 2.4.

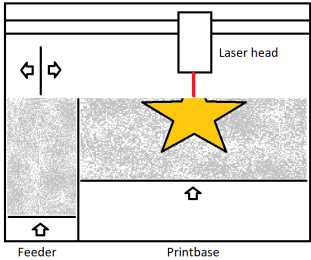
Powder Bed Fusion	
	Resolution x,y: not specified Resolution z: 100 μm -300 μm Materials: Polymers (Nylon, PEEK) Metals
	Advantages: Strong parts Complex geometries Self supporting Disadvantages: Small build volume Very expensive

Table 2.5: Powder Bed Fusion characteristics [5]

Powder Bed Fusion: The powder bed fusion process functions by fusing a powder through the application of heat in specific locations, directly fusing each layer to the part suspended in powder differentiating it from binder jetting. This heat can be provided through several manners such as lasers, thermal print heads and electron beams [8]. Heat treatment is often used after the process for consolidation and strengthening, resulting in thermal deformation which also can result from the printing process itself [5]. Material costs are generally very high as material cannot be reused due to contamination as layers are fused. The machines themselves are also comparatively costly for the provided build volume [97]. An overview of the technique is shown in table 2.5.

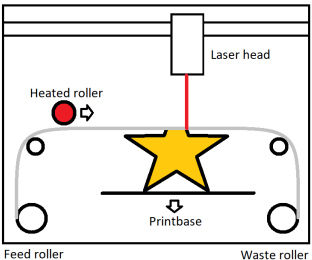
Sheet Lamination	
	Resolution x,y: Defined by cutting tool Resolution z: Sheet thickness Materials: Metals, Ceramics Polymer (Nylon, Peek, Composites) Papers
	Advantages: Color capabilities Mixed material bonding High speed Disadvantages: Limited materials Layered finish

Table 2.6: Sheet Lamination characteristics [9]

Sheet Lamination: In this process layers of material are first cut, and then laminated to a stack to form the final part. Machining can be integrated in between layer to allow for more complex products, with the resolution being defined by the layer thickness and the cutting method. Colored paper/polymers are available as well as metals depending on the process, additionally milling might be implemented as well. Since sheet materials are used, the materials are often relatively low cost, with machine costs dependant on the process [9]. In table 2.6 an illustration of the process and a listing of its properties are provided.

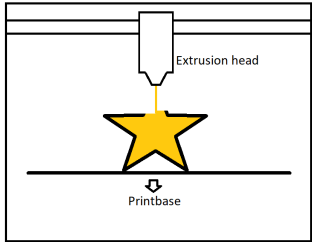
Material Extrusion	
	Resolution x,y: 500 μm Resolution z: 100 μm Materials: Polymers (neat, filled)
	Advantages: Material availability Flexible process Low cost
	Disadvantages: Material warping low/anisotropic strength Layered finish

Table 2.7: Material extrusion characteristics [5]

Material Extrusion/FFF: Being one of the currently most commonly used processes in the home and lab, material extrusion process operates through an extruding head which deposits layers of molten (polymer) material. Due to the widespread use of these machines, low material and equipment costs are realized, and many materials are available, including ones with additional fillers [5]. A big downside to this technique is the inherent void formation during printing resulting in anisotropic properties dependent on printing orientation [32], allowing mostly only use for prototyping parts or low strength applications.

2.3 Motivation for Fused Filament Fabrication

Given the many available processes, a few initial deciders had to be put in place as to determine a suitable process for 3D printing electronics. The initial restraint put in place is the need for both an electrically insulating material and a conductive material to allow for the formation of separated supported conductors. In conventional electronics these are commonly metals with low resistivity for conduction and ceramics as insulators, whereas both these and doped polymers are available in 3D printing, which can be used in neat form as an insulator and as a conductor in doped form.

From the basis of this initial process, several techniques remain that are able to combine both conductors and insulators: VAT Polymerisation, Material Jetting and Material Extrusion. Although VAT Polymerisation is able to be provide multi-material printing with some workarounds [93] and conductive polymers are possible [95], these are not yet commercially available, resulting in the choice to not make use of the technique.

Material Jetting was also explored, and usage of the Dragonfly printer was proposed, which is able to print both a conductive silver ink as well as an insulating photopolymer at very high resolutions although within a limited volume of 160 mmx160 mmx3 mm aimed at circuit boards [68]. An initial sample was designed and proposed to Nano Dimension for review, however due to the high cost of a single sample and the technologies already well characterized performance it was chosen not to proceed with this approach as well.

2.3.1 Printing process

The basis of the FFF printing process is the extrusion of a polymer filament by feeding it through a heated nozzle, which is moved across an often heated printbase, to form the final product. Layers are creating by moving the nozzle upward in the z-axis, whereas each layer is defined by printed lines made in the XY-plane, which we will call traxels. In figure 2.1 an illustration of this system is shown, where it should be noted that the initial layer height is provided by Z_0 whereas subsequent layer heights are given by Z_n . This differentiation is made as the initial layer is often printed with additional height and/or material flow to provide compensation for a potential uneven printbase surface at the cost of a potential edge at the bottom of a

print, commonly referred to as an elephants foot. The second thing to note is that the traxels are not round but squished ovals, with a defined line width often equal to the nozzle diameter or wider to ensure sufficient material extrusion. The layer height is often set to half to a quarter of the printnozzle diameter depending on quality requirements, and is also constrained by the printers mechanical construction which defines the attainable heights.

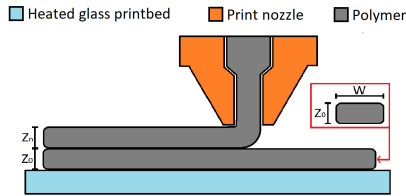


Figure 2.1: Filament fusion process

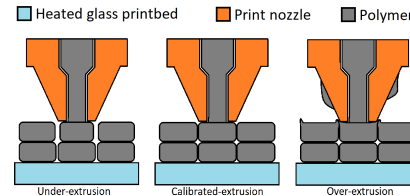


Figure 2.2: Illustration of extrusion calibration

Filaments are provided in standard diameter with a specified tolerance and will melt at varying rates depending on the material properties of the filament being used, this leads to the need for calibration of the required extrusion multiplication for optimal extrusion. This concept is illustrated in figure 2.2 where it can be observed that in case of under-extrusion voids are formed between print lines, leading to a weakening and anisotropy. In the case of over-extrusion, additional material fills the voids but it also curls up depositing material on the nozzle and showing characteristic ridges at the top of the print. In the case of a calibrated extrusion, an optimum is determined between both parameters, judging from the print by observing the ridges. Voids are more difficult to observe in the case they are not located at the outside surface requiring cutting or x-ray techniques.

Following from our layer wise method of part construction, several definitions are made in the so called slicing software, which is used to take a 3D object, slice it into layers of the desired height and convert it into g-code which the machine can interpret for printing. The first definition is shown in figure 2.3, where a part is first build up from a given amount of layers to provide a solid sheet of the parts underside, followed by the outside walls, leaving an inside space, which is then capped by a certain amount of solid sheet top layers. Due to the successive nature of layers building upon one another, it is important to keep an ideal temperature between melting and solidification, such that successive layers adhere but do remain self supporting. This is done through several settings; first, the printbase temperature, determining the rate at which the part is allowed to cool in conjunction with the ambient temperature. The second control is the use of an additional cooling fan blowing on the extruded filament, allowing for self supporting overhangs within bounds of the cooling rate of the material and sharper definitions in the part, at the cost of interlayer adhesion.

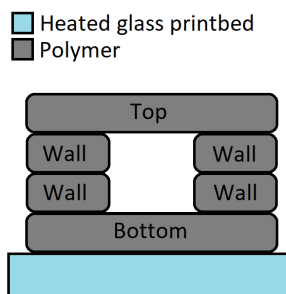


Figure 2.3: Part components

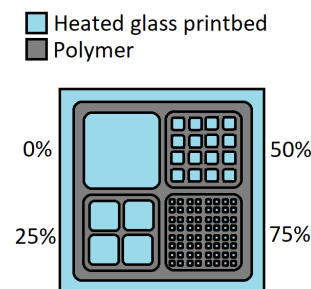


Figure 2.4: Infill concept

In order to prevent having to solidly print a part whilst retaining an internal supportive structure, the inner space can be filled with a percentage of infill structure, as illustrated in figure 2.4. These structures are commonly in the XY-plane, however 3D patterns are also available through the slicing software. This type of low density structure can also be used to provide a supportive function to the print being completed which can later be removed manually, or dissolved if an additional soluble material is used for printing.

Another important side effect of this line by line based part construction is an observed reduction in strength along the traxel to traxel interfaces in comparison to alongside the traxels [32]. This anisotropic behaviour due to the bond formed at the interface was also found to exist within the conduction through the interface of doped filaments in comparison to alongside the traxels [21]. It is therefore important to be able to clearly define where a traxel ends or continues, requiring a well performing and rigid motion system and a properly calibrated extruder.

2.3.2 Materials

Given the many fabrication processes available, a study of materials strongly depends on the chosen process. Therefore all materials suitable for our process, will be described in the following section, ending with an additional listing of experimental filaments.

2.3.3 Conductive Filaments

Several conductive filaments exist on the current market, which are listed below on the basis of their base polymer. Their description will focus on intended application and typical characterisations from the perspective of the properties gained from the filler. The base polymers mechanical properties will be taken as a constant for this section, although it has been shown that fillers can greatly affect material properties [61], an aspect to be considered on the basis of the intended application.

Polylactic Acid (PLA)

Protoplasta Electrically Conductive Composite PLA Protoplasta electrically conductive filament is a PLA based carbon black (CB) filled filament with $15 \Omega \text{ cm}$ resistivity [89]. It is aimed at home users and is reported to have good printing characteristics and above average ductility. The product is also priced to target this market with a cost of €10 per 100 g of filament and is available in both 1.75 mm and 2.85 mm filament diameters.

BlackMagic3D Conductive Graphene PLA BlackMagic3D conductive graphene filament was a PLA based graphene filled filament with $1 \Omega \text{ cm}$ resistivity [17]. It was produced by Graphene Laboratories who provide several graphene products, amongst which PLA-graphene pellets were also available. The product was aimed at the home user/professional and is priced at €100 per 100 g of filament and is available in 1.75 mm diameter. At the time of initial research the filament was currently out of stock due to supply chain related issues resulting from the Covid pandemic, with it now being discontinued.

Filoalfa Alfaohm conductive PLA Filo-Alfa Alfa-Ohm is a PLA based carbon nanotube (CNT) filled filament with $15 \Omega \text{ cm}$ resistivity [29]. It is aimed at home and industrial users and promoted for use where conductivity is required. It is priced at €35 per 100 g of filament and is available in 1.75 mm and 2.85 mm diameters.

Fabbrix CNT conductive PLA Fabbrix conductive is a PLA based carbon nanotube (CNT) filled filament with $10 \Omega \text{ cm}$ resistivity [26]. It is aimed at home users and promoted to be used in diy electronics in conjunction with Arduino microcontrollers. It is priced at €18 per 100 g of filament and is available in 1.75 mm and 2.85 mm diameters.

Thermoplastic Polyurethane (TPU)

NinjaTek Eel Flexible Conductive Filament TPU NinjaTek Eel filament is a flexible TPU filament filled with carbon black (CB) particles with $1.5 \text{ k}\Omega \text{ cm}$ resistivity [80]. It is aimed at the automotive, the industrial and the fashion (wearable electronics) market. It is priced at €14 per 100 g of filament and is available in 1.75 mm and 2.85 mm diameters.

Palmiga Innovation 85-750 Carbon Black ETPU Palmiga Innovations 85-750 Carbon Black is a flexible TPU filament filled with carbon black (CB) particles, characterized by Schouten [94] to have a resistivity of $7.43 \Omega \text{ cm}$. The material is not commercially available and therefore aimed at academia, its mechanical could possibly be considered comparable to the 95-250 variant offered by the same company [83] aimed at the home/industrial market and is promoted for both conductive as more stable rubber 3D printing applications due to the materials improved UV stability. This alternative more resistive variant is priced at €8 per 100 g of filament and is available in 1.75 mm and 2.85 mm diameters.

Proprietary

Multi3D Electrifi Multi3D Electrifi is a polyethylene (PE) based filament filled with copper nano-wires with $6 \text{ m}\Omega \text{ cm}$ resistivity [65]. The material is aimed at the creation of highly conductive prints for electronics applications. It is priced at €175 per 100 g of filament and is available in 1.75 mm and 2.85 mm diameters.

Add North G1 Koltron AddNorth G1 Koltron is a graphene filled filament with $2 \Omega \text{ cm}$ resistivity [2]. The material is aimed at the market for sensors, wearable electronics, cooling, shielding and printed electronics. It is priced at €85 per 100 g of filament and is available in 1.75 mm and 2.85 mm diameters.

2.3.4 Magnetic Filaments

Magnetic filaments were only found to be available in a Polylactic Acid (PLA) based filament, and shall therefore directly be listed below with a characterisation on the basis of the properties gained from the used filler material.

Protopasta Magnetic Iron PLA Protopasta Magnetic Iron is a PLA based iron filled filament with a 62 mHm^{-1} to 100 mHm^{-1} permeability translating to a relative permeability of 5 to 8 independent of frequency up to 1 MHz whilst magnetically saturating at 0.15 T [90]. It is aimed at home consumers for its rusted appearance and its weight alongside its magnetic properties. It is priced at €6 per 100 g of filament and is available in 1.75 mm and 2.85 mm diameters.

BlackMagic3D Ferromagnetic PLA BlackMagic3D Ferromagnetic was a PLA based iron filled filament, which was previously offered and discontinued, but is still available in a large quantity in the research groups lab. It was aimed at home users and the educational market for creation of actuators, cast iron appearance and sensors [18]. It was priced at €30 per 100 g of filament and is available in 1.75 mm diameter.

2.3.5 Experimental filaments

Several experimental materials with varying polymer basis and fillers have been shown in research papers, leading to interesting applications. Those found to be most interesting for 3D printing electronics are shown below.

Graphene

Graphene has most commonly been described in literature in the form of nano-plates or nano-flakes which are very thin flat sheets of graphene [98]. It has interesting properties in terms of electrical resistance and thermal conductivity, due to its 2d structure. In experimental fila-

ments it has been shown to work in a blended ABS filament to create a thermally and electrically conductive filament [98]. Furthermore it also has been shown to be a great conductive dispersant for CNT/graphene based PLA filament, where the addition of graphene particles in the blend resulted in improved conductivity, and thermal performance compared to filament filled with CNT's alone [39].

Silver

Silver is commonly used due to its high conductivity, although the materials cost is a limiting factor. It has been found in literature in combination with a HDDA transparent polymer in the form of nano-wires for the use case of solar panel interconnects, whilst also being shown in a capacitor demonstrator [34]. Silver has also been shown to be useful in the form of 2 dimensional silver flakes, that can be printed on several organic and polymer substrates suspended in Poly-Styrene (PS) and Polyvinyl Butyral (PVB) filaments. Which resulted in highly conductive flexible prints useful for embedding traditional electronic components [51]. CNT's have also been combined with Silver nano-particles to break up agglomerated CNT networks in a TPU base polymer. This combination was used to show highly linear strain sensing and human interfacing sensors [113]. Similar TPU based silver conductive inks, without CNT's were also used to print flexible devices with integrated conventional electronic components as well as human interfaces [106].

Copper

Copper nano-particles have been shown in literature by taming the thermal oxidation of the material with several coatings, including graphene, polymers and Silver [55]. The graphene coating showed an unexpected decrease in conductivity whereas the silver coating resulted in a usable RFID antenna demonstrator [55].

Nickel/Tin

Nickel and tin alloys appear in literature mixed with Nylon-6 and high density polyethylene (HDPE) to create low resistance conductive filaments. Interestingly in the hydroscopic nylon material resistivity degradation was observed, whereas the hydrophobic HDPE is not affected [101].

2.3.6 Conductive liquids

In literature and application the use of conductive liquids is also often shown, in the form of a carrying liquid for the conductive particles which are left in a structural form after the liquid evaporates. Silver filling with the use of a liquid has been demonstrated for capacitances, inductances and resistances, by creating a hollow shape filled by a liquid which is left to dry [112]. Carbon nanotubes have also been shown as a suitable filler, when combined with PLA dissolved in dichloromethane (DCM) mixed with a low (1-5%) filling of multi walled CNT's. This method showed self supporting prints after evaporation, with good conductivity and 100 micrometer resolution [86].

2.3.7 Direct deposition

Direct deposition is a process where the conductive material is applied without a carrying material. This can be achieved by printing with Pb-Sn-Bi alloy and making use of insulating spacers, resulting in easily created PCB traces as commonly found in circuit boards used for prototyping [44]. Another approach is the use of electrodeposition, which can be used up to the nanometer scale to deposit copper material with high aspect ratios in 3D structures [37].

2.3.8 Selected filaments

Given the many options available for investigation, two criteria were set as to the selection of the filaments. Firstly the filament had to be available through a vendor in 1.75 mm diameter, to ensure compatibility with the Diabase multi-material FFF printer available at the Nifty group. Secondly the material had to have a resistivity in the tens of ohms or a significant magnetic permittivity to allow for aid in the creation of electronics components. This leaves us with the selection of the following materials:

- Protopasta Electrically Conductive Composite PLA [89]
- Protopasta Magnetic Iron PLA [88]
- Palmiga Innovation 85-750 Carbon Black ETPU [83]
- NinjaTek Eel Flexible Conductive Filament TPU [80]
- Multi3D Electrifi [65]

Given that in previous findings within the group it was observed that the resistivity of Ninjatek EEL was much lower than cited, it was decided to also be included in the experiments. AddNorth G1 Koltron was also chosen to be included, however, it did not arrive in time to be used. As previously stated a quantity of BlackMagic3D Ferromagnetic PLA was still available, however whilst performing a test print with the material the filament was found to be so brittle that it could not be printed successfully. Lastly it can be observed that none of the carbon nanotube (CNT) filled filaments were used, this was decided due to the potential health risks involved [54, 87], resulting in a ban on CNT's within our labs.

2.4 Discussion

On the basis of the background provided above, some additional specification can be provided to the subjects of the experiments described in the following chapters.

2.4.1 Conventional electronics

In terms of the discussed conventional methods of electronics construction, it was noted that in the flexible electronics sector a lot of innovation was already present in terms of integrating all sorts of screen printed passive components and even semiconductors. It would therefore be more beneficial to explore the options of the rigid conventional substrates such as IC's and PCB's with the various coatings available for PCB substrates allowing for simulation of contact to traditional gold and tin IC and PCB bond pads.

2.4.2 3D printed electronics

Following from the already provided motivation for the choice of the FFF process, it should be noted that great potential is still available from other processes such as VAT polymerisation and Material Jetting if these processes are realized in an accessible commercial form. One of the great challenges for the VAT polymerisation technique is the requirement of a dielectric and a conductive material for the creation of electronic components, requiring two baths of different materials or a mix where the desired properties can be attained in some differentiating manner of curing. The largest downside of the Material Jetting process at this point in time are the prohibitive cost involved due to the speed of the process itself and the high required accuracy of the machines involved.

2.4.3 Selected approach

As previously mentioned the FFF process was chosen for both the availability of multi material machines as well as the commercial availability of several conductive and magnetic filaments.

It should however be noted that the use of the commercial filaments leaves quite some open questions as to the composition used, the potential for optimisation of the current formulation and the consistency in between and within the same reel of material. The tune-ability of the printing settings even with the commercially available printers also leaves quite some margin for error which could result in a bias to results not resulting from the experiment itself, which should carefully be considered.

3 Material Characteristics and Operating Conditions: Temperature and Resistivity

The first experiment devised as described during this chapter aimed towards getting a sense of the performance of printed conductive polymers at typical conventional electronic operating temperatures. In order to characterise this performance, samples were created in the four selected conductive filaments, which were subsequently exposed to either room temperature conditions or a selected temperature profile in an oven whilst their resistance was observed. Through the means of these measurements the effects of annealing, rest after printing and the volume resistivities were determined, providing a basis for the determination of the feasibility of the integration of these materials.

3.1 Previous work

3.1.1 Resistivity

Palmiga Innovations ETPU 85-700+ Carbon Black: The initial electrical characterisation of this material at the group was performed by Schouten [94], who determined the material to have a resistivity in the order of $7.43 \Omega \text{ cm}$ passing a current through the Z-plane. The characterisation of the conductance in the XY-plane was conducted by Dijkshoorn [21] who conducted an experiment where a current was applied in the XY-plane. These experiments resulted in a resistivity in the order of $0.4 \Omega \text{ cm}$ along a printed traxel.

These previous result hint towards an anisotropy in sample conduction depending upon the print orientation. It should also however be considered that differences in printing settings and geometry could also have contributed to these deviating results. No further work upon the characterisation of this material was discovered at the time of this writing and unfortunately no characterisation was found to be available from the manufacturer to allow for confirmation of these findings.

Protopasta Conductive PLA The Protopasta filament was previously investigated within the group by Neuvel [78] in terms of electrical contact formation, however no specific material resistivities were determined. Fortunately Flowers [31] determined the resistivity of printed samples of various conductive polymers by varying the amount of stacked layers of alongside traxels in the XY-plane. Currents were passed through the samples at each end, where contacts were formed with the use of silver paint, resulting in a resistivity of $12 \Omega \text{ cm}$. Lazarus [49] determined a similar figure through printing 50 mm long samples with traxels aligned with the current flow in the XY-plane, resulting in a $6 \Omega \text{ cm}$ resistivity.

Ninjatek EEL 3D Printer Filament (90A) Characterisation for the Ninjatek filament was only obtained by Stano [99] for usage in a strain gauge on the basis of printing parameter optimization. A figure of $3.8 \text{ k}\Omega$ resistance was obtained for a M-shaped strain gauge with an active length of 9 mm and current conduction along the traxels in the XY-plane.

Multi3D Electrifi Conductive Filament Electrifi filament has been described multiple times in literature, however is often characterized by the manufacturers claimed resistivity. Flowers [31] also characterized this material in the same manner as was used for the Protopasta filament, resulting in a resistivity of $14 \text{ m}\Omega \text{ cm}$.

3.1.2 Thermal effects

Thermal effects associated with carbon black filled filaments has been shown previously in the form of a temperature sensor based on Protopasta created by Lazarus [49], making use of its thermal resistivity change. They noted a 50% resistance change over a 30°C temperature

change, which results into a $0.016\text{ }^{\circ}\text{C}^{-1}$ thermal constant of resistivity. Daniel [19] also investigated the Protopasta filament and noted a constant of $0.01\text{ }^{\circ}\text{C}^{-1}$ to $0.03\text{ }^{\circ}\text{C}^{-1}$ for both the printed and raw filament. Stano [99] researched CNT filled filaments in comparison to Ninjatek EEL, and obtained a constant of $0.007\text{ }^{\circ}\text{C}^{-1}$ for the Ninjatek filament.

Additionally, Gao [32] provided several examples of thermal annealing of the material, which allows for improvement of the materials mechanical performance after heat treatment. Furthermore, within our research group annealing has been shown to be an effective way to reduce the required time for the resistance drop after printing [111, 94].

3.2 Sample design

The sample designs had to consider two main problems, the first one being the requirement of scale given a certain nozzle size, as the interest of the experiment is in the characterisation of bulk properties in contrast to the properties of a single traxel. The second is related to the potential deformation that might occur during printing referred to as warping, which was found to be dependant upon sample thickness.

Final rectangular sample dimensions were chosen to be 20 mm by 60 mm by 3 mm. As to ensure XY-plane current conduction through the samples, the thickness was chosen to be relatively small in relation to the samples other dimensions. The current applied to the samples were applied through rectangular contact pads of 5 mm by 20 mm on top of the sample, making the assumption of a sheet conduction as a result of this geometry imperative.

3.2.1 Infill design

Given the goal of determining effect of the interfaces in between traxels, in comparison to the bulk behaviour of the conductive polymer filament, the samples were built up from stacked traxels. The traxel paths were created perpendicular to or alongside the length of the sample, vertically stacking upon one another.

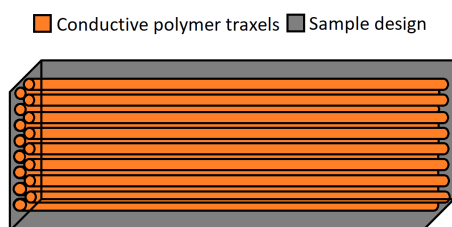


Figure 3.1: Alongside Infill pattern

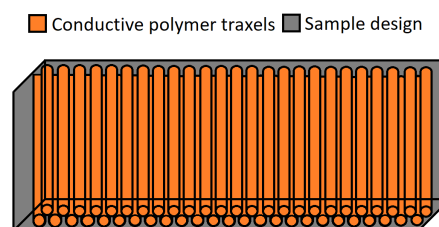


Figure 3.2: Perpendicular Infill pattern

In figure 3.1 the 3d structure of the samples with the traxels alongside the length of the sample are shown. The structure of the sample with traxels perpendicular to the length of the sample are shown in figure 3.2.

3.2.2 Slicer settings

For the printing of the samples custom Cura Slicer [105] setting were created as shown in table 3.1, based upon calibration prints and the recommendations by the filament producers [80, 83, 89, 65]. In order to allow for single traxels as described in the previous section, all non-infill structures were disabled. With the use of the 'Lines' infill pattern, and a 99.9% infill percentage, the slicing software could produce the desired gcode pattern.

For the bed adhesion of the Electrifi filament unbranded double sided tape was used, as this was found to be the only successful manner of attaching the Electrifi prints to the room tem-

	Ninjatek [80]	Palmiga [83]	Protopasta [89]	Electrifi [65]
Bed	60°C	60°C	60°C	Room
Nozzle	230°C	210°C	230°C	140°C
Flow	110%	110%	100%	110%
Layer height	0.2mm	0.2mm	0.2mm	0.2mm
Nozzle Size	0.4mm	0.4mm	0.4mm	0.4mm
Infill pattern	Lines	Lines	Lines	Lines
Infill percentage	99.9%	99.9%	99.9%	99.9%
Infill orientation	[0,0] or [90,90]	[0,0] or [90,90]	[0,0] or [90,90]	[0,0] or [90,90]
Wall/Top/Bottom	none	none	none	none
Bed adhesion	Spray adhesive	Spray adhesive	Spray adhesive	Adhesive tape
Print cooling	none	none	none	none

Table 3.1: Custom Cura Slicer profiles for sample creation

perature glass printbed. For all other prints, use was made of Dimafix[22] or 3Dlac[47] spray adhesive which is commonly used in FFF 3D printing

3.2.3 Contact formation

To allow for electrical contact to the top surface of the samples, conductive epoxy [66] was used to attach wires to the samples. Since a specific contact spacing was required to accurately determine the volume resistivity, as elaborated upon in section 3.3.1, a 3d printed mask was created as shown in figure 3.3. Due to the viscous nature of the epoxy resin, this was found to not provide an accurate mask, and paper masking was used instead. The resulting covering of the samples is shown in figure 3.4.

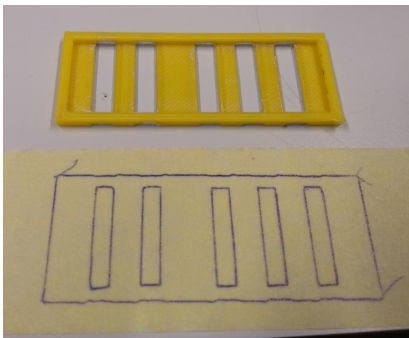


Figure 3.3: Mask Creation



Figure 3.4: Pattern Application

With the masks applied to the samples, a gram of conductive epoxy is mixed thoroughly and applied with the use of a cotton swab. The masks are carefully peeled away, and any potential contamination is carefully removed with isopropyl alcohol (IPA). The resulting formed pads are shown in figure 3.5. To complete the samples, prepared wires [92, 67] are rolled in another prepared batch of conductive epoxy, and attached to the uncured pads. After a 15 minute cure in the oven at 65°C, or a few hours in the oven at 40°C for the sensitive Electrifi samples, the contacts have now been formed as shown in figure 3.6.

The formed five contacts are spaced apart with distances of 10 mm, 15 mm, 10 mm and 10 mm as taken from contact center-line to contact center-line, from left to right in figure 3.6. The outside most contacts of the sample were created in such a manner that 5 mm of material was left to each side not covered by the contacts. The resulting uncovered sections of the sample had lengths of 5 mm, 5 mm, 10 mm, 5 mm, 5 mm and 5 mm from left to right.



Figure 3.5: Pad Creation



Figure 3.6: Wire Addition

3.3 The experiment

3.3.1 4-Wire measurement

For the characterisation of the samples, use will be made of the 4-wire kelvin resistance measurement. This method allows for the removal of the contact and wire resistances from the measurement, by separating the paths of the measurement voltage and the measurement current. The concept of this measurement method is provided in figure 3.7.

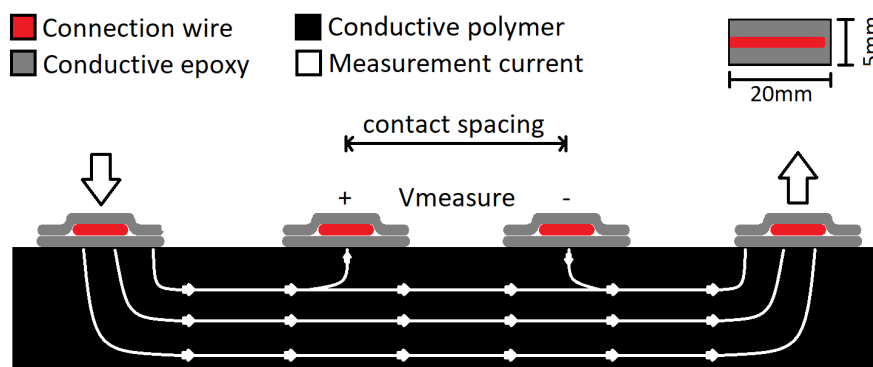


Figure 3.7: 4-wire measurement concept

In figure 3.7 a measurement current is applied to the outside 2 contacts on top of the sample, which results in a current flow through it. If the voltage resulting from this current were to be directly measured, the voltage generated across the resistance of the contact interface would inevitably also be observed. To resolve this a set of additional contacts are added, across which the resulting voltage is obtained [14]. As a voltmeter ideally has infinite input impedance, only a very small portion of the measurement current will flow through the meter and the inner two contact pads, allowing for an accurate measurement of the voltage generated by the samples resistance.

$$R_{measure} = R_s \frac{L}{W} \quad (3.1)$$

The from this measurement derived sample resistance as a function of the width W , contact length L and sheet resistance R_s is provided in equation 3.1. By making use of the contact spacing as provided in figure 3.9, a slope can be derived as graphically shown in figure 3.8, on the basis of the pairs of center contacts in our 5-contact samples.

With the use of this slope in Ωcm^{-1} equation 3.2 can be applied which multiplies the slope by sample width W to obtain the sheet resistance.

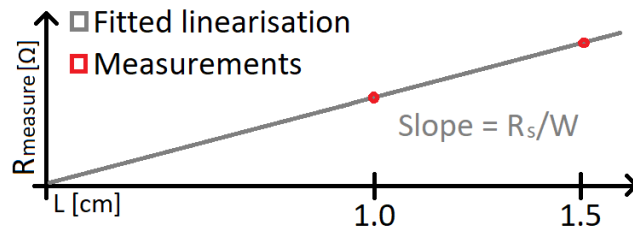


Figure 3.8: Resistivity extrapolation example

$$R_s = Slope \cdot W \quad (3.2)$$

This obtained sheet resistance in $\Omega\Box$ is then used in equation 3.3 with sample thickness T to arrive at the desired volume resistivity in Ωcm .

$$\rho_{volume} = R_s \cdot T \quad (3.3)$$

3.3.2 Real Time observation

Following from the goal to characterize the annealing and resting behaviour of the materials, a manner of performing real time observation will be described in this section. A system as described in figure 3.9 was created capable of performing continuous 4-wire measurements, for a set of samples. Samples were exposed to room and oven controlled conditions during a period of several days, where both the oven and the measurement equipment were controlled by a MATLAB script containing multiple processes for the simultaneous control of the various measurement devices[56].

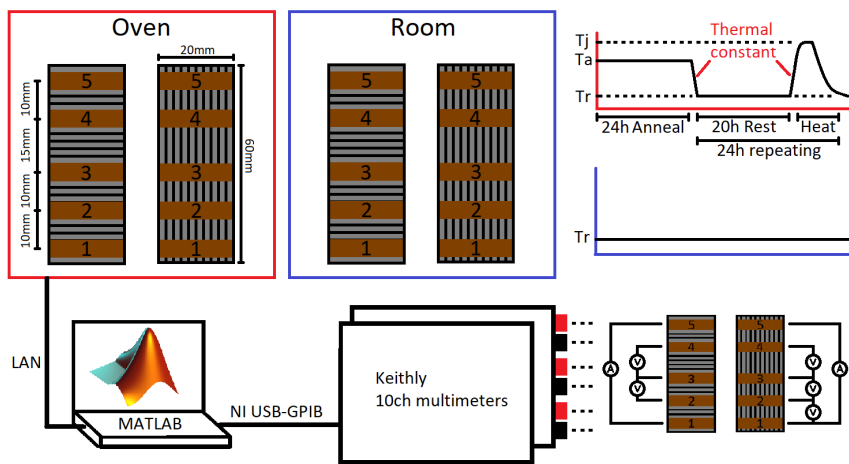


Figure 3.9: Real Time measurement setup

For the experiment two Keithley 2000 SCAN [41] were used, one for the samples inside of the oven, one for the samples outside of the oven. Since these multimeters come equipped with five 4-wire channels, a temperature sensor with a negative temperature coefficient was added to the room measurements, and a measurement between the #1 and #2 contact was added for the oven measurements to inspect the integrity of the contacts. The temperature in the Mammert UF30 [60] oven was controlled and measured via a LAN interface.

3.3.3 Thermal profiles

In order to ensure that all samples are optimally conductive before exposing them to the desired operating conditions, the samples were first annealed for a period of 24 hours. The an-

nealing temperature was chosen to be half of the printing temperature as supported by results by Wolterink[111] who cited a resistive drop at a temperature of 110°C for the Palmiga filament, which was found to be repetitive during several heating cycles. Electrifi was once more the exception, as it was recommended by the manufacturer[65] to not exceed 40°C for optimal conductivity.

After sample annealing, the samples were left to rest for a period of 20 hours, after which, temperature was raised to a typical operating temperature of 150-175°C for silicon components[10]. Due to the conductive epoxy[66] that was used for the formation of contacts, the operation temperature had to be limited to 150°C to remain within the manufacturers recommendations. This temperature was maintained for a period of an hour, after which the sample was given 23 hours to cool before the next exposure by means of turning of the oven without additional control.

This time period was decided upon to allow for a full cool down of the samples as it was observed previously that the samples had a tendency to drop in resistance in the hours following after printing at room temperature, whilst also taking into account the thermal constant of the closed oven which resulted in a cooldown period of several hours to room temperature. In total the samples were submitted to three of these exposures, with the temperature profile as used for the Protopasta and Ninjatek samples exemplified in figure 3.11.

3.4 Results

The result section will be a summarized version of the full real time measurements as are available in Appendix A. Key results will be highlighted as taken from the recorded profiles and corresponding result tables for both the room and the oven.

3.4.1 Resistivity

The initial result to be highlighted is the resistivity of samples placed in room conditions after printing as well as the resistivity of the oven exposed samples. These resistivities were derived from the recorded resistances as provided in the appendix in section A.2 with the method as proposed in section 3.3.1.

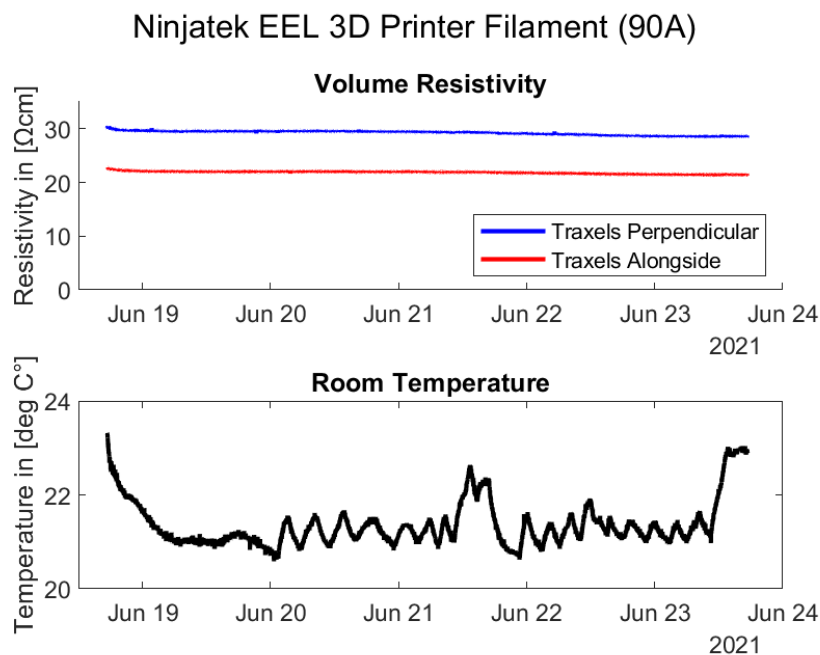


Figure 3.10: Example of room recorded room sample resistivity over time

In figure 3.10 an example is provided of the resulting derived resistivities with a corresponding recording of the room temperature conditions to which the samples were exposed. By taking the initial and final resistivity recorded, for both the traxels alongside and perpendicular to the current conduction path, the reductions as provided in table 3.2 were obtained.

Room reduction	Ninjatek	Palmiga	Protopasta	Electrifi
Alongside	95%	90%	95%	87%
Perpendicular	94%	80%	95%	93%

Table 3.2: Resistivity reduction derived from measured resistivities

The same type of derivation was conducted on the basis of the resistivities recorded for the oven samples exposed to the temperature profile as also provided in example figure 3.11.

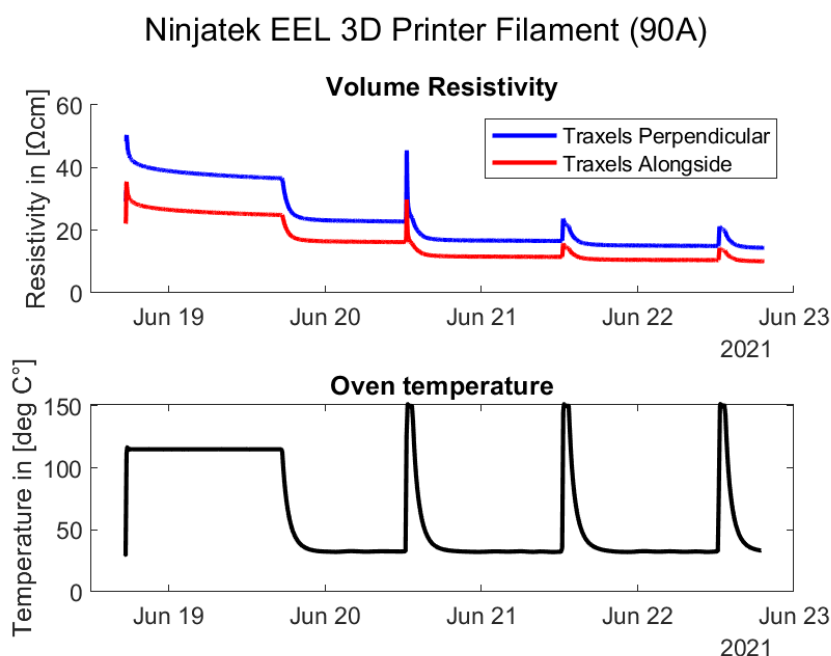


Figure 3.11: Example of recorded oven sample resistivity over time

Once more for this figure the initial and final resistivities were taken, to result in a figure of the resistance reduction achieved across the measurement period as provided in table 3.3. Since the Electrifi sample greatly degraded during the first high temperature exposure, the end values for this material were taken at the end of the first resting period after annealing.

Oven reduction	Ninjatek	Palmiga	Protopasta	Electrifi
Alongside	28%	4%	11%	35%
Perpendicular	29%	3%	11%	33%

Table 3.3: Resistivity reduction derived from measured resistivities

In addition to the reductions derived from the resistivities the ratio of anisotropy between alongside and perpendicular traxels could be determined as provided in table 3.4, with the ratio being defined with respect to the lower alongside traxel resistivities observed.

Anisotropy ratio	Ninjatek	Palmiga	Protopasta	Electrifi
Room	1,3	1,7	1,5	3,4
Oven	1,4	2,5	1,4	5,9

Table 3.4: Anisotropy ratio derived from measured resistivities

Most notable is the result of the Palmiga filament which shows a major reduction in resistivity after the thermal exposure in comparison to the samples exposed to only room temperature conditions. Its change in anisotropy ratio in the XY-plane along the current path also indicates that the process altered the material significantly.

The other carbon black filled Ninjatek and Protopasta filaments also show this clear reduction in resistivity, but do however maintain the same anisotropy ratio. The Electrifi filament showed a change in anisotropy ratio as well, which might however been caused by the initial overshoot of the oven past the set annealing temperature, increasing the recorded starting resistances.

3.4.2 Annealing

The annealing effect which was observed during measurement which occurred both during the set out annealing period as during the exposures to the higher temperatures, is represented by graphs as exemplified in figure 3.12 which are provided for all materials in appendix section A.3. The colored lines represent the sample resistance across the 10mm spaced contacts with the black lines representing the temperature as recorded by the integrated temperature probe of the oven.

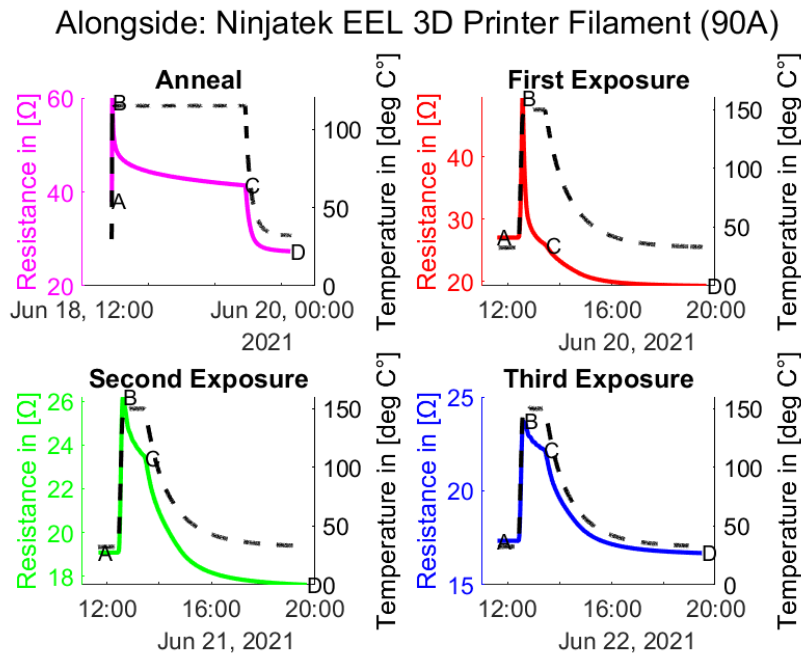


Figure 3.12: Example of anneal and exposure curves

In these figures four letters were manually added to each graph, representing the phases in the temperature profile. The letter A represents a start at room temperature at either the start of the measurement or at the end of a cooling period. The letter B represents the highest resistance recorded at the moment the oven reaches its set temperature. The point where the oven is turned off and let to cool according to its thermal mass, is indicated by the letter C. The last

point to be marked by letter D is picked to be where the temperature decrease flattens off and approximate room temperature is achieved.

Alongside	Ninjatek	Palmiga	Protopasta	Electrifi
Anneal	69%	13%	54%	36%
Expo #1	52%	65%	46%	28%
Expo #2	90%	67%	93%	
Expo #3	93%	73%	95%	

Table 3.5: Resistance changes due to Annealing and Exposure for Alongside samples

The section of interest in the case of annealing is that in between letters B and C, where the material is intentionally kept at elevated temperatures to result in annealing. In table 3.5 and 3.6 the resulting percentages of the impedance reductions observed during these periods are provided, as a function of the fraction of the observed final resistance at C and the initial resistance B at the annealing temperature.

Small percentages indicate that the material is very responsive to annealing, resulting a greater reduction in the samples resistance. As for the exposures, the most interesting pattern is the subsequent reduction in resistance per exposure step, with high percentages indicating that the material is close to saturation in terms of annealing.

Perpendicular	Ninjatek	Palmiga	Protopasta	Electrifi
Anneal	70%	11%	50%	37%
Expo #1	50%	52%	47%	25%
Expo #2	89%	73%	93%	
Expo #3	93%	78%	94%	

Table 3.6: Resistance changes due to Annealing and Exposure for Perpendicular samples

Interestingly subsequent heating steps show similar resistance values between marker B and marker C, pointing towards some form of memory effect in the material where after cooling and reheating the same state is achieved. This effect holds for all three carbon black filled filaments, with the copper filled Electrifi being the exception as it increases most in resistance during the cooling period. This is also the reason for the missing 2 exposures for this material, due to the severe degradation of the contacts at elevated temperatures.

3.4.3 Thermal dependence

The third result that could be derived from the data was resistance change as a function of temperature. In figure 3.13 and example of the resistance versus temperature curves color coded in correspondence to the graphs in figure 3.12 are provided as are available for all materials in appendix section A.4.

It can be observed that the resistance decrease at the constantly kept temperature is now represented by the vertical drop in the curve, with the lines from left to right representing the heating and cooling cycle. These graphs also provide a clear representation of the saturation behaviour of the resistance decrease as a function of the annealing process.

$$\alpha \Delta T = \frac{\Delta R}{R_0} \quad (3.4)$$

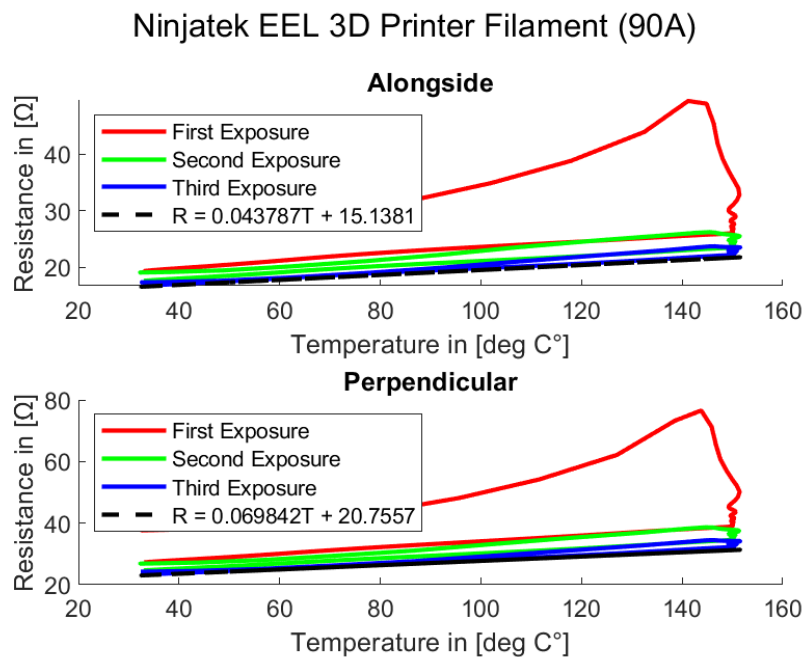


Figure 3.13: Example of thermal resistance of oven samples

In order to derive a thermal coefficient of resistance, equation 3.4 will be defined as its definition [76]. By taking an approximation through a linear fit of the cooldown period from C to D for the third exposure with the MATLAB[56] polyfit() function, a set of parameters as described by equation 3.5 can be determined.

$$R(T) = p_1 T + p_0 \quad (3.5)$$

By realizing that the fitted slope $p_1 = \frac{\Delta R}{\Delta T}$ and that $p_0 = R_0$, whilst also rewriting equation 3.4 the combination yields equation 3.6.

$$\alpha = \frac{\Delta R}{\Delta T} \frac{1}{R_0} = \frac{p_1}{p_0} \quad (3.6)$$

The resulting parameters as found for the carbon black filled filaments are shown in tables A.13, A.14 and A.15 in section A.4 of the Appendix. Electrifi was left out as it had fully degraded by the third exposure rendering the result inconclusive. The with the use of equation 3.6 calculated thermal coefficients of resistance are provided in table 3.7.

α	Ninjatek	Palmiga	Protopasta
Alongside	$0.003 \text{ } ^\circ\text{C}^{-1}$	$0.007 \text{ } ^\circ\text{C}^{-1}$	$0.059 \text{ } ^\circ\text{C}^{-1}$
Perpendicular	$0.003 \text{ } ^\circ\text{C}^{-1}$	$0.009 \text{ } ^\circ\text{C}^{-1}$	$0.058 \text{ } ^\circ\text{C}^{-1}$

Table 3.7: Derived temperature coefficients by linear fit

An interesting note on these results is the apparent isotropic nature of the thermal resistivity in contrast to the previously observed anisotropy of the resistivities as a function of the traxel orientation in the XY-plane.

This isotropy would however require some consideration of the state of anneal of the material considered during the observation of these coefficients, as the slope is still subject to change

when the material has not fully achieved the desired annealed state. The validity of the assumed linearity of the response is also subject to investigation as slight deviations could already be observed from the obtained fit, especially for the Protopasta filament which will be discussed in detail in the discussion section of this chapter.

3.5 Discussion

3.5.1 Resistivity

Given that several traxel orientations and sample conditions were tested, the final observed non annealed room and annealed oven sample resistivities have been summarized in tables 3.8 and 3.9.

Starting with the Ninjatek filament a remarkable reduction of the materials resistivity is observed in comparison to the materials manufacturer [80] who quotes a volume resistivity that is 2 orders of magnitude larger. Results by Stano [99] are difficult to use for comparison as they are not suitable for direct conversion to the desired unit of measurement. It is suggested that the large variation observed from the filament manufacturers data might be due to a change in filament composition.

Room resistivity	Ninjatek	Palmiga	Protopasta	Electrifi
Alongside	21.52 Ω cm	69.00 Ω cm	10.84 Ω cm	0.01 Ω cm
Perpendicular	28.49 Ω cm	119.96 Ω cm	16.00 Ω cm	0.03 Ω cm

Table 3.8: Final volume resistivities derived for non-annealed samples

For the Palmiga filament values are inline with findings by Schouten [94]. They do however deviate from findings by Dijkshoorn [21] potentially due to the use of single layer samples providing improved conductance and silver ink contacts allowing for potential conductive sample contamination. The two values provided by literature for the Protopasta filament by Flowers [31] and Lazarus [49], agree with the determined non-annealed resistivity, which was improved upon by annealing.

Oven resistivity	Ninjatek	Palmiga	Protopasta	Electrifi
Alongside	10.07 Ω cm	11.81 Ω cm	3.45 Ω cm	0.01 Ω cm
Perpendicular	14.38 Ω cm	29.87 Ω cm	4.88 Ω cm	0.03 Ω cm

Table 3.9: Final volume resistivities derived for annealed samples

The last material to be discussed is the Electrifi filament, which was determined to have a very low resistivity both in room conditions and after a 24h anneal at 40°C. These values are inline with the manufacturers [65] claim and findings by Flowers [31].

3.5.2 Drift

Referencing table 3.2 in terms of the change in material resistivity in the period after printing and contact formation, it can be observed that the change is fraction of the total sample resistance (80-95%) given a observation period of 5 days. However the observed resistivity continues to drop along the entire observed period, suggesting a continuous drift.

The effect might result from an external influence such as absorption of humidity from the surrounding environment, or from a relaxation process that occurs after printing within the material. In the latter case this effect might be resolved by applying annealing, as will be discussed

in the next chapter which has been shown to also significantly reduce the materials resistivity. The former might be tested by varying the external humidity of the sample during observation.

3.5.3 Annealing

One of the most important derivatives of this experiment is the period required for annealing the samples such that they achieve their optimal resistivity. As before the period from label B to label C where the material is exposed to a constant temperature will be taken as the annealing period. In figures 3.14, 3.15, 3.16 and 3.17 the annealing periods are highlighted for the 10mm contact spacings of the alongside traxel samples.

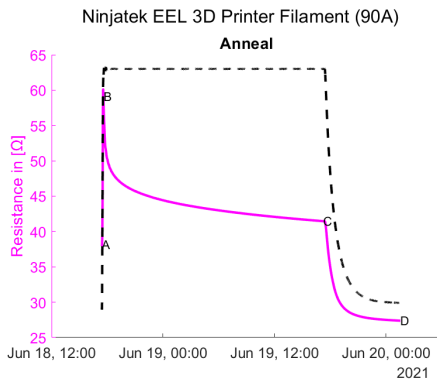


Figure 3.14: Ninjatek

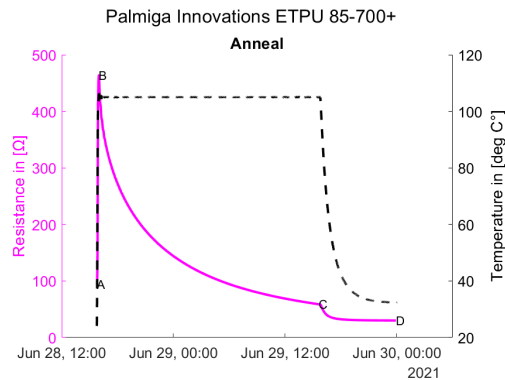


Figure 3.15: Palmiga85

By taking a look at the curve of the resistance drop during the period from B to C, an estimate of the completion of the anneal can be derived. Figures 3.16 and 3.17 show a clear flattening of the curve over a long period, suggesting that the initial curved section would be sufficient for a full anneal. The TPU samples as shown in figures 3.14 and 3.15 appear to require a longer period to fully anneal, with the Palmiga filament requiring an even longer period if the flattening of the Ninjatek filament' curve is considered.

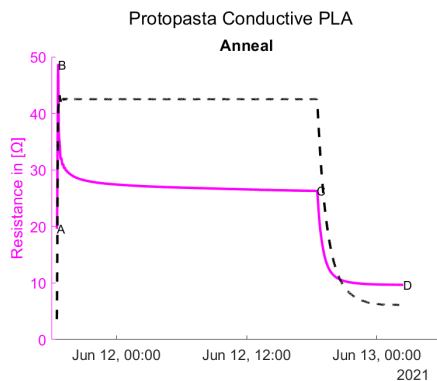


Figure 3.16: Protopasta

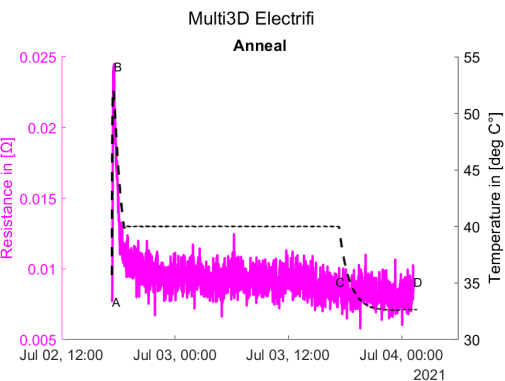


Figure 3.17: Electrifi

3.5.4 Exposure

After the initial annealing period, the samples were exposed to higher temperatures which are comparable to traditional operating conditions for electronics. Discussing the overall shape of the exposure curves as provided by the figures in appendix section A.4, the TPU filaments appear to saturate to a linear curve, which can easily be fitted with a first order polynomial. The Electrifi filament was left out of this curve fitting effort due its severe degradation.

The Protopasta filament shows an interesting kink in the curve at a temperature of 115°C, at which it was annealed initially, despite it appearing to have almost fully saturated after the first exposure. This effect might be used to tune a non-linearity in the response of the material, by annealing up to a certain temperature to create a pivot point in the materials response. However to confirm this further experiments at varying annealing temperatures would be required as it might also be a result of the filaments composition or previous unknown treatments.

In addition it should also once more be noted that a memory effect was observed in resistance observed between subsequent labels C and B for the carbon black filled samples. As the samples were exposed to the same temperature multiple times, the material appeared to return to the same annealed state it 'recalled', once more suggesting a tunable non-linearity.

As a final interesting note, the response of the Electrifi filament as shown in figures A.24 and A.25 in the appendix, is an increase in the resistance at label C as to oven is turned off after the initial exposure. This is interesting since the carbon black filled materials show a similar response up to this point, deviate from the Electrifi sample for this short section and then the Electrifi samples behave like the carbon filled samples once more.

3.5.5 Material degradation

The Electrifi samples showed such severe degradation that the measurements of the last two high temperature exposures were deemed unusable. This degradation is clearly observed in figure A.4 in the form of cracks and warping, as was inline with manufacturers recommendations [65] who stated to expect thermal degradation above 50°C. This however is severely limiting for the application of this material in combination with conventional electronics.

The TPU based filaments showed no warping, due to their flexible properties, with the Ninjatek filament not showing visual degradation. The Palmiga filament showed slight discoloration of the silver contacts as observed in figure A.2 hinting at some chemical reaction with the epoxy or out-gassing of the material. The PLA based Protopasta filament showed slight warping as shown in figure A.3 and no discoloration and or brittleness.

3.5.6 Thermal coefficient

For the discussion of the thermal coefficients the values as found in literature were summarized in table 3.10, which will be used as a basis of comparison to the derived values in table 3.7.

α	Literature
Palmiga [99]	0.007 °C ⁻¹ to 0.009 °C ⁻¹
Protopasta [49]	0.016 °C ⁻¹
Protopasta [99]	0.01 °C ⁻¹ to 0.03 °C ⁻¹

Table 3.10: Thermal coefficients for filaments as found in literature

For the Palmiga filament the derived coefficient matches up well with the value as derived by Stano, where the other TPU filament as made by Ninjatek is off by a factor of 2. Since both materials are similarly resistive and carbon black filled TPU materials, this difference might be explained by a difference in polymer composition as also supported by their difference in annealing response.

For the Protopasta filament a coefficient of almost a factor two to six larger than what was encountered by Lazarus and Daniel was observed. This might be explained by the additional non-linearities observed in the temperature versus resistance curves, resulting in an incorrectly estimated coefficient. The derived values are however relatively close to those as observed for

the Palmiga filament, so potentially they also could have arisen from the much higher temperatures used for characterisation in comparison to previous studies.

3.6 Conclusions

3.6.1 Material conductivity

During the experiment it was discovered that the resistivity of the selected carbon black filled was in the range of several [Ω cm]. The copper filled Electrifi filament offered the best conductivity providing a resistivity in [$m\Omega$ cm]. The resistance of the samples was also observed to drift over time, with the largest resistance drop occurring directly after printing, followed by an approximate constant decrease with time.

Additionally it was discovered that the materials conductivity could be improved by applying an annealing process for the carbon black filaments. This provided a reduction of a factor of two for the Ninjatek filament, a reduction factor of six for the Palmiga filament and a factor of three reduction for the Protopasta filament. This annealing effect appeared to saturate for the for the Protopasta filament over a period of 24 h with the TPU based Palmiga and Ninjatek filaments potentially requiring additional annealing time to show the same saturation effect.

3.6.2 Temperature resistance

The Electrifi material was found to strongly degrade at the increased temperature as commonly found conventional silicon electronics, whereas the carbon black based filaments were resistant. It should be noted however that the Palmiga showed indications of potential outgassing of the material, potentially resulting degradation with prolonged exposure.

3.6.3 Thermal dependence

The carbon black materials also showed a increase in resistance with an increased temperature, for which thermal coefficients were derived. This would result in additional losses in the application of a real world circuit, as well as a potential damage of the conductor as the heat input increases with increasing resistance as the current is kept constant.

4 Material Characteristics and Operating Conditions: Current Density

In order to round out the material characterisation, another important parameter was derived for each material, describing the materials ability to sustain current conduction. This property called current density describes the amount of current that can safely flow through a material without it degrading due to the heat generated by the power dissipation resulting from its resistivity. It is commonly defined as a given current through a surface area, defining the cross section of a material, which will be the description maintained for this experiment.

4.1 Previous work

To ascertain some reference material as to the results of the experiment, a brief summary on the relevant thermal properties of polymers will be provided. Additionally a summary of previous current density experiment with conductive polymer filaments will be provided.

4.1.1 Thermal properties polymers

Given the heating as resulting from the materials resistivity when a current is conducted, its ability to shed the generated heat in the form of dissipation along with its capacity to retain heat will provide a limit to the maximum current density achievable. If a wire were to be suspended in a medium whilst conducting a current, a heat flow can occur through its outside face or faces dependant upon the mediums temperature. If the temperature of this medium were to be lower the wire would be able to dissipate energy to the medium, with the magnitude of this difference affecting magnitude affecting the achievable heat flow.

Three main parameters describe the thermal diffusivity of a material in $\text{m}^2 \text{s}^{-1}$ which provides a measure of a materials ability to transfer heat generated throughout a sample as described by equation 4.1 [16]. The first parameter is the specific heat capacity c_p in $\text{JK}^{-1} \text{kg}^{-1}$, describing the quantity of energy required to heat a unit mass by a certain temperature. The second property is the materials thermal conductivity κ in $\text{Wm}^{-1} \text{K}^{-1}$ describing its ability to conduct the heat present in the material across a unit distance. The last factor to consider is the materials density ρ in kgm^{-3} which defines how much material mass is contained per unit volume.

$$\alpha = \frac{\kappa_c}{\rho c_p} \quad (4.1)$$

This combined material property provides a limit for the rate at which a material is able to shed heat through the outside surface of a sample, given its limit on the internal heat transfer. Most of the heat transfer is expected to occur through convection and to a lesser extend radiation if the sample is surrounded by an air medium, due to the minimal conduction between a solid and a gas as resulting from the requirement for interaction between molecules and atoms. Radiation is highly dependant upon temperature was expected to be insignificant at the during the experiment to be achieved temperatures.

Due to convection being determined by the flow of mass, through either forced flow or thermal expansion resulting in buoyancy, it is not simply derived from material properties. Therefore thermal diffusivity was taken as a material property derived reference as to the available heat transfer of a material to the outside environment.

Material	Density	Melting	Decomposition	Autoignition
Ninjatek	1.2 g cm ⁻³	N/A	221 °C	>400 °C
Palmiga ¹	1.3 g cm ⁻³	>120 °C	>250 °C	>340 °C
Protopasta	1.24 g cm ⁻³	195 °C-225 °C	250 °C	300 °C-400 °C
Electrifi ²	2.5 g cm ⁻³	60 °C	250 °C	N/A

Table 4.1: Filament polymer properties derived from medical safety data sheets [79, 84, 88, 64]

Unfortunately filament manufacturers often do not elaborate upon these figures in their technical data sheets, or no datasheet is even available such as is the case for the used Palmiga 85-700+ filament, requiring substitution by data from the deviating 95-250 variant. Due to the high filler contents in these filaments, a comparison with bulk polymer properties can be troublesome as observed by Ivanov [39], who showed significantly differing thermal conductivities, diffusivities and electrical resistivities for PLA filaments filled with from 0-6% carbon black.

As to still be able to provide some sense as to the materials thermal abilities, data was taken from the filaments medical safety datasheets, as shown in table 4.1. Given similar densities of the carbon black filled materials, their melting points might provide some insight, taking that their thermal diffusivity would be dominated by the high diffusivity of carbon [24] and their filler content is comparable. This high diffusivity would also suggest that the available surface area in contact with the external medium might provide a limit to the available dissipation.

4.1.2 Current Density

From literature no current density experiments were found for the carbon black filled materials, however the manufacturers of the Electrifi [65] filament provided several figures of current for a given surface-area. They also provided a relationship between current density and the surface area to volume ratio, showing the relation between surface area available for transfer of heat and the amount of material in which heat is created due to a current flow.

As only two actual values from the experiment were provided, 200 mA for a 1 mm by 1 mm, 20 mm long wire and 3.5 A for a 8 mm by 8 mm wire of the same length, we will take these values as reference for the current density of Electrifi. The 1x1 wire provides a current density of 200 mA mm⁻², the 8x8 wire provides a current density of 55 mA mm⁻², showing the effect of a increase in volume compared to surface ratio, reducing the wires dissipation ability. Additionally a recommendation of a safety factor of two was also provided for the current that is allowable through a wire for safe operation.

4.2 Sample design

To allow for a comparable experiment to the one provided for electrifi, similar current density samples were created which allowed for an easily scaleable cross-sectional area. The samples were also provided with a larger contact area than this cross-sectional area to ensure that current carrying capacity of the contact would be more than the tested section of conductor.

Figure 4.1 provides a sketch of the in FreeCAD [91] created sample geometry, with a 20 mm by 1 mm wire section in the center and 5 mm by 10 mm contact pads. The center wire section could be widened whilst also extruding the sample vertically to achieve the desired square cross-sectional area.

¹Taken from available ETPU 95-250 datasheet

²Decomposition temperature based upon suggested maximum temperature

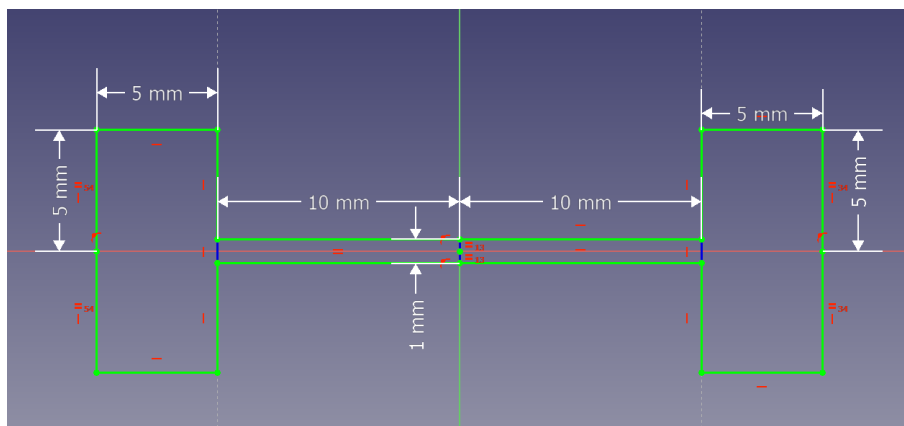


Figure 4.1: 2D sketch of sample geometry used

In order to derive a distribution of current carrying capabilities, samples with 1 mm by 1 mm, 2 mm by 2 mm, 3 mm by 3 mm, 5 mm by 5 mm and 8 mm by 8 mm cross-sectional area were created. The size of the contact pads and the length of the wire were kept consistent.

4.2.1 Infill design

Given the right angled edges at the transition point between the wire and the contact point, a well chosen infill design was required to allow continuous traxels from contact to contact. To ensure this, the slicer was configured to create the samples out of concentric walls, also aligning the traxels alongside current flowing through the wire.

An overview of the sliced print lines is shown in figure 4.2, where for convenience all samples are put side by side. In the actual prints samples were printed 3 at a time per cross-sectional area as shown in figure 4.3.

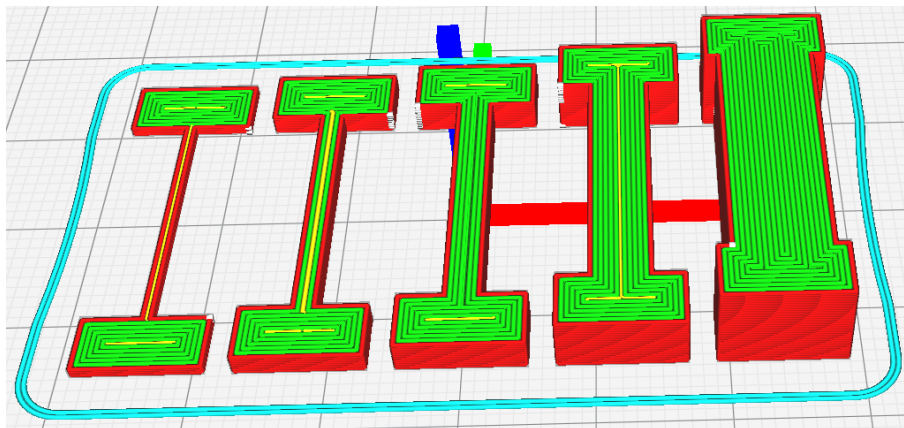


Figure 4.2: Traxel layout for 1x1mm, 2x2mm, 3x3mm, 5x5mm, 8x8mm samples

4.2.2 Slicer settings

The slicer setting chosen for the current density samples were created on the basis of settings used in for previous characterization as provided in section 3.2.2. Several alterations were made such as the usage of the concentric walls instead of infill, and the flow setting used for the Protopasta filament. The flow percentage was altered due to a noticeable under extrusion formed in the long wire sections, which was resolved by this change without resulting over extrusion in other sections of the sample. The slicer setting are show in table 4.2.

	Ninjatek [80]	Palmiga [83]	Protopasta [89]
Bed	60°C	60°C	60°C
Nozzle	230°C	210°C	230°C
Flow	110%	110%	110%
Layer height	0.2mm	0.2mm	0.2mm
Nozzle Size	0.4mm	0.4mm	0.4mm
Top/Bottom	none	none	none
Wall line count	∞	∞	∞
Wall thickness	0.4mm	0.4mm	0.4mm
Bed adhesion	Spray adhesive	Spray adhesive	Spray adhesive
Print cooling	none	none	none

Table 4.2: Custom Cura Slicer profiles for sample creation

4.2.3 Contact formation

Due to a malfunction with the firmware of the used Diabase H5 printer [20] binding of the filament in the feeder tubes would occur during retraction. The firmware issue resulted the top filament feeders to be disabled providing a resistance to the reversing of the filament. As a result of disabling retraction blobs of excess material were formed during printing as shown in figure 4.3 which were removed with the use of a sharp knife.

After this cleanup, the samples contacts were carefully coated on all sides not facing the current carrying wire, with a conductive silver paint [23]. This coating ensured a low resistance connection to the samples traxels, and was left to dry according to the manufacturers recommendation. The resulting coated samples are shown in figure 4.4.

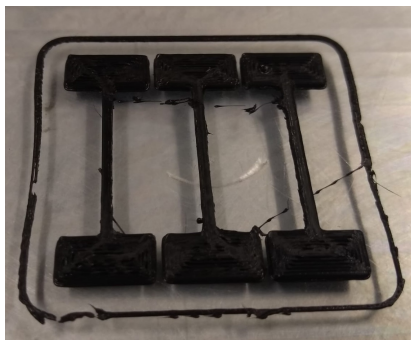


Figure 4.3: Samples after printing

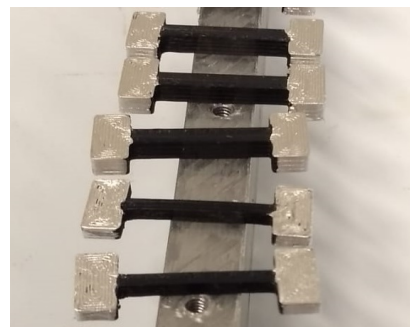


Figure 4.4: Silver paint coated samples

4.2.4 Annealing

The last step in the formation of the samples was a 12 hour long anneal at a 110 °C in a Memmert oven [60]. The 110 °C was picked as a middle ground between the annealing temperatures as selected in section 3.3.3 as all samples were simultaneously placed in the oven.

4.3 The experiment

The experiment chosen to derive the current density was relatively simple, and relied on the samples resistance to result in a current flow proportional to a set voltage across the wire section. In order to also get a sense of the power dissipated within the sample, the temperature was also recorded.

4.3.1 Measurement system

The measurement system created for the experiment consisted of a parallel script running in MATLAB [56], providing instructions to a Keithley 2000 multimeter [41] and a HP E3631A programmable power supply [4] via a GPIB interface. The Keithley multimeter was used to record the temperature of the sample surface with the use of a K-type thermocouple placed on top of the middle of the conducting wire. The HP programmable power supply was used to both set the voltage across the sample and to measure the current flowing through the sample.

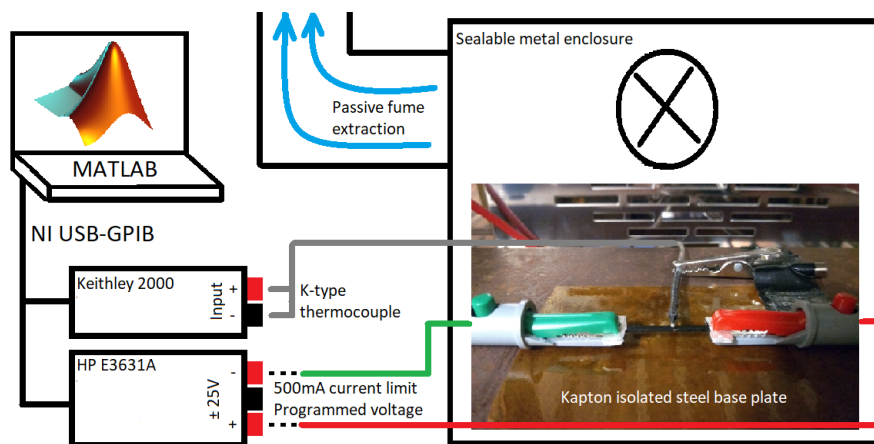


Figure 4.5: Measurement setup used for current density experiment

Figure 4.5 provides an overview of the used measurement setup. The sealable metal enclosure shown was the oven also used for annealing [60], which was equipped with a passive fume extraction system. As the samples would occasionally combust at their failure point, a 500 mA current limit was set to prevent the larger 5 mmx5 mm and 8 mmx8 mm samples from damaging the claps and wiring. It was later discovered during the experiment that this current limit should have been set higher as it affected the observable measurement, however care should be taken as samples were observed to self-combust in certain occasions at higher currents.

4.3.2 Voltage/Current profile

Given that the materials tested during this experiment all showed a positive temperature coefficient of resistivity in the oven experiment, it is expected that the samples resistance would go up as its internal temperature raises due to the current flow. This relationship between temperature and resistance could result in an issue with thermal runaway if we were to use a current controlled system. When the current controlled system would attempt to decrease the voltage to reduce the current, the samples temperature and thus its resistance could rise more rapidly than the response of the controller, defeating the control scheme.

To prevent this potential scenario the decision was made to apply voltage control, whilst recording the current, in order to ensure control loop stability as the samples resistance rises with temperature. Given the 50 V maximum output voltage provided by the programmable power supply, a profile of 1 V steps every 5 seconds was chose as shown in figure 4.6. This rate allowed for measurements with a duration of approximately 4 minutes per sample.

4.4 Results

The experiment was performed on three samples of the same cross-sectional area per material, for all five sizes, during a period of two days. The results of the real time measurements have been provided in appendix B and are provided as an average of these 3 measurements per sample. Graphs of resistances recorded before and after the experiment and post-experiment pictures showing the degradation of the samples are also provided.

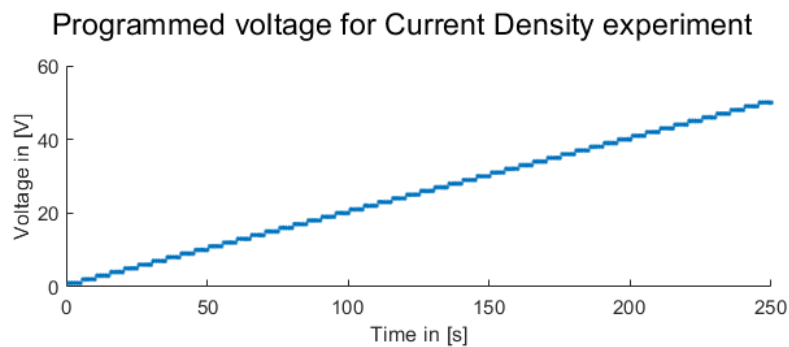


Figure 4.6: Voltage profile programmed during current measurements

4.4.1 Resistance

The first result that was obtained were measurements of the pre- and post-experiment resistances, showing the relationship with cross sectional area and resistivity. These values also provide an estimate of the currents which would result from the applied voltage.

The measurements as obtained by probing the samples with a multimeter [102], are shown in tables 4.3, 4.4 and 4.5. Samples for which the wire in between the contacts were dismantled are provided with a not available indication, due to their resistance being immeasurable after the experiment.

Ninjatek EEL 3D Printer Filament (90A)					
	1x1mm	2x2mm	3x3mm	5x5mm	8x8mm
Average pre	4717 Ω	1017 Ω	417 Ω	123.7 Ω	49.0 Ω
Average post	5383 Ω	N/A	N/A	90.2 Ω	27.9 Ω

Table 4.3: Average sample resistances measured for ninjatek current density samples

It can be derived from the tables that for the samples that were not destroyed during measurement, in general very little resistance change occurred. Larger cross-sectional area samples were affected the most which might be explained by a higher temperature being achieved in the core of the larger sample wires as an effect of a limiting thermal diffusivity.

Palmiga Innovations ETPU 85-700+					
	1x1mm	2x2mm	3x3mm	5x5mm	8x8mm
Average pre	7837 Ω	3033 Ω	1464 Ω	570 Ω	220.9 Ω
Average post	7340 Ω	2784 Ω	1413 Ω	716 Ω	355.2 Ω

Table 4.4: Average sample resistances measured for palmiga current density samples

It should also be noted that for the larger cross-sectional area ninjatek samples, a lower resistance was observed after the experiment. This would suggest an annealing effect, lowering the samples conductivity when exposed to the heat resulting from current flow. The palmiga and protopasta samples show the opposite effect, suggesting breakdown of contacts within the material due to the exposure.

Protopasta Conductive PLA					
	1x1mm	2x2mm	3x3mm	5x5mm	8x8mm
Average pre	619 Ω	167.5 Ω	79.4 Ω	31.4 Ω	14.0 Ω
Average post	N/A	N/A	N/A	60.1 Ω	12.1 Ω

Table 4.5: Average sample resistances measured for protopasta current density samples

This theory is also confirmed by the sample images as provided in figures B.2, B.5 and B.8, where degradation of the samples with higher resistance can be observed. The transition between the two effects can be observed the image for the 8x8 protopasta sample, which shows the onset of degradation as well as a slightly lowered resistance in table 4.5.

4.4.2 Current Density

In order to arrive at a derived current density, the currents passing through the samples were recorded as a function of time and therefore the applied voltage. These currents are provided as averages over the three measurements performed for each sample type in graphs as exemplified in figure 4.7, in which several key points have been marked in the form of symbols. The initial peak current achieved was marked by a circle, the following dip in current marked by a square. The last triangular marker indicates the peak current achieved which is either the point of failure or the point where the set current limit was achieved.

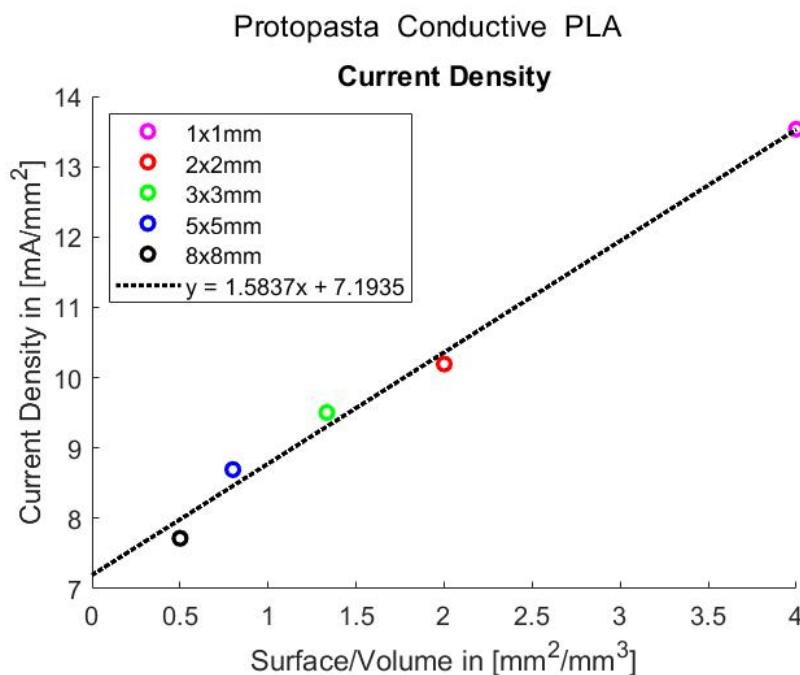


Figure 4.7: Example of marked current and temperature plots

The complete current measurements for the three tested materials are shown in figures B.1, B.4 and B.7, with the respective recorded maxima and minima being summarized in tables B.1, B.4 and B.7. With the currents derived, equation 4.2 can be defined for deriving the current density in mAmm^{-2} with I in mA the initial peak current marked by the circle symbol and A in mm^2 the cross-sectional area of the samples wire section.

$$j_{max} = \lim_{I \rightarrow max} \frac{I}{A} \quad (4.2)$$

The calculated current densities along with the area to volume ratio are provided in table 4.6 where surface area to volume ratio is also provided on the basis of the wire section in between the contact pads. The surface to volume ratio provides insight in the amount of material in which heat is being generated with respect to the outside faces through which it can be dissipated.

	Current Density				
	1x1mm	2x2mm	3x3mm	5x5mm	8x8mm
Ninjatek	7.1 mAmm ⁻²	5.3 mAmm ⁻²	4.7 mAmm ⁻²	4.7 mAmm ⁻²	4.4 mAmm ⁻²
Palmiga	4.9 mAmm ⁻²	2.3 mAmm ⁻²	1.7 mAmm ⁻²	1.3 mAmm ⁻²	1.2 mAmm ⁻²
Protopasta	13.5 mAmm ⁻²	10.2 mAmm ⁻²	9.5 mAmm ⁻²	8.7 mAmm ⁻²	7.7 mAmm ⁻²
A/V ratio	4,0 mm ⁻¹	2,0 mm ⁻¹	1,3 mm ⁻¹	0,8 mm ⁻¹	0,5 mm ⁻¹

Table 4.6: Derived current densities from measurement current and cross sectional area

Looking towards the results achieved for the current density, a relationship between the area to volume ratio and the available maximum current density can be observed. The lower the available area for dissipation in relation to the volume in which heat is generated, the lower the maximum current density achievable.

To get a sense of this relationship figures B.3, B.6 and B.9 were created, showing a plot of the current density as a function of the area volume ratio. In addition a linear relation of this slope was derived with the use of MATLAB's polyfit() [56] function, to derive a first order polynomial. This resulted in the relation between current density j in mAmm⁻² and surface to volume ratio r in mm⁻¹ as provided in equation 4.3 for the ninjatek samples. The relationship for the palmiga samples is provided in equation 4.4 and the relationship for the protopasta filament is provided in equation 4.5.

$$j = 0.77r + 3.89 \quad (4.3)$$

$$j = 1.07r + 0.45 \quad (4.4)$$

$$j = 1.58r + 7.20 \quad (4.5)$$

4.4.3 Temperature

In conjunction with the recorded currents, figures B.1,B.4 and B.7 also contain the observed temperatures at the surface of the samples. To provided some additional use to these recordings, the temperatures as recorded during the key points marked for the current are also provided in tables B.2, B.5 and B.8.

Interestingly the Protopasta samples maintained a temperature of approximately 35 °C raised from room temperature during the peak current, in comparison to the Ninjatek and Palmiga samples which both were observed to reach temperatures of approximately 50 °C. Potentially as a result of the larger resistivity of the latter two as determined in chapter A.2, requiring a higher voltage to arrive at the same power dissipation. This would result in a longer period during which the samples were exposed to heating, allowing for time to spread the heat throughout the sample.

For the temperature recorded up to the dip in the current a continuous approximately linear heating could be observed with the minimum in the recorded current serving as a transition point. After this point, the onset of a steep increase in temperature as a result of the steep

increase in current towards the failure point was observed with the failure temperature being the highest recorded for all samples.

4.5 Discussion

4.5.1 Current zones

One of the key decisions for the current density experiment lies in the pick of the marked point in the current and temperature measurements. These key points as exemplified in figure 4.7, were selected on the basis of a simple local maximum and minima basis.

The initial maximum achieved in the current as marked by a circle, was chosen as the sustainable peak current without material degradation. This was done based on the basis of the current drop that followed indicating an increase in sample resistance, corresponding to material degradation following from exceeding the samples ability to dissipate sufficient heat. The temperature increase from exceeding this threshold is best observable in the temperature plot for protopasta highlighted in figure 4.7 where following the circular marker, the temperature recorded at the samples surface is observed to rise.

Proceeding from this marked point to the following minimum in current as marked by a square, a sudden transition towards a lowering resistance is observed. This sudden change in behaviour might be explained by the sample reaching a state of annealing where the diffusion of carbon black particles in the polymer is increased. Furthering this suspicion would be the observation that the temperature recorded at this point is around 70°C, where carbon black filled PLA filaments were shown to soften at a glass transition temperature of 64,5°C [100].

As the temperature increases from this turning point onward, the temperature of the sample starts to increase to the point of either failure or the set current limit as marked by a triangle. It should be noted however that a similar result could not be obtained for the Palmiga samples, as the samples high resistance did not allow for sufficient power dissipation to reach the point of failure. The point of the transition was only reached for the 8x8 sample, providing limited insight into the further behaviour of the material.

The Ninjatek samples showed a lesser pronounced, but comparable, dip at around 70°C for the bigger samples, with a much steeper rise in current afterwards than observed for the PLA samples. The change in material properties observed at these temperatures could be explained by volatile agents in the TPU filament, which are known to be affected by temperatures of around 80 °C [103].

4.5.2 External influences

Due to the many temperature and dissipation dependant processes observed during this experiment, it is important to consider the effect of the testing environment itself. If these same experiments were to be conducted at, for example, a temperature of 30°C instead of the climate controlled environment of 21°C, the amount of available margin of temperature differential up to the 70°C transition point would be much reduced.

The humidity of the testing area could also affect results, since both PLA and TPU are well known to be hygroscopic materials [103]. As the samples were annealed their moisture content should have been reduced, but given the experiments took two days, re-absorption could have occurred, affecting the materials properties.

Lastly it should be mentioned that the passive fume extraction applied to the measurement setup would result in a slight draft which might also have affected the available rate of cooling. The enclosed environment might also have contributed to the containment of generated heat in the sample as it was designed to function as an oven intended to keep heat in.

4.5.3 Experimental improvements

In order to accurately determine the power being dissipated in the sample, a voltage measurement directly at the samples contacts would have been a great addition. The contact resistance would also have to be considered in this scenario, which could be characterized in a similar manner to previous work performed in section A.2.2 for the silver conductive paint.

It might prove insightful to create heat flow graphs specific to the materials in this manner, allowing for insight in the materials glass transition, crystallization and melting points. Furthermore a measurement of the temperature and moisture of the environment surrounding the sample might provide insightful.

4.5.4 Current density limit

The most important experimental derivation where the current densities as provided in table 4.6 in combination with the relation as to the area/volume ratio as provided by equations 4.3, 4.4 and 4.5. The relations as derived provide a fixed achievable current density, which is improved as the surface area/volume ratio is increased.

This suggested allowable current density even when a minimal external area is available contradicting the assumption made in section 4.1.1 that convection would provide the majority of heat transfer. Fortunately an alternative mechanism is provided in the same section, suggesting the potential of thermal diffusivity to be a limiting factor.

This would suggest a time dependence of the observed effect, which is the case, since the observed offset is much less for the Palmiga samples. Due to the high resistance of the Palmiga material, more time would have been required to achieve the high currents with the voltage ramp as provided by 4.6. This would allow the heat to spread out evenly throughout the larger samples, preventing the potential for observation of a higher than sustainable current density in equilibrium due to the samples thermal inertia.

Despite this observed thermal inertia, the rate as observed for the 1x1, 2x2 samples still provides some insight into the attainable current densities in equilibrium with the available heat dissipation. With current densities being achieved in the range of 5 mAmm^{-2} to 12 mAmm^{-2} , suggesting the same currents being achievable continuously for a wire of 1 mm by 1 mm.

4.6 Conclusions

4.6.1 Achievable current density

The highest achievable current density would be that of Electrifi as provided by its datasheet [65], being in the range of several [A]. The carbon black doped materials as tested during the experiment achieved lower maximum current densities as would be expected provided the difference in volume resistivity as derived in chapter A.2, provided the same sample sizing.

The Protopasta achieved the highest current density during the experiment, with a value of 13.5 mAmm^2 . Ninjatek followed with a value of 7.1 mAmm^2 , with Palmiga achieving a not fully verifiable 4.9 mAmm^2 due to the limit in achievable current as a result of the high sample resistances.

4.6.2 Area/Volume ratio

The current densities mentioned in the section above were taken for the 1 mm x 1 mm samples, with larger cross sections reducing the achievable current density. This effect could be related to the area to volume ratio, describing the material volume in which heat was generated to the area through which this heat could be dissipated. Providing an additional constraint to the achievable current density in relation to the conductor geometry.

4.6.3 Experimental improvements

During the experiment three main constraints were discovered, the first being the achievable current. This current was limited both by a configured current limiter on the programmable power supply itself as the achievable voltage by the power supply, limiting the achievable current for samples with high resistance.

The second constraint was found in the ramping rate set for the power supply voltage instead of the current. This resulted in different rates for differently resistive samples, resulting in difficulty observing effects due to thermal inertia in the relation between samples.

The third constraint resulted from the need of fume extraction for the experiment, resulting in a draft affecting heat dissipation convection. Ideally this flow would be well characterized and constant for all samples, which was not verified during this experiment.

5 Adhesion to Traditional Substrates: Printed Circuit Boards

With the material characterisation completed the ability of interfacing the printed conductors to conventional substrates was investigated. This first chapter on the characterisation of adhesion to conventional substrates will focus on the interaction of the material with traditional gold and tin contacts. These are commonly found on both printed circuit boards and silicon substrates containing integrated circuits as an interface amongst circuit components.

5.1 Previous work

5.1.1 3D printed circuits

As to gain some insight into previous work regarding the integration of 3D printed circuits, a literature study was performed into the manners of interfaces commonly applied. In general 2 of the for the experiments chosen materials were mentioned in literature for the creation of circuits interfacing with conventional surface mount components. Protopasta as demonstrated by [49, 50] and Electrifi as demonstrated by [50, 69]. Additionally, [106] demonstrated the use of a silver filled TPU ink to integrate traditional components and to create functional circuit elements with the material itself.

The usage of conventional circuit boards was not encountered during the literature study, due to authors making use of 3d printed traces as the component interconnects instead. This is surprising as the usage of conventional copper tracks could lead to lower impedances and a higher placement accuracy in comparison to these printed interconnects [31, 69]. This higher placement accuracy could allow for hybrid circuits, integrating conventional electronic components with larger more complex 3d printed structures such as inductive elements and antennas, which are difficult/expensive to manufacture conventionally.

5.1.2 Polymer metal bonding

Following from the fact that most printed circuit boards make use of a copper conductor coated with one of several metal/metal-alloy coatings [25]. And provided that a study on their interaction with printed polymers will be performed, a literature study into conventional metal-polymer bonding was also performed. Yoo [114] showed a comparison of several methods for the bonding of flexible Parylene micro electro-mechanical systems (MEMS), amongst which were conductive epoxy glue, ultrasonic wire bonds clamping two sections together as well as anisotropic conductive films (ACF) to form bonds in between gold coated silicon wafers and gold conductor containing polymers. ACF bonding was also shown by Yoon [115] for the interconnection of printed flexible circuit boards created from copper traces covered in gold though the ENIG method.

The ACF film typically consists of a polymer film wherein solder balls are suspended, as pressure is applied the solder balls connect the traces. The aspect ratio of the film in combination of the raised height of the traces ensures that only conduction in the desired orientation is achieved. The conductive epoxy and ultrasonic wire bonds were shown to operate in a similar manner, where the material is used as a conductor and a rivet mechanically locking the polymer in place for a reliable contact.

Another method of interconnecting substrates is to make use of so called bumping, where gold and tin coated bumps are used to provide a contact to gold or nickle-gold coated substrates. The two samples are pressed together at a raised temperature, forming a solder bond which

is suitable for adhering silicon flip-chips to both flexible polymer or conventional FR-4 circuit boards [116].

5.1.3 Traxel transmission line model

The third subject significant to the circuit board interface is the conduction of the 3d printed material itself at higher frequencies, given that impedance analysis will take place at higher frequencies. In previous work within the NIFTy group [21] a model describing the conduction model in within traxels was devised, including both the capacitive effect of the voids within the traxels themselves and their contact with other printed lines which is also effected by the axis along which the interface occurs. Anisotropic conduction was noted when a comparison was made with the conduction along the traxels when compared to conduction across the interfaces in between printlines, and it was suggested that the voids observed in between traxels could provide for capacitances along the interfaces.

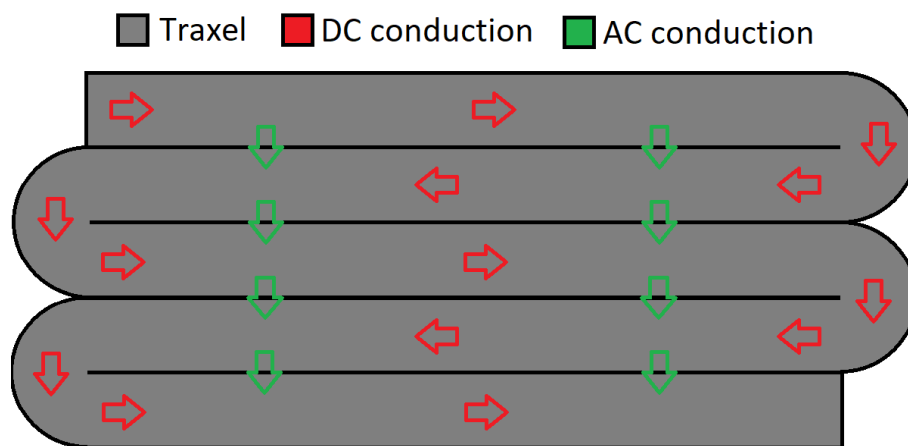


Figure 5.1: Traxel conduction model

Following along with the terminology introduced by [21] this anisotropic conductance resulted in a behaviour as shown in figure 5.1, where three main types of conduction are described. Bulk conduction, as shown in the figure by the green arrows where the material acts as an isotropic material, Traxel conduction as shown by the red arrows, where the current flows along the traxel and Mixed conduction where a combination of both effects occurs. In the described DC model, both modes can occur depending on the anisotropy ratio, defining the ratio of conduction along the traxel and in between the traxels.

Following from the interest in the creation of capacitive and inductive components, the behaviour of the material for AC signals is very relevant as they could affect component performance significantly. It has been theorized that the capacitance of the interface will result a dominant bulk conduction for AC signals, whereas for DC signals the traxel conduction will dominate. This would result in a series circuit of capacitance and resistance when crossing across the interfaces, which theoretically would be less pronounced for those samples where less traxels are crossed. If this theory holds a variation in traxel orientations should be able to provide a distinguishable difference, with traxels alongside and perpendicular to the current flow, providing a different impedance.

5.2 Sample design

In the case of the experiments for the contact in between printed circuits and conventional printed circuit boards, the samples will consist of two parts. Firstly a printed circuit board had to be designed which allows for the testing of the contact interface and provides a substrate on

which a conductive polymer can be printed. The second part of the sample will consist of a specific pattern of traxels on top of the printed circuit board.

5.2.1 Printed Circuit Board

Starting with the printed circuit board, a 1.6 mm thick FR-4 circuit board was designed to contain six 5 mm wide traces of 1 ounce copper. The contacts were spaced with respect to the other contact by 10 mm, 10 mm, 15 mm, 20 mm and 10 mm respectively. These traces were left exposed and coated either with HASL or ENIG. Lead-free HASL is a Tin based metal alloy coating which is flattened through a hot air blade commonly used to form solderable contacts. ENIG is a Nickel Gold coating which is also solderable, wire bondable and wear resistant [25]. Additionally these traces were formed to allow for standard 2.54 mm pins at each end, whilst spanning a marked printing area with a width of 20 mm, as shown in figure 5.2.

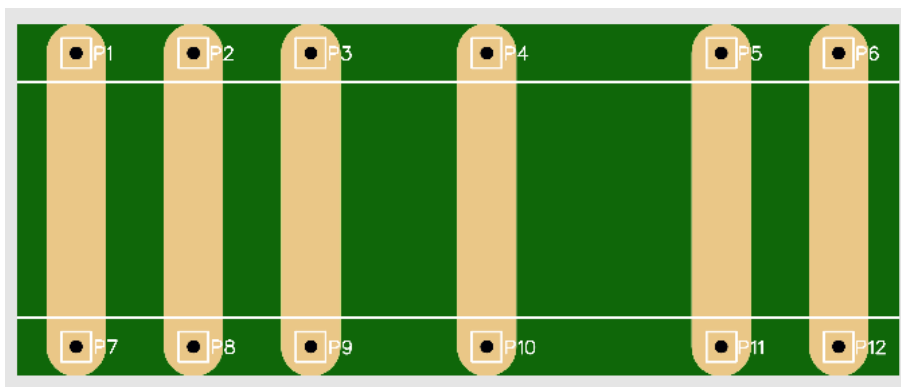


Figure 5.2: Design of printed circuit board

Various additional coatings were also considered which might be interesting for additional experiments, amongst which were Silver, which is very solderable and flat. Silver however can degrade due to Sulphur in the atmosphere and will therefore degrade over time if left exposed. A fourth option would have been a Carbon coated contact pad, which is a mechanically strong coating with good resistivity. Carbon also does not oxidize and could yield in an improved interface for carbon black filled polymers [25].

5.2.2 Infill design

The second part of the sample design is the traxel pattern as used for the sample printed on top, which are shown in figures 5.3 and figure 5.4. A total of 4 layers was printed on each PCB, resulting from the 0.3 mm initial layer defined by the slicing software for improved print adhesion, followed by three 0.2 mm layers. The provided design before slicing itself had dimensions of 1 mm x 20 mm x 75 mm, to cover the entire length of the printed circuit board.

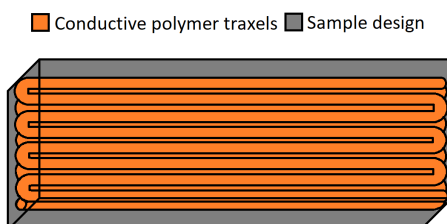


Figure 5.3: Alongside Infill pattern

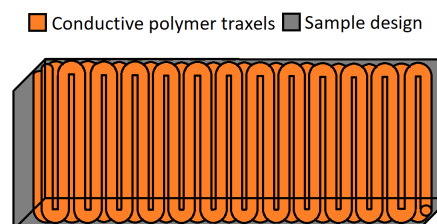


Figure 5.4: Perpendicular Infill pattern

5.2.3 Slicer settings

In table 5.1 the customized Cura slicer setting used for the polymer part of the samples are shown. No bed adhesion method was applied except for a cleaning of the PCB samples with IPA before printing, as the direct adhesion to the PCB and its coated pads was to be investigated. The infill orientations were chosen to be at 0° and 90° angles with a meandering infill pattern to allow for investigation of the transmission line model.

	Ninjatek [80]	Palmiga [83]	Protopasta [89]	Electrifi [65]
Bed	60°C	60°C	60°C	21°C
Nozzle	230°C	210°C	230°C	140°C
Flow	110%	110%	100%	110%
Layer height	0.2mm	0.2mm	0.2mm	0.2mm
Nozzle Size	0.4mm	0.4mm	0.4mm	0.4mm
Infill pattern	Meander	Meander	Meander	Meander
Infill percentage	100%	100%	100%	100%
Infill orientation	[0,0] or [90,90]	[0,0] or [90,90]	[0,0] or [90,90]	[0,0] or [90,90]
Wall/Top/Bottom	none	none	none	none
Print cooling	none	none	none	none

Table 5.1: Custom Cura Slicer profiles for sample creation

Additionally this meandering pattern allows for more consistent traxels improving adhesion, as the printer is not required to retract the filament from the printhead in between lines ensuring consistent material flow. Material printing settings were maintained to be similar to those used during the material characterisation in section 3.2.2 to allow for comparable conductivity, despite the potential for higher printing temperatures to increase adhesion as the material. This improved adhesion of materials is suggested to be a result of the filament maintaining a longer period above the glass transition temperature, allowing for it to conform more effectively to the surface as subsequent layers are added [32].

5.2.4 Locating jig

Given that our PCB could not directly be attached to the print bed, a manner of attachment had to be created. The devised solution was to coat the printbed in DimaFix [22] adhesion spray, after which a generic PLA jig could be printed allowing for exact placement relative to the coordinates of the printer.

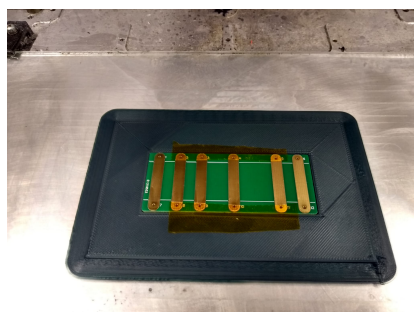


Figure 5.5: PCB locating jig

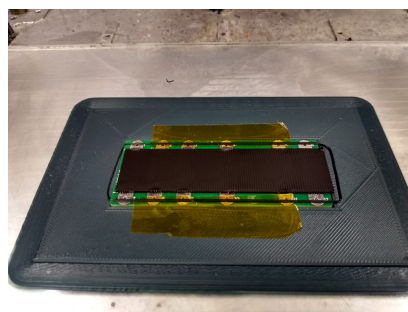


Figure 5.6: PCB after print

In order to prevent this jig from detaching the bed was kept at a constant 60 °C, with exception of the Electrifi print, for which the jig was taped to the glass bed after cleaning off the adhesion spray around the edges. Images of the jig with a PCB sample taped into place as well as a the jig after a print are shown in figures 5.5 and 5.6.

5.3 The Experiment

The experiment itself will make use of 2-wire based measurements allowing for the determination of complex impedances across a range of frequencies, in order to be able to determine the difference between observed contact impedances and the impedance of the material itself.

5.3.1 Transfer Length Method

The transfer length method was developed for the semiconductor industry [104] to characterize a materials properties whilst simultaneously deriving the properties of the contacts assuming those are sufficiently homogeneous. The method holds in situations where contacts are made on top of a thin piece of material, allowing for the assumption of a sheet current. This assumption holds for high aspect ratios as the current is forced to flow along the length of the sample whilst being minimally allowed to travel through the samples thickness. Equal contact spanning the whole width of a strip of material are placed at varying spacing, after which the impedance is determined across them through a 2-wire measurement method, including the contribution of the contact impedance.

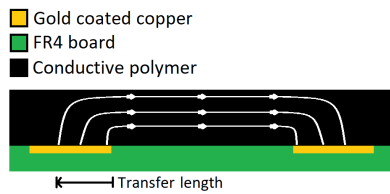


Figure 5.7: Transfer Length Visualized

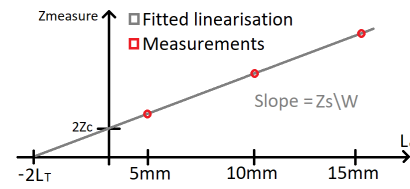


Figure 5.8: Transfer length derivation

Given that our samples are created in a slightly different manner than the usual transfer length samples, an illustration of the concept is provided in figure 5.7. As observed in the figure, the edge of the contact will be the point where the most current will flow, as the conductive polymer will have the lowest impedance across this span. Following the contact to the outside edges, the current will reduce, as the impedance of the polymer in between increases. In order to achieve a figure of impedance per unit area for the contact, a transfer length will be derived, which represents the effective length of the contact.

Since no direct method of measuring this impedance is available, measurements are taken at various contact spacings as shown in figure 5.8, measured as a function of the distance between the closest contacts. From these measurements a slope can be determined, providing sheet impedance over contact/sample width, as shown by equation 5.1. The contact impedance is represented by Z_c in Ω , the sheet impedance is given by Z_s in Ω and L_c and W provide the contact spacing and contact width in cm. The observed impedance during measurement Z_{dut} is also provided in Ω .

$$Z_{dut} = 2Z_c + Z_s \frac{L_c}{W} \quad (5.1)$$

By extrapolating this derived slope back to the zero crossing of the vertical axis, which would represent the edges of the contacts touching. The impedance of both contacts in series can be extrapolated as a function of the materials sheet impedance, sample width and the transfer length in cm. This relationship is provided in equation 5.2, relating it to the effective contact area.

$$Z_c = \frac{Z_s}{W} L_T \quad (5.2)$$

The relationship between the observed impedance and the length of the sample across which an effective current would flow is further clarified by equation 5.3, relating the graphs slope to the respective contact transfer length and contact spacing.

$$Z_{\text{dut}} = \frac{Z_s}{W}(L_c + 2L_T) \quad (5.3)$$

Given that the desired result would be the materials volume impedance in $\Omega \text{ cm}$ and contact impedance in $\Omega \text{ cm}^{-2}$, equations 5.4 and 5.5 are defined. The volume impedance being derived by multiplying the sheet impedance by the sample thickness T in cm, and the contact impedance per unit area being a result of the division of the observed contact impedance by the effective contact area.

$$\rho_{\text{volume}} = Z_s \cdot T \quad (5.4)$$

$$\rho_{\text{contact}} = \frac{Z_c}{L_T W} \quad (5.5)$$

5.3.2 LCR Measurement

For the measurements performed on the samples, use was made of a E5061B network analyzer [43], configured in a Gain-Phase series measurement configuration as shown in figure 5.9. This configuration is capable of providing a 10% measurement accuracy for impedances of roughly 10Ω to $10 \text{ k}\Omega$ from 1 kHz up to 30 MHz . In addition to the measurement schematic itself, the measurement probes and contacts are also shown, providing a interface to the device under test (DUT).

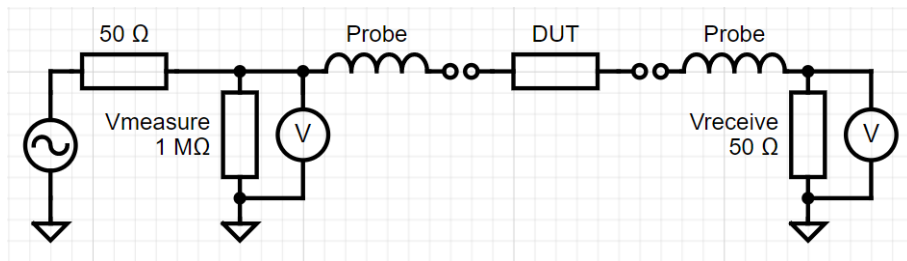


Figure 5.9: GP series measurement configuration for E5061B Network analyzer

However the measurement configuration as shown in figure 5.9 does not account for the contribution of the probes themselves to the measurement circuit. In figure 5.10 an overview of the expected real world measurement model is provided, with C_{stray} , L_{probe} and R_{probe} to represent the parasitic properties of the measurement probes.

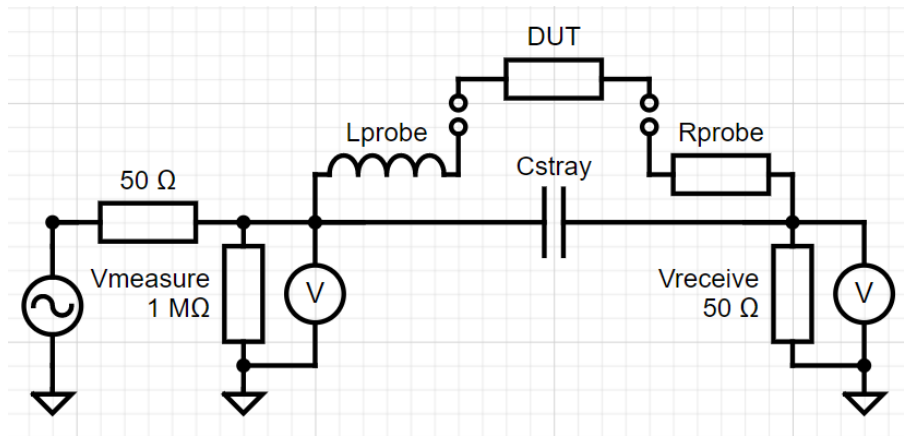


Figure 5.10: Overview of calibrated measurement system

In order to account for the capacitive, inductive and resistive contribution of the measurement probes and contacts, a set of calibration models is proposed for determining these characteristics as shown in figures 5.11, 5.12 and 5.13.

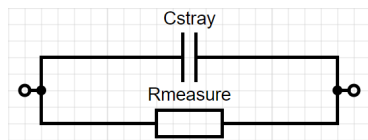


Figure 5.11: Open probes

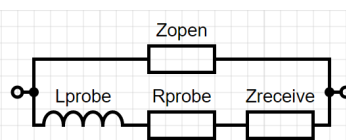


Figure 5.12: Shorted probes

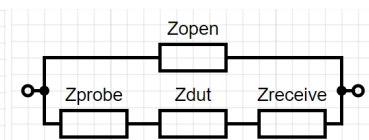


Figure 5.13: Loaded probes

Three configurations are provided the first being the open configuration. This measurement configuration consists of both measurement probes being left open, to determine the effect of the stray capacitance. Given that in this open circuit configuration has a very high impedance, the normally insignificant device measurement impedance $R_{measure}$ of $1\text{ M}\Omega$ should also be included in the measurement model, to ensure correct characterisation.

The second is the shorted probe model, where the probes are shorted together with a shorting bar or wire. Despite the low impedances expected for this characterization, the open model is contained in Z_{open} to allow for the contribution of the stray probe capacitance and the measurement impedance. The short results in the inclusion of the inductance and resistance of the probe wires, as well as the from the receiver port expected contribution $Z_{receive}$. This additional contribution which will be numerically captured instead of fitted, is suggested by the LCR datasheet [43] to contribute significantly past 1 MHz.

The third configuration shown is the loaded scenario, where a device to be tested is connected at the end of the measurement probes. For the calibration, use was made of a $50\text{ }\Omega$ Agilent 85033-60010 reference load [3]. The use of this reference load allowed for the validation of the achieved calibration with the use of Z_{open} , Z_{probe} and $Z_{receive}$ as performed before each measurement set.

5.3.3 LCR Fitting

Given that the derivation of component values from measurement requires a translation of the equivalent circuit to a model, a complex impedance model was defined for the components. The rules and equations describing this model are provided in table 5.2, where the behaviour of each component is characterized by its parameter p and angular velocity ω .

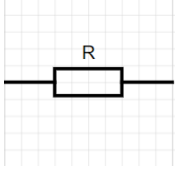
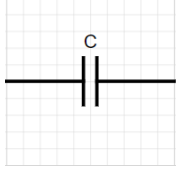
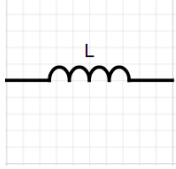
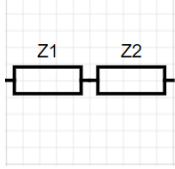
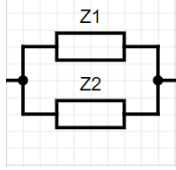
Resistive	Capacitive	Inductive	Series	Parrallel
				
$Z = p_R$	$Z = \frac{1}{j\omega p_C}$	$Z = j\omega p_L$	$Z = Z_1 + Z_2$	$Z = \frac{Z_1 Z_2}{Z_1 + Z_2}$

Table 5.2: Complex impedance modelling

The selected LCR measurement device was configured to obtain phase and impedance data, which relates to the complex impedance domain with the relation provided in equation 5.6. This conversion step was required as the MATLAB software [56] as used for processing is optimized for numerical operations upon complex numbers.

$$Z = |Z| e^{j\omega} \quad (5.6)$$

The obtained complex impedances are then fitted with the use of the `isqnonlin()` function offered by the MATLAB package, on the basis of previous work on equivalent circuit fitting within the group [94]. The `isqnonlin` function allows for the non-linear least square solving of a user defined error function on the basis of a provided initial estimate of function parameters with optional lower and higher bounds. Two error functions were defined as provided in equations 5.7 and 5.8 representing the fit of the real and imaginary part of the complex impedance respectively.

$$f_{\mathbb{R}} = \left| \log \frac{\mathbb{R}(Z_{fit}(\mathbf{p}, \omega))}{\mathbb{R}(Z_{meas}(\omega))} \right| \quad (5.7)$$

$$f_{\mathbb{I}} = \left| \log \frac{\mathbb{I}(Z_{fit}(\mathbf{p}, \omega))}{\mathbb{I}(Z_{meas}(\omega))} \right| \quad (5.8)$$

In the above provided error functions Z_{meas} represents the recorded measurement data, where Z_{fit} describes the achieved fit with the complex impedance model based upon the equivalent circuit. The angular velocity ω represents frequency at which the complex impedance was determined with \mathbf{p} representing the parameters being estimated. The `isqnonlin` function then takes this error vector and continuously updates the parameters within the specified bounds to arrive at a minimal solution of the sum of the squares of the error function across the whole set of recorded frequencies.

5.4 Results

5.4.1 Adhesion during printing

The first result indicating the ability of a material to adhere to the printed circuit board substrate and its coated traces is the manner wherein the print lines lay down on to the material. Images of the initial layer for each material will be shown for the samples where perpendicular infill was used, as these samples were most likely to detach, due to the print lines not spanning both the FR-4 and the coating materials.

The first print that was completed made use of the Ninjatek filament, which as is shown in figure printed well on the gold printed PCB as shown in figure 5.14. The print on top of the tin coated samples did not print as well as shown in figure 5.15 as observed from the slightly curling edges at the sides of the tin coated traces. This might stem from the slight curvature present in

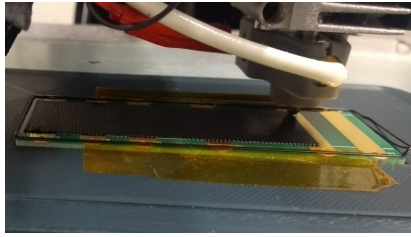


Figure 5.14: Ninjatek Gold print

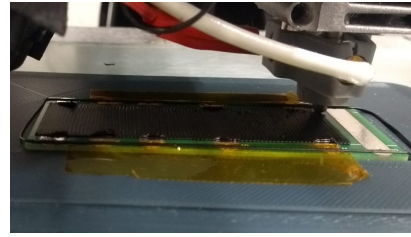


Figure 5.15: Ninjatek Tin print

these traces, resulting in a raised section in comparison to the rest of the board. After printing, both samples adhered well however, and remained attached up to the time of writing.

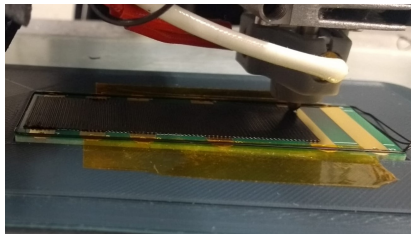


Figure 5.16: Palmiga Gold print

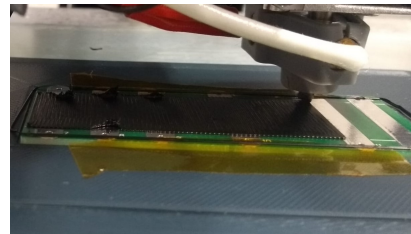


Figure 5.17: Palmiga Tin print

The second material to be attempted was the Palmiga filament, which also makes use of a TPU base polymer. As would be expected it laid down evenly on the gold covered sample as shown in figure 5.16. The tin sample initially showed to lift of the print during the first layer at the edges of the coated traced, as shown in figure 5.17. The sample however recovered afterwards, possibly due to variation in coating thickness. As with the other TPU based material this print also remained attached up to the moment of writing.

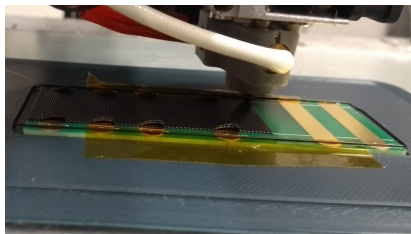


Figure 5.18: Protopasta Gold print

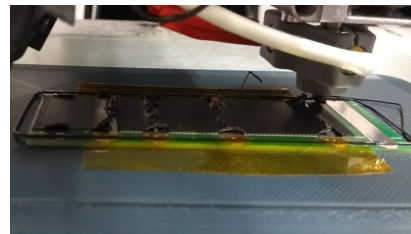


Figure 5.19: Protopasta Tin print

The first detaching print was that of the Protopasta filament, which printed considerably worse on top of the gold coated sample, as shown in figure 5.18. The tin coated sample print almost detached from the substrate as it appeared to not adhere to the traces with the same curling as observed previously around the edges for the TPU and tin samples. Although the print completed successfully, the print detached eventually and was discovered detached a few days after printing in the laboratory.

Given the initial success of these prints, a second attempt was made where an initial TPU buffer layer was printed, followed by three layers of Protopasta. Both Ninjatek and Palmiga filament were attempted as a buffer layer, but after printing it quickly became clear that the PLA filament had a tendency to warp and pulling off the substrate. The prints initially adhered well, but eventually were discovered to have partially lifted from the PCB sample, this warping is the sample images as provided in Appendix C.1.3 and C.1.4.

The last print that was made was that using the Electrifi filament, which was only attempted for the gold coated traces, as it despite showing improved adhesion as the print progressed failed

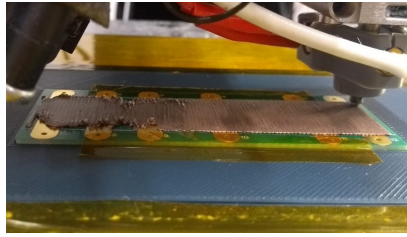


Figure 5.20: Electrifi Gold print

through detaching during printing. Given that the tin coated samples showed worse adhesion for all other samples it was decided not to proceed. The first printed layer on the gold coated traces is shown in figure 5.20.

5.4.2 Measured Impedance

Before LCR measurements were performed, a calibration was performed of the PCB samples which is described in detail by appendix C.2. The PCB samples were then connected to the network analyzer for which the resulting measurements after compensation will be provided in the following section.

In addition to these measurements, tables with a determined transfer length fit will be provided. These fits were derived with the use of MATLAB's `polyfit` function [56] to derive a first order polynomial on the basis of means of the measurement. These means were determined with the `mean` function for the impedances within the range of 100 kHz up to 30 MHz, as to provide an estimate of the average AC impedance obtained.

Ninjatek - Gold coated PCB

The first set of succesful samples to be tested were those of Ninjatek printed on top of gold coated PCB's for which the alongside traxel orientation is shown in figure 5.21 and the perpendicular traxel orientation is provided in figure 5.22.

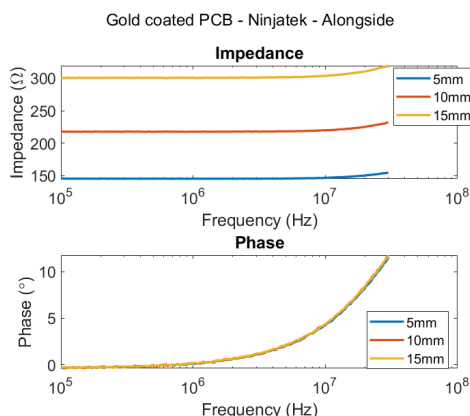


Figure 5.21: Ninjatek Gold Alongside

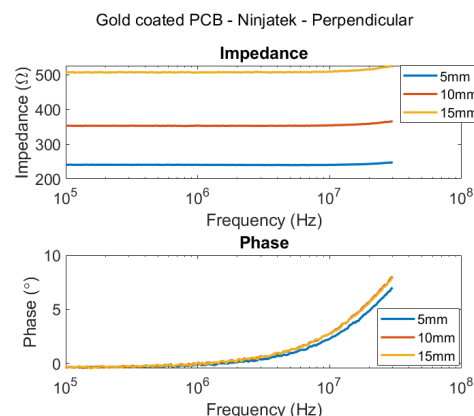


Figure 5.22: Ninjatek Gold Perpendicular

From the provided figures it can be observed that the samples are behaving like a resistor, with inductive behaviour at the higher frequencies. In table 5.3 the derived parameters for the transfer length model are provided as fitted from the means of the observed impedances.

For both the alongside and the perpendicular samples a transfer length that is shorter than the 0.5 cm contact pad length is derived. This validates the use of the transfer length method as the pad to material interface is sufficiently conductive to conduct all current along the contact path

Ninjatek	$2Rc$	Rs/W	T_L	ρ_{contact}	ρ_{volume}
Gold Alongside	66.54 Ω	156.23 Ωcm^{-1}	0.21 cm	78.12 Ωcm^{-2}	281.2 Ωcm
Gold Perpendicular	99.90 Ω	267.96 Ωcm^{-1}	0.19 cm	133.98 Ωcm^{-2}	482.3 Ωcm

Table 5.3: Determined resistivities of Ninjatek Gold samples

allowing for material characterisation. The contact and material resistivities also scale equally with an anisotropy ratio of 1,72.

Ninjatek - Tin coated PCB

The second set of succesful samples was the set of Tin coated PCB's upon which Ninjatek filament was printed, for which the alongside and perpendicular traxel orientation samples are shown in figures 5.23 and 5.24 respectively.

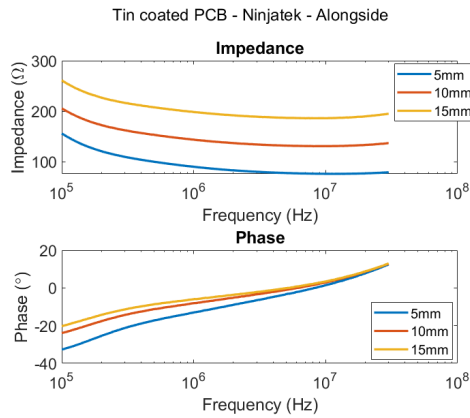


Figure 5.23: Ninjatek Tin Alongside

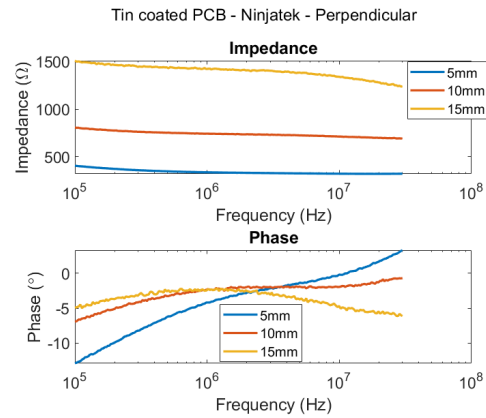


Figure 5.24: Ninjatek Tin Perpendicular

Unlike the Gold coated samples the Tin coated samples show a slightly capacitive behaviour for the lower frequencies up to 1 MHz within the magnitude of impedances, as is also reflected in the phase. After this initial phase shift a resistive behaviour occurs up until the previously shown point for which the inductive behaviour starts to come into effect. This effect is less expressed in the perpendicular samples hinting towards a capacitive influence even at higher frequencies.

In table 5.4 the derivations of the transfer length, the contact resistivity and the materials resistivity are provided. Due to the non-linear increase observed for the impedances of the perpendicular samples as the contact spacing was increased, only a negative transfer length resulted from the first order polynomial fit providing an invalid result for the resistivities as calculated. This could potentially be resolved by removing the 15 mm contact from the interpolation, however to maintain a fair comparison this was decided against as it might have skewed the results.

Ninjatek	$2Rc$	Rs/W	T_L	ρ_{contact}	ρ_{volume}
Tin Alongside	38.32 Ω	108.91 Ωcm^{-1}	0.18 cm	54.46 Ωcm^{-2}	196.0 Ωcm
Tin Perpendicular	-231.58 Ω	1057.98 Ωcm^{-1}	-0.11 cm	N/A	N/A

Table 5.4: Determined resistivities of Ninjatek Tin samples

Palmiga - Gold coated PCB

Continuing with the Palmiga filament samples printed on gold coated PCB's the resulting measurements are provided in figures 5.25 and 5.26 for the alongside and perpendicular orientations respectively.

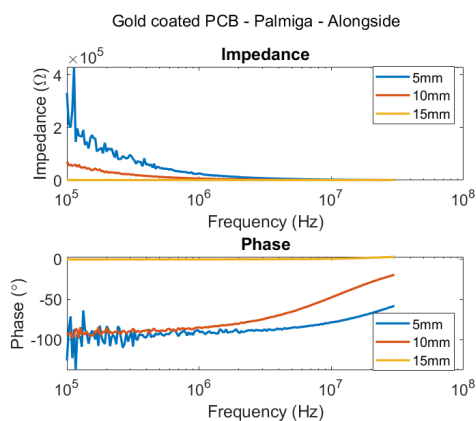


Figure 5.25: Palmiga Gold Alongside

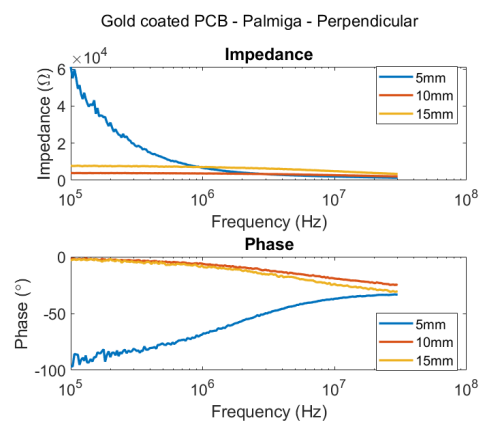


Figure 5.26: Palmiga Gold Perpendicular

From the figures it can quickly be derived that 5 mm and the 10 mm spaced contacts failed for the alongside sample and that the 5 mm contact failed for the perpendicular sample. The impedance slope and phase observed for these failed contacts behave as a capacitor, with a -90° phase shift and an exponentially decaying impedance, suggesting contact separation at the interface forming a parallel plate capacitance.

Palmiga	$2Rc$	R_s/W	T_L	ρ_{contact}	ρ_{volume}
Gold Alongside	$59\,722.74\ \Omega$	$-41\,523.65\ \Omega\text{cm}^{-1}$	$-0.72\ \text{cm}$	N/A	N/A
Gold Perpendicular	$11\,788.24\ \Omega$	$-4846.64\ \Omega\text{cm}^{-1}$	$-1.22\ \text{cm}$	N/A	N/A

Table 5.5: Determined resistivities of Palmiga Gold samples

In table 5.5 the resulting derivation of the transfer length is shown, with a negative length for both samples. In this scenario the method indicates that the contact provided was insufficient to conduct the current required to characterize the material on top. Therefore the derived contact and volume resistances are not provided, as they could not be accurately derived with the provided contact area.

Palmiga - Tin coated PCB

The fourth and last set of successfully adhered samples were the Palmiga filament prints on top of tin coated PCB's, for which the measurements are provided in figures 5.27 and 5.28 for the alongside and perpendicular travel orientations respectively.

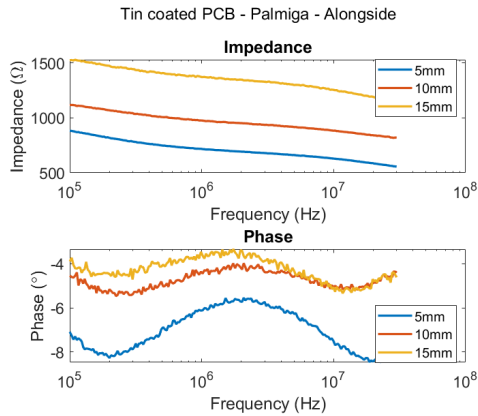


Figure 5.27: Palmiga Tin Alongside

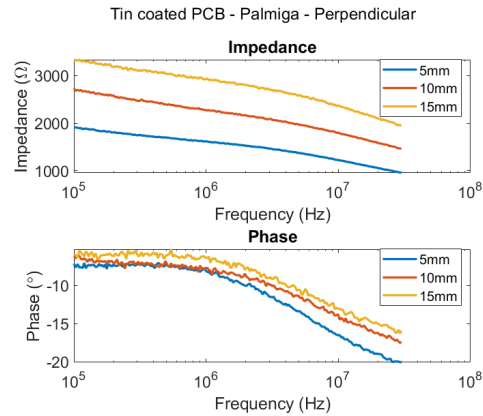


Figure 5.28: Palmiga Tin Perpendicular

As observed in the figures, the tin coated samples form a mostly resistive contact with a slight capacitive contribution as observed in the negative phase and the decreasing impedance with increasing frequencies. This capacitive contribution appears to be more pronounced for higher frequencies suggesting a secondary effect occurring.

Palmiga	$2Rc$	R_s/W	T_L	ρ_{contact}	ρ_{volume}
Tin Alongside	362.34 Ω	642.28 $\Omega \text{ cm}^{-1}$	0.28 cm	321.14 $\Omega \text{ cm}^{-2}$	1156.1 $\Omega \text{ cm}$
Tin Perpendicular	876.57 Ω	1256.89 $\Omega \text{ cm}^{-1}$	0.35 cm	628.44 $\Omega \text{ cm}^{-2}$	2262.4 $\Omega \text{ cm}$

Table 5.6: Determined resistivities of Palmiga Tin samples

In table 5.6 the derivation of the transfer length for the samples is provided, which validate for both samples with being shorter than the PCB contact pads. The resulting contact and material resistivity both scale with an anisotropy factor of 1,95.

5.5 Discussion

5.5.1 Material adhesion

The most important goal of this experiment was set to determine the ability of conductive polymers to adhere to both the FR-4 circuit board substrate as the gold and tin contact pads as representative for both PCB and silicon die substrates. During the creation of the samples itself it was noted that the management of the samples temperature was of great importance for the adhesion of the printed polymer. As indicated by the flexible TPU polymers only being able to remain adhered to their substrate, and the PLA Protopasta filament which adhered initially detaching.

Potentially either a polymer blend to match the thermal expansion of the substrate or a form of mechanical clamping of the polymer to the underlying substrate would provide a solution to the warping encountered as an effect of the internal stresses during and after printing. The alternative solution of including a flexible buffer layer in between the warping polymer and the substrate was also attempted, but resulted in similar detachment of the prints. This suggests that for a successful implementation of this method a stronger substrate-buffer bond would be desired.

5.5.2 Interface quality

Given the only sets of successful samples were of the carbon black doped TPU filaments, the characterization of the interface will be provided for these materials.

Gold interface

The first set of samples to discuss are both the Ninjatek and Palmiga prints on gold coated PCB traces, for which two types of behaviour were observed. The first being the behaviour of a well adhered contact, where the polymer is laying flat on top of the contact making uniform contact, resulting in a resistive behaviour as observed for the Ninjatek on gold prints and the 15 mm Palmiga on gold contact spacing. This behaviour is described as the left scenario as shown in figure 5.29, and provides a 0° phase shift in theory. However due to the properties of wires at higher frequencies a slight inductance appears, which will not be considered for the contact characterisation.

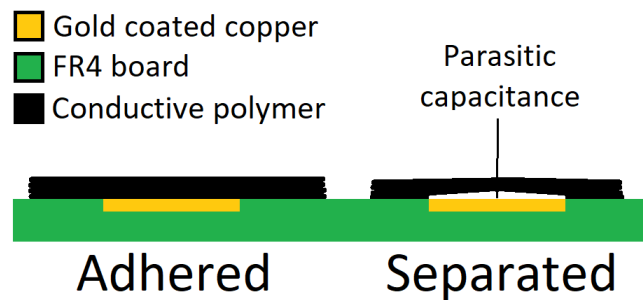


Figure 5.29: Gold contact behaviour

The second scenario for a gold contact was observed for the capacitive contacts found for the 5 mm and 10 mm alongside and 5 mm perpendicular palmiga prints on gold contacts where the contact is expected to have lifted from the contact pad, resulting in the right structure as shown in figure 5.29. The behaviour of this structure is shown to be that of a RC-series circuit, where initially the impedance drops with frequency until the series resistance minimum is reached. This RC circuit consists of the capacitance between the pad and the material and the resistance being formed by the section of material in between the contacts themselves. This theory is also supported by the observed initial -90° phase shift, matching to a RC-series circuit.

In the case that partial contact remains, as is suspected for the perpendicular 10 mm and 15 mm contact spacings, a RC-parallel circuit in between the contact pad and the material is formed. This would have the effect of an initial impedance equal to the impedance of this contact in series with the material, which eventually starts to decrease as this contact resistance is bypassed by the capacity between the material and the contact. This theory also aligns with the observed initial 0° phase shift with it moving to -20° as the impedance starts to decrease in contrast with the previously observed 10° inductive phase shift for a similar resistive contact sample.

Tin interface

The interface to the tin coated samples is inherently more difficult to characterize, as it consists of three regions in the observed impedance and phase. The first region observed for both the Ninjatek and Palmiga samples is a decrease in impedance, until a certain limit is reached in combination with a negative phase shift. This suggests an RC-series circuit as formed by the materials resistance and a capacitance between the material and the contact pad.

This region is followed by an approximately constant region in phase and impedance. This is followed by decreasing impedance for most samples, suggesting an RC-parallel circuit between the material and the contact pad. This mixed set of effects can be explained with the use of figure 5.30.

Due to the tin oxidizing there will always be a slight capacitance between the material resistance and the contact pad, forming the RC-series circuit responsible for the initial decrease in impedance up to the material resistance. The secondary capacitive effect can be explained

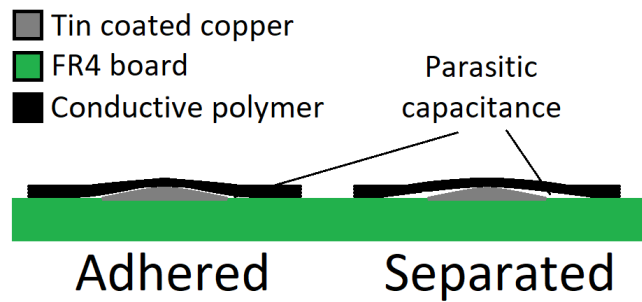


Figure 5.30: Tin contact behaviour

by the voids formed in between the material and the contact pads for the curved tin coating during printing resulting in a parasitic capacitance at the edges of the contacts as can also be observed in progress in figure 5.19.

This secondary capacitance starts to conduct at higher frequencies effectively shortening the length of the material printed on top, resulting in a impedance drop. It can also be noted that the corresponding phase shift is most pronounced for the perpendicular samples, where the traxels are printed along the contact pads instead of across, resulting in a smaller void. This agrees with the expectation that a smaller air gap in a capacitor leads to a greater capacitance, meaning that a lower impedance is achieved at the same frequency than for a smaller capacitance. This would initiate the impedance drop at a lower frequency confirming the non-intuitive result that for Tin coated samples the parasitic effects are more defined for the uniformly adhered samples.

It should also be noted that this effect is observed to a lesser extend in the Ninjatek on Tin samples, potentially due to the better adhesion of the material minimizing void formation. This results in the domination of the inductive effect for the alongside and part of the perpendicular samples.

5.5.3 Carbon interface

Although not covered in this set of experiments the usage of carbon contacts could provide several benefits as derived from the gold and tin experiments. Carbon does not oxidize like with gold resulting in the inherent capacitance as observed for the tin samples due to the oxide layer. However where gold is a relatively smooth surface, carbon is rough providing a potential for improved layer adhesion, whilst also providing a flat surface as it is directly printed on top of the copper layer [25]. It is therefore highly advisable to test this surface coating in future experiments where contacts to 3D printed polymers are desired.

5.5.4 Conduction

The conceptual traxel transmission line concept would suggest that the material resistivities observed during these high frequency experiments would be significantly lower than the material resistivities as determined at DC in chapter 3. This however turns out not to be the case, with the anisotropy factor actually increasing for both the Ninjatek and the Palmiga filament given the from the Ninjatek Gold samples derived 1.72 ratio and the from the Palmiga Tin samples derived 1,95 ratio, as compared to the previously determined 1,32 and 1,74 ratios.

This increase in inter-traxel impedance is also observed from the derived resistivities with $281.2 \Omega \text{ cm}$ alongside and $481.6 \Omega \text{ cm}$ perpendicular for the Ninjatek filament in comparison to the previously observed $21.52 \Omega \text{ cm}$ alongside and $28.49 \Omega \text{ cm}$ perpendicular resistivities. With the same being observed for the Palmiga filament with $1153.7 \Omega \text{ cm}$ alongside and $2259.1 \Omega \text{ cm}$

perpendicular in comparison to the previously observed $69.00 \Omega \text{ cm}$ alongside and $119.96 \Omega \text{ cm}$ perpendicular resistivities.

This unexpected increase points towards a change in printing conditions, which was not accounted for in the print settings as these were kept identical across both characterizations. The introduction of the printing jig and the FR-4 substrate might have contributed to a reduction in the ability of the heated bed to effectively pre-heat the material during printing, resulting in reduced inter-layer fusion that could account for the difference in the anisotropy ratio.

The large deviation in observed volume resistivity however is more difficult to clarify, and might be related to the by a factor three reduce vertical layer count in comparison to the previously characterized samples. This would suggest a difference between xy-plane inter-traxel impedance and z-plane inter-traxel impedance.

5.6 Conclusions

5.6.1 Contact

The gold contact material in combination with the Ninjatek filament resulted in the most effective contact, whereas the Palmiga filament on the same contact material resulted in release from the substrate. The Tin contacts resulted in a capacitive contact contribution as an effect of the natural tin oxide, however its curved surface did result in improved adhesion for both the Ninjatek and Palmiga filaments.

It was also discovered that the still Protopasta and Electrifi materials were not suited for direct adhesion to the PCB and contact material. Electrifi immediately released after being disturbed by the printhead after the first layer, Protopasta tended to initially stick however after being left to cool down it would release. This is theorized to be related to the different rates of thermal expansion effectively straining the interface, which cannot be accommodated for in the stiff materials.

5.6.2 Reliability

The reliability of the adhesion of samples created with the TPU filaments was found to be sufficient to maintain adhesion to at minimum the PCB substrate for the several months that passed up to the time of writing. The Protopasta samples as mentioned appeared to adhere initially but were discovered to have failed after several days, Electrifi failed immediately during printing. Several attempts were made to improve the adhesion of the Protopasta filament through the use of a TPU buffer layer, for both of the selected TPU materials these attempts also failed after several days.

5.6.3 Improving adhesion

Following from the experimental results, it is strongly suggested that a carbon coating of the contacts is attempted. This would both provide a material that does not result in capacitance due to an oxide layer as well as a textured surface for improved layer adhesion. Material wise matching of the thermal expansion of the printed polymer and the substrate could avoid stresses observed during cooling, especially affecting the stiff materials.

6 Adhesion to Traditional Substrates: Silicon wafers

Given that many modern electronics are based on integrate circuits created with the use of a silicon substrate, the adhesion of conductive polymers to this material was also tested. Given that the common contact materials available in silicon processes have already been covered by the experiments in chapter 5, only the adhesion to the silicon material itself will be attempted.

6.1 Previous work

6.1.1 Silicon contact pads

As we wish to take a look into printing directly on top of silicon wafers, a manner in which contact is achieved should also be discussed. Typically contact to silicon dies is made by a wire bond between a special metal bond pad on the die and an exterior package to be used for connection to a circuit board substrate. The materials for these bonding pads are typically gold, aluminium or palladium with the wires connecting to them being formed from either gold, copper, coated copper or silver [52]. Given that the rest of the silicon wafers surface is typically covered by a passivation layer, such as silicon oxide (natural oxide) or silicon nitride [53]. It is desirable to attain adhesion to these materials as well, with the contact pads serving as the interface to the printed conductive polymer.

6.1.2 Silicon-Polymer bond

In order to investigate the ability to adhere silicon and its passivation layer to the polymer, various wafer to wafer bonding methods were compared. In many of these bonding processes a polymer is involved, which could be used as to derive a reference. One example is the use of polyimide and polybenzoxazole as a buffer layer that will adhere to both silicon-oxide and silicon-nitride passivation layers, allowing for adhesion of traditional wafers [53, 11]. Another example commonly used in the creation of lab-on-a-chip devices are permanent photosensitive dry-films, which are patternable polymers capable of adhering both to glass and silicon substrates to form channels and microfluidic channels [40].

The creation of a bond through a mechanical lock between materials is also commonly observed in literature. Several techniques were presented by [114] such as the creation of a bond through conductive epoxy, ultrasonic riveting, polymer-ultrasonic-on-bump (PUB) bonding and solder bumping. The first two of these methods function by creating a perforation of the material, allowing for mechanical retention of the material. The second pair of methods relies on the formation of a metal to metal bond, by application of heat/ultrasonic energy and pressure.

6.2 Sample design

For the silicon wafer adhesion experiment the samples consisted of two parts, the first being a silicon wafer which were drilled with the use of diamond drill to add a centered 5 mm hole. The second part consisted of a conductive polymer plug which is printed in place with the use of a small locating shim. This centering shim was initially printed on the bed to ensure correct placement of the wafer in relation to the printer.

6.2.1 Infill design

The centering shim was printed with a loose tolerance to the 5 mm hole in the wafer. Its height was chosen to be than less than that of the 525 μm wafer at 300 μm . As for the infill pattern a concentric pattern was chosen to ensure a consistent circumference and is provided in figure 6.1.

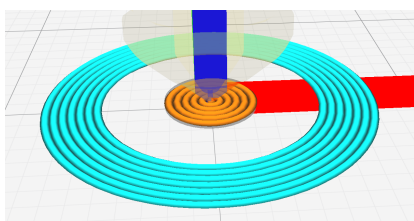


Figure 6.1: centering shim infill

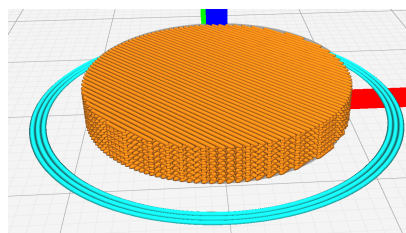


Figure 6.2: Plug infill

The polymer plug was printed after the wafer was placed on top of the printed centering shim. Its infill pattern consisted of a typical 45° cross lamination of traxels, as commonly used for solid areas of 3d printed parts. The resulting slice of the 20 mm diameter, 3 mm tall cylinder is shown in figure 6.2.

6.2.2 Slicer settings

The centering shim was printed out of a in water soluble polyvinyl alcohol (PVA) material, as it was initially intended to be dissolved. It was later discovered that this dissolving process resulted in the release of the plug printed on top, resulting in the usage of a polyimide covering instead in combination with a reduction of its height.

The conductive polymer plugs were printed in all of the selected conductive filaments, with print settings optimised on the basis of manufacturer recommendations. An overview of the used slicer settings is provided in table 6.1.

	Ninjatek [80]	Palmiga [83]	Protopasta [89]	Electrifi [65]	PVA
Bed	60°C	60°C	60°C	21°C	60°C
Nozzle	230°C	230°C	210°C	140°C	215°C
Flow	100%	110%	110%	110%	100%
Layer height	0.2mm	0.2mm	0.2mm	0.2mm	0.2mm
Nozzle Size	0.4mm	0.4mm	0.4mm	0.4mm	0.4mm
Infill pattern	Lines	Lines	Lines	Lines	Concent
Infill percentage	100%	100%	100%	100%	100%
Wall/Top/Bottom	none	none	none	none	none
Print cooling	none	none	none	none	none

Table 6.1: Custom Cura Slicer profiles for sample creation

6.2.3 Order of operations

Due to the various steps involved in the production of the wafer-based samples, a detailed description will be provided. The management of the warming and cooling of the silicon wafers was found to have a great effect on the adhesion of the printed polymers in initial experiments, requiring special care during sample preparation.

The first step was to prepare the wafer by a drilling operation the result of which is shown in figure 6.3. This operation is followed by a thorough cleaning with IPA to get rid of any residue left by the drilling operation.

The second step is shown by figure 6.4 and involves the preparation of the wafer by covering the 5 mm hole with a 11 mm adhesive circular piece of polyimide film. The film is carefully and thoroughly stuck down after which an additional IPA clean of potential contaminants is performed.

Polymide film was chosen as a covering material due to its well known high temperature resistance and ability to provide a printing substrate for FFF processes [57]. The wafer was then placed on the print bed centered on the basis of the PVA shim and attached with the use of additional polyimide film adhesive tape.

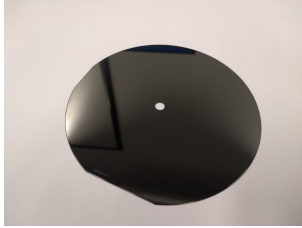


Figure 6.3: 5mm drilled wafer

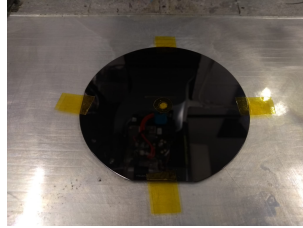


Figure 6.4: PVA shim infill

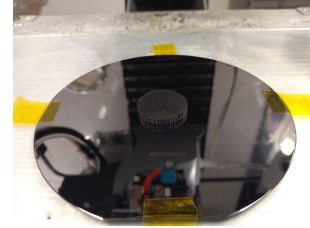


Figure 6.5: Sample printing

The third step was to allow the wafer to warm up to the printbed temperature for a period of 15 min. The plug was then printed and subsequently left to cool down slowly, with a result as provided in figure 6.5. This slow cooldown was achieved by leaving the sample on top of the printbed, which cooled to 30 °C in a period of 30 min after being switched off.

6.3 The Experiment

The experiment itself was devised to allow for a method that represents a combinatory form of the pull and peel tests as defined by ASTM D903 and D4541 [12, 13] for the testing of coatings and adhesive bonds. A conceptual drawing of the experiment is shown in figure 6.6, where the wafer with the printed plug on top, is clamped in between two aluminium plates. On either side of the wafer O-ring seals support and seal the wafer against the pressure of the applied gas pressure.

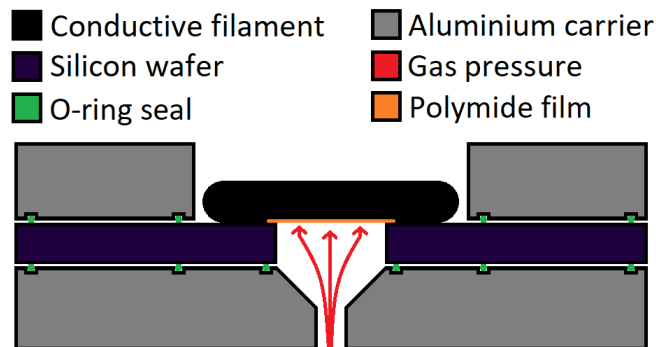


Figure 6.6: Wafer experiment concept

Peeling tests are commonly performed in a manner where an average force required for peeling is derived at a fixed peeling rate. The bounding geometry is given by the width of the peeled piece of material, providing a relationship in force required to peel an area per unit time. The metric provided for pull-off tests is given in required force for release per unit area, with also commonly the rate at which the test was performed being recorded. Meaning that both tests are based on a similar figure, although separated by the time required for release.

For stiff materials the proposed pressure test should behave as a pull-off test, determining the maximum pressure and thus force per unit area required for the sample to pop off the wafer. For flexible materials a peeling effect is expected, where the the sample deforms under pressure allowing the sample to pull away from the wafer. However due to this additional exposed area, the net force per unit of attached area increases as a result of the pressure. The aim of this

runaway effect is to result in a sample quickly releasing as it starts to pull away, resulting in the time metric for all materials being related to the rate of pressure increase.

6.3.1 Wafer pressure jig

The realization of the suggested experimental setup is provided in an aluminium clamping jig with embedded o-ring grooves as shown in figure 6.7. The center featured a countersunk threaded hole on one of the two plates for the insertion of an gas fitting, where the other plate offered a hole for the printed plug to fit into. The two plates were held together with six M6 bolt, which are only tightened by finger, as to keep the two plates from separating.



Figure 6.7: Wafer clamping jig

Additional force to increase clamping pressure was attempted, however due to the fragile nature of the thin wafers this resulted in fracturing along the crystal lines. This potentially could have been resolved with the use of a torque wrench, however due to the small forces required for damaging the wafers and the limited stock, this was not attempted. Fortunately gravity along with a finger tightening of the bolts provided sufficient clamping force to provide a seal.

6.3.2 Pressure supply and recording

During the experiment itself, pressure was taken from a lab 10 bar dry nitrogen gas feed and fed into a Festo [27] manual pressure regulator with a dial indicator. In order to ensure an accurate readout of the pressure, a GEMS [33] pressure transmitter was included at the termination leading to the wafer jig. This provided a 0 V to 5 V linear readout for pressures from 0 bar to 6 bar, which were logged at 1 kHz with the use of the analog input of a National Instruments MyDAQ [71]. In figure 6.8 an overview of the setup and connections is provided with the inclusion of the protective enclosure also used during the experiment.

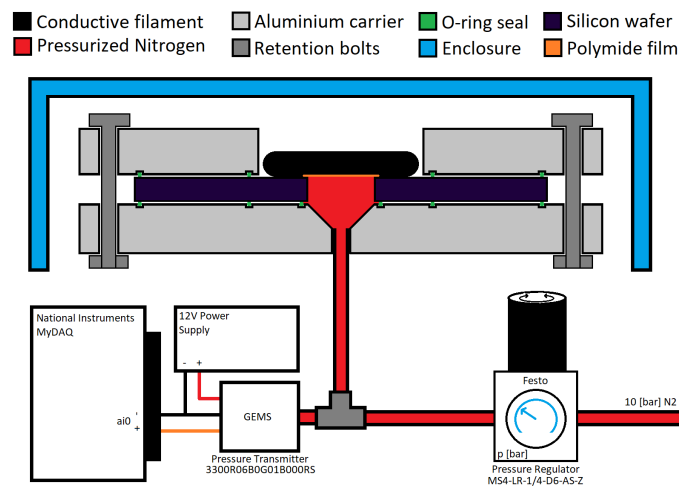


Figure 6.8: Experimental pressure testing setup

6.4 Failure point measurement

Given relative nature of this test, the unit of measurement will be the pressure applied when failure occurs. Failure being indicated by the pressure dropping as the sample is released from the wafer substrate. The contribution of the polimide adhesive film will be accounted for by taking a control sample only containing the film covering in order to determine the required pressure for its release from the wafer substrate.

For this failure point analysis to hold a few assumptions are required. The first being that no leakage occurs past the sample, which would result in a pressure drop across the opening and therefore the sample. The second assumption is that the 3d printed plug is not porous, releasing the provided pressure through internal voids. The third assumption is that a pressure drop will be observed as the sample is released, which could not be the case if the orifice through which the air is passed to the wafer is small in relation to the flow, resulting in sufficient restriction to retain pressure.

6.5 Results

The results following from this set of experiments will be presented in two parts, initially a look at the adhesion observed during printing will be provided, which will then be followed by the pressures recorded at which separation occurred for the various samples.

6.5.1 Adhesion during printing

The first indication if a material is likely to adhere well to the silicon wafer is its behaviour during printing, materials that warp upwards away from the build surface indicate a bad adhesion, whereas materials that stick to the surface are more likely to remain adhered. In the case of the tested conductive polymers, both the TPU filaments showed to adhere, with a slight warping being observable. As shown in figure 6.9 the Ninjatek filament had a tendency to warp slightly upwards at the edges, this was also observed to a lesser extent in the Palmiga filament, which as shown in figure 6.10.

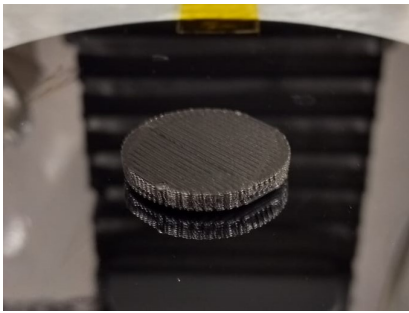


Figure 6.9: Ninjatek printing result

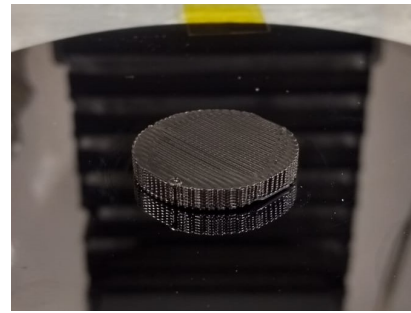


Figure 6.10: Palmiga printing result

The other two less flexible filaments as also observed during the PCB experiments, had a much greater tendency for warping, and resulted in incomplete prints being abandoned after the first 2 layers in order to prevent the nozzle from pushing the filament from the wafer. The curvature can clearly be observed in figures 6.11 and 6.12 for the Protopasta and Electrifi filaments respectively. Due to these incomplete prints it was decided to only continue with a single sample for each of these materials.

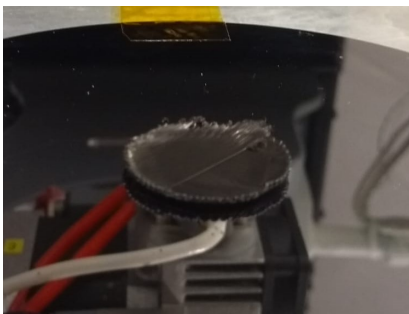


Figure 6.11: Protopasta waferprint top

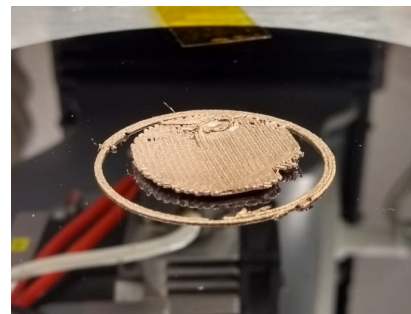


Figure 6.12: Electrifi waferprint botom

6.5.2 Seperation pressure

The second part of the determined adhesion is the results following from the pressure testing. During all shown measurements the pressure was increased manually until the sample was observed to detach, after which the pressure regulator was closed. The shown data was pre-processed to provide the voltage to pressure conversion. The signals recorded were also filtered with the use of a thirty point moving mean windowing function realized in MATLAB with the use of the `movmean()` function [56], to reduce part of the noise spikes observed in the measurements.

The first set of recordings are provided for the Polyimide film control, the Electrifi filament and the Protopasta filament in figure 6.13. The Polyimide film is shown to reach the lowest pressure before failure, with the electrifi sample following closely, arguably within the margin of error. The protopasta sample has a notably faster pressure ramp, due to the inaccuracy of the pressure increase with the manual regulator. The observed noise was due to the sample detaching whilst with the film only partly detaching, resulting in an audible oscillation in the flow past it.

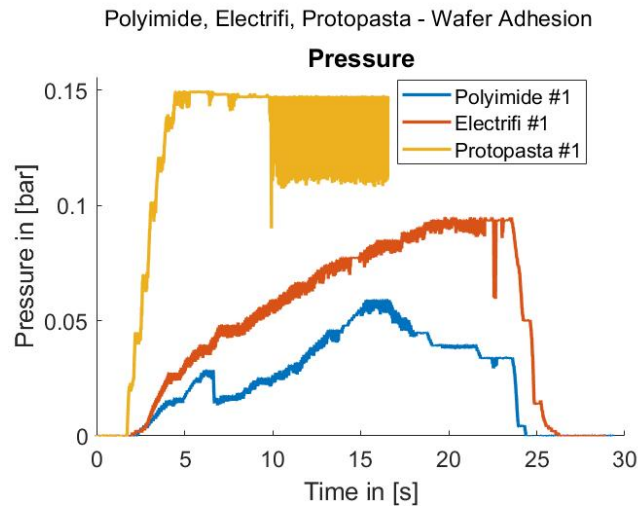


Figure 6.13: Pressure graphs observed for polyimide film, electrifi and protopasta samples

The measurement results for the ninjatek samples are provided in figure 6.14. It can clearly be observed that samples two and three failed at a pressure similar to that as observed for the Polyimide film. The first sample is observed to have been attached to the wafer, resulting in a higher attained pressure before detachment.

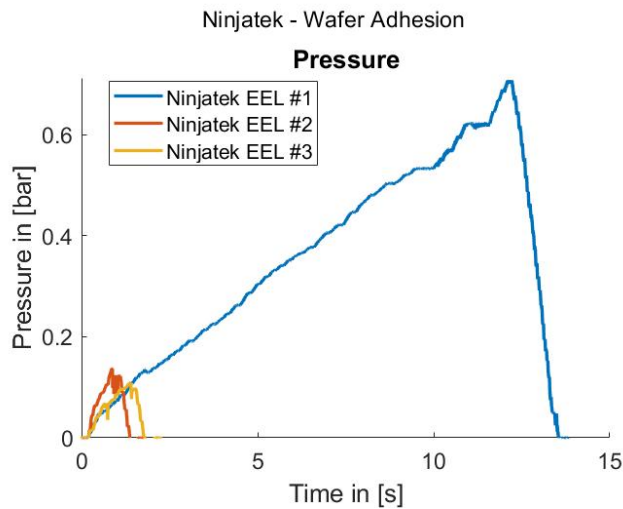


Figure 6.14: Pressure graphs for ninjatek samples

The palmiga samples as shown in figure 6.15 provide a similar behaviour. The second sample appears to have released at a pressure similar to that of the Polyimide film, with samples two and three attaining higher pressures.

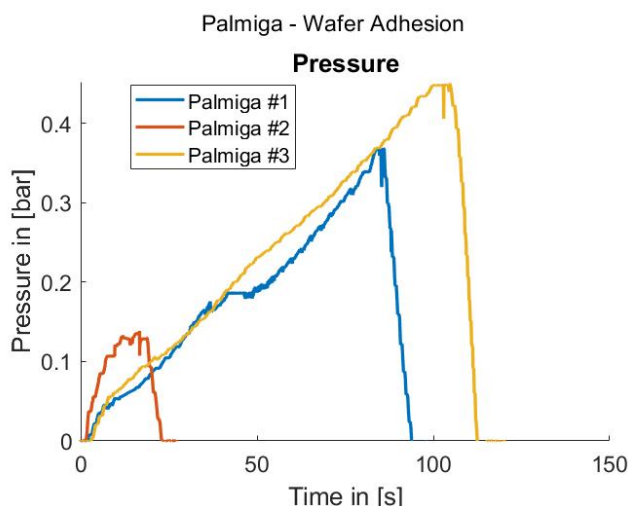


Figure 6.15: Pressure graphs for palmiga samples

The peak pressure observed will be taken as the point of detachment, given that as soon as the sample was observed to detach (which was associated with an audible sound the gas pressure being released), the setting was held until this was visually confirmed. Due to the orifice in the wafer jig being significantly smaller than the available gas supply line, a constant pressure was still able to be maintained by the regulator after sample separation.

The resulting values observed are shown in table 6.2 below. It should be noted that for several samples the wafer itself appeared to be the point of failure, as also shown in the pre and post experiment pictures provided in appendix D. In the provided table, samples for which the wafer appeared to have failed are underlined.

Material	Sample #1	Sample #2	Sample #3
Ninjatek	712.2 mbar	<u>137.4 mbar</u>	<u>110.5 mbar</u>
Palmiga	<u>372.2 mbar</u>	<u>139.1 mbar</u>	452.3 mbar
Protopasta	155.8 mbar		
Electrifi	99.8 mbar		
Polyimide (control)	64.7 mbar		

Table 6.2: Recorded polymer-wafer separation pressures

6.6 Discussion

Given the varying nature of the results even for samples created with the use of the same material and print settings, deriving a concrete conclusion provides some challenge. In order to be able to provide some insights as gained from the experiment, three discussion points will be provided. Adhesion to silicon, failure-mode of samples and finally suggestions for an improved experimental method.

6.6.1 Adhesion to silicon

The most important conclusion as intended to be drawn from this experiment is the adhesion ability of commercial conductive filaments to a smooth silicon surface as used integrated circuit fabrication. Looking purely at the initial warping observed during printing, it can be stated that the flexible TPU based materials show a clear advantage. This is further confirmed by the results of the pressure experiment itself, with the only samples exceeding the roughly a 150 mbar pressure barrier being of the TPU variant.

The stiff materials represented by electrifi and protopasta show a warping away from the substrate, with adhesion being so minimal that the nozzle would detach the print before completing the print. Additional adhesion might have been gained by subsequent compacting by further layers, however this could not be confirmed due to the prints failing prematurely.

6.6.2 Failure-mode

The second parameter to discuss is the manner wherein the samples were observed to degrade, with many of the samples degrading at a pressure close to the value obtained for the purely Polyimide film covered control wafer. This suggests that for these samples little to no additional adhesion was achieved to the wafer. The minor increase in achieved pressure can be attributed to the faster manual ramping of the pressure and/or the added stiffness provided from the partial print of the plug on top of the Polyimide film.

It should also be noted, as shown in appendix D, that a slight correlation between a broken wafer and a lower adhesion value was observed as shown in table 6.2 by the underlined measurements. Suggesting that in case the wafer had not broken that possibly more consistent values would have been observed.

6.6.3 Experimental method

Drawing from the points stated above it is clear that the measurement method requires significant improvement to yield more predictable results. Firstly the manual pressure control could be improved by implementing a constant ramp, either electronically or mechanically controlled, ensuring each sample is exposed to a comparable stress. The pressure should be measured directly underneath the wafer past the orifice to prevent the measurement of any pressure drop present.

Secondly a method should be obtained for improving the strength of the wafer substrate. This could be achieved by the use of either a thicker wafer or the thickening of the wafer by gluing on a backing plate for additional support.

The last improvement that is suggested is the removal of the Polyimide cover allowing for a uniform surface height relative to the printing nozzle upon which is being printed whilst also preventing an additional contribution to the adhesion observed. This was initially attempted through the use of a soluble PVA plug filling up the hole in the wafer, however it was discovered that this process resulted in the detachment of the conductive filament plugs.

Potentially moving away from a pressure based experiment and making use of a pull-off test inspired by ASTM D4541 [13] might a solution to aforementioned problems. The fragile silicon wafer would in this scenario be adhered to a stiff supporting base, with the plug being pulled of the surface. The deformation of the material as result of the varying hardness would however need to be considered carefully, as this could result in an uneven pull-off of the material. As the material deforms less surface area would remain attached to the wafer, resulting in a increase force per unit area, affecting the measurement depending on material stiffness.

6.7 Conclusions

6.7.1 Adhesion

In the experiment it was determined that similarly to the PCB experiments as performed in chapter 5, the TPU filaments resulted in the best adhesion. The stiff Protopasta and Electrifi filaments also performed as would be expected from the PCB experiments with Electrifi immediately detaching after the first layer and Protopasta showing minimal adhesion.

6.7.2 Improvements to experiment

The experimental method was found to be insufficient for deriving a consistent comparison for similar samples. In addition the substrate was observed to disintegrate during several experiments as a result of the pressure applied to test the material adhesion. The need of the currently applied method for a covering Polyimide film underneath the sample is also less than ideal, and could affect experimental results.

Therefore a method in the form of a pull-off test is suggested allowing for support of the wafer and removal of the covering and hole placed in the center of it. This would require careful consideration however as material stiffness could affect the comparability of results achieved.

7 Components; Manufacturing, Performance and Prediction: Resistors

Starting off the chapters on the creation of passive circuit components is the most basic component of all, the resistor, which can be as simple as a single wire. Ideally these components allow for a wide range of resistances for a similar size structure, requiring a mechanism of resistance change different from component dimensions alone.

7.1 Previous work

7.1.1 Printed resistors

The resistive element has often been described in literature, as every track of material with a resistance can be considered to be a resistor. Examples of these resistive elements were already discussed in detail during the literature investigation into the material resistivities in section 3.1.1, as these are commonly derived with the use of printed geometry with a constant cross sectional area. The focus of this literature section was therefore put towards the possibility of printing parameters being used to affect the resistance of fixed geometries.

Lazarus [49] observed that simple extruded rectangular sections of the conductive Protopasta filament resulted in volume resistivities of $6.0 \Omega \text{ cm}^{-1}$. Daniel [19] observed a difference in resistivity between the raw filament at $6.4 \Omega \text{ cm}^{-1}$ to a printed single traxle at $2.2 \Omega \text{ cm}^{-1}$, as well as an increased resistivity for a rectangular block consisting of multiple layers at $1497.7 \Omega \text{ cm}^{-1}$. This suggests both the heat input into the filament as the printing orientation and resulting inter-traxel interfaces affect the materials resistivity as also confirmed by the experiments in chapter 3.

Stano [99] ranked printing parameters on the basis of their effect on resistance of 3d printed strain gauges. It was observed that for both CNT filled filaments as for the carbon black filled Ninjatek filament the most statistically significant parameter was the specified layer height, followed up by the infill orientation. It was also noted that greater layer heights would result in lower resistances potentially due to a reduction in the inter-traxel voids/interfaces being formed, as fewer stacked elliptical traxels would be required.

7.2 Sample Design

The samples to be used for the resistor experiments were designed to make use of the resistance change as an effect of the traxel orientations with respect to the current flow. The layer height was chosen to be kept consistent although [99] concluded it to be the major contributor to sample resistance, given that for a fixed nozzle size only a limited amount of layer height variation would be allowable in comparison to the available infill orientation variation.

The samples were created with the use of the stiff protopasta PLA based filament, which came with the added benefit of being well suited for filament retraction given the precise nature of the prints. In order to prevent effects resulting from bending or flexing of the samples, distorting the interfaces in between the traxels the flexible TPU materials were excluded from the test. The Electrifi filament was also excluded from the test due to its low resistance, which resulted in significant measurement noise as noted in appendix A.2.

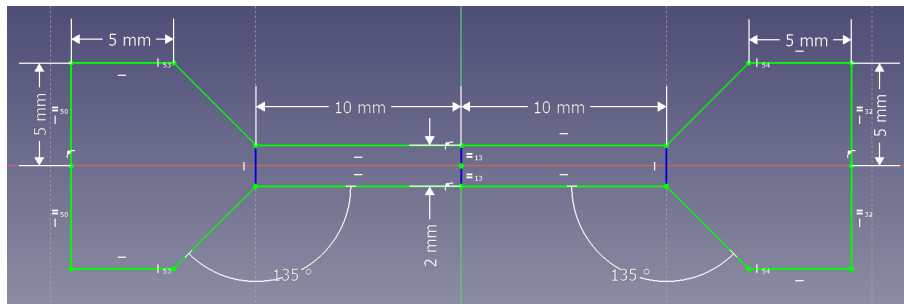


Figure 7.1: Sample dimensions

Due to the interfaces also affecting the manner in which contact can be made to the samples, a design with large contact pads was chosen with a thin 2 mm by 2 mm center section providing the resistance, as shown in figure 7.1. The samples differ in the addition of the taper from the current density samples presented in section 4.2 as to allow for the infill pattern to gradually walk into the thin section without forming unintended bridges where traxels are end/turn. This was not an issue with the current density samples as they only featured alongside and perpendicular orientations to the current flow.

7.2.1 Infill design

With the shape of the samples determined, the infill patterns to be used for the samples is provided in figure 7.2, with seven fixed angles being chosen.

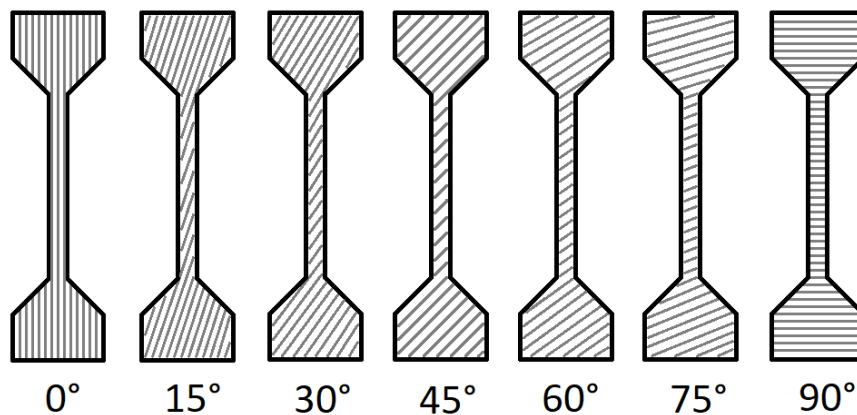


Figure 7.2: Sample infill orientations

Additionally to the infill orientation, a manner of turning the corner has to be determined for the traxel, as two options are available. The first one being a 'lines' infill pattern, where after the completion of the traxel the printer will stop its extrusion and if needed retract the filament from the nozzle to prevent accidental leaking called oozing. The resulting infill pattern as sliced for this method is provided in shown in figure 7.3. The second infill method is the 'meandering' pattern, where the printer is allowed to continue extrusion linking every traxel creating continuous lines. The resulting infill pattern as sliced slice is shown in figure 7.4.

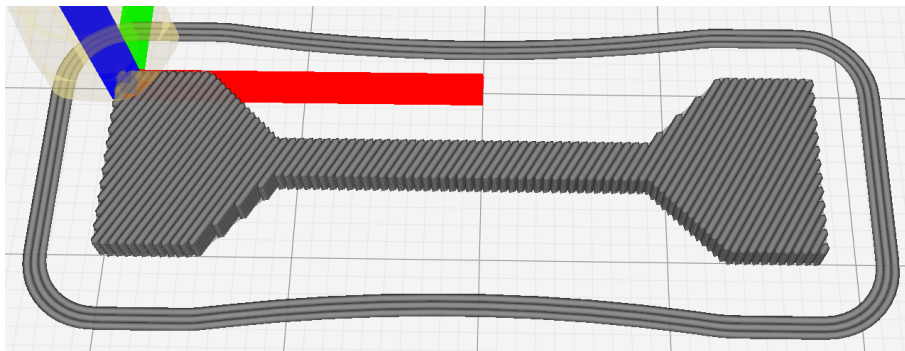


Figure 7.3: Resistor slice type A - Lines

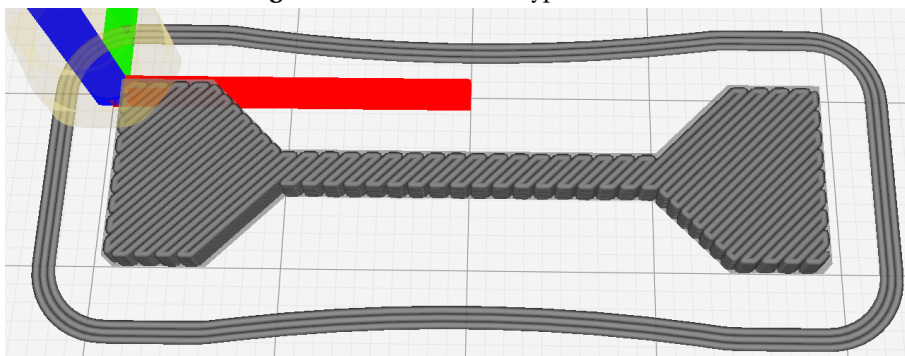


Figure 7.4: Resistor slice type B - Meander

7.2.2 Slicer settings

The settings used to result in these final sliced parts are provided in table 7.1, with variable θ being used to designate the infill angles as shown in figure 7.2.

	Protopasta - A [89]	Protopasta - B [89]
Bed	60°C	60°C
Nozzle	205°C	205°C
Flow	110%	110%
Layer height	0.2mm	0.2mm
Nozzle Size	0.4mm	0.4mm
Infill pattern	Lines	Zig Zag
Infill percentage	100%	100%
Infill orientation	$[\theta, \theta]$	$[\theta, \theta]$
Wall/Top/Bottom	none	none
Print cooling	yes	yes

Table 7.1: Custom Cura Slicer profiles for sample creation

7.2.3 Contact improvement

From previous experience in the group it was observed that the interfaces between traxels have a large effect upon the conductivity [110], requiring an improved contact to the larger contact pads. For this purpose silver conductive paint [23] was applied in the same manner as used in section 4.2.3, the result of which is shown in figure 7.5

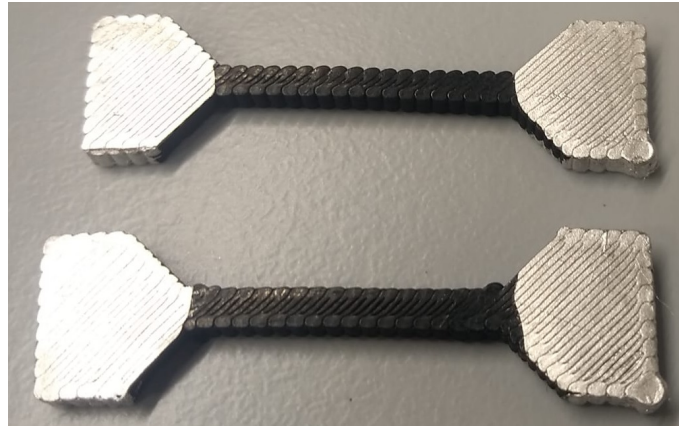


Figure 7.5: Resistor samples with silver painted contacts

7.2.4 Annealing

After the contact pads were coated, a final anneal was performed to stabilize the materials resistivity. The anneal was performed for a 12 h period at a temperature of 110 °C in a Memmert UF30 oven [60].

7.3 The Characterization

7.3.1 Theoretical behaviour

Taking the assumption that the silver conductive coating is sufficient to lower the large contacts pad resistance to a value negligible in comparison to the resistance of the center section. Whilst also assuming that the measurement current provided through these pads is flowing through the 2 mm by 2 mm cross section with a length of 20 mm. Use can be made of equation 7.1 [77], which describes the resistance of a section of material with cross-sectional area A , length l and resistivity ρ .

$$R = \rho \frac{l}{A} \quad (7.1)$$

In order to provide an estimate of the resistivity as a function of the printing orientation chosen for the Protopasta samples, equation 7.2 was created. It describes the resistivity of the sample on the basis of alongside ρ_0 and perpendicular ρ_{90} resistivities for the material, by taking the assumption that ρ_0 describes the traxel resistivity where ρ_{90} provides the combined resistivity of the traxel interfaces and the traxel itself.

$$\rho_{\theta} = \rho_0 + (\rho_{90} - \rho_0) \sin(\theta) \quad (7.2)$$

The resulting equation takes ρ_0 as the always included traxel resistance, with a varying contribution of the interface as derived by taking the component of the difference between the alongside and perpendicular resistivities.

7.3.2 Resistance measurement

The measurement of the resistances was performed with the use of a Temna [102] multimeter to which to standard banana plug cables of a length of 25 cm were attached. The samples were connected through the means of the crocodile clips and measurements were recorded in resistance mode with a 2-wire measurement configuration.

7.4 Results

7.4.1 Calculated resistance

In order to derive an accurate estimated resistivity and resistance for the printed components, the values for the annealed Protopasta samples as provided in chapter 3 will be used. These were $3.45 \Omega \text{ cm}$ for the alongside traxel samples (ρ_{θ}) and $4.88 \Omega \text{ cm}$ for the perpendicular samples (ρ_{90}).

The resistances were calculated with the use of the according to equation 7.2 calculated resistivity, These were entered into equation 7.1 in combination with the previously defined sample length and cross section. The resulting values are provided in table 7.2 and provide an estimate for the 'lines' type infill pattern as this was also the type of infill chosen for the characterization in chapter 3.

	0°	15°	30°	45°	60°	75°	90°
ρ_{θ}	3.45 $\Omega \text{ cm}$	3.82 $\Omega \text{ cm}$	4.17 $\Omega \text{ cm}$	4.46 $\Omega \text{ cm}$	4.69 $\Omega \text{ cm}$	4.83 $\Omega \text{ cm}$	4.88 $\Omega \text{ cm}$
R	172.5 Ω	191.0 Ω	208.3 Ω	223.1 Ω	234.4 Ω	241.6 Ω	244.0 Ω

Table 7.2: Calculated estimates of sample resistivity and resistance

7.4.2 Measured resistance

As previously mentioned the resistances were obtained through a simple 2-wire measurement, for which the results are provided in table 7.3.

	0°	15°	30°	45°	60°	75°	90°
R for lines	188.1 Ω	209.3 Ω	231.8 Ω	244.8 Ω	275.3 Ω	265.5 Ω	257.0 Ω
R for meander	266.5 Ω	225.1 Ω	241.9 Ω	250.2 Ω	251.8 Ω	258.6 Ω	251.8 Ω

Table 7.3: Measured resistances for varying traxel orientations

7.5 Discussion

7.5.1 Calculation vs Observation

To provide a slightly clearer overview of calculation and measurement results, figure 7.6 was created providing a plot of all results in graph form with the circular markers providing the actual data.

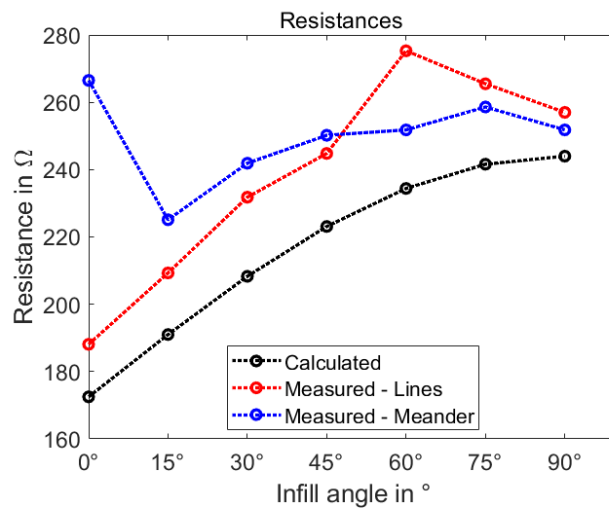


Figure 7.6: Resistances measured

It can be observed in the figure that a similar slope for the lines measurements and the calculated values was obtained, with the exception of the 60° sample. This exception could also not be explained by the sample images in appendix E, as no difference from the other samples could be observed. The meandering samples also appear to provide a similar slope, with a clear outlier for the 0° sample, which could be explained by looking at the sample images in appendix E. It can clearly be observed that due to the slicer settings, the meandering sample formed 4 parallel traxels whereas the lines sample formed 5 parallel traxels, resulting in an increased resistance.

The minimal difference observed between the lines infill pattern and the meandering pattern could be explained by two theories. The first theory would be that the interfaces in between the traxels are still sufficiently conductive in comparison to the total resistance along the continuously printed traxel to make conduction through these interfaces the main form of conduction, minimizing any effects that occur at the traxel ends. The second theory is highlighted in figures 7.7 and 7.8 describing the differences observed between real world prints and the theoretical as sliced patterns from sample pictures.

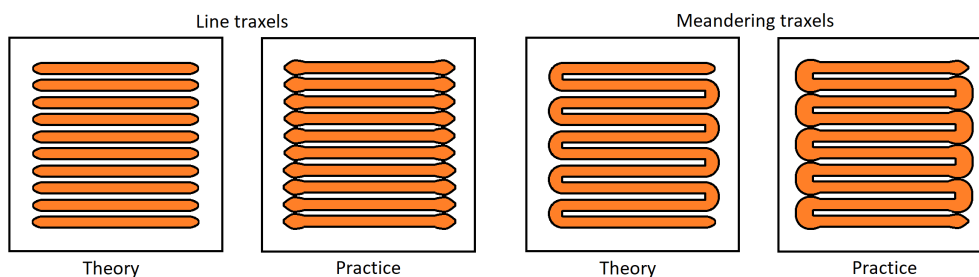


Figure 7.7: Line printing effects

Figure 7.8: Meander printing effects

In reality the printer is never fully able to stop extrusion at the moment it reaches the end of the traxel, resulting in blobs that interconnect the ends of each line in a similar manner as the meandering patterns would. Additionally due to the printer having to slow at the edges of the meandering pattern to account for the inertia of the printhead, a similar over-extrusion effect can be observed at these edges. This once more provides an additional bridge between traxels, increasing the similarity between the edges of the lines and meandering infill patterns.

7.5.2 Performance

Given the accuracy of the calculated values in comparison to the actual measurements obtained, it can be said that the concept of using the infill orientation as a manner to create tunable resistances is potentially viable. The small offset observed between calculated values and recorded values could be contributed to differences between prints as used for the creation of the resistors and those used to characterize the reference values applied.

The concept could further be tested by creating samples with different cross sectional areas to derive if the observed orientation to resistance relation holds when samples are scaled to provide different ranges of resistance values. In order to provide a detailed description of reproducibility, several additional resistors would have to be produced, to provide statistically significant data on the variability resulting from the printing process.

7.5.3 Scaling

The designed resistors as currently proposed have a major downside when it comes to uniform down-scaling. As the resistors cross sectional area is decreased by reducing the width dimension, the ratio of edge to traxel length for which an inter-traxel interface is present changes. When this scaling would be continued, at some point the conduction would mainly occur through the edges, resulting in the removal of the ability to affect the resistance by changing the infill orientation. Therefore, scaling in the height or z-axis orientation would be recommended instead, which would be the equivalent of placing similar resistances in parallel.

Another option for scaling would be to change the set layer height as mentioned by Stano [99], which would decrease or increase the amount of inter-traxel voids for a given section of material. The latter, in combination with a scaling of the width to alter the edge to interface ratio, would provide additional possibility to tune the resistor whilst maintaining a similar required occupied surface area.

7.6 Conclusions

7.6.1 Varying resistance

The experiment showed the potential usage of the infill orientation as a parameter for changing the resistance of a sample with fixed dimensions. Further scaling is suggested with the use of vertical scaling varying the amount of stacked layers to result in the desired total resistance. Scaling the samples in the XY-plane is not recommended due to effects resulting from the edges becoming more dominant in relation to the infill effects in the scenario of down-scaling.

7.6.2 Edge effect

The limitation suggested on down-scaling in the XY-plane results from the observation that very minimal differences were observed between line and meandering infill patterns. These differences could be attributed to excess extrusion at the end of traxels as the print head was slowed and moved in the opposite direction for the next line. It is believed that these slight over extrusions occurring at the edges of the prints resulted in a connection between traxel ends for both infill types leading to similar resistances for the samples.

7.6.3 Future suggestions

From the literature study and the experiment itself several additional parameters are suggested which could provide tunable resistance. Changing the layer height and corresponding nozzle size would result in fewer layer interfaces and thus a lower resistance.

Changing the distance in between the printed traxels in the XY-plane would also result in an alteration of the interface count, resulting in an expected increase in resistance if decreased. The opposite would also be achievable by increasing the distance between traxels, although limited

by the size of the printing nozzle containing the extruded filament. Increasing the size past this limit would result in a air gap between traxels, effectively creating a thin meandering wire.

8 Components; Manufacturing, Performance and Prediction: Capacitors

Going by order of geometric complexity, the next passive circuit component to be discussed is the capacitor, consisting of a set of parallel plates separated by dielectric. Given the dependence of capacitance upon overlapping plate area, both the contribution of the dielectric as the plate geometry will be explored. The created components will also be compared to their theoretical behaviour to gain insight into the modellability of the printed components.

8.1 Previous work

8.1.1 Printed Capacitors

As to get a sense of the possibilities with respect to the 3D printing of capacitors, a literature study was done as to the various methods applied by others. Starting off with techniques outside of the FFF domain, Glier [34] demonstrated the creation of flexible planar capacitors by creating a HHDA polymer containing silver nano wires. The initial methodology was implemented though planar printing, however eventual use of the material in 3D printing is suggested.

Wu [112] showed a different manner of creating 3D printed capacitors by silver filling a hollow print of a parallel plate capacitor, with good results. The most similar 3D printed capacitor to the devices created in this work were those produced by Flowers [31]. Flowers produced a several layer parallel-plate capacitor with the use of Electrifi filament as a conductor and PLA as a dielectric, whilst also showing the usage of bronze filled PLA as an improved dielectric material.

8.2 Sample designs

For the capacitors, a single stackable design is proposed that could be stacked in groups from one to five standard plate sets. The dielectric will be varied to result in additional tuning parameter as well.

8.2.1 Capacitors

The capacitor design is shown in figure 8.1, which is a simple two plate design. The proposed design allows for each layer of the plates and the dielectric material to have the thickness of a single traxel, for the designed layer height of 0.2 mm. Additionally the design was created in such a way that it could be stacked vertically, to result in multi-plate capacitors. Each layer stacked on top would provide two additional pairs of parallel plates to the stackup, with an overlapping area of 4 cm².

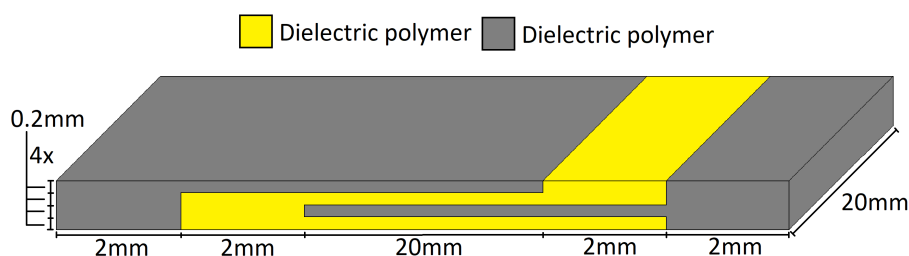


Figure 8.1: Capacitor dimensions

Infill design

The infill design chosen for the capacitors was such that the conductive polymer and the dielectric material were printed exactly perpendicular to each other. It was found that this minimized the cross-contamination, as any conductive material picked up by the dielectric printing nozzle would be pushed past the edge of the conductive plates. This would not have been the case if printing orientations would have aligned, due to shorts forming at the ends between the plates. The result is shown in the sliced profile as provided in figure 8.2, where the capacitor is provided. A priming tower was also implemented however not shown, for the prevention of cross-material contamination is shown on the right.

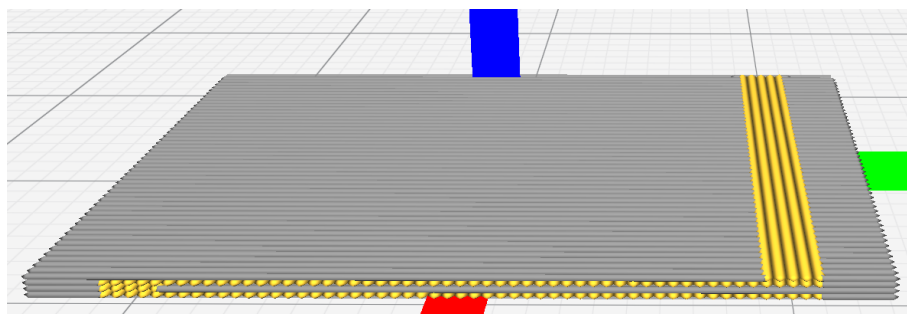


Figure 8.2: Sliced capacitor design for a single stack

Slicer settings

The slicer setting used to create the profile as shown in figure 8.2 are provided in table 8.1. For the dielectric material identical settings were used provided they are both a PLA material to minimize any potential variations in plate spacing and dielectric contamination as an effect of printing settings. Both a Prusament PLA and Protopasta Magnetic PLA were used as a dielectric, as it was previously shown by [31] that the introduction of metallic filling could result in an increase dielectric strength.

	Protopasta Conductive [89]	Neat PLA	Protopasta Magnetic [90]
Bed	60°C	60°C	60°C
Nozzle	205°C	200°C	200°C
Flow	110%	100%	100%
Layer height	0.2mm	0.2mm	0.2mm
Nozzle Size	0.4mm	0.4mm	0.4mm
Infill pattern	Lines	Lines	Lines
Infill percentage	100%	100%	100%
Infill orientation	[0,0]	[90,90]	[90,90]
Wall/Top/Bottom	none	none	none
Print cooling	yes	yes	yes

Table 8.1: Custom Cura Slicer profiles for capacitor creation

Annealing

The capacitors were printed for both dielectric materials in one up to five stack configurations, after which an anneal was performed for 12 h at a temperature of 110 °C. Due to the annealing, slight warping did occur as shown in figure 8.3, resulting in the decision to only continue the experiment with the minimally warped three to five-stack samples.

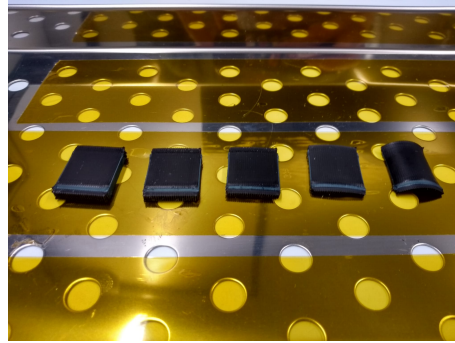


Figure 8.3: Annealed capacitors

It was also noted that between initial measurements with a LCR meter that before and after annealing a 17% reduction in capacitance was observed. This change could be attributed to moisture removed from the samples given the high dielectric constant of water [73].

8.3 The Characterisation

8.3.1 Theoretical behaviour

The simplest description of a capacitor is found in the parallel plate capacitor, where two parallel plates with a known dielectric in between allow for charge storage, as shown in figure 8.4

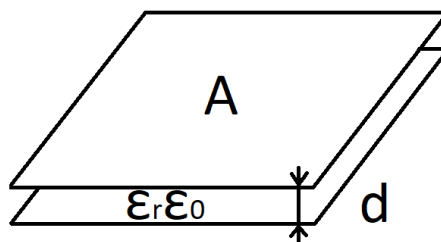


Figure 8.4: Plate capacitor

Its capacitance C in [F] is described by equation 8.1 [75], where two plates of area A [m^2] are separated by distance d in [m] by a dielectric with a relative permittivity of ϵ_r a multiplication factor of the vacuum permittivity ϵ_0 in [$\text{F} \cdot \text{m}^{-1}$].

$$C = \frac{\epsilon_r \epsilon_0 A}{d} \quad (8.1)$$

Given that the capacitor plates are not of infinite conductance, care must be taken to also consider the contributions of the plate and interconnect resistances in series with the observed capacitance. The concept of the contribution of the materials resistivities is shown in figure 8.5.

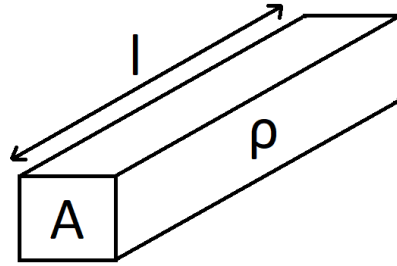


Figure 8.5: Material resistance

In order to derive these resistances use of equation 8.2 [77] will be made once more with R resistance in $[\Omega]$, ρ the materials resistivity in $[\Omega \text{ cm}]$, l the length of wire in $[\text{cm}]$ and wire cross-section A in $[\text{cm}^2]$. In the case of the plates the wire will consist of a thin wide cross section of alongside traxels, in the case of the side connections it will consist of a rectangular cross section of perpendicular traxels provided the connection points on the samples created.

$$R = \rho \frac{l}{A} \quad (8.2)$$

8.3.2 Component quality

The quality of capacitive and inductive elements is often associated with their ability to form resonant circuits. Their ability to sustain this oscillation is indicated by the Q factor, representing the circuits losses. This factor is typically defined for a RLC-circuit with a given natural oscillation frequency of $f = \frac{1}{2\pi\sqrt{LC}}$. It can however also be related to a capacitor with a series resistance as shown in equation 8.3 [85] or to an inductor with a series resistance as shown equation 8.4 [85].

$$Q_C = \frac{1}{2\pi f C \cdot ESR} \quad (8.3)$$

Components with a higher Q factor are closer to their ideal theoretical behaviour for the provided frequency f in $[\text{Hz}]$, which will depend on the resonance frequency desired.

$$Q_L = \frac{2\pi f L}{R_{wind}} \quad (8.4)$$

The series resistance of the inductor will make it such that up to a certain frequency it is a simple resistor, beyond which it becomes inductive with the slope of the rise in impedance depending on the inductance L in $[\text{H}]$. The capacitor has an inverse relation to this problem, where the impedance initially reduces with an increase in frequency up to the point where the series resistance is achieved and the impedance no longer drops, with the initial slope of the impedance drop depending on C in $[\text{F}]$.

This results in an optimal frequency range for a resonator circuit constructed from their combination, meaning that the Q -factors also affect the suitable bandwidth of the resonator, for which a Q factor can also be defined at a desired frequency as provided by equation 8.5.

$$Q = \frac{1}{\frac{1}{Q_C} + \frac{1}{Q_L}} \quad (8.5)$$

8.3.3 Impedance fitting

The impedances of the capacitors were fitted with the use of the method as proposed in section 5.3.3 after a calibration was performed with the models as described in section 5.3.2. The specific calibrations as performed for the capacitor samples can be found in appendix section E.3. The equivalent model to be fitted to the capacitors as printed was based upon common models as found in literature [42] and is shown in figure 8.6.

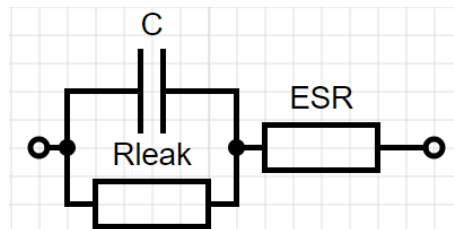


Figure 8.6: Capacitor equivalent model

The model consists of an ideal capacitor with a resistor across its plates to represent a leakage current. This leakage is resultant from the dielectric material itself and any contamination during printing with conductive material. As with typical theoretical models an equivalent series resistance was also included to represent the contribution of the plate resistances. The usage of a series inductance was omitted given that no component leads are present and the 2.54 mm contact pins were directly attached to the sides of the parallel plates.

8.4 Results

8.4.1 Calculated Impedance

To provide a basis of comparison of the measurements that will be performed, expected component and parasitic values will be calculated. These will consist of the expected capacitance and series resistance as derived from the material resistivity of the plates. The leakage resistance was left to be derived experimentally as it is expected to result mostly from cross-material mixing of the plate and the dielectric material.

In table 8.2 the values used for the calculation of the capacitance for a single plate pair with a neat PLA dielectric separator are provided, as were used in combination with equation 8.1 to derive a figure of 47.1 pF. The capacitance for the plates with the use of Protopasta Magnetic Iron as a dielectric could not be determined, given no permittivity was provided in the datasheet.

C_{plate}	Symbol	Value
Plate spacing	d	0.2 mm
Relative permittivity [31]	ϵ_r	2.66
Vacuum permittivity	ϵ_0	8.854 pF m^{-1}
Plate area	A	400 mm^2

Table 8.2: Calculation parameters used to derive plate capacitance

In table 8.3 the values used for the calculation of the resistance of the plates themselves is provided. The alongside traxel characterisation of annealed conductive Protopasta was applied to equation 8.2, resulting in a resistance of 190Ω per plate pair.

R_{plate}	Symbol	Value
Plate length	l	22 mm
Resistivity	ρ_{along}	3.45 Ω cm
Plate cross-section	A	4 mm

Table 8.3: Calculation parameters used to derive plate resistance

The last impedance to be calculated for the capacitor is that of the plate interconnects on the sides, for which the perpendicular characterisation of the conductive Protospasta was used. In table 8.4 the values that were applied to equation 8.2 are provided, resulting in a 610 Ω interconnect resistance for a single stack capacitor.

R_{inter}	Symbol	Value
Interconnect length	l	22 mm
Resistivity	ρ_{perp}	4.88 Ω cm
Interconnect cross-section	A	1.6 mm

Table 8.4: Calculation parameters used to derive interconnect resistance

With each contribution determined, the total capacitance and resistance for stacked multiples of the capacitor can be derived. This is achieved by the realization that for a homogeneous current distribution assumption currents of a single plate pair only have to flow through $R_{inter} + R_{plate} + C_{plate}$. When these plates are stacked a series circuit is formed between the parallel interconnect resistances and the parallel plates. Multiplying the capacitance by the plate count and reducing the total plate resistance by a factor of one over the plate count whilst also scaling the interconnect resistance by one over the stack count. The results of the contributing parts for multiple stacks are given in table 8.5.

Neat PLA capacitor	Capacitance	ESR
Three stack	236 pF	241 Ω
Four stack	330 pF	180 Ω
Five stack	424 pF	143 Ω

Table 8.5: Capacitance and series resistance as calculated for neat PLA dielectric capacitors

8.4.2 Measured Impedance

Neat PLA dielectric capacitors

The first set of capacitors to be characterised on the basis of the model as provided in section 8.3.3 are those with a neat PLA dielectric material. In figures 8.7, 8.8 and 8.9 their measurements and corresponding derived fit are shown.

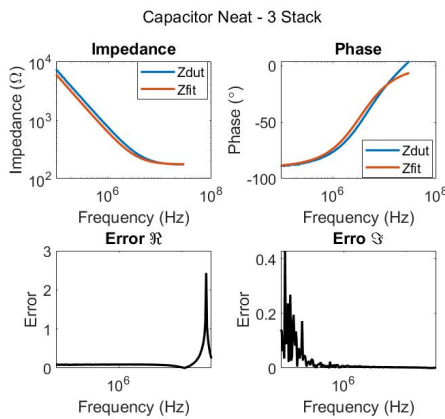


Figure 8.7: Five plates - PLA dielectric

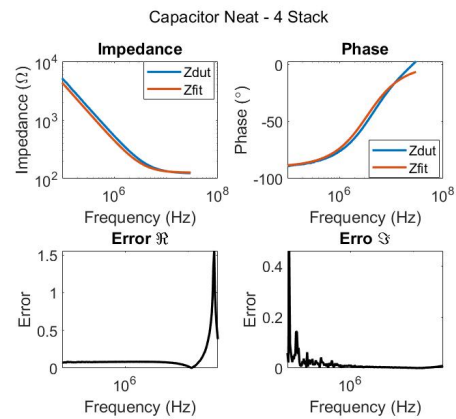


Figure 8.8: Seven plates - PLA dielectric

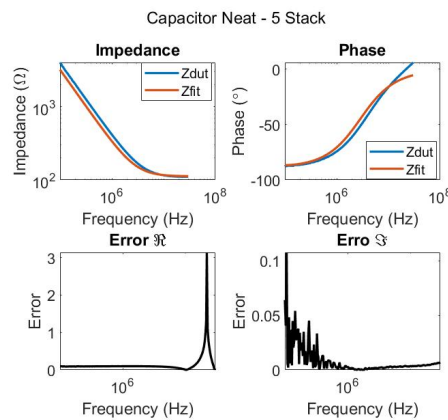


Figure 8.9: Nine plates - PLA dielectric

From the figures it can be noted that the compensation appears to be accurate, with the impedance and phase as recorded not showing any unexpected curvature. The fit attained from the proposed equivalent circuit shows a slight deviation in the phase, rolling into zero as it approaches. This might be the result of the component lead inductance coming into effect, pushing the phase towards positive values, which was not accounted for in the equivalent model. This slight deviation however is deemed to be small enough to still consider the achieved fit valid.

In table 8.6 the determined capacitances, leakage resistances and equivalent series resistances are shown. It can be noted that for each pair of plates approximately 54 pF of capacitance was added, following along with the five, seven and nine plate pairs. The leakage resistance was high for all capacitors, pointing towards functional dielectric layers. The equivalent series resistance was also shown to drop as the quantity of plate pairs was increased, showing its relation to the resistance of the capacitors plates opposed to losses in the dielectric material.

	Estimate	lb	hb	Cap 3 Neat	Cap 4 Neat	Cap 5 Neat
Capacitance	10 pF	100 pF	1000 pF	265.67 pF	368.22 pF	496.63 pF
Leakage resistance	1 MΩ	1 kΩ	1 TΩ	155.73 GΩ	222.91 GΩ	139.22 kΩ
ESR	100 Ω	10 Ω	1000 Ω	174.38 Ω	125.95 Ω	112.24 Ω

Table 8.6: Fitted capacitor model for Neat filled PLA dielectric

Iron filled PLA dielectric capacitors

The second set of capacitors to be tested were those with a PLA dielectric that was modified by an iron filling. Unfortunately the five stack capacitor of this type suffered a contact failure, with only the measurements for the three and four stack capacitors being shown in figures 8.10 and 8.11.

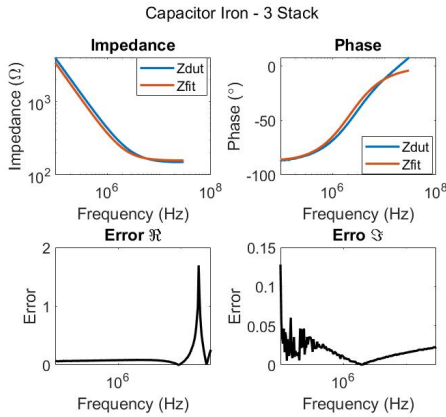


Figure 8.10: Five plates - Iron dielectric

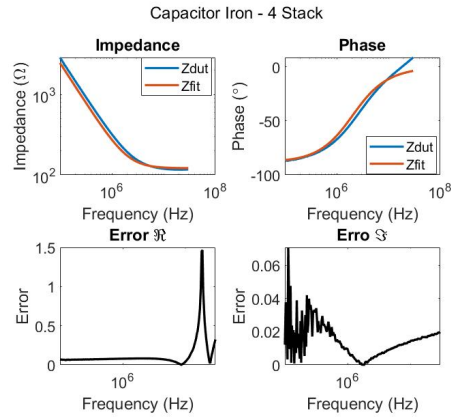


Figure 8.11: Seven plates - Iron dielectric

Similarly to the neat PLA capacitors at higher frequencies a shift in the phase is observed with relation to the compensated measurement, attributed to the inductance of the component leads not included in the equivalent circuit model. The shift is once more deemed small enough to deem the fit achieved valid.

In table 8.7 the resulting estimate values are shown for the iron filled capacitors, showing an approximate 92 pF increase in capacitance per plate pair, indicating an increased dielectric strength as an effect of the iron filling. The leakage resistance was observed to be of comparable magnitude to the neat PLA dielectric capacitors where it was found to not be in the GΩ as was the equivalent series resistance.

	Estimate	lb	hb	Cap 3 Iron	Cap 4 Iron
Capacitance	10 pF	100 pF	1000 pF	468.86 pF	644.25 pF
Leakage resistance	1 MΩ	1 kΩ	1 TΩ	132.93 kΩ	134.45 kΩ
ESR	100 Ω	10 Ω	1000 Ω	157.29 Ω	121.38 Ω

Table 8.7: Fitted capacitor model for Iron filled PLA dielectric

8.5 Discussion

8.5.1 Model accuracy

Given that before measurements analytical models were created of each component, a study of the differences between the produced components and their theoretical behaviour will be provided.

The capacitance of the designed capacitors was found to be within 15% of the expected value derived through calculation with the use of a neat PLA dielectric constant as previously derived by Flowers, with the observed capacitances leading to a derived neat PLA dielectric constant of $\epsilon_{pla} = 3.03$. For the Iron filled PLA dielectric no estimates were provided in literature, however from measurements a derived dielectric constant of $\epsilon_{iron} = 5.16$ was obtained with the use of a rewritten form of equation 8.1. This result is in line with expectations for metal filled PLA

dielectrics, as Flowers derived a $\epsilon_r = 7.35$ for bronze filled PLA[31] increasing the obtainable capacitance per unit area.

The series resistance of ESR of the capacitors observed for the neat PLA dielectric samples showed an approximate 35% reduction in comparison to the calculated combined plate and interconnect resistances, with the iron filled PLA dielectric samples showing an approximate 50% reduction in interconnect resistance. This might have resulted from the silver epoxy coating of parts of the interconnects in order to attach contact pins, which for a short covering on both current carrying sides could result in a sufficient ESR reduction to explain the difference.

The last parameter in the capacitor equivalent circuit model that could not be calculated, is that of the leakage resistance, which was approximated to be in the order of 100 k Ω to 1 M Ω for the produced samples. Provided that a rather large variation in these values are observed and that no relation with plate count is apparent, the leakage resistivity can be estimated to be 60 Ωmm^{-2} taking the worst case scenario of Cap 5 Neat in table 8.6.

8.5.2 Quality

The next point of discussion is the usability of the produced parts, making use of equation 8.3 to provide insight into the losses within the created capacitors in typical applications.

The set of values chosen to derive an approximate natural frequency were 400 pF representing the neat PLA capacitors and 200 nH representing both the planar and the solenoid inductors, resulting in a natural frequency of 17.8 MHz. At this natural frequency a Q_C of 0.17 would result for the five stack neat PLA dielectric capacitor created.

In order to represent the gains observed from the use of the Protopasta Magnetic Iron filament as both a dielectric and a magnetic core material, a 550 pF capacitance and a 550 nH inductance with a resulting natural frequency of 9.2 MHz were chosen to represent an oscillator created from these components. This natural frequency provides a Q_C of 0.23 for the four stack iron filled PLA dielectric capacitor.

These low Q factors lead to the conclusion that the created components are quite lossy due to their series resistance resulting from the high series resistance as an effect of the conductive polymer resistivity.

8.5.3 Design

The capacitor design could be improved in order to increase its capacitance without altering its external dimensions in two ways. The first would be to reduce the thickness of the dielectric and conductive layers, however this would also result in an increase in series resistance, and could result in a greater effect of cross-material mixing in the dielectric layer resulting in a larger leakage current. The second method would be to make use of a filled PLA material with a higher relative permittivity, which could be achieved with a higher filler percentage or the use of an alternative filler material with higher permittivity.

Additionally it should be considered to make use of the Electrifi material for the plates such that the series resistance is decreased improving the Q-factor and allowing operation at higher frequencies. If this is done care should be taken to manage the heat input into the sample, given the tendency of Electrifi to easily melt at lower temperatures and degrade as a result of prolonged exposure to higher temperatures.

8.6 Conclusions

8.6.1 Performance

The capacitors as designed were found to be well scalable, through means of stacking with a predictable relationship to the total capacitance. The Q-factor of the created capacitances

was determined to be in the range of 0.17-0.23 depending on dielectric as resulting from the high series resistance, indicating in a lossy overdamped component if used in oscillator applications. On the basis of the series resistance the components are expected to be operatable up to multiple MHz.

8.6.2 Modellability

The model created for the capacitor design was found to be accurate, given a 15% deviation from the calculated capacitance for the neat PLA dielectric capacitors. The parasitic series resistance was also found to be within 35% of the expected value for the neat PLA dielectric capacitors and within 50% for the iron filled PLA dielectric capacitors, possibly explained by the epoxy contact process. The leakage resistance was not initially modelled and observed to be in order of 100 k Ω to 1 M Ω for the capacitors varying with no apparent relation to the samples structure.

8.6.3 Improvements

The high series resistance of the components could be improved with the use of a more conductive plate material such as Electrifi. The capacitance could also be improved by lowering layer heights at the cost of cross-material mixing or by altering the dielectric to attain a higher permittivity.

9 Components; Manufacturing, Performance and Prediction: Inductors

The most complex passive circuit component is the inductive element, requiring a wound geometry with a dielectric insulator as well as a core material. Two geometries will be explored, as commonly found in conventional applications, as well as the contribution of the dielectric material to coil performance. The usage of a magnetic core material will also be explored and the printed components behaviour will be compared to its theoretical behaviour.

9.1 Previous work

9.1.1 Printed Inductors

3D printed inductors have previously been described in literature by Flowers [31] who made use of a planar coil design on top of a PLA dielectric. The inductance could be scaled through varying the winding count and was in accordance with conventional planar coil models. Wu [112] also introduced a solenoid inductor consisting of a silver filled cavity design which could be scaled on the basis of the winding count in the solenoid.

9.2 Sample designs

The inductors will be provided in two designs, the first being a typical solenoid design where an air or an iron filled core could be applied. The second solenoid design consisted of a planar coil which was either printed on top of or embedded in a dielectric material. In the following sections the designs of each of these will be highlighted.

9.2.1 Solenoid Inductors

The simple solenoid inductor design was created with the use of square wires wound around a circular cylinder as shown in figure 9.1.

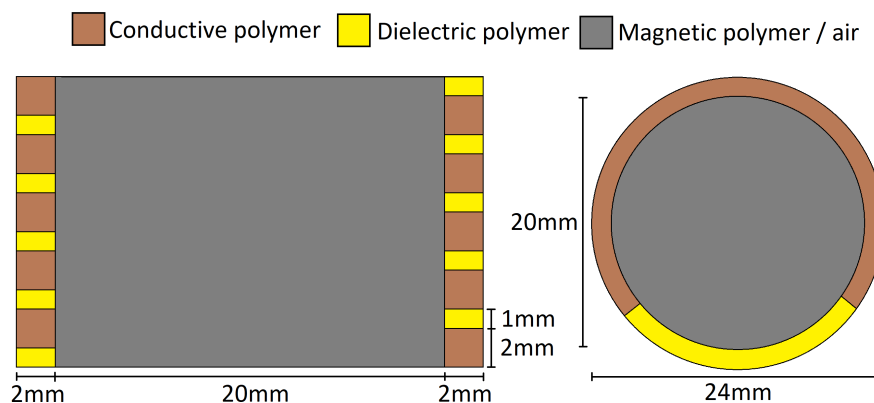


Figure 9.1: Solenoid inductor dimensions

The windings were chosen to have a pitch of 3 mm with a 2 mm by 2 mm profile, being separated by a 1 mm by 2 mm dielectric layer. The coil was designed in such a manner that the internal diameter was equal to 20 mm, with a total designed height of 15 mm in which a core of magnetic material could be printed.

Infill design

Two realizations of the design were created in the slicer with one containing a Protopasta magnetic iron core and the other making use of an air core. The windings and insulation were created with a concentric infill pattern to result in perfectly filled sections, with the iron core being formed with two walls on the outside to form a separation layer between the windings and the core. The center section of the core was filled with a conventional cross hatched lines infill pattern.

The resulting sliced inductors are shown in figure 9.2 for the air core inductor and in figure 9.3 for the cored inductor. As with previous multi-material prints a prime tower was also used during printing, however removed in the figures for a clearer picture of the sliced sample.

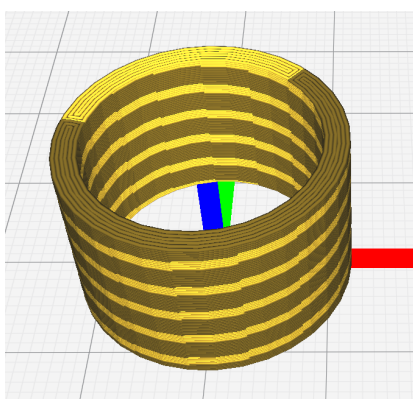


Figure 9.2: Sliced air core solenoid design

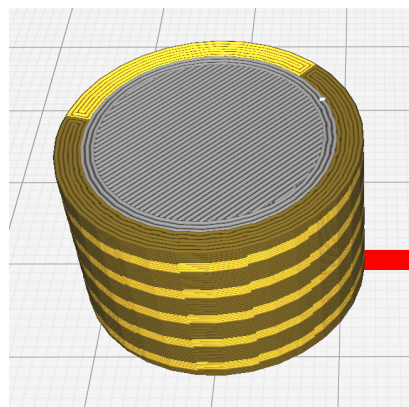


Figure 9.3: Sliced iron core solenoid design

Slicer settings

In table 9.1 the used slicer setting for the created solenoid coils are provided, where printing settings according to recommendations of the manufacturers were used. Due to the requirement for Electrifi to be printed upon a bed surface that cannot be heated to result in optimal conductivity, use was made of thin generic double sided flooring tape to provide sufficient bed adhesion. Recommended printing surfaces such as cardboard, construction paper and PET were attempted, but did not provide sufficient adhesion for these larger samples.

	Electrifi [65]	Neat PLA	Protopasta [90]
Bed	room	room	room
Nozzle	140°C	200°C	205°C
Flow	110%	100%	100%
Layer height	0.2mm	0.2mm	0.2mm
Nozzle Size	0.4mm	0.4mm	0.4mm
Infill pattern	Concentric	Lines	Concentric
Infill percentage	100%	100%	100%
Infill line thickness	0.35mm	0.4mm	0.35mm
Wall/Top/Bottom	none	2 walls	none
Print cooling	none	none	none

Table 9.1: Custom Cura Slicer profiles for solenoid inductor creation

9.2.2 Planar Inductors

The planar inductor was designed to have a coil winding outwards to create a 2d structure with multiple windings. The design consists of four windings and a solid conductive center of 3 mm.

The windings themselves had were sized to be 1 mm by 1 mm squares separated by 1 mm gaps. These gaps were filled by either air or a dielectric polymer, with the coil for the windings not being covered in dielectric being as shown in figure 9.4.

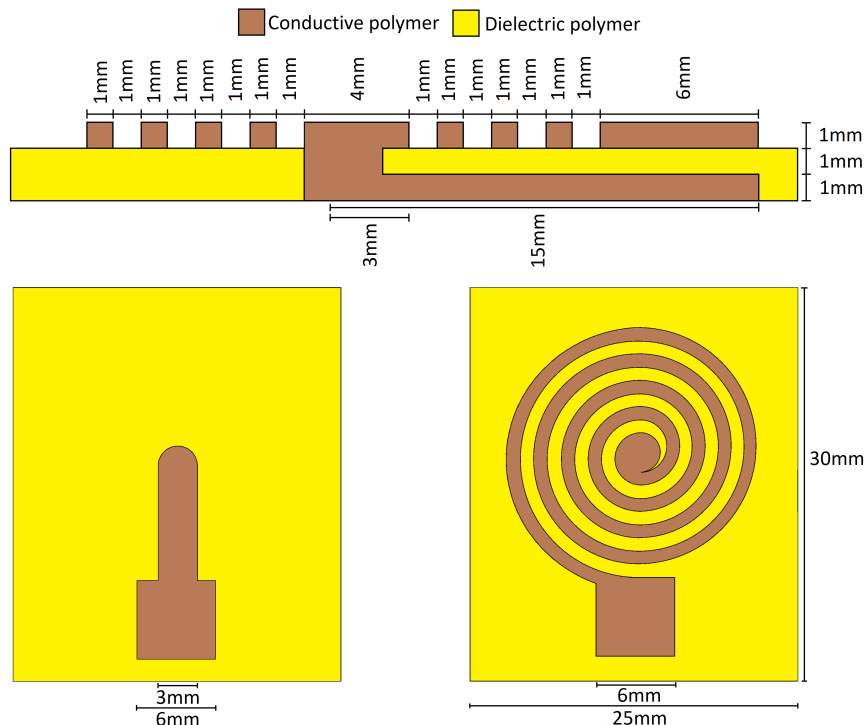


Figure 9.4: Planar inductor design

Due to the planar coil requiring both a center and an edge connection, a insulated connecting structure was also embedded in the dielectric support material, with additional 6 mm by 6 mm contact pads. The connection itself was formed by a 3 mm by 1 mm strip, blending into a pillar of the same diameter connecting to the center of the coil and the start of the windings. The dielectric for the covered coil was simply placed in the remaining air space for the top mm, which can also be observed in the figures of the infill design.

Infill design

The sliced designs of the non-embedded and embedded planar inductors are shown in figures 9.5 and 9.6 respectively. Likewise as for the solenoid inductor the priming tower is not shown in the figures, but was applied in the actual prints to prevent cross-material mixing. The coil itself was printed with the use of concentric infill for optimal filling, and the dielectric was chosen to be printed with a generic meandering pattern that overlapped in a crosshatch pattern.

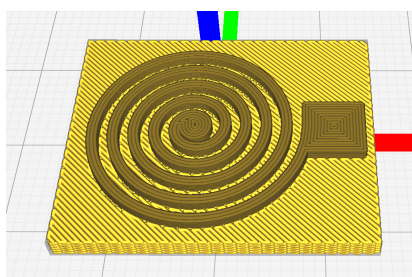


Figure 9.5: Sliced on top planar design

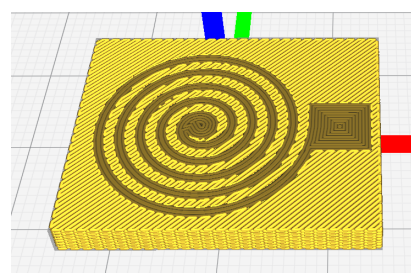


Figure 9.6: Sliced embedded planar design

Slicer settings

Corresponding to the settings chosen for the creation of the solenoid coils, manufacturers recommendations were followed for the Electrifi filament forming the conductor. Similarly to the solenoidal inductors the printbed was formed with the use of double sided tape to aid adhesion to the unheated printbed.

In order to ensure a solid print of the concentric windings as generated by the slicer, the infill line thickness was varied for the Electrifi material. The PLA dielectric once more was used with generic PLA filament settings as provided by Cura. The resulting settings are provided in table 9.2

	Electrifi [65]	Neat PLA
Bed	room	room
Nozzle	140°C	200°C
Flow	110%	100%
Layer height	0.2mm	0.2mm
Nozzle Size	0.4mm	0.4mm
Infill pattern	Concentric	Zig Zag
Infill percentage	100%	100%
Infill line thickness	0.30-0.32mm	0.4mm
Wall/Top/Bottom	none	none
Print cooling	none	none

Table 9.2: Custom Cura Slicer profiles for planar inductor creation

9.3 The Characterisation

9.3.1 Theoretical behaviour

Solenoid inductor

The simplest description of a solenoid's inductance is found in a combination of an idealized version of Ampere's law and Faraday's law. This results in a description of the field in a long solenoidal coil as provided in equation 9.1 [74]. To provide some insight into the relevant parameters in this equation, figure 9.7 has been created.

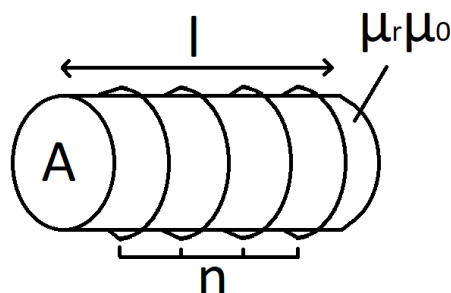


Figure 9.7: Solenoid with core material

The number of turns is provided by n , with the length of the solenoid being described by l in [m]. The cross-sectional area of the coil is provided by A in [m²]. The contribution of the core material is dictated by μ_r which provides a material dependant multiplier of the magnetic permeability of free space μ_0 [Hm⁻¹].

$$L = \mu_r \mu_0 \frac{n^2 A}{l} \quad (9.1)$$

With an estimate of the coils inductance calculated, the next contributing factor to the coils behaviour is its series resistance. This can be derived by taking the cross-sectional area of each winding wire in combination with the circumference of the coil windings. The derived relation is provided in equation 9.2 for the solenoids series resistance in $[\Omega]$ as a function of radius r in $[\text{cm}]$, coil turns n , material resistivity ρ in $[\Omega\text{cm}]$ and the cross-sectional area of the coil windings A in $[\text{cm}^2]$

$$R_{wind} = n\rho \frac{2\pi r}{A} \quad (9.2)$$

In addition to the series resistance of the windings a inter-winding capacitance will also be present. The effective value of this capacitance can be estimated by taking the approximation that each coil winding can be represented as a flat hollow ring, stacked by the total amount of windings. This idea is illustrated by figure 9.8, which also provides the insight that these capacitances are in a series circuit across the ends of the coil.

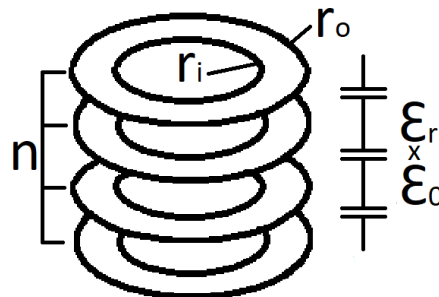


Figure 9.8: Solenoid winding capacitance

The equation resulting from this approximation as a function of inner and outer winding radius r_i and r_o in $[\text{m}]$, number of turns n , dielectric thickness d in $[\text{m}]$. As well as the relative permittivity of the dielectric material and the vacuum permittivity in $[\text{Fm}^{-1}]$ is provided in equation 9.3.

$$C_{wind} = \frac{\epsilon_r \epsilon_0}{d(n-1)} \pi(r_o^2 - r_i^2) \quad (9.3)$$

A second empirical equation describing the inductance of a air cored solenoid is provided by one of Wheeler's equations for radio coils as provided by equation 9.4. The turns of the inductor are once more provided by n , with r and l representing the radius and solenoid length in imperial inches, with the equation providing the inductance in $[\mu\text{H}]$.

$$L = \frac{r^2 n^2}{9r + 10l} \quad (9.4)$$

The empirical nature of this simplified equation results in the requirement for conversion of metric dimensions, however for coils where $l > 0.8r$, a 1% accuracy is achieved [108]. The meaning of the dimensions as used in the equation are shown in figure 9.9.

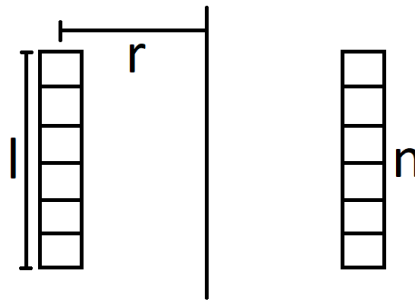


Figure 9.9: Solenoid with air core

Planar inductor

For the planar inductor another Wheeler's equation will be applied, as given by equation 9.5 describing windings in a flat plane. The dimensions applied in the equation are further clarified by figure 9.10 and are in imperial inches. Provided parameters r and w being coil radius and width respectively, with the equation providing the estimate inductance in $[\mu\text{H}]$.

$$L = \frac{r^2 n^2}{8r + 11w} \quad (9.5)$$

Notes with respect to this equations accuracy suggest 5% for coils for which $w > 0.2r$, which with the chosen coil design will not be achieved. However since the requirement of $r > w > 0.2r$ has been achieved, the usage of this formula is still recommended by Wheeler [108].

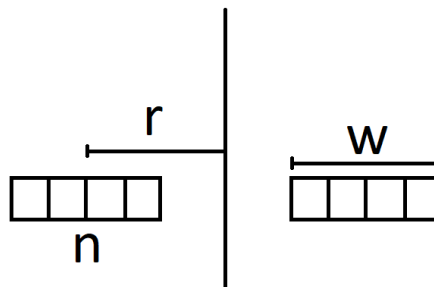


Figure 9.10: Planar with air core

The winding resistance of the planar conductor is slightly harder to determine, given the spiral consists of many half circles with different radii. The same holds for determining the effect resulting from the inter-winding capacitance as the spiral has a resistance along its entire length forming a non-trivial RC network within itself. The proposed simplification is provided in figure 9.11, where by assuming constant radius circles an estimate of the total winding resistance can be made.

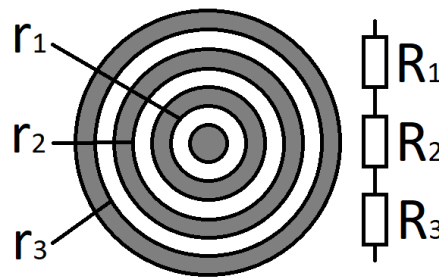


Figure 9.11: Planar inductor winding resistance

The resulting resistances based upon the inner coil radii, starting from the first coil from the center wire can be calculated according to equation 9.6. Given the nature of the separate circles, resistances are calculated independently and summed afterwards. The windings turns are represented by n , material resistivity is indicated by ρ in [Ωcm] and the cross-sectional area of the coil windings A in [cm^2].

$$R_{wind} = \sum_{x=1}^n \rho \frac{2\pi r_x}{A} \quad (9.6)$$

The capacitance in between the concentric circles is slightly more difficult to calculate and is described as shown by figure 9.12. The concentric capacitances are in series with one another and non-equal resulting in more complicated computation of the resulting combined capacitance. The parallel plate approximation was replaced by a circular capacitor approximation which is provided in equation 9.7 [72].

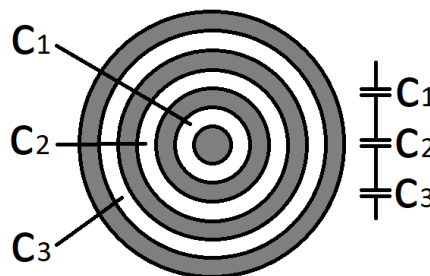


Figure 9.12: Planar inductor winding capacitance

The capacitance in equation 9.7 provides the capacitance for a set of concentric circles in [F]. The parameters are r_x and r_{x-1} in [m] the radii of the facing circles, t the coil thickness in [m] and ϵ_r and ϵ_o the relative permittivity of the dielectric material and the vacuum permittivity in [Fm^{-1}].

$$C_{wind,x} = \frac{\epsilon_r \epsilon_o}{\ln\left(\frac{r_x}{r_{x-1}}\right)} 2\pi t \quad (9.7)$$

The final step in determining the winding capacitance of the planar coil is to calculate the equivalent capacitance for the series of capacitors according to equation 9.8

$$C_{wind} = \frac{1}{\frac{1}{C_1} + \dots + \frac{1}{C_n}} \quad (9.8)$$

9.3.2 Component quality

The component quality for the inductive elements will be derived through the same method as provided in section 8.3.2.

9.3.3 Impedance fitting

The impedance of the inductors will be derived with the same method as proposed by section 8.3.3, applying the same calibration configuration give the same probes and similar components were being tested. The equivalent model as used for the estimation of the inductors properties as based upon models commonly found in literature [42] is provided in figure 9.13.

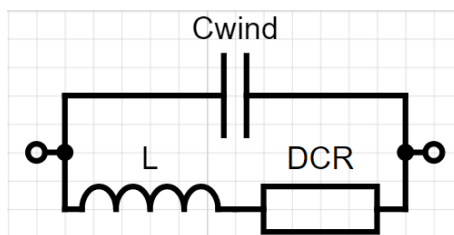


Figure 9.13: Inductor equivalent model

The inductor model consists of the ideal inductance with a series resistance to represent the contribution of the windings created from the Electrifi filament. Due to the limited separation of the windings, a capacitive effect between them was also included in parallel to the inductance and the winding resistance.

9.4 Results

9.4.1 Calculated Impedance

To provide a basis of comparison for the measurements that will be performed, expected component and parasitic values were calculated on the basis of previously determined equations.

Solenoid inductors

For the solenoid inductors, the inductance will be calculated in twofold, initially with the analytical model after which Wheeler's empirical model will follow. The inductors winding resistance and capacitance will also be calculated. Starting with the use of equation 9.1 in combination with the values as provided in table 9.3, an inductance of 478 nH was derived for the three winding air cored solenoid and a inductance of 3.98 μH was obtained for the five winding iron filled core solenoid.

L	Symbol	Air core	Iron core
Coil windings	n	3	5
Relative permeability [90]	μ_r	1	5
Vacuum permeability [74]	μ_0	$0.4\pi \mu\text{H m}^{-1}$	$0.4\pi \mu\text{H m}^{-1}$
Coil area	A	$121\pi \text{ mm}^2$	$121\pi \text{ mm}^2$
Coil length	l	9 mm	15 mm

Table 9.3: Calculation parameters used to solenoid inductance

The next step is to confirm these values with a comparison to empirically determined radio frequency air cored coil inductances as determined by equation 9.4 with the values as provided in table 9.4. After converting the metric lengths to inches, an inductance of 227 nH was obtained

for the three winding solenoid and an inductance of 478 nH was achieved for the five winding solenoid.

L	Symbol	Three windings	Five windings
Coil windings	n	3	5
Coil length	l	9 mm	15 mm
Coil radius	l	11 mm	11 mm

Table 9.4: Calculation parameters used to derive solenoid inductance

Proceeding by calculating the coil resistances with the use of the values provided by table 9.5 and equation 9.2 where the previously derived alongside resistivity for the Electrifi filament was used. The expectation of a series resistance of 5.18 Ω was obtained for the three winding solenoid with an expected 8.64 Ω resistance being obtained for the five winding solenoid.

R_{wind}	Symbol	Three windings	Five windings
Resistivity	ρ_{along}	0.01 Ω m	0.01 Ω m
Coil windings	n	3	5
Coil radius	r	11 mm	11 mm
Coil cross-section	A	4 mm ²	4 mm ²

Table 9.5: Calculation parameters used to derive solenoid winding resistance

The final value to be calculated for the solenoid inductors was their winding capacitance as given by equation 9.3. The calculated winding capacitances on the basis of the values provided in table 9.8 were determined to be 3.11 pF for the three winding solenoid and 1.55 pF for the five winding solenoid.

C_{wind}	Symbol	Three windings	Five windings
Coil windings	n	3	5
Winding spacing	d	1 mm	1 mm
Relative permittivity [31]	ϵ_r	2.66	2.66
Vacuum permittivity	ϵ_0	8.854 pFm ⁻¹	8.854 pFm ⁻¹
Inner coil radius	r_i	20 mm	20 mm
Outer coil radius	r_o	22 mm	22 mm

Table 9.6: Calculation parameters used to derive solenoid winding capacitance

Planar inductors

For the planar inductors only Wheeler's empirical radio coil model for flat coils was applied to determine the inductance, with a concentric circle approximation being applied for the winding resistance and capacitance calculations. With the use of equation 9.5 and the values as provided in table 9.7 after conversion to inches a theoretical inductance of 211 nH was calculated.

L	Symbol	Value
Coil windings	n	4.5
Coil width	l	8 mm
Coil radius	l	6 mm

Table 9.7: Calculation parameters used to derive planar coil inductance

The winding resistance for the planar inductors was determined with the use of the values provided in table 9.8 and equation 9.6. The total sum resulted in 12.6Ω , with the use of the along-side Electrifi resistivity as determined in chapter 3.

R_{wind}	Symbol	Value
Resistivity	ρ_{along}	$0.01\Omega m$
Coil radius 1	r_1	2 mm
Coil radius 2	r_2	4 mm
Coil radius 3	r_3	6 mm
Coil radius 4	r_4	8 mm
Winding cross-section	A	1 mm^2

Table 9.8: Calculation parameters used to derive planar coil winding resistance

The calculation of the winding capacitance was slightly more involved and required the usage of equation 9.7 in combination with the values in table 9.9. The derived capacitances for the concentric windings are provided in table 9.10, where the radii of the for the approximation used concentric circles are also provided.

C_{wind}	Symbol	Value
Coil thickness	t	1 mm
Relative permittivity air[72]	ϵ_r	1.00
Relative permittivity pla[31]	ϵ_r	2.66
Vacuum permittivity	ϵ_0	8.854 pFm^{-1}

Table 9.9: Calculation parameters used to derive planar coil winding capacitance

These derived capacitances could then be combined into a series circuit with the use of equation 9.8 to provide a 0.06 pF capacitance for the coil printed in the air, and a 0.16 pF capacitance for the in neat PLA embedded coil.

r_i	r_o	C_{air}	C_{pla}
4 mm	6 mm	0.14 pF	0.36 pF
8 mm	10 mm	0.25 pF	0.66 pF
12 mm	14 mm	0.36 pF	0.96 pF
16 mm	18 mm	0.47 pF	1.26 pF

Table 9.10: Derived concentric circle capacitances for planar coil winding resistance estimate

9.4.2 Measured Impedance

Solenoid inductors

Continuing with the inductor samples, the first set of inductors characterized on the basis of the equivalent model also provided in section 9.3.3 were those of the solenoid type. Their measurements and subsequent fit being shown in figures 9.14 and 9.15.

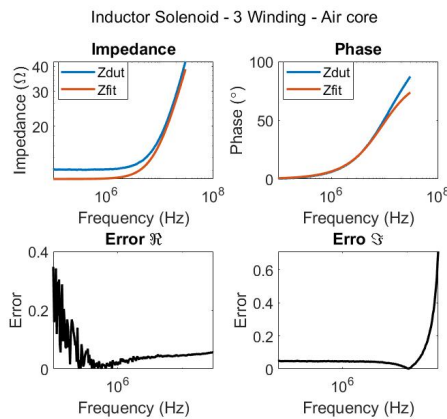


Figure 9.14: Three windings - Air core

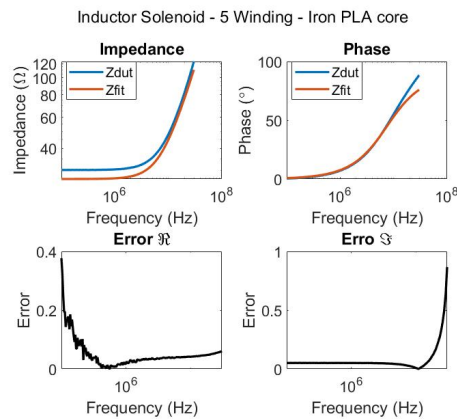


Figure 9.15: Five windings - Iron PLA core

From the compensated measurements in the figure it can be observed that no strange additional probe parasitic can be observed for the device under test. What can be observed however is a slight tapering of the phase at higher frequencies, which is not to be expected from an inductive element. This potentially might be a result of a capacitance not accounted for by the equivalent circuit model as the fitted winding capacitance always ended up at the lower bound, minimizing its contribution.

In table 9.11 an overview is provided of the derived inductance, winding resistance and winding capacitance. It can be observed that the winding resistance was not able to be measured, as it hit the lower bound far below the expected pF capacitance, indicating that its contribution was not measurable within this frequency range. Fortunately the inductance and winding resistance were determined successfully showing inductances in the several hundreds of nH, with relatively low winding resistances of approximately 5 Ω per loop.

	Estimate	lb	hb	Air 3 winding	Iron 5 winding
Inductance	100 nH	1 nH	1 μH	197.16 nH	569.79 nH
Winding Resistance	10 Ω	1 Ω	100 Ω	10.876 Ω	26.955 Ω
Winding Capacitance	1 pF	1 fF	1 nF	1 fF	1 fF

Table 9.11: Fitted inductor model for solenoid inductors

Planar inductors

The planar inductors were also fitted to the same equivalent circuit model, for which the derived fits are shown in figures 9.16 and 9.17.

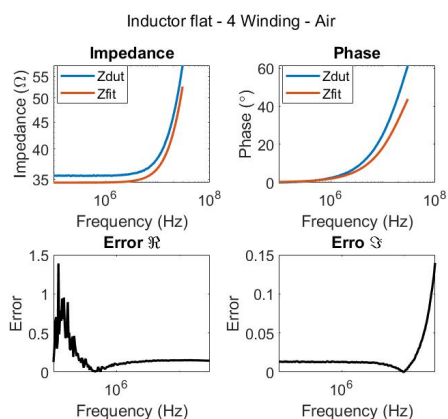


Figure 9.16: Four windings - Coil in air

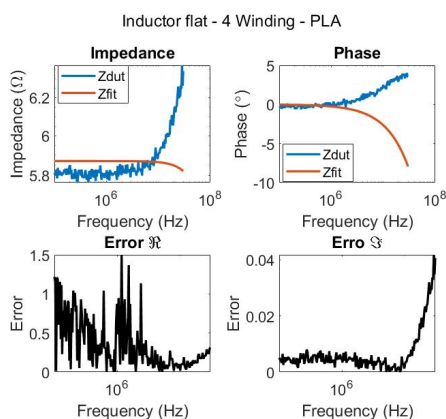


Figure 9.17: Four windings - Coil in PLA

With the planar inductors a different deviation was observed in the phase as well as the impedance for the in air surrounded planar coil. This suggests that the fitting tool was not able to arrive a fully accurate fit, potentially due to it attempting to result in the best fit overall, leading to overfitting of the least squares sum. The embedded planar coil can be observed to have shorted and therefore resulted in a non-functional inductor, with an inaccurate fit.

In table 9.12 the determined inductance, winding resistance and winding capacitance for the flat inductors is shown. Likewise to the solenoid inductors the winding capacitance could not accurately be determined due to the limited frequency range being tested, as no roll-off of the impedance is observed at the higher frequency as an effect of the inter-winding capacitance. The winding resistance of the air coil appears to be within the expected range, with the embedded coil being a factor of 6 lower, suggesting shorting of the coils windings.

	Estimate	lb	hb	Air 4 Winding	PLA 4 Winding
Inductance	100 nH	1 nH	1 μ H	192.87 nH	1 nH
Winding Resistance	10 Ω	1 Ω	100 Ω	34.517 Ω	5.8707 Ω
Winding Capacitance	1 pF	1 fF	1 nF	6.9333 pF	154.73 pF

Table 9.12: Fitted inductor model for solenoid inductors

9.5 Discussion

9.5.1 Model accuracy

Given that before measurements analytical models were created of each component, a study of the differences between the produced components and their theoretical behaviour will be provided.

Solenoid inductors

The inductance of the solenoid inductors as derived on the basis of Wheeler's approximation appears to have been most accurate, with measurements being within 20% of the estimated three winding air core inductance and within 5% of the estimated five winding iron core inductance. The calculated values of these inductances were off by 110% for the three winding air core and off by 830% for the five winding iron cored inductance, suggesting that a deviation from the long solenoid model was present due to the coils short length and the that modelled contribution of the iron core was incorrect. Given the accuracy of the Wheeler approximation for air cores for both the three and five wire core it is suspected that the iron in the Protopasta

magnetic material did not contribute to an increased magnetic field strength in the inductor, for a yet to be determined reason.

The winding resistances of the solenoid inductors were found to be a factor 2 larger than initially calculated for the three winding inductor and a factor 3 larger for the five winding inductor. It is proposed that this effect resulted from the additional heat input provided by the molten PLA material added in between and on the sides of the Electrifi tracks which have been found to increase rapidly in resistivity at temperatures above 40 °C. Given that the sides of the tracks were only exposed for the five winding inductor, this would also explain the observed additional deviation between the two created coils.

Although winding capacitance was calculated for the solenoid inductors, no successful fit of similar values could be obtained during on the basis of these measurements. This can be explained by deriving the poles of the RLC circuit formed by the calculated capacitance, measured resistance and measured inductance with a pole at 210 MHz for the three winding inductor and a pole at 182 MHz for the five winding inductor. These poles being located far beyond the achieved measurement range, with the capacitive contribution coming into effect at these frequencies, no accurate fit could be derived.

Planar inductors

The inductance of the planar inductors was only derived with the use of Wheeler's approximation, which achieved an accuracy of 5% for the planar inductor printed on top of the PLA material. The in the PLA material embedded inductor however only achieved a fraction of this total inductance despite being of the same design, this in combination with the lower winding resistance suggesting shorts being formed in between windings reducing the total inductance achieved.

The determined winding resistance itself deviates with a factor of 2.7 increase for the in air printed planar coil and with a 0.4 factor decrease for the embedded planar coil. As suggested previously the embedded coil is suspected to have shorted in between windings reducing the total impedance achieved, given that other work on embedding Electrifi filament in PLA resulted in an increase conductor resistance [69].

As with the solenoid inductances the winding capacitances were not successfully determined with the poles from the measured inductance and resistance in combination with the as calculated capacitance being around 1.4 GHz for the air coil and 1.7 GHz for the embedded coil. Both poles being far past the frequency range recorded during measurement.

9.5.2 Quality

The next point of discussion is the usability of the produced parts, making use of equation 8.4 to provide insight into the losses within the created inductors in typical applications.

The set of values chosen to derive an approximate natural frequency were 400 pF representing the neat PLA capacitors and 200 nH representing both the planar and the solenoid inductors, resulting in a natural frequency of 17.8 MHz. At this natural frequency a Q_L of 2.14 would result for the three winding air cored solenoid, a Q_L of 0.72 would result for the four winding planar air coil.

In order to represent the gains observed from the use of the Protopasta Magnetic Iron filament as both a dielectric and a magnetic core material, a 550 pF capacitance and a 550 nH inductance with a resulting natural frequency of 9.2 MHz were chosen to represent an oscillator created from these components. This natural frequency provides a Q_L of 1.12 for the five winding iron cored inductor.

These larger Q-factors for the inductors suggest the components should be usable in an oscillator circuit leading to underdamped behavior.

9.5.3 Design

The solenoid inductor design could be improved to increase its inductance without altering its outside in two manners as well. Firstly the layer height could be reduced in order to fit more windings on top of one another, at the cost of increased winding resistance and capacitance. Secondly the use of an effective core material could be made, resulting in a greater impedance per winding, at the cost of any potential energy losses in the core material.

The planar inductor design could be improved to increase its inductance for the same outside dimensions, by changing the winding widths and separation at the cost of increased series resistance due to the reduced winding cross-section, and closer spaced windings forming a larger capacitance. The embedded planar inductor design could be improved by increasing the inter-winding spacing, to prevent shorting and additionally decrease inter-winding capacitance, at the cost of a lower winding count.

9.6 Conclusions

9.6.1 Performance

The performance of the designed inductance was observed to be scalable with winding count, and to be inline with expectations. The Q-factor however came in in the range of approximately 0.72-2.14 which indicates a underdamped system capable of oscillating, despite the series resistance being expected to limit its useful bandwidth of inductive behaviour. The calculated capacitances and observed resistance suggest that this bandwidth lies somewhere in between MHz and GHz.

9.6.2 Modellability

The solenoid inductance was found to be very accurate to the predictions from Wheeler's approximation, with the tree winding core being within 20% and the five winding core being within 5% of the intended inductance. The iron core included in the five winding solenoid was found to not contribute given the 830% deviation of its inductance from the long solenoid inductance equation accounting for the core. The long solenoid equation was also found to deviate with 110% for the air cored three winding solenoid, suggesting it is more suited for longer coils than tested.

The calculated winding resistance was observed to be a factor of 2-3 off which is suggested to be resultant from the heat input into the Electrifi filament. This theory was further confirmed by the larger error for the cored inductor, which saw additional heat input due to the core being printed. The parasitic capacitance was not verifiable due to the high frequencies at which they were expected to be observable not being attained by the measurement equipment.

The planar coils inductance was only modelled through Wheeler's planar equation for which a 5% accuracy was obtained for the by air surrounded inductor. The embedded inductor was found to have shorted and was therefore considered not comparable to the model.

The winding resistance of the air printed core was found to be a factor 2.7 larger than estimated similarly to the solenoid inductors, presumably due to the heat input into the Electrifi material. The shorts in the embedded coil once more allowed the embedded core not to be comparable to the model at a factor 0.4 decrease from the calculated resistance. The parasitic capacitance was also not verified due to the high frequencies not being attained by the measurement equipment.

9.6.3 Improvements

The solenoid inductors inductance could be improved without increasing its size by increasing winding density for a given length as well as by making use of an effective core material. The

planar inductors inductance could be improved by increasing the winding density as well. Additionally the embedded planar inductor could benefit from improved winding spacing, better optimized printing settings, to prevent shorts from forming.

10 Conclusions

Following from the research done into the materials, interfaces and creation of circuit components of conductive FFF 3d printing, answers can be provided to the research questions as initially provided in the introductory chapter. Answers will also be provided to the combined research questions, resulting in conclusions about the feasibility of certain future technologies, before answering the main research question.

10.1 Are 3d printed electronics compatible with typical electronic operating conditions?

In terms of operating conditions it was found that the most conductive tested material, Electrifi was not suitable for conventional electronics operation conditions despite its high current carrying ability, due to its significant degradation at temperatures above 40 °C.

The less conductive carbon black filled TPU and PLA filaments however were able to withstand temperatures up to 150 °C without degrading, where it was noted that the drift due to an annealing effect appeared to gradually settle. The feasible current densities for these materials were found to be related to the surface to volume ratio of the conductive section of material, with mA mm^{-2} current densities being observed, which should be sufficient for simple electronic circuits.

10.2 Are 3d printed components compatible with traditional substrates?

The interface quality was investigated for two types of substrates: Printed circuit boards coated with gold and tin, to both represent the adhesion to the FR-4 material as to the pad coatings which also represent the materials commonly found in silicon die bond paths for wire bonds. The second substrate was the use of silicon itself in the form of 100 mm wafers, upon which a direct printing of the conductive polymers was attempted, with a pressure test being used to derive adhesive strength.

During these experiments it was found that only the TPU filaments were capable of adhering to the substrates sufficiently due to the thermal stress induced during cooling after printing, with the interface quality to silicon reaching reaching separation pressures past the control for these materials in several samples. For the printed circuit board samples the TPU filaments were also found to be the most suitable for adhesion with other samples detaching after the print cooled. The gold contacts were found to provide a qualitative resistive interface, with the tin contacts resulting in a contact containing a capacitive contribution due to the oxide separating the tin metal from the polymer printed on top as well as the slight curvature resulting from the tin coating forming air pockets resulting in capacitive effects at higher frequencies.

10.3 Are printed components performing sufficiently for typical use?

In order to test the abilities and the alignment of 3d printed electronic components, resistors, capacitor and inductors were created and analysed on the basis of conventional analytical models in comparison to observations made about these components through measurement.

It was observed that the created resistors aligned well with the models created for an infill orientation based variation in resistance. The created capacitors also aligned well to the estimated capacitance as found from literature using a PLA dielectric, with it also being shown that the use of filled PLA dielectrics would increase the resulting capacitances. The parasitic series resistance also aligned with expectations according to the material characterizations performed.

The created inductive components aligned to the analytic model with respect to the empirically derived Wheeler's equations, with no effect being found from the applied iron filled PLA core

material tried. The series resistance as calculated with the use of the for Electrifi characterized volume resistance was found to be roughly doubled, although this could be contributed to the thermal degradation of the PLA filament being printed in conjunction at higher temperatures. Winding capacitances were also calculated but however not verified during measurement given that the frequencies achieved were too low to arrive at resulting poles.

The series resistances of the resulting components resulted in a relatively low Q-factor at attainable oscillation frequencies, making them less suited for high performance circuitry, although their behaviour was found to be repeatable and according to model expectations.

10.4 Are Hybrid circuits a possibility?

Combining the conclusions provided to the feasibility of 3d printed conductive polymers in typical operation conditions and the suitability of these polymers with integration to traditional substrates, it can be concluded that hybrid circuits could most definitely be a possibility. Due to the high resistivities of the suitable materials however it should be taken into account that these materials are only suitable for low current densities and simpler circuitry.

10.5 Are Fully printed circuits a possibility?

Following up on the feasibility of the combination of traditional and conventional electronics, it can also be considered if fully 3d printed circuits are within the realm of possibilities. Given that functional components were produced, although with a relatively low Q-factor, and that certain polymers were proven capable of typical operation conditions fully printed circuits would be possible.

However one should take into account the materials resistivity, given that for the use of inductive elements the Electrifi would be required which is only capable of sustaining temperatures below 40 °C with the other materials providing only capabilities for capacitive and resistive elements due to the high resulting series resistances.

11 Recommendations

On the basis of notes made during the experiments, a list of suggested recommendations is proposed for further research and component designs.

11.1 Improvements to material properties

The first set of recommendations is proposed for obtaining improved material properties over the commercially available materials, by creating application specific filaments with the use of a filament extruder system.

11.1.1 Experiment with base materials

The base material used for the polymer being printed has a large effect upon the materials resistance to temperature, its mechanical properties and its ability to adhere to various materials. Additionally the choice of material could affect the ability to integrate with other polymers used in potential products where the 3d printed electronics is applied, making the choice of base material an important factor to explore.

11.1.2 Experiment with fillers

The fillers used in the conductive and magnetic polymers also would provide a great research topic, provided that metal nano-wires, carbon nano-tubes, carbon black particles, PEDOT:PSS and graphene flakes have all been shown in previous work. By making use of mixtures of these filler materials, improved mechanical properties as well as tuneable thermal and electrical conductivity could be achieved.

11.1.3 Experiment with filling content

The last factor easily varied during experimentation is the filler content of the various materials, allowing for a trade off between printability, mechanical properties and additional thermal and electrical properties.

11.2 Improvements to interface and adhesion

The second section of recommendations is contributed to suggested manners of improving the electrical and mechanical interface between conductive polymers and traditional substrates on the basis of experimental findings.

11.2.1 Material stress relieve

The first problem to sort out would be to figure out a manner to reduce the observed thermal stresses resulting during and after printing in the material itself as well as between the material and the substrate. The Ninjatek and Palmiga filament were found to be able to cope with this due to their flexible nature, however a clear problem in the adhesion of non-flexible materials was observed. Potentially the usage of a heated surrounding or a controlled oven cool-down above the polymers crystallization temperature could resolve these issues.

11.2.2 Mechanical lock

The next suggestion to be investigated is to create a mechanical connection between the substrate, forming a permanent mechanical bond instead of the surface bonds formed by the shown direct adhesion. This technique should also allow for continuous strain on the printed parts for potential sensing applications, although care has to be taken to consider the prevalent creep often observed in polymers.

11.2.3 Buffer layer (glue)

The last suggestion as also found in literature is the use of an interfacing layer, aiding the adhesion and compensating for potential differences in material expansion with temperature and composition. As also suggested in literature metallic conductive particles could be included in this inter-facial layer, separating the requirements for the adhesive and the conductor.

11.3 Improvements to component design

The third section of recommendations is focussed on suggestions for improving the designs created for the printed resistors, capacitors and inductors.

11.3.1 Resistors

the first set of suggestions will be for the resistors, for which it is suggested to attempt different infill patterns and different infill percentages to form the completed resistor to allow for more variation in the achieved resistance given a the same perimeter. Additionally completely hollow structures could be created to possibly allow for more cooling capacity by increasing the area to volume ratio, increasing the allowable current density.

11.3.2 Capacitors

For the capacitors as already previously suggested, a smaller distance between opposing plates or a different dielectric material could be used to create larger capacitances given a provided volume. Additionally the power of 3d printing could be used to create three dimensional patterns to optimize the surface area in between capacitor plates, although this would result in greater difficulty in predicting the resulting capacitance and series resistance.

11.3.3 Inductors

The inductors could mainly be improved by usage of a more conductive and an effective core material, allowing for larger inductances with lower series resistance to improve the Q of the resulting inductive components. Stacked multi layer planar coils or cross wound coils could also be attempted to provide the advantage of mutual inductance between coil windings, without increasing the series resistance.

A Long term measurements

Due to the many measurements taken during the real time material characterization experiment, it was decided to place the abbreviated results into the appendix highlighting only the key results in the main chapter. The first section will introduce a description and images of the created samples, followed by a chapter on the derived material resistivities for both heat-treated and non-heat-treated samples. The effects observed of this heat treatment will be highlighted in a section on the annealing effect, followed by a final chapter on the thermal effects observed affecting the resistivity of these samples.

A.1 Produced samples

The first set of samples exposed to room conditions and oven controlled thermal profiles were created from a TPU based carbon black filled filament with a 90A Shore hardness produced by Ninjatek[80]. The samples were printed one by one in direct succession, with optimized settings for minimal void formation or over extrusion. Images of the prepared samples before oven and room exposure as well as after oven exposure are provided in figure A.1. Very little warping could be observed after exposure to the oven's temperature profile and the samples did not appear to have degraded after a visual inspection.

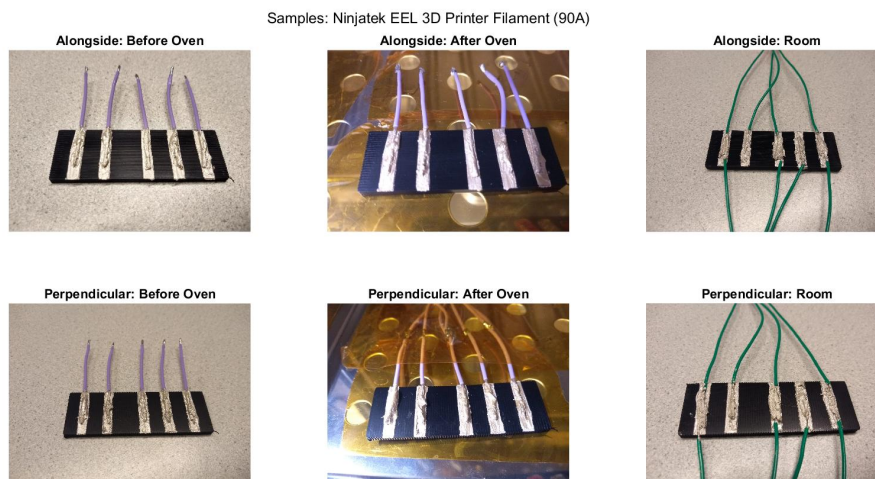


Figure A.1: Ninjatek samples used for real time experiment

The second material to be subjected to the material characterisation was another carbon black filled TPU filament with a Shore hardness of 85A produced by Palmiga Innovations [83]. The samples were printed one after the other with settings optimized for minimal under or over extrusion. As with the previous material the samples before and after oven exposure as well as the samples kept at room condition are provided in figure A.2.

The Palmiga samples also showed minimal warping, due to their flexible nature in combination with gravity ensuring they remained in the same shape. It can also be observed from the images that the samples showed minimal degradation, although a noticeable color change could be observed for the conductive epoxy contacts. This might be explained by certain chemicals from the polymer blend outgassing during the anneal or exposure cycles.

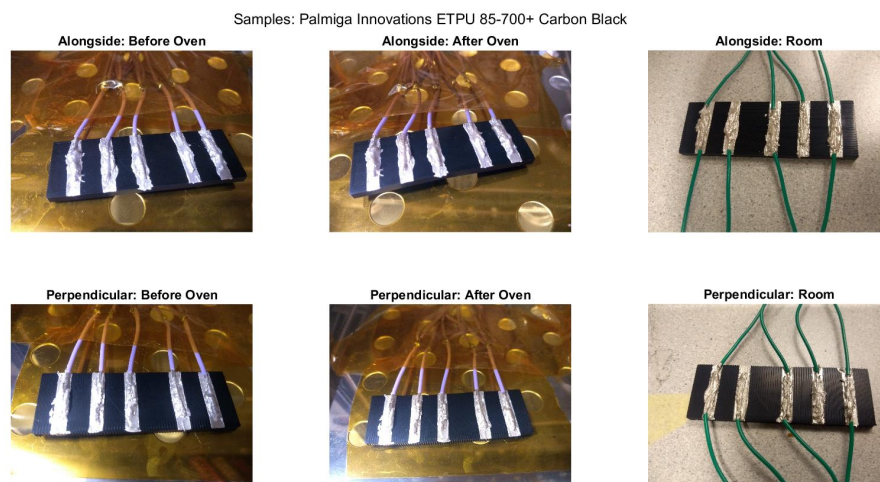


Figure A.2: Palmiga samples used for real time experiment

The first and only PLA based material exposed to the real time measurements was a Carbon Black filled filament by Protopasta [89]. The samples were printed successively once more, and printed according to the manufacturers recommended settings as this provided a perfectly extruded sample.

In figure A.3 the produced samples before and after oven exposure as well as the samples exposed to room conditions are shown. No discoloration of the contacts after oven exposure could be observed, whereas slight warping could be observed. The samples appeared to not have degraded due to the temperature exposure.

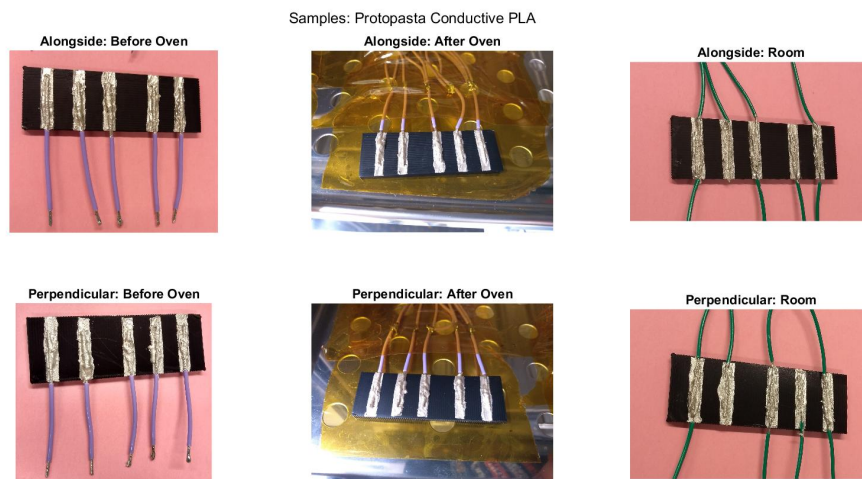


Figure A.3: Protopasta samples used for real time experiment

The last material to be subjected to the real time measurements was a copper nano-wire filled polyester produced by Multi3D referred to as Electrifi [65]. Samples were printed successively on double sided tape for adhesion to a room temperature glass printbed, as the adhesive sprays did not provide sufficient retention at these temperatures. Use was made of the manufacturers

recommended extrusion multiplier, unfortunately the inconsistency of the filament diameter would result in several underextruded traxels.

This is clearly observed in the sample images shown in figure A.4, where it can also be observed that the samples contacts discolored, along with clear degradation and warping of the samples. What is not observable was the significant lightening of the samples and their brittleness, crumbling apart after these pictures were taken.

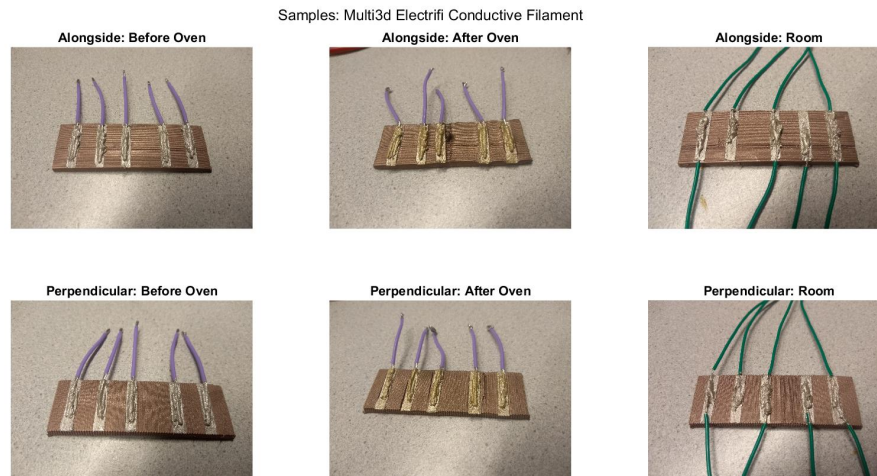


Figure A.4: Electrifi samples used for real time experiment

A.2 Resistivity

In this section the obtained material resistivities on the basis of the method as defined in section 3.3.1 will be provided. These derived results were created with the resistances as recorded with the Keithley scan 2000 multimeter [41], and processed afterwards in MATLAB [56] with the use of dimensions as provided in chapter 3 for the created samples.

A.2.1 Room Samples

The initial set of samples characterized were those exposed to room temperature conditions, with the from the recorded resistances derived resistivities being shown for the Ninjatek filament in figure A.5. For these samples an anisotropy between the two traxel orientations with respect to the measurement current can be observed, as well as an initial steeper decrease in the resistivity proceeding into a continuous drift. The figure also includes the room temperature which was recorded with the use of a calibrated temperature probe, which shows the stability of the room temperature across the measurement period.

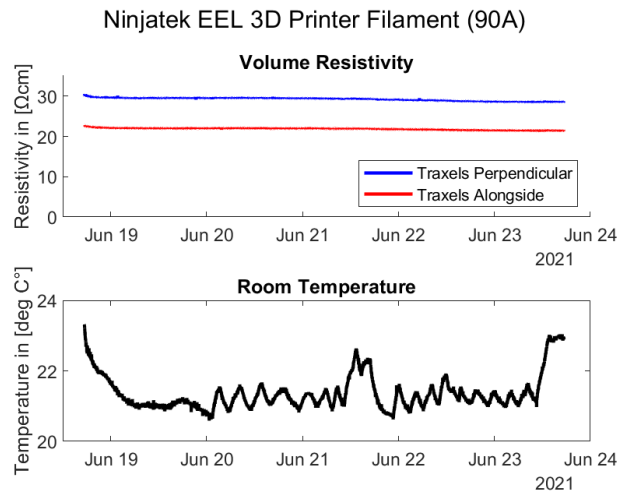


Figure A.5: Resistivity derived for Ninjatek samples during room measurement

In table A.1 the from these graphs derived initial and final resistivities, the resistivity reduction and the obtained anisotropy ratio are provided. The anisotropy ratio provides a measure of the increase observed in the resistivity of the perpendicular traxel orientation with respect to the measurement current resulting in more inter-traxel interface. The reduction provides a measure of the drift observed in the materials resistivity after printing over a period of five days.

Ninjatek EEL 3D Printer Filament (90A)		
	Alongside	Perpendicular
Room start	22.73 Ω cm	30.30 Ω cm
Room end	21.52 Ω cm	28.49 Ω cm
Reduction	95%	94%
Ratio	1	1,3

Table A.1: Resistivity reduction and ratio derived for Ninjatek samples during room measurement

In figure A.6 the resistivity derived for the room condition palmiga samples is provided. Interestingly at the start of this measurement significant variation is visible in the resistance which appears to disappear after 12 hours. This might have been caused by an error in the mixing ratios of the epoxy compound which would affect the curing time required for the formation of a stable contact.

The remainder of the measurement appears stable however, and a similar drift is observable as noticed for the Ninjatek material. The initial steep decrease in resistivity can also be observed in especially the perpendicular measurement, but might be obscured by noisy initial measurement.

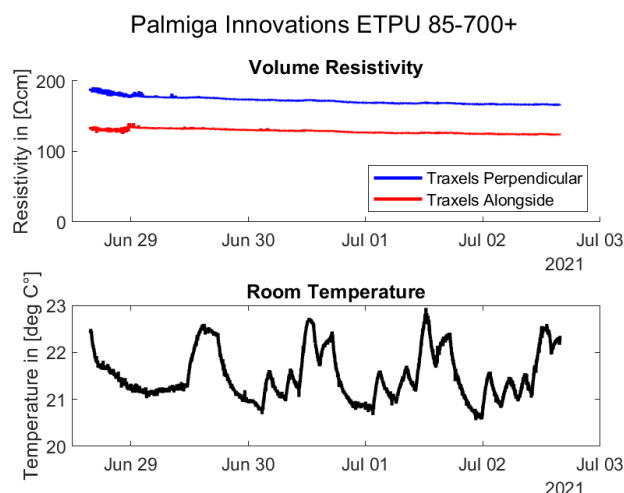


Figure A.6: Resistivity derived for Palmiga samples during room measurement

In table A.2 the summary table for these derived measurements is provided, showing that the drift observed for this material across the five day period is several percent more than observed for the Ninjatek material. The anisotropy ratio also provides a greater difference in resistivity for the Palmiga filament with respect to the Ninjatek TPU filament.

Palmiga Innovations ETPU 85-700+		
	Alongside	Perpendicular
Room start	76.46 Ωcm	150.75 Ωcm
Room end	69.00 Ωcm	119.96 Ωcm
Reduction	90%	80%
Ratio	1	1,7

Table A.2: Resistivity reduction and ratio derived for Palmiga samples during room measurement

In figure A.7 the derived resistivity and recorded room temperature for the room temperature exposed protopasta samples is presented. Initially a steep decrease in resistivity is observed as with the other carbon black filled materials, which is followed by a less steep continuous drift.

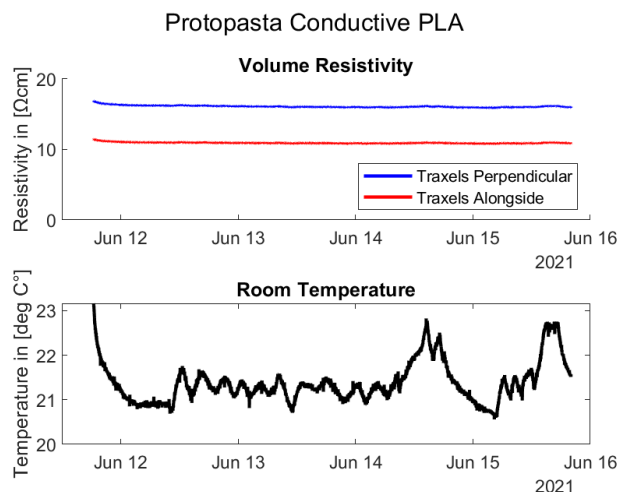


Figure A.7: Resistivity derived for Protopasta samples during room measurement

These observations of a similar drift are also confirmed by table A.3 where a similar reduction percentage to the Ninjatek filament is observed. The anisotropy ratio achieved is also within the same range as the other two carbon black filled TPU based filaments, suggesting correspondence in the inter-traxel defect mechanisms resulting in additional resistance.

Protopasta Conductive PLA		
	Alongside	Perpendicular
Room start	11.47 Ω cm	16.91 Ω cm
Room end	10.84 Ω cm	16.00 Ω cm
Reduction	95%	95%
Ratio	1	1,5

Table A.3: Resistivity reduction and ratio derived for Protopasta samples during room measurement

The room condition measurements for the Electrifi filament as presented in figure A.8 show a relatively large contribution of noise in the measurements. This is a result of the proximity to the minimum $100\mu\Omega$ measurement range of the measurement equipment[41], in combination with the long measurement cables being used.

At these low resistances for a fixed maximum measurement current, a small resulting measurement voltage will be obtained. This is troublesome as long leads tend to work as antenna which couple external signals into the measurement signal, normally measurement voltages are relatively large and this noise is hardly observable. However in the low resistance scenario, our voltages are small and thus the coupled noise can significantly impact our measurements. For future measurements this could be improved by making use of shielded measurement cables, counteracting this coupling effect of external signals.

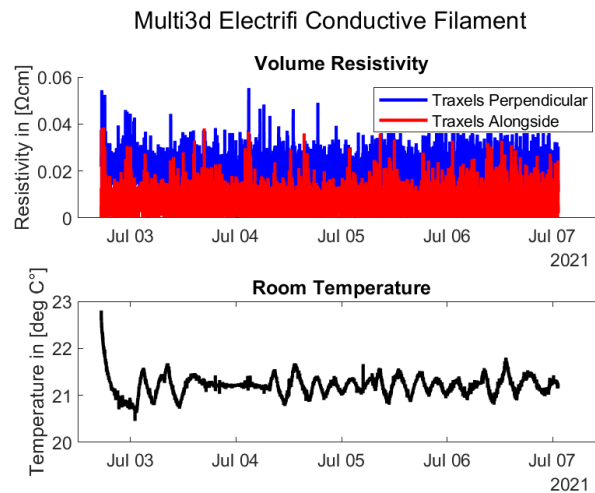


Figure A.8: Resistivity derived for Electrifi samples during room measurement

Despite the noise the values provided in table A.4 were still derivable by taking the first and last resistivities observed. The observed reduction as the samples resistivity drifted over time could be considered comparable to the carbon black filled materials, although this result is debatable due to the noisy signal sampled.

The observed anisotropy ratio however can be deemed to be trustworthy as it is consistent across the measurement period, and significantly larger than was observed for the carbon black filled materials. This points towards a larger inter-traxel resistance, which would be inline with

the occasional under-extrusion observed during printing as a result of inconsistent filament diameter.

Multi3D Electrifi		
	Alongside	Perpendicular
Room start	0,01	0,03
Room end	0,01	0,03
Reduction	87%	93%
Ratio	1	3,4

Table A.4: Resistivity reduction and ratio derived for Electrifi samples during room measurement

A.2.2 Contact validation

In order to ensure the stability of the created contacts at the elevated temperatures to which the oven samples were exposed, a subtraction of a 4-wire measurement and a 2-wire measurement was determined providing an estimate of the contact resistivity. This validation strategy is best explained with the use of figure A.9, which shows us the flow of measurement current and the locations at which a voltage measurement was taken to derive the samples resistance.

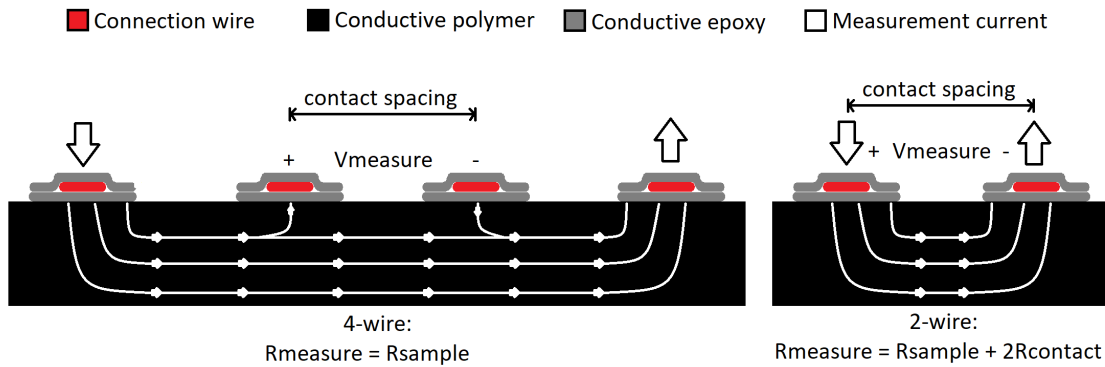


Figure A.9: A comparison of 2- and 4-wire resistance measurements

Due to the measurement current flowing through the voltage observation contacts in the 2-wire measurement, inherently their resistance will also be included in measurement. Since 2 contacts are within this measurement loop, a measured resistance as described by equation A.1 will be obtained.

$$R_{measure_2} = R_{sample} + 2R_{contact} \quad (A.1)$$

With a 4-wire measurement, this problem is resolved by adding a second set of contacts in between the contacts through which the measurement current flows. This in combination with the ideally infinite impedance of the voltage measurement equipment results in no current flow through the contact resistance, allowing for a measurement result as described by equation A.2.

$$R_{measure_4} = R_{sample} \quad (A.2)$$

By taking both a 2- and a 4-wire measurement, whilst retaining the same contact spacing for the voltage measurement, a contact resistance can be derived with the use of equation A.3. It should be noted however that for this approximation to be accurate, it is required that the

samples resistance R_{sample} remains consistent as well as that both contacts have comparable resistances for both measurements.

$$R_{contact} = \frac{R_{measure_2} - R_{measure_4}}{2} \quad (\text{A.3})$$

Fortunately in our measurement scenario both the two wire and the four wire contacts are formed in an identical fashion. The section across which the material resistance is observed was also kept as a constant, as the center two contacts remained the voltage measurement contacts for both characterisations. During measurement with the use of relay switches within the measurement card of the multimeter [41] the measurement contacts were moved from the inner two contacts to the outer two available on the sample.

In figure A.10 the recorded resistances for the Ninjatek filament samples placed in the oven are provided. It can be observed that the contact resistance derived initially peaks at the start of the annealing cycle, but quickly reduces to a fraction of the observed material resistance. In further and the initial measurements of the material resistance through the four wire method these spikes are also observed, whilst being observed to a much lesser degree in the derived contact resistance. This suggests that these spikes do not stem from contact degradation, but however from an initial increase in material resistivity.

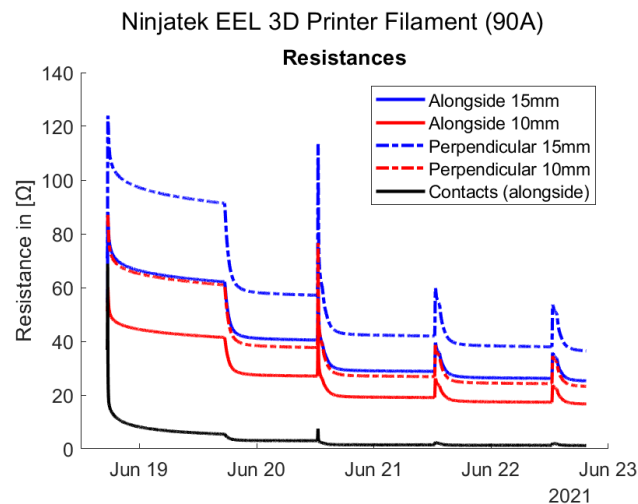


Figure A.10: Resistances observed for Ninjatek samples during oven measurement

The resistances recorded for the Palmiga filament samples are provided in figure A.11, where a missing section of contact resistance data is observed for the initial start of the annealing cycle. This missing data might have been caused by a not fully cured epoxy contact which resolved during the heating cycle or a brief disturbance of the measurement wires. Fortunately the contact regained integrity, allowing for a successful measurement of the remaining data.

It is also interesting to note that the four wire measurements taken did not show this temporary lapse of data, as both the alongside 10 mm measurement and the contact measurement shared the same contacts. This would hint at a failure in the wiring between the multimeter and the samples wires. Although this puts the derived contact resistance into doubt it appears to remain a suitably low fraction of the materials resistance across the recorded exposure period.

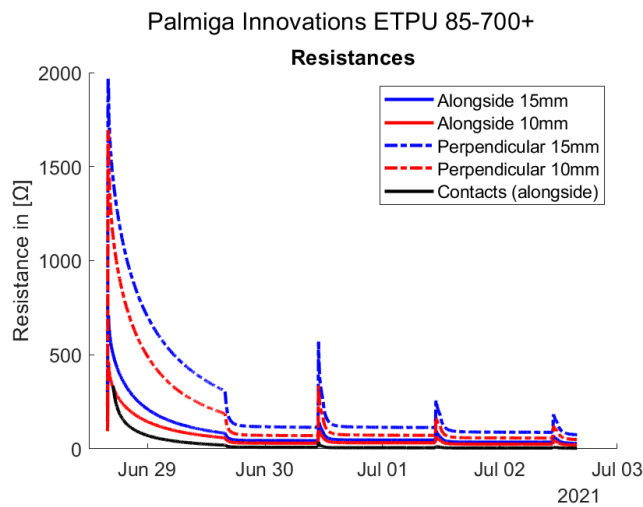


Figure A.11: Resistances observed for Palmiga samples during oven measurement

Figure A.12 provides a similar overview for the protopasta samples, where the contact resistance does not appear to show the initial spike observed for the TPU materials. The first exposure does show some spiking in the contact resistance, however this is relatively little in comparison to the material resistance spike observed. In general the contact resistance appears to be a sufficiently small fraction of the material resistance, to validate the contacts created.

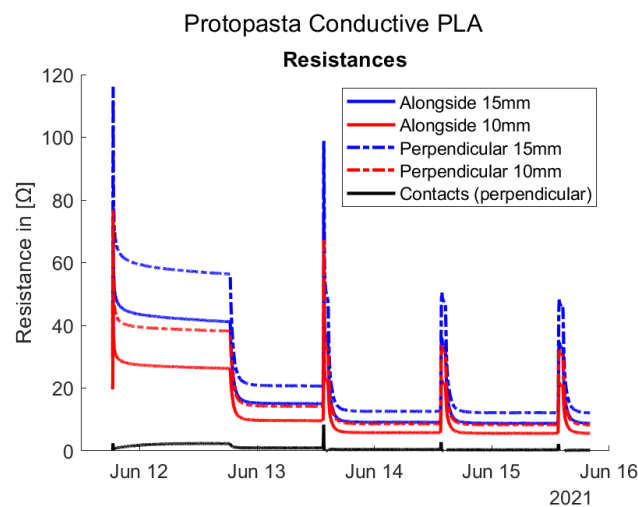


Figure A.12: Resistances observed for Protopasta samples during oven measurement

An example of partial contact failure is provided in figure A.13 where the resistances as recorded for the Electrifi material are provided. Initially the contacts behave as would be expected from previous resistance graphs, although showing a similar resistance to the material due to Electrifi's exceptionally good conductance.

During the first exposure contact integrity is mostly maintained although a gap in the perpendicular 10 mm resistance recording suggests one of the contacts already failed temporarily. The second exposure shows a clear contact degradation resulting in missing data, as does the third exposure. Interestingly as the samples cool contact is restored, however at a similar resistance as observed for the material suggesting that the interface also degrades along with the material. Due to this degradation the trust put into these measurements after the initial exposure should be considered with care even when contact is recovered.

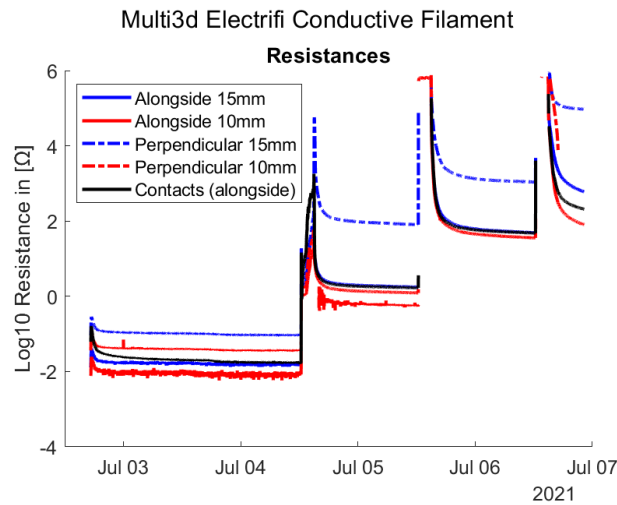


Figure A.13: Resistances observed for Electrifi samples during oven measurement

A.2.3 Oven Samples

With the stability of the contacts confirmed with the exception of the Electrifi samples, which degraded themselves at elevated temperatures, the high temperature exposed oven sample resistivities will now be provided.

In figure A.14 the derived resistivity of the Ninjatek samples on the basis of the resistance measurements and the dimensions as specified in chapter 3 are provided. The temperature in the oven is also provided as recorded with the use of the internal probe of the used Mammert UF30 oven[60], showing an initial anneal period, followed by three high temperature exposures and subsequent cooling periods.

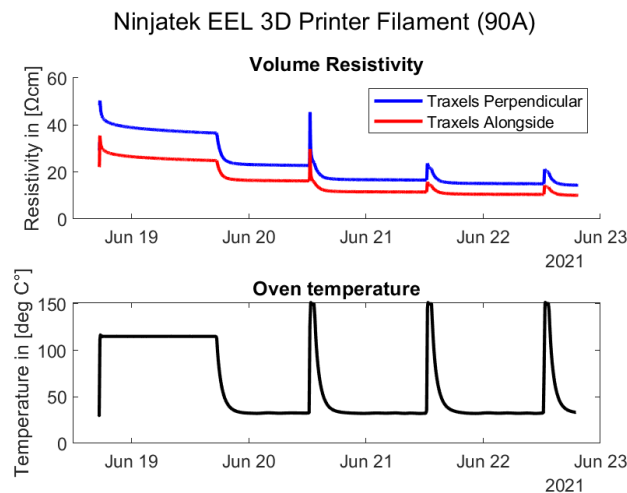


Figure A.14: Resistivity derived for Ninjatek samples during oven measurement

Table A.5 shows the derived initial resistivity and final resistivity for each measurement as with the room condition samples. The effect of the initial annealing period and subsequent exposures to high temperatures as was already observable in the figure led to a much greater decrease in resistivity. The anisotropy ratio however remains almost identical to the in table A.1 provided values, suggesting that the inter-traxel contact defects are not affected by these high temperature exposures.

Ninjatek EEL 3D Printer Filament (90A)		
	Alongside	Perpendicular
Oven start	35.48 Ω cm	50.39 Ω cm
Oven end	10.07 Ω cm	14.38 Ω cm
Reduction to	28%	29%
Ratio	1	1,4

Table A.5: Resistivity reduction and ratio derived for Ninjatek samples during oven measurement

In figure A.15 a much stronger resistivity drop as an effect of the initial annealing period is clearly observable, for the Palmiga filament samples exposed to the temperature profile as discussed previously. Due to the Palmiga samples being printed at a slightly lower temperature than those of the Ninjatek filament, the annealing temperature observed in the temperature profile is also slightly reduced with respect to the previous figure.

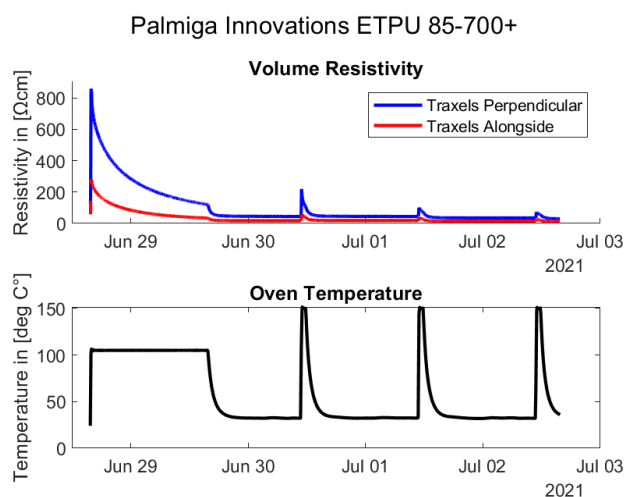


Figure A.15: Resistivity derived for Palmiga samples during oven measurement

The increased observed resistivity drop is also clearly reflected in the summarizing table A.6, where a reduction to only several percent of the original value is obtained for the Palmiga filament samples. The anisotropy ratio is also observed to deviate significantly from the previously determined value in table A.2, suggesting the interface mechanism behind the increased resistance is affected by high temperature exposure for the Palmiga material.

Palmiga Innovations ETPU 85-700+		
	Alongside	Perpendicular
Oven start	282.48 Ω cm	858.78 Ω cm
Oven end	11.81 Ω cm	29.87 Ω cm
Reduction to	4%	3%
Ratio	1	2,5

Table A.6: Resistivity reduction and ratio derived for Palmiga samples during oven measurement

The protopasta samples for which the derived resistivities are provided in figure A.16, also provide insight into the annealing response at the slightly lowered annealing temperature to account for the lower printing temperature of the samples. As with the Ninjatek samples initial

spiking is observed as the temperature is raised, which quickly reduces after the anneal and first exposure cycle, although to a greater extent. It appears that this spiking is related to the introduction of a not previously attained elevated temperature, as for the second and third exposure this effect is not observed.

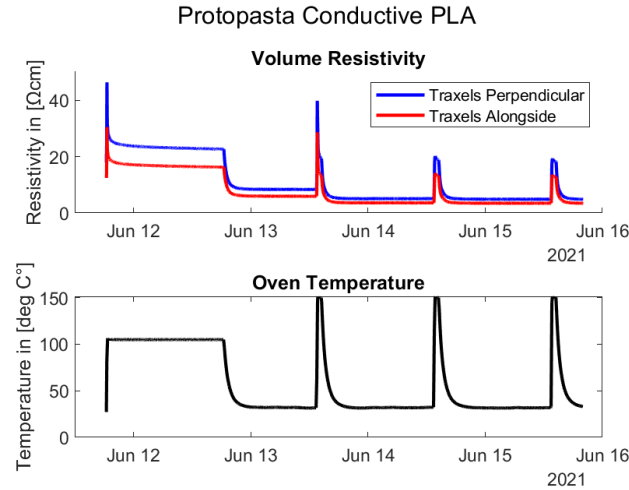


Figure A.16: Resistivity derived for Protopasta samples during oven measurement

The effect of this spike followed by a reduction is clearly observed in table A.7 where a reduction to approximately a ninth of the original resistivity is observed for the samples. The anisotropy ratio is comparable to the value attained for the room condition samples characterized by the results in table A.3.

Protopasta Conductive PLA		
	Alongside	Perpendicular
Oven start	30.45 Ω cm	46.33 Ω cm
Oven end	3.45 Ω cm	4.88 Ω cm
Reduction to	11%	11%
Ratio	1	1,4

Table A.7: Resistivity reduction and ratio derived for Protopasta samples during oven measurement

Due to the thermal degradation of the Electrifi filaments, the measurements provided in figure A.17 make use of a logarithmic scale. It can be observed that except for an initial overshoot of the oven of the lowered annealing temperature set to maintain a threshold below the manufacturers recommendations [65], that a comparable annealing effect occurs. As the material is subsequently exposed to elevated temperatures, the degradation sets in with the resistivity increasing by orders of magnitude at a time.

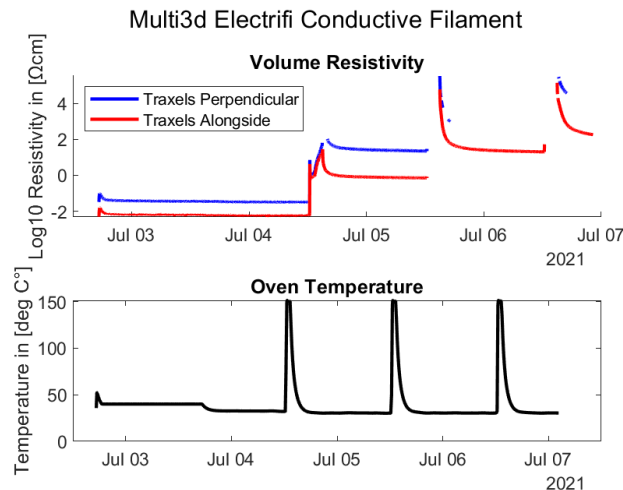


Figure A.17: Resistivity derived for Electrifi samples during oven measurement

As to avoid these increases in resistivity, the values provided for Electrifi in table A.8 were taken from the initial observation to the last point of the resting period after the anneal before the first exposure. From the reduction percentage it would initially appear that the annealing period improved the conductivity of the Electrifi filament, however when considering the results of table A.4 it is clear that the obtained resistivities are larger.

The anisotropy ratio suggests that some sort of discrepancy existed within the perpendicular and to a lesser extent the alongside traxel orientation sample, as a larger resistivity was observed than shown by the theoretically identical room temperature samples at the start of the experiment. It is however interesting that if annealing temperatures are kept sufficiently low, that the original low resistivity attained can be restored, reducing to values matching those of the room conditioned samples.

Multi3D Electrifi		
	Alongside*	Perpendicular*
Oven start	0.02 Ω cm	0.10 Ω cm
Oven end	0.01 Ω cm	0.03 Ω cm
Reduction to	35%	33%
Ratio	1	5,9

Table A.8: Resistivity reduction and ratio derived for Electrifi samples during room measurement (*measured to end of first resting period)

A.3 Annealing

The annealing effect already noted to be observable in the resistivity graphs for the high temperature exposed samples, will be highlighted in this section in the form of labelled plots. The A label indicates the start of the measurement period at room temperature, B corresponds to the moment at which the sample had achieved the exposure temperature. Label C corresponds to the end of the exposure cycle, where the oven is turned off to allow for an uncontrolled cooldown. Label C concludes the observed annealing cycle with the sample having returned to room temperature. The provided highlights are taken from the 10 mm spaced contacts for all materials.

The first set of annealing cycles represented are those of the alongside and perpendicular traxel orientation samples of the Ninjatek material. The curves attained as shown in figure A.18 and figure A.19 show a relation between the initial exposure to a certain temperature and the sub-

sequent rapid drop in material resistance. After a certain amount of time at this temperature has passed, this drop starts to taper off, suggesting the material is saturating.

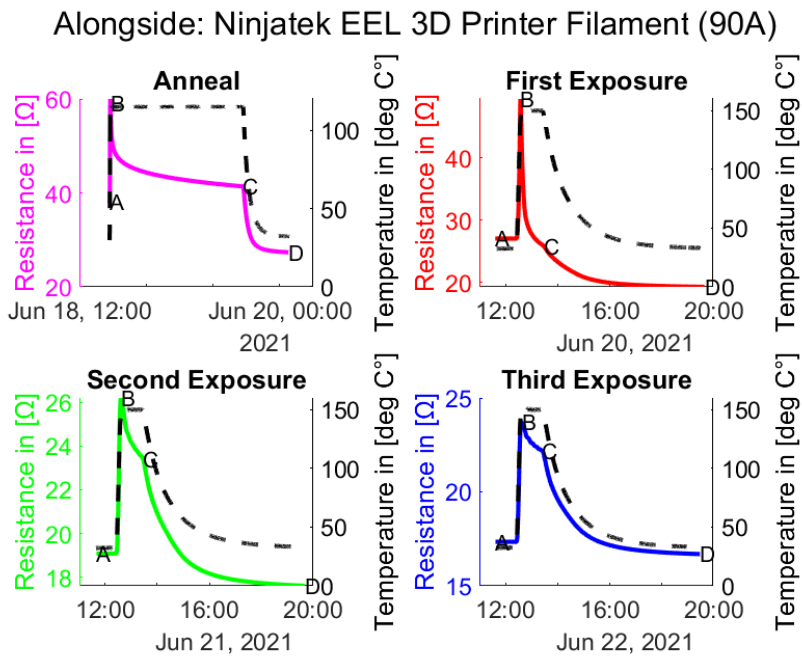


Figure A.18: Labeled anneal curves for Ninjatek alongside traxel samples

The annealing effect can also be observed to occur after the initial annealing period after exposure to the higher temperature of the first exposure cycle, with the same gradual tapering off being observed in subsequent exposures. The material can be observed to continue from the previously observed resistance at the exposure temperature for subsequent exposures, despite the cooling and resting period allowed in between.

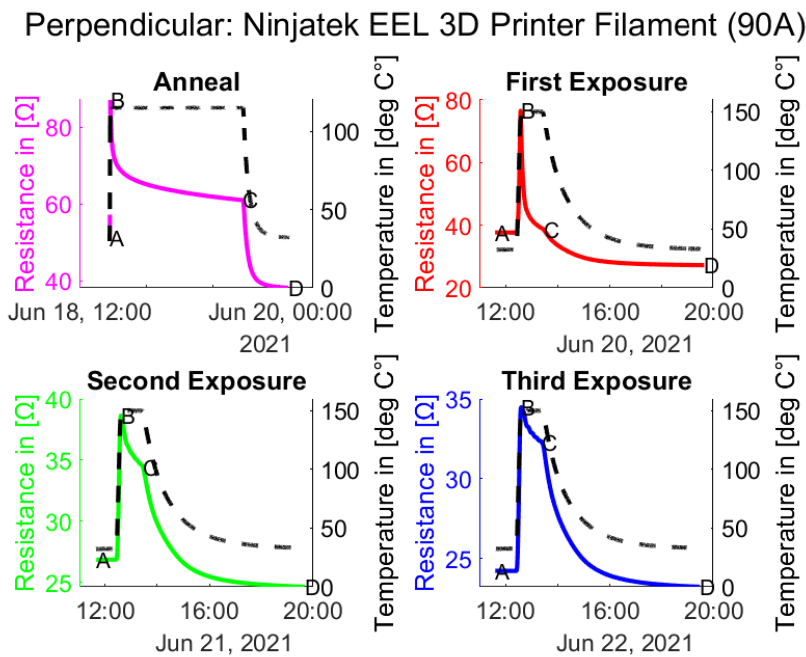


Figure A.19: Labeled anneal curves for Ninjatek perpendicular traxel samples

The resistance reductions as obtained from these exposures to high temperatures resulting in annealing between labels B and C are provided in table A.9 along with the corresponding resistances recorded at these labels. The initial big reduction observed for an exposure to a higher than previously encountered temperature is clearly reflected, with the results for exposure two and three clearly showing a saturation effect with a lesser reduction in the observed resistance.

Ninjatek EEL 3D Printer Filament (90A)			
	Anneal (B)	Anneal (C)	Reduction
Alongside	60.10 Ω	41.43 Ω	69%
Perpendicular	87.03 Ω	60.98 Ω	70%
Expo #1 (B) Expo #1 (C) Reduction			
Alongside	49.41 Ω	25.86 Ω	52%
Perpendicular	76.58 Ω	38.66 Ω	50%
Expo #2 (B) Expo #2 (C) Reduction			
Alongside	26.21 Ω	23.46 Ω	90%
Perpendicular	38.64 Ω	34.41 Ω	89%
Expo #3 (B) Expo #3 (C) Reduction			
Alongside	23.69 Ω	22.13 Ω	93%
Perpendicular	34.48 Ω	32.12 Ω	93%

Table A.9: Resistance changes due to Annealing and Exposure for Ninjatek filament

The previously noted strong response of the palmiga filament to the annealing and exposure temperatures can be observed in figures A.20 and A.21. In the graphs for the anneal a steep decrease in the resistance can be observed from the moment the annealing temperature is achieved. The same steep decrease is observed for subsequent high temperature exposures, where unlike as with the ninjatek material, little saturation of the resistance drop is observed.

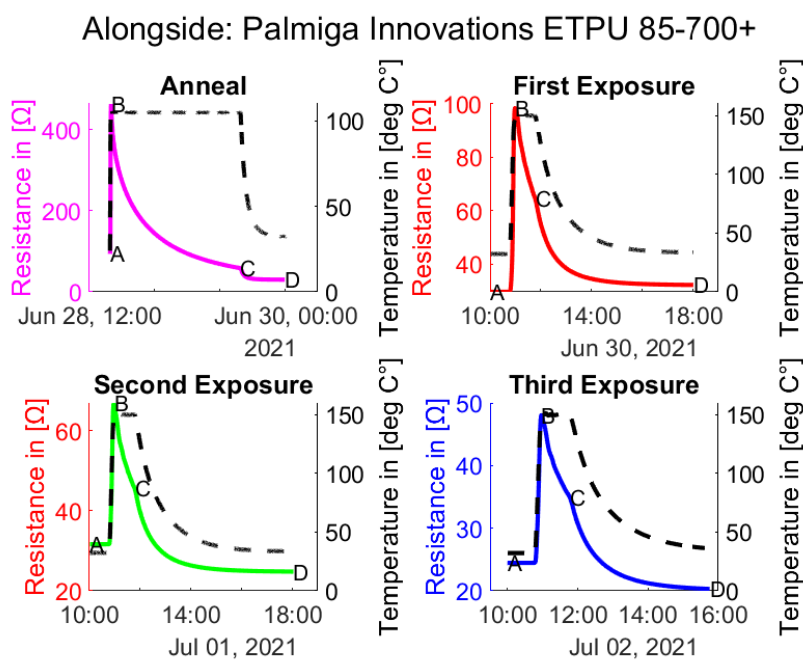


Figure A.20: Labeled anneal curves for Palmiga alongside travel samples

This lack of saturation observed during both the annealing period as subsequent exposures suggests that the material would require a longer period to saturate and could achieve even lower resistances. It would be valuable to extend the period of the annealing cycle for future experiments, to gain insight into the required annealing period to reach saturation if that is achievable.

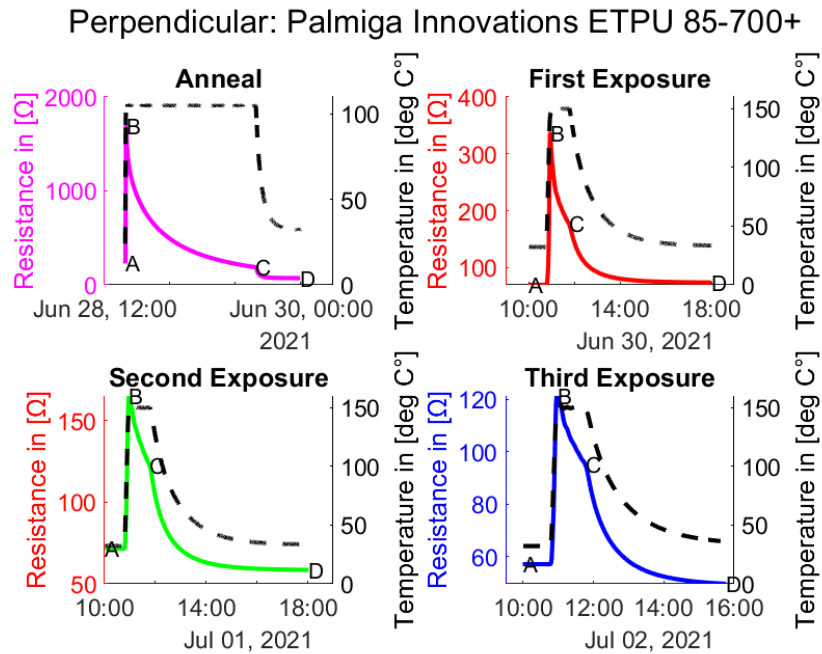


Figure A.21: Labeled anneal curves for Palmiga perpendicular traxel samples

The summarized reductions and corresponding resistances recorded are provided in table A.10. From the reduction percentages in provided for the exposures, it can be observed that the onset of some form of saturation appears to occur, as the percentages increase per exposure. The perpendicular sample also appears to follow a steeper anneal slope, with the initial resistance reduction being much greater, whilst also moving towards saturation earlier.

Palmiga Innovations ETPU 85-700+ Carbon Black			
	Anneal (B)	Anneal (C)	Reduction
Alongside	463.57 Ω	58.96 Ω	13%
Perpendicular	1695.35 Ω	187.80 Ω	11%
	Expo #1 (B)	Expo #1 (C)	Reduction
Alongside	98.51 Ω	63.83 Ω	65%
Perpendicular	335.70 Ω	175.34 Ω	52%
	Expo #2 (B)	Expo #2 (C)	Reduction
Alongside	66.96 Ω	44.75 Ω	67%
Perpendicular	165.16 Ω	120.56 Ω	73%
	Expo #3 (B)	Expo #3 (C)	Reduction
Alongside	48.04 Ω	34.84 Ω	73%
Perpendicular	121.27 Ω	94.31 Ω	78%

Table A.10: Resistance changes due to Annealing and Exposure for Palmiga filament

An example of a material that does quickly saturate during the annealing cycle is provided by protopasta. In the highlighted graphs provided in figures A.22 and A.23, a clear flattening out can be observed of the resistance drop as a result of the high temperature exposure.

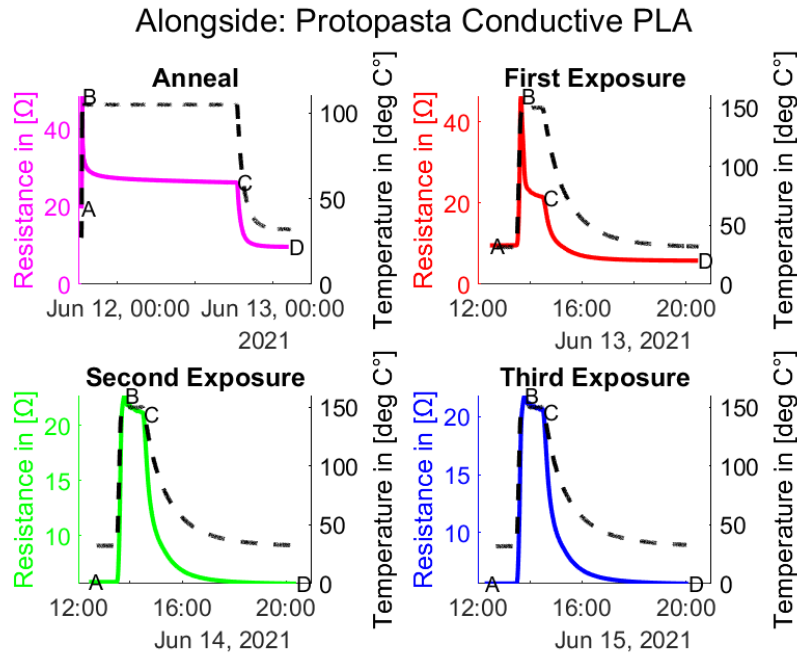


Figure A.22: Labeled anneal curves for Protopasta alongside traxel samples

When the graphs are observed in terms of the effects that occur during the high temperature exposures, a similar saturation can be observed. The initial exposure shows a steep drop in resistance, which quickly tapers off to result in a near relatively constant value for both the second and third exposure with a slight slope still observable.

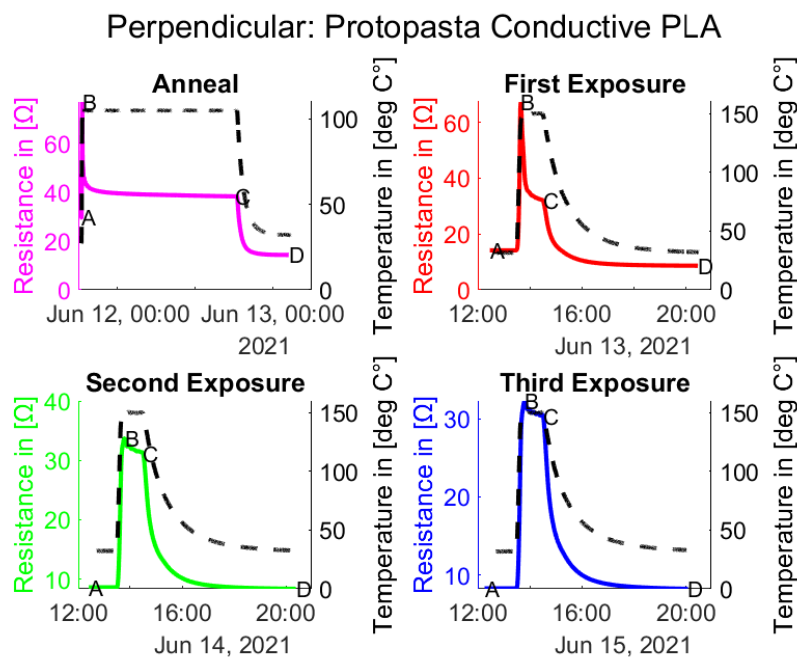


Figure A.23: Labeled anneal curves for Protopasta perpendicular traxel samples

These observations are also confirmed by the reduction ratios as provided in table A.11, where the initial anneal and exposures result in a reduction by approximately half of the resistance. The second and third exposure contribute a minimal reduction, providing example of the materials saturation.

Protopasta Conductive PLA			
	Anneal (B)	Anneal (C)	Reduction
Alongside	48.58 Ω	26.28 Ω	54%
Perpendicular	76.79 Ω	38.20 Ω	50%
	Expo #1 (B)	Expo #1 (C)	Reduction
Alongside	46.36 Ω	21.30 Ω	46%
Perpendicular	67.33 Ω	31.58 Ω	47%
	Expo #2 (B)	Expo #2 (C)	Reduction
Alongside	22.60 Ω	20.99 Ω	93%
Perpendicular	33.68 Ω	31.17 Ω	93%
	Expo #3 (B)	Expo #3 (C)	Reduction
Alongside	21.84 Ω	20.69 Ω	95%
Perpendicular	32.28 Ω	30.29 Ω	94%

Table A.11: Resistance changes due to Annealing and Exposure for Protopasta filament

The degradation of the electrifi filament can be observed in the highlighted graphs provided in figures A.24 and A.25. The same note as provided for the resistivity measurements upon the measurement noise holds for the observation of the annealing cycle, where although the noise obscures part of the measurement a reduction in resistance is observed.

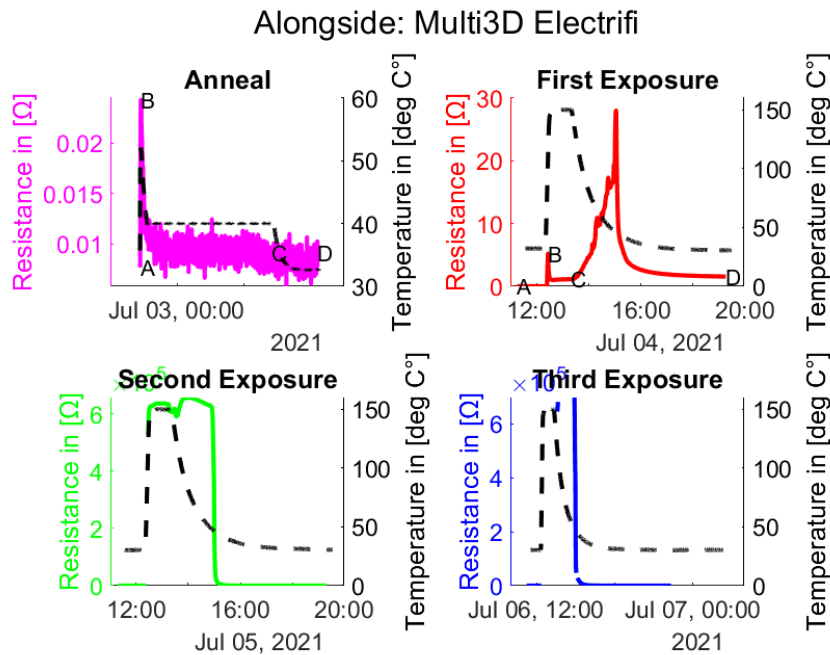


Figure A.24: Labeled anneal curves for Electrifi alongside traxel samples

Considering the exposures to the higher temperatures, the degradation is immediately observed, with resistances increasing by a order of magnitude for the first exposure. For a yet

to be determined reason at point C where the oven is turned off and the material is allowed to cool, a increase in resistance is observed after which a drop occurs as would be expected. For the second and third exposures the samples are degraded to such a degree that most of the resistance has gone unrecorded due to contact failure.

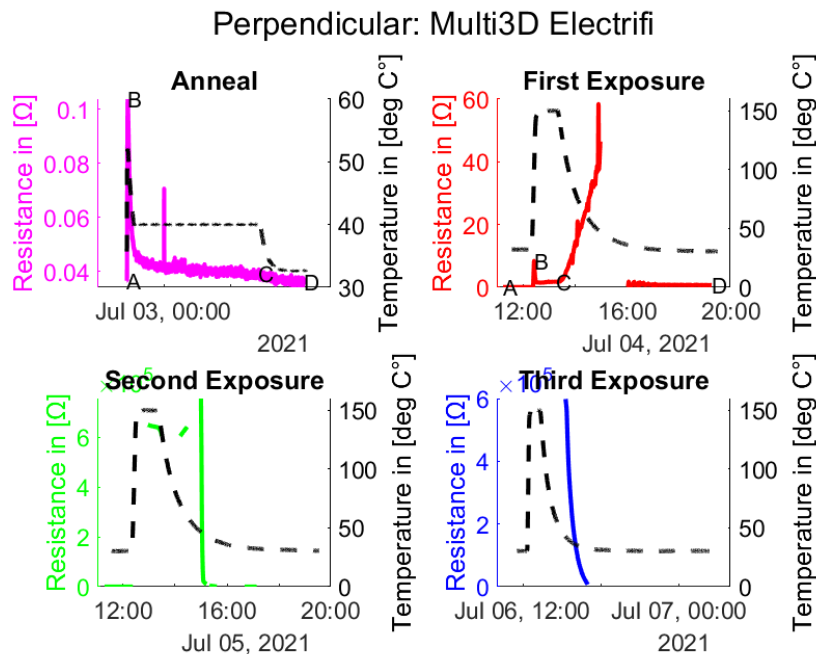


Figure A.25: Labeled anneal curves for Electrifi perpendicular traxel samples

Due to this degradation only the observed reductions in resistance for the annealing cycle and the first exposure are provided in table A.8.

Multi3D Electrifi			
	Anneal (B)	Anneal (C)	Reduction
Alongside	0.02 Ω	0.01 Ω	36%
Perpendicular	0.10 Ω	0.04 Ω	37%
	Expo #1 (B)	Expo #1 (C)	Reduction
Alongside	5.21 Ω	1.45 Ω	28%
Perpendicular	8.44 Ω	2.12 Ω	25%

Table A.12: Resistance changes due to Annealing and Exposure for Electrifi filament

A.4 Temperature Coefficients

The previously provided exposure graphs can also be shown in a different manner, by plotting the observed measurement in terms of resistance versus temperature, omitting the time axis. Such a figure allows for a different perspective on the annealing response as well as a look into the influence of temperature on the materials resistance.

In figure A.26 such plots are provided for the ninjatek samples, where the initial annealing by the first thermal exposure can clearly be observed. The second and third exposures are also provided, with the color scheme as retained from the annealing figures. The last addition to this graph is the inclusion of a estimated linearization of the cooldown of the sample after the last exposure.

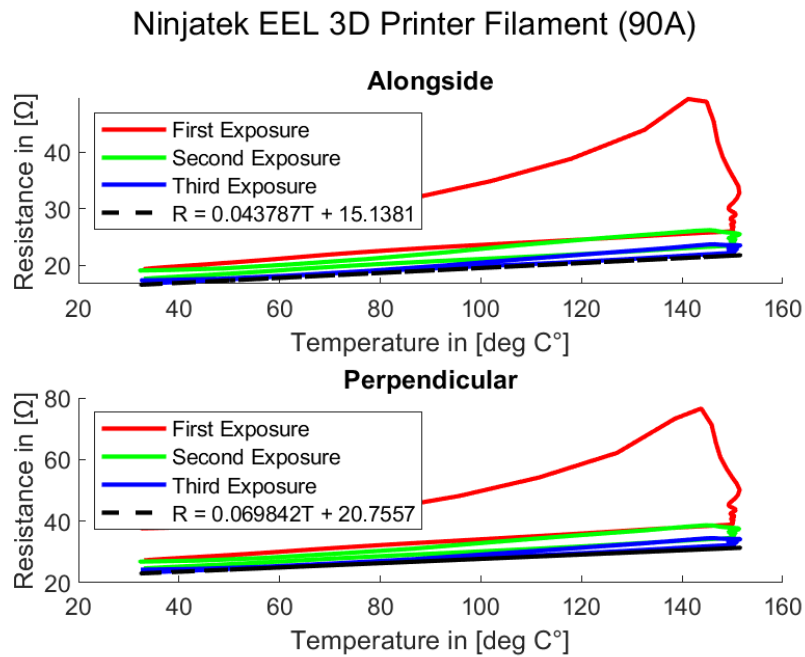


Figure A.26: Thermal response of Ninjatek samples during exposure

With the use of the method as described in section 3.4.3 this linearization could be used to derive the thermal coefficient of resistances as provided in table A.13. Parameter $p1$ represents the observed slope, whereas parameter $p0$ provides the offset or material resistance at $T = 0$.

Ninjatek EEL 3D Printer Filament (90A)		
	Alongside	Perpendicular
p1	$0.04 \Omega^{\circ}\text{C}^{-1}$	$0.07 \Omega^{\circ}\text{C}^{-1}$
p0	15.14Ω	20.76Ω
alpha	$0.003^{\circ}\text{C}^{-1}$	$0.003^{\circ}\text{C}^{-1}$

Table A.13: Estimated thermal coefficient for Ninjatek filament

The previously obtained insight about the slow saturation of the palmiga filament with respect to the other materials tested is clearly reflected in the resistance versus temperature plot in figure A.27. It can be observed that the vertical drop at the rightside of the figure at a temperature of 150°C continues for each subsequent exposure, with the inside area of the drawn exposure curve shrinking slightly for each exposure. It is also clear as was noted before, that the perpendicular sample showed a different initial resistance decrease, as illustrated by the vertical drop between the two travel orientations.

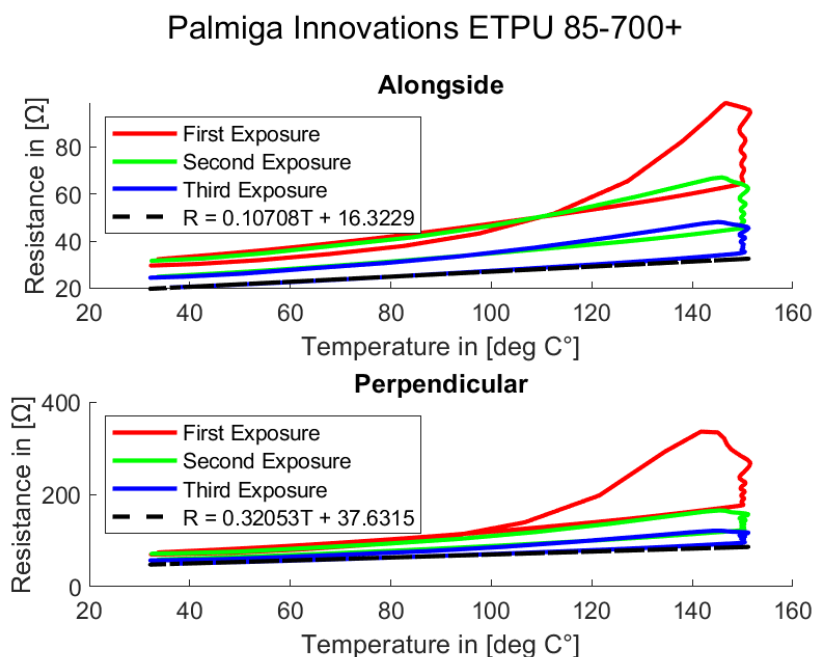


Figure A.27: Thermal response of Palmiga samples during exposure

In table A.14 the parameters and from calculation resulting coefficients of thermal resistance are provided, as derived from the linearization applied to the cooldown curve of the last exposure.

Palmiga Innovations ETPU 85-700+		
	Alongside	Perpendicular
p1	$0.11 \Omega^{\circ}\text{C}^{-1}$	$0.32 \Omega^{\circ}\text{C}^{-1}$
p0	16.32Ω	37.63Ω
alpha	$0.007^{\circ}\text{C}^{-1}$	$0.009^{\circ}\text{C}^{-1}$

Table A.14: Estimated thermal coefficient for Palmiga filament

The resistance versus temperature curves for the protopasta filament as provided in figure A.28, show the effect of a material that saturates quickly. The initial exposure provides a vertical drop in the resistance, however subsequent exposures result in a very similar curve being drawn. In addition a slight kink is observed in the curve around a 115 °C where the material was annealed initially, suggesting that a longer exposure might still result in a linear relationship.

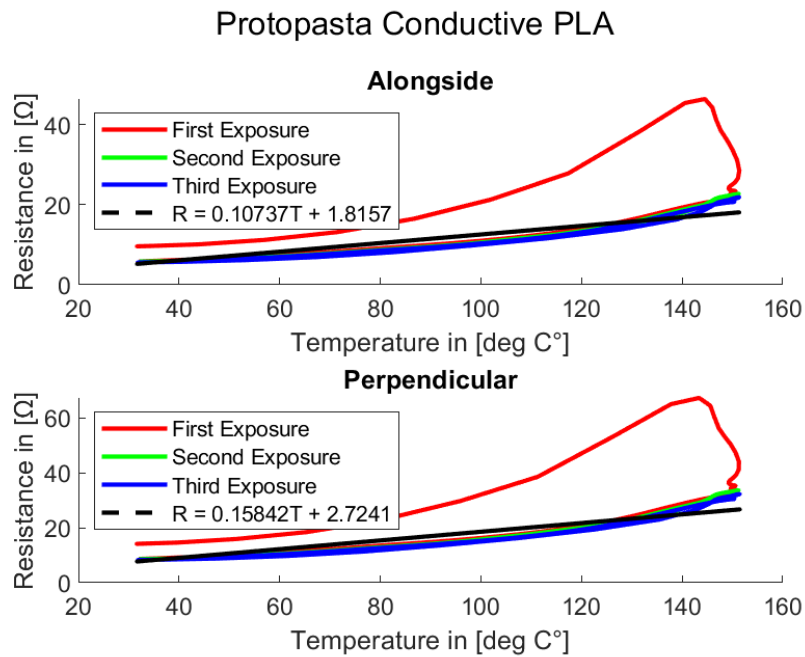


Figure A.28: Thermal response of Protopasta samples during exposure

The parameters as found by linearizing this slightly non-linear curve are provided in table A.15 as well as the coefficients of thermal resistance derived on the basis of these parameters.

Protopasta Conductive PLA		
	Alongside	Perpendicular
p1	$0.11 \Omega^{\circ}\text{C}^{-1}$	$0.16 \Omega^{\circ}\text{C}^{-1}$
p0	1.82Ω	2.72Ω
alpha	$0.059^{\circ}\text{C}^{-1}$	$0.058^{\circ}\text{C}^{-1}$

Table A.15: Estimated thermal coefficient for Protopasta filament

Due to the degradation of the electrifi filament, no conclusive exposure curve could be drawn for all three exposures as shown in figure A.29. However the first exposure was still characterized at least for the initial section up to label C, where a clear increase in impedance is observed around the point where a temperature of approximately 65°C is achieved.

As the temperature is raised further the resistance is observed to actually decrease despite the materials degradation, which would hint at the material possessing a negative temperature coefficient. This observation also holds for the cooldown cycle, where it is also to be noted that during the whole of the high temperature exposure period at 150°C no resistance drop can clearly be derived from these graph, as observed with the carbon black filled materials.

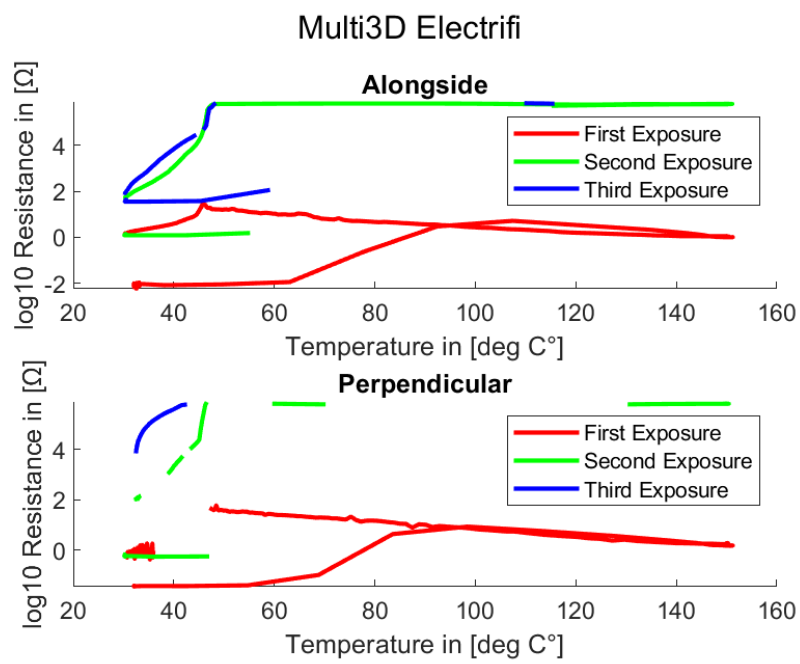


Figure A.29: Thermal response of Electrifi samples during exposure

B Current density experiments

Since for the current density experiment several real time measurements were performed and since several sample pictures were taken after the experiment had taken place, these were not all included in the main chapter. Below an overview of these complete results is provided alongside with a brief description for each.

B.1 Ninjatek Samples

The first material to be exposed to the current density experiment was the Ninjatek filament, for which the average of 3 samples were taken to result in the graphs as shown in figure B.1. The top graph shows the current carried by the sample, with the bottom graph providing the temperature recorded at the surface of the samples conducting wire for the varying cross-sectional areas.

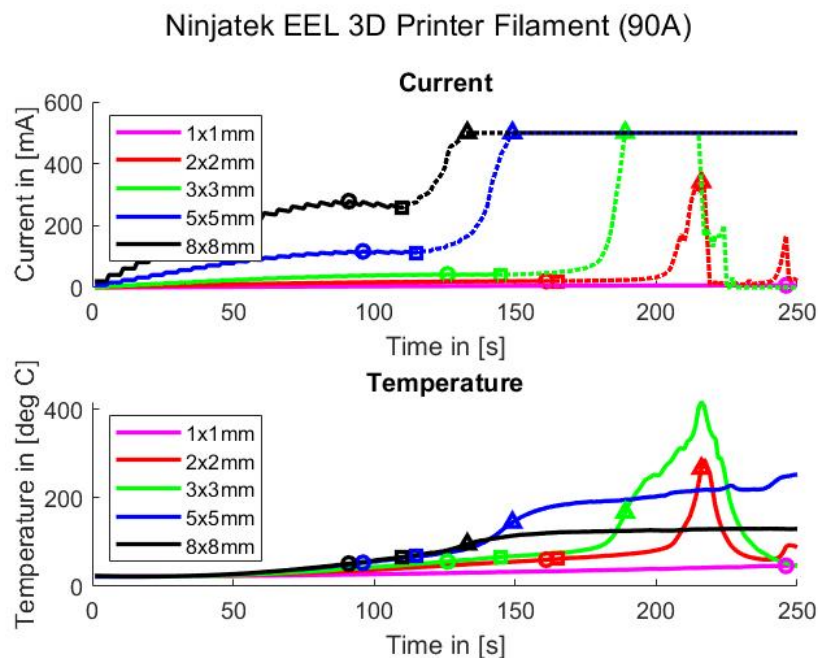


Figure B.1: Current and temperature measurements for Ninjatek current density experiment

In table B.1 the currents recorded at the in the figure marked points are provided, with table B.2 providing the corresponding observed surface temperatures at these points. The circles indicate the first maximum encountered in the current recorded, the squares mark the first minimum encountered and the triangles mark the second current maximum encountered.

Ninjatek EEL 3D Printer Filament (90A)					
Key point	1x1mm	2x2mm	3x3mm	5x5mm	8x8mm
Peak (circle)	7.1 mA	21.2 mA	42.5 mA	117.0 mA	279.0 mA
Dip (square)	N/A	20.8 mA	41.7 mA	113.0 mA	258.3 mA
Failure (triangle)	N/A	340.9 mA	500.6 mA	499.6 mA	499.6 mA

Table B.1: Current flow achieved at marked points in current measurements for Ninjatek samples

Ninjatek EEL 3D Printer Filament (90A)					
Key point	1x1mm	2x2mm	3x3mm	5x5mm	8x8mm
Peak (circle)	46.6 °C	60.3 °C	56.3 °C	53.3 °C	51.5 °C
Dip (square)	N/A	61.9 °C	66.5 °C	67.9 °C	66.1 °C
Failure (triangle)	N/A	266.7 °C	167.2 °C	144.6 °C	95.6 °C

Table B.2: Temperatures achieved at marked points in temperature measurements for ninjatek samples

As to provide some additional insight into sample degradation, sample residences were recorded pre and post experiment as provided in table B.3. It can be observed that all of the 2x2 and the 3x3 samples, and one of the 5x5 samples dismantled the connection between the contacts due to degradation. This is also observable in the post-experiment sample images provided in figure B.2 as charring or missing sections.

Ninjatek EEL 3D Printer Filament (90A)					
Sample	1x1mm	2x2mm	3x3mm	5x5mm	8x8mm
#1 pre	3850 Ω	985 Ω	421 Ω	125.0 Ω	47.9 Ω
#2 pre	4820 Ω	953 Ω	416 Ω	120.3 Ω	50.9 Ω
#3 pre	5480 Ω	1114 Ω	415 Ω	125.8 Ω	48.1 Ω
Average:	4717 Ω	1017 Ω	417 Ω	123,7 Ω	49,0 Ω
#1 post	4920 Ω	N/A	N/A	131.6 Ω	30.0 Ω
#2 post	5360 Ω	N/A	N/A	N/A	24.8 Ω
#3 post	5870 Ω	N/A	N/A	48.8 Ω	28.8 Ω
Average:	5383 Ω	N/A	N/A	90,2 Ω	27,9 Ω

Table B.3: Ninjatek sample resistances recorded pre and post current density experiment

Ninjatek Current Density Samples

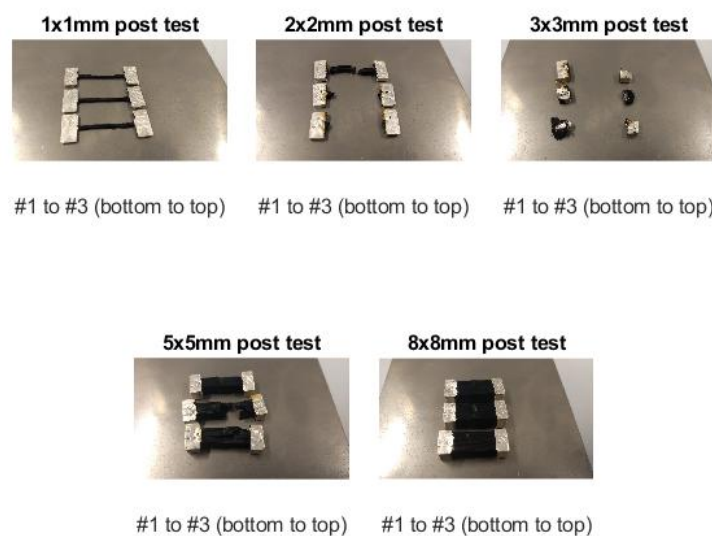


Figure B.2: Ninjatek samples post current density experiment

The achieved current densities as provided in table 4.6 where plotted against the wire surface area to volume ratio to derive the relation of convection to the achievable current density. The resulting graph with linear fit of the relationship achieved is provided in figure B.3.

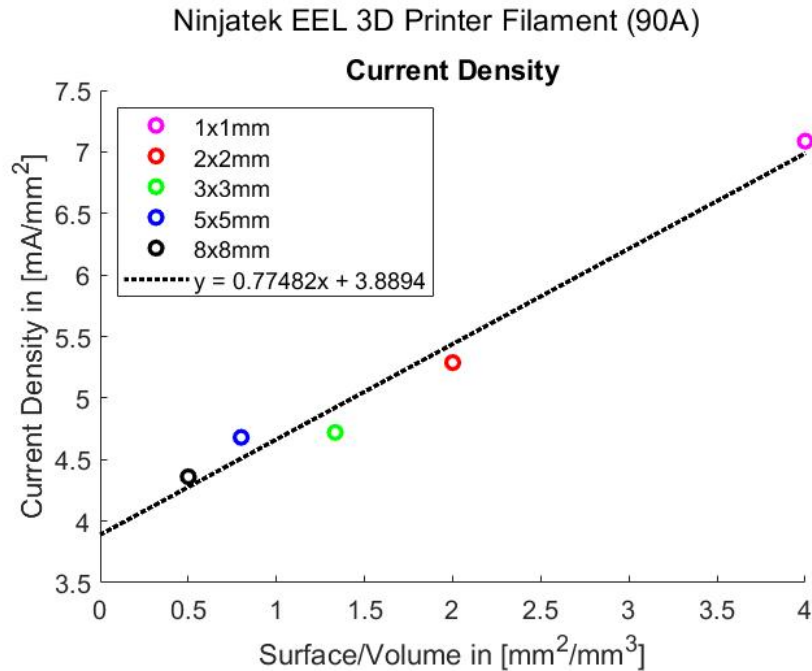


Figure B.3: Ninjatek current density limitation on the basis of surface area to volume ratio

B.2 Palmiga Samples

The second material exposed to the current density experiment was the Palmiga filament. Due to the materials resistivity in combination with the limited voltage range of the used power supply, a limited part of the desired curve was attained as shown in figure B.4.

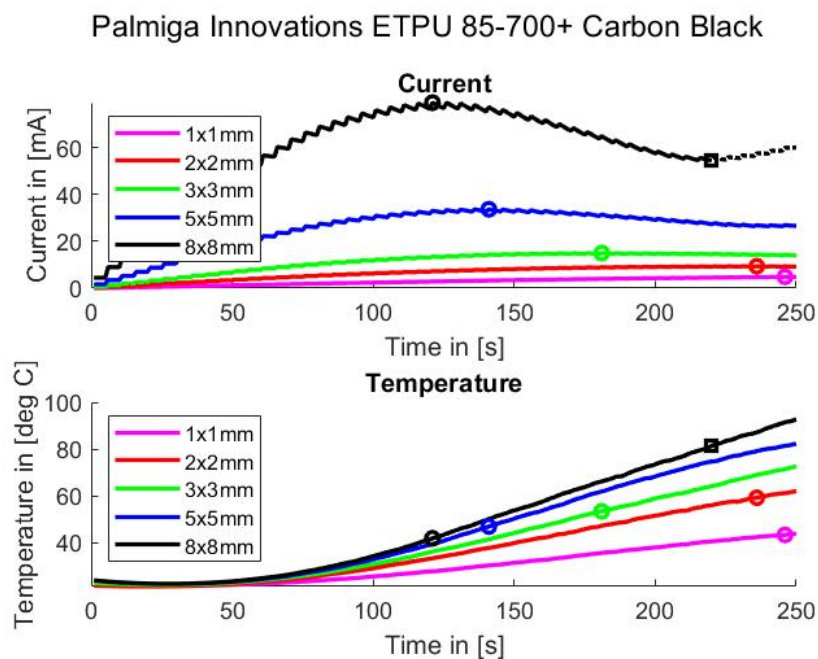


Figure B.4: Current and temperature measurements for Palmiga current density experiment

Despite this limited view of the for the material achievable currents and temperatures, for the 8x8mm sample the initial peak (circle) and transitional point (square) were achieved. The remaining samples of smaller cross sectional areas only achieved the initial current peak with the values for the 1x1mm and 2x2mm being less clearly defined. The resulting recording of the remaining marked currents and temperatures that were achieved are presented in tables B.4 and B.5.

Palmiga Innovations ETPU 85-700+					
Key point	1x1mm	2x2mm	3x3mm	5x5mm	8x8mm
Peak (circle)	4.9 mA	9.4 mA	15.0 mA	33.7 mA	79.3 mA
Dip (square)	N/A	N/A	N/A	N/A	54.6 mA
Failure (triangle)	N/A	N/A	N/A	N/A	N/A

Table B.4: Current flow achieved at marked points in current measurements for Palmiga samples

Palmiga Innovations ETPU 85-700+					
Key point	1x1mm	2x2mm	3x3mm	5x5mm	8x8mm
Peak (circle)	43.5 °C	59.3 °C	53.5 °C	47.1 °C	42.0 °C
Dip (square)	N/A	N/A	N/A	N/A	81.4 °C
Failure (triangle)	N/A	N/A	N/A	N/A	N/A

Table B.5: Temperatures achieved at marked points in temperature measurements for Palmiga samples

The resistances as provided in table B.6 provide the insight that after the samples are cooled back down to room temperature, that the samples resistance is only slightly altered despite exposure to the initial peak current. The larger 5x5 and 8x8 samples did reach the point of current reduction as reflected by their resistance increase. Since none of the samples reached the point of failure as also reflected by the post-experiment sample pictures in figure B.5, no degradation of the samples occurred for the smaller cross sectional areas. The 5x5 and 8x8 samples showed slight warping suggesting that a melting/softening temperature was achieved.

Palmiga Innovations ETPU 85-700+ Carbon Black					
Sample	1x1mm	2x2mm	3x3mm	5x5mm	8x8mm
#1 pre	7060 Ω	2899 Ω	1471 Ω	571 Ω	228.3 Ω
#2 pre	8950 Ω	3366 Ω	1437 Ω	575 Ω	214.1 Ω
#3 pre	7500 Ω	2835 Ω	1484 Ω	563 Ω	220.3 Ω
Average:	7837 Ω	3033 Ω	1464 Ω	570 Ω	220,9 Ω
#1 post	8430 Ω	2758 Ω	1405 Ω	702 Ω	323.4 Ω
#2 post	7340 Ω	3049 Ω	1371 Ω	699 Ω	343.1 Ω
#3 post	6250 Ω	2546 Ω	1462 Ω	747 Ω	399.0 Ω
Average:	7340 Ω	2784 Ω	1413 Ω	716 Ω	355,2 Ω

Table B.6: Palmiga sample resistances recorded pre and post current density experiment

Palmiga Current Density Samples

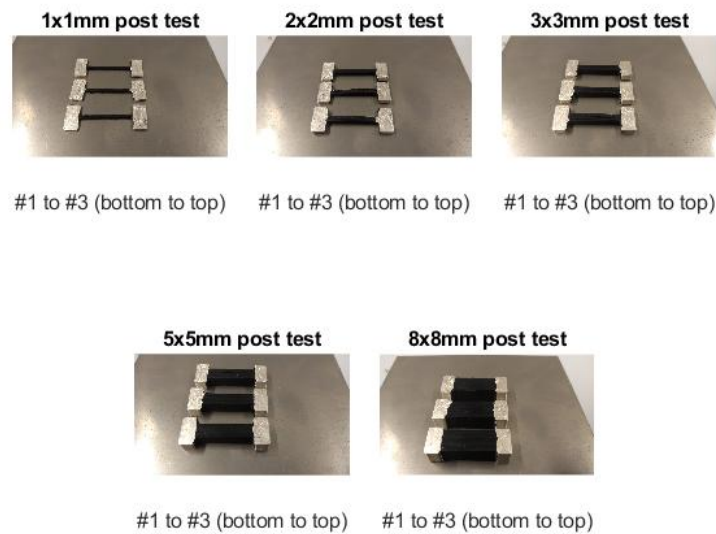


Figure B.5: Palmiga samples post current density experiment

The achieved current densities as provided by table 4.6 were once more plotted against the surface area to volume ratio's for the produced sample wires. The resulting plot including a linear estimate of the relationship between surface area and heat input is provided in figure B.6

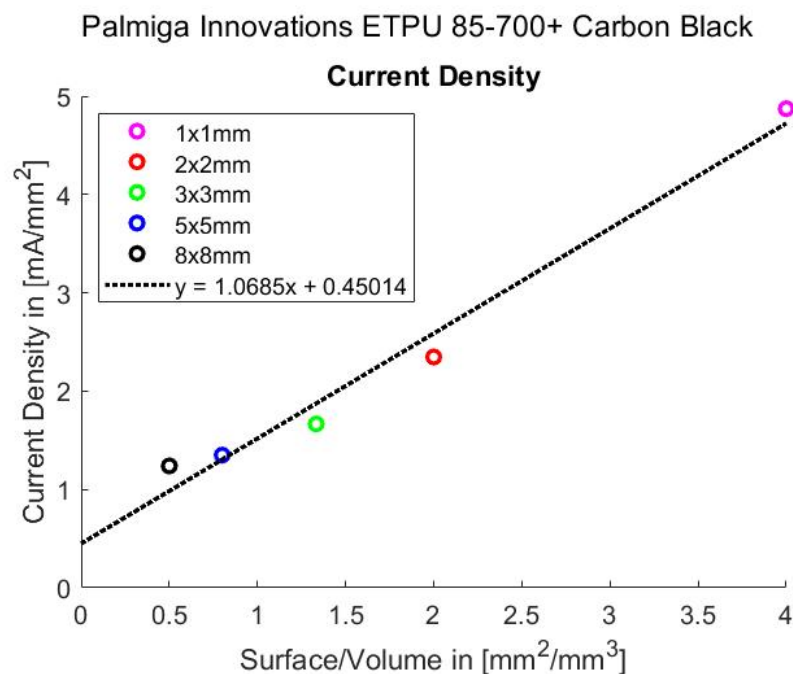


Figure B.6: Palmiga current density limitation on the basis of surface area to volume ratio

B.3 Protopasta Samples

The last material to be exposed to the current density experiment was the Protopasta filament which showed the highest achieved current density out of all the tested filaments. In figure B.7

the marked current graphs and corresponding surface temperature graph are provided. The graphs provide a clear initial current peak as marked by the circles, transition points marked by squares and the point of failure/current limit as marked by the triangles.

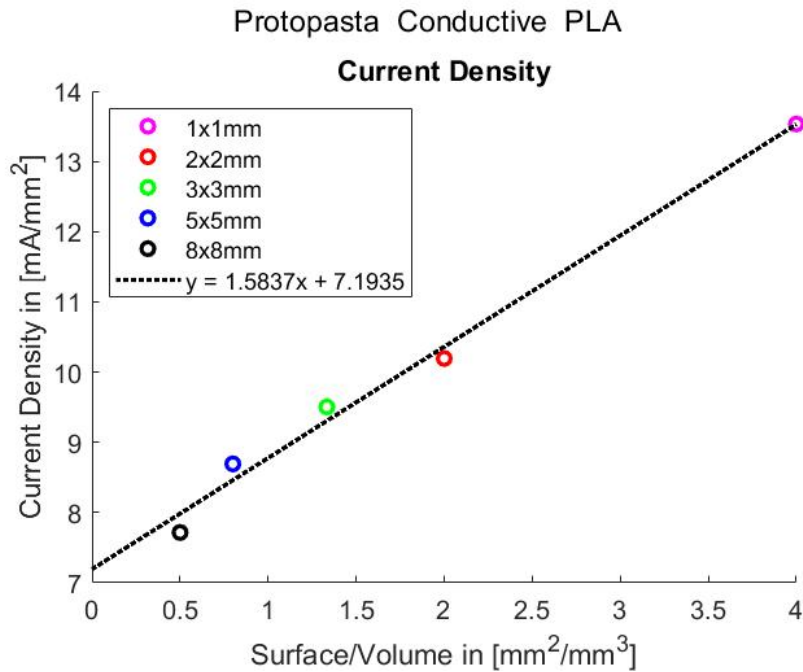


Figure B.7: Current and temperature measurements for Protopasta current density experiment

The marked currents at the maxima and minima achieved with the corresponding recordings of sample surface temperatures are provided in tables B.7 and B.8.

Protopasta Conductive PLA					
Key point	1x1mm	2x2mm	3x3mm	5x5mm	8x8mm
Peak (circle)	13.5 mA	40.8 mA	85.5 mA	217.3 mA	493.8 mA
Dip (square)	13.08 mA	31.9 mA	63.0 mA	142.4 mA	318.6 mA
Failure (triangle)	55.09 mA	212.6 mA	499.6 mA	499.7 mA	499.7 mA

Table B.7: Current flow achieved at marked points in current measurements for Protopasta samples

Protopasta Conductive PLA					
Key point	1x1mm	2x2mm	3x3mm	5x5mm	8x8mm
Peak (circle)	37.0 °C	33.8 °C	34.9 °C	33.4 °C	32.6 °C
Dip (square)	54.2 °C	67.9 °C	76.3 °C	68.8 °C	66.7 °C
Failure (triangle)	132.1 °C	236.4 °C	270.8 °C	147.9 °C	82.2 °C

Table B.8: Temperatures achieved at marked points in temperature measurements for Protopasta samples

Due to the point of failure being reached for the 1x1, 2x2 and the 3x3 samples as also observable from the post-experiment sample images as provided in figure B.8, the post experiment resistance values are not provided in figure B.9. However as the 5x5 and 8x8 samples managed to reach the current limit their temperature was kept relatively constant as also observed in

figure B.7. This resulted in an reduced resistance for the 8x8 sample, whereas the 5x5 sample increased in impedance.

This difference can be explained by taking a look at the actual surface temperature, which was maintained at 110 °C-130 °C for the 8x8 sample resulting in an annealing effect. The surface temperature achieved for the 5x5 sample maintained 210 °C-230 °C, resulting in the samples partial destruction. This partial destruction is also observed in figure B.8 in the form of of cracks and swelling.

Protopasta Conductive PLA					
Sample	1x1mm	2x2mm	3x3mm	5x5mm	8x8mm
#1 before	619 Ω	163.8 Ω	79.8 Ω	31.2 Ω	14.6 Ω
#2 before	605 Ω	168.1 Ω	79.1 Ω	31.8 Ω	13.7 Ω
#3 before	632 Ω	170.6 Ω	79.3 Ω	31.3 Ω	13.7 Ω
Average:	619 Ω	167,5 Ω	79,4 Ω	31,4 Ω	14,0 Ω
#1 after	N/A	N/A	N/A	78.0 Ω	12.1 Ω
#2 after	N/A	N/A	N/A	42.1 Ω	12.5 Ω
#3 after	N/A	N/A	N/A	N/A	11.8 Ω
Average:	N/A	N/A	N/A	60,1 Ω	12,1 Ω

Table B.9: Protopasta sample resistances recorded pre and post current density experiment

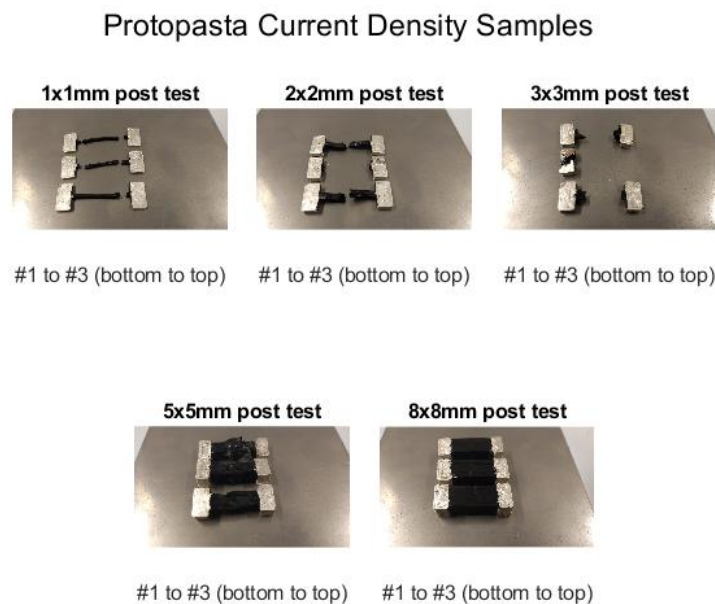


Figure B.8: Protopasta samples post current density experiment

The relationship between the current density and the surface area to volume of the sample wire for the Protopasta samples is provided in figure B.9.

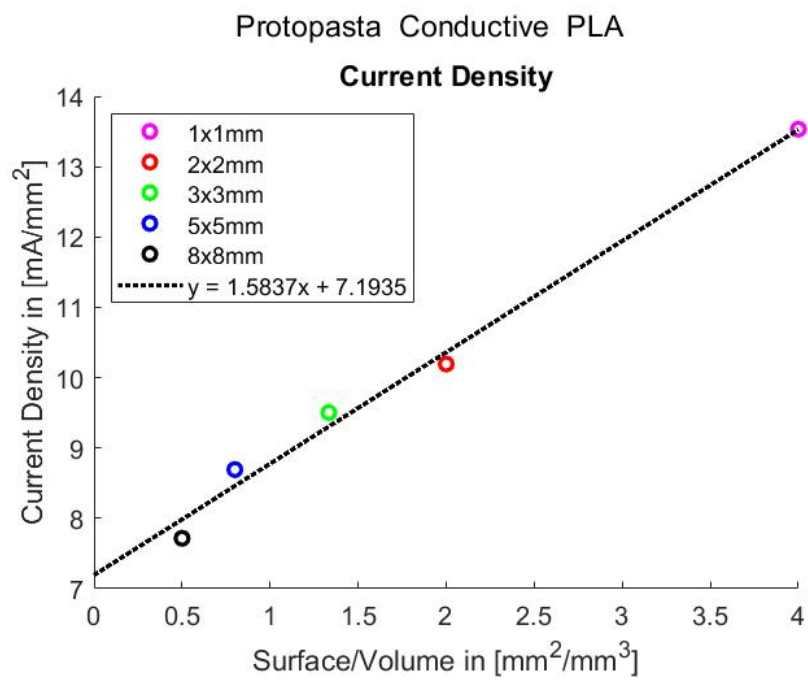


Figure B.9: Protopasta current density limitation on the basis of surface area to volume ratio

C Printed Circuit Board Experiment

Given the large amount of data and samples that were generated during the PCB adhesion experiments, the following section of the appendix will highlight the creation and measurement of these samples. At first images and a brief description of the samples will be provided, followed by a description of the used calibration method for the impedance characterisation. In conclusion the impedance measurements will be provided representing the electrical characteristics of conductive polymers on printed circuit board substrates along with a determined equivalent circuit model and its component values.

C.1 Samples

Since for each material and their combinations four different samples were created, their pictures were taken after printing. For both the gold and the tin coatings a alongside traxel infill and perpendicular traxel infill pattern was printed on top. Since the Electrifi and Protopasta samples detached during printing or quickly thereafter, they will not be included in this overview.

C.1.1 Ninjatek

For the Ninjatek filament samples, the first two samples, printed on gold are shown in figures C.1 and C.2. For which the note can be made that the alongside print lines appear to have been slightly under extruded, as a result of using the same settings as initially calibrated for the perpendicular samples. For both samples the print adhered well, with no observable curling as the material detaches.

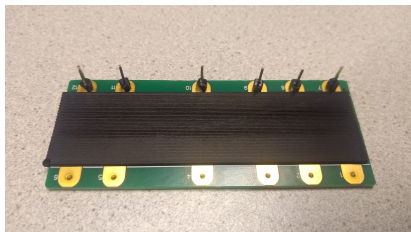


Figure C.1: Ninjatek Alongside Gold

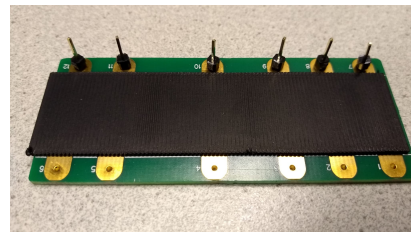


Figure C.2: Ninjatek Perpendicular Gold

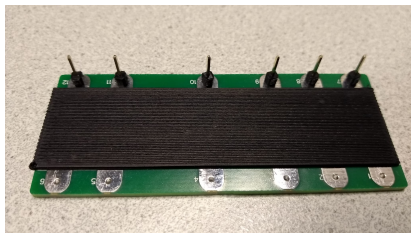


Figure C.3: Ninjatek Alongside Tin

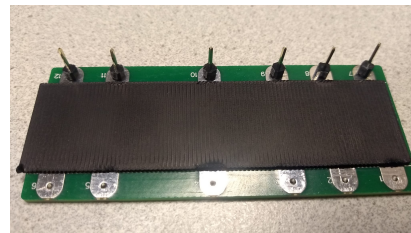


Figure C.4: Ninjatek Perpendicular Tin

The Ninjatek samples on top of tin coated circuit boards are shown in figures C.3 and C.4, where a similar slightly under extruded print line is observed for the alongside print in comparison to the perpendicular print, as with the gold coated samples. The print also attached nicely, with only a slight curling due to detachment visible in the perpendicular sample for certain traces.

C.1.2 Palmiga85

The Palmiga samples printed on a circuit board with gold coated traces are shown in picture C.5 and C.6, where a slight under extrusion is observed. The prints both adhered well, with only a minimal curling visible on the perpendicular sample for a single contact.

The under extrusion was also noted during printing, however would result in over extrusion at the edges if the extrusion percentage was increased. It was found that slowing down the moving speed of the printer would resolve this issue, pointing to a limit in the nozzles ability to heat the filament at this lower extrusion temperature compared to that of the Ninjatek filament. As this both significantly increased the sample printing time and would expose the samples to the heat of the nozzle for longer than the other samples, it was chosen not to alter the print speeds to allow for a fair comparison between samples.

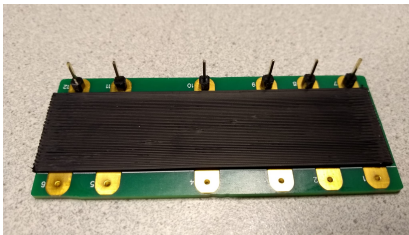


Figure C.5: Palmiga Alongside Gold

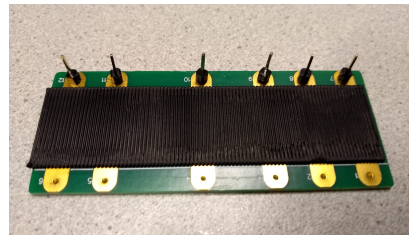


Figure C.6: Palmiga Perpendicular Gold

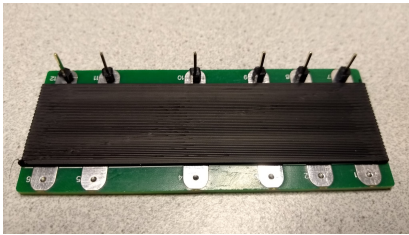


Figure C.7: Palmiga Alongside Tin

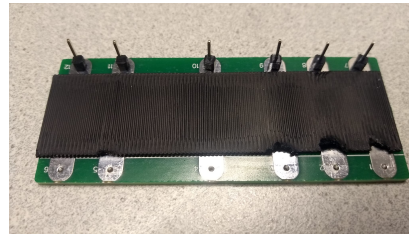


Figure C.8: Palmiga Perpendicular Tin

In figures C.7 and C.8 the samples printed on the tin coated circuit boards are shown. As expected from the results for the Ninjatek filament the flexible sample also printed and adhered well to this substrate, with a bit more curling observable on the perpendicular sample than for the Ninjatek samples suggesting lesser adhesion to the tin coating.

C.1.3 Ninjatek + Protopasta

In order to get an idea of the possibilities of using a buffer layer, an attempt was made to use a single initial layer of Ninjatek TPU filament followed by three layers of Protopasta PLA filament which previously failed, to improve its adhesion. In figures C.9 and C.10 the resulting samples for the gold coated circuit boards are shown, where a slight apparent over extrusion of the protopasta layer is observed on the alongside sample, which might have resulted from interaction between the two materials. The warping effect in the Protopasta filament is also clearly observable in the perpendicular sample, showing an upwards curl at the edges.

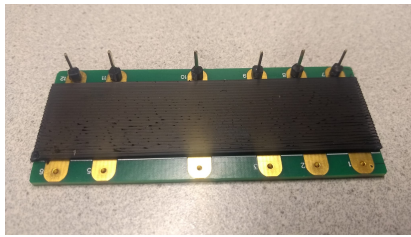


Figure C.9: Ninjatek & Protopasta Alongside Gold

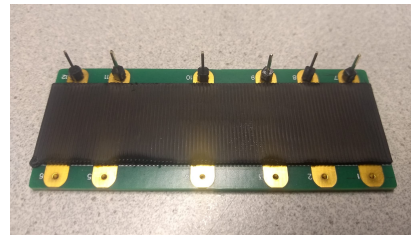


Figure C.10: Ninjatek & Protopasta Perpendicular Gold

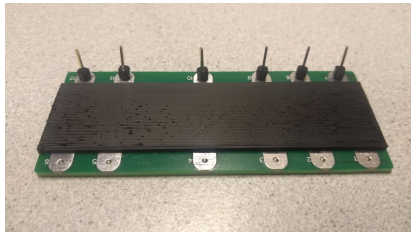


Figure C.11: Ninjatek & Protopasta Alongside Tin

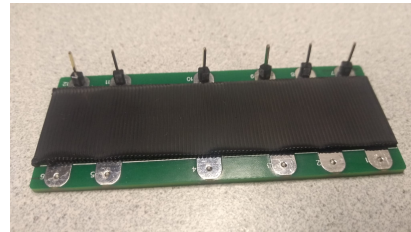


Figure C.12: Ninjatek & Protopasta Perpendicular Tin

The samples printed on top of the tin coated boards can be observed in figures C.11 and C.12, showing the same slight over extrusion for the Protopasta filament and the pulling of the warp in the filament on the perpendicular sample.

C.1.4 Palmiga85 + Protopasta

The same buffer layer concept was applied to the Palmiga and Protopasta filament, with the use of a single initial Palmiga layer followed by three Protopasta layers. The samples created in this manner for the gold coated circuit boards are shown in figures C.13 and C.14, with the same overextrusion being observed for the Protopasta layers in the alongside sample, and a slight warp and pull observed in the perpendicular sample.

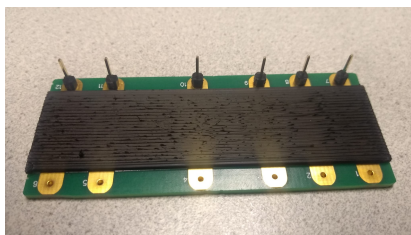


Figure C.13: Palmiga & Protopasta Alongside Gold

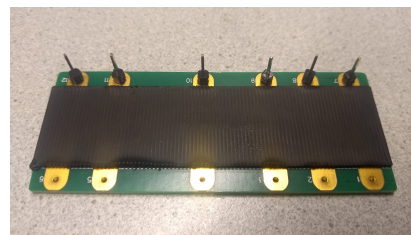


Figure C.14: Palmiga & Protopasta Perpendicular Gold

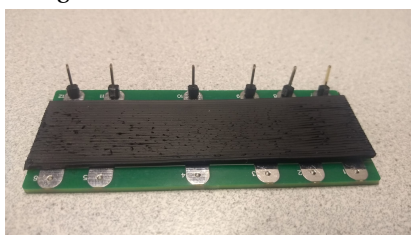


Figure C.15: Palmiga & Protopasta Alongside Tin

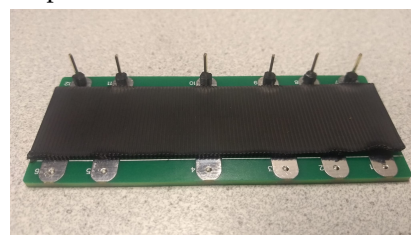


Figure C.16: Palmiga & Protopasta Perpendicular Tin

The tin coated samples were more telling as observed in figures C.15 and C.16, as for the alongside sample the effect of the warping is clearly shown as the sample is pulled from the substrate

for part of the print. The same effect is also observed in the perpendicular sample, where next to the as expected curling around the edges of the traces the pull off effect is also observed, which eventually occurred on all of the buffer layered samples.

C.2 LCR calibration

Due to the contributions of the measurement probes and the measurement equipment to the measurement of the impedance of the PCB samples, a calibration had to be performed on the basis of the calibration models as provided in section 5.3.2. Calibration models and their fit will be provided for the 5 mm, 10 mm and 15 mm contact spacing along with an image of the for the calibration method used sample.

C.2.1 Gold: open circuit

The first calibration performed were those of the open contacts, estimating stray capacitance whilst fixing the resistive contribution of the measurement resistance. The sample upon which these measurements were performed is shown in figure C.20, where for a bare PCB with 2.54 mm contacts was used. With the 5 mm, 10 mm and 15 mm contact spacings being shown in figures C.17, C.18 and C.19 respectively.

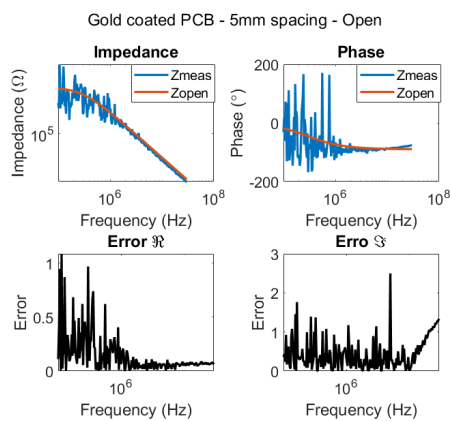


Figure C.17: 5 mm Gold open circuit

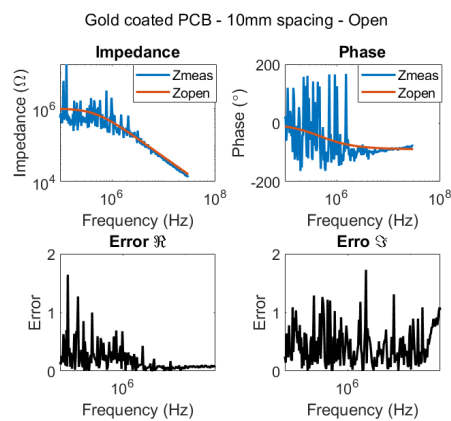


Figure C.18: 10 mm Gold open circuit

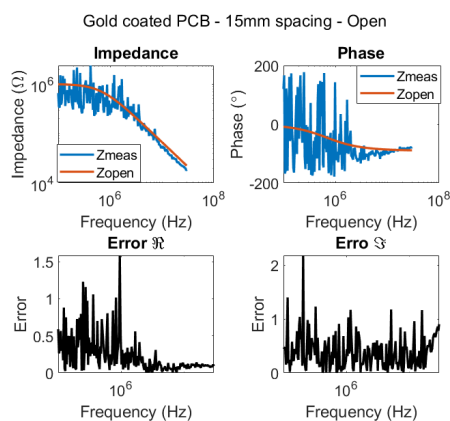


Figure C.19: 15 mm Gold open circuit

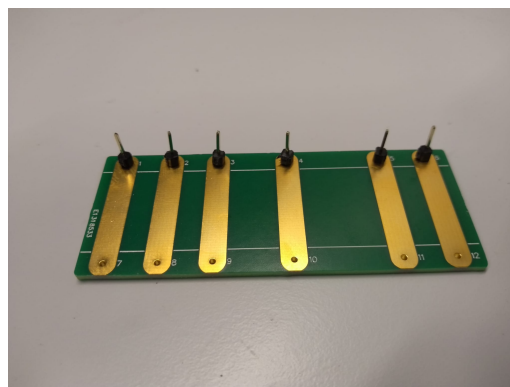


Figure C.20: Gold open circuit configuration

It should be additionally noted that due to the high impedances of the open circuit measurements, the quality of the measurement is reduced being outside the specified 10% accuracy window of the equipment [43]. This is also reflected by the noise observed in the data, which can be observed to reduce as the impedance is reduced.

The resulting estimates are provide in table C.1, where the measurement resistance was fixed to the 1 MΩ of the used E5061 network analyzer in GP series configuration [43]. The capacitance was allowed an 0.1 pF to 10 pF estimation range. In correspondence with expectations the observed capacitance decreased as contact spacing increased.

	Low bound	Estimate	High bound	Fit 5mm	Fit 10mm	Fit 15mm
$R_{measure}$	1 MΩ	1 MΩ	1 MΩ	1 MΩ	1 MΩ	1 MΩ
C_{stray}	0.1 pF	1 pF	10 pF	0.538 pF	0.335 pF	0.236 pF

Table C.1: Fitted open calibration values

C.2.2 Gold: short circuit

The next measurement configuration consisted out of a gold coated PCB sample, across which a length low resistance copper solder braid was connected to provide a short as shown in figure C.24. With the 5 mm, 10 mm and 15 mm contact spacings being shown in figures C.21, C.22 and C.23 respectively.

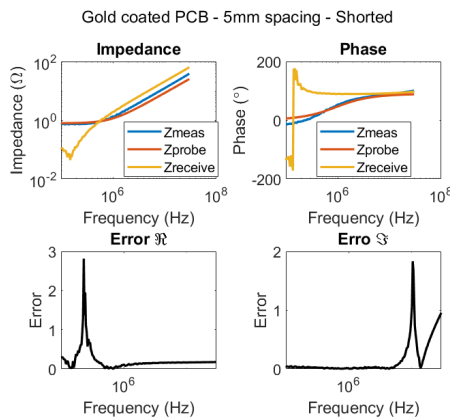


Figure C.21: 5 mm Gold shorted circuit

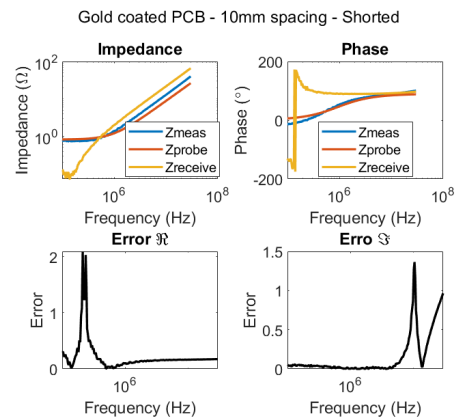


Figure C.22: 10 mm Gold shorted circuit

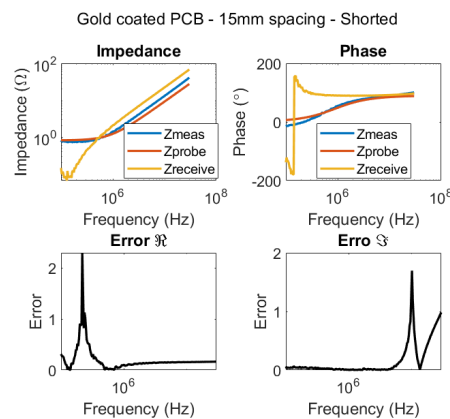


Figure C.23: 15 mm Gold shorted circuit

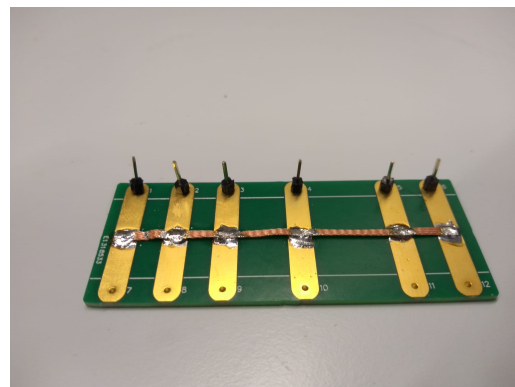


Figure C.24: Gold shorted circuit configuration

Following from the equivalent circuit model suggested in section 5.3.2, a little rewriting had to be done. This in order to derive the contribution of the receiver port and the probe impedances from the previous open circuit calibration and the total impedance determined through measurement. Starting off with the measured impedance according to the equivalent circuit:

$$Z_{measure} = Z_{open} // (Z_{probe} + Z_{receive}) \quad (C.1)$$

$$Z_{measure} = \frac{Z_{open}(Z_{probe} + Z_{receive})}{Z_{open} + (Z_{probe} + Z_{receive})} \quad (C.2)$$

$$(Z_{probe} + Z_{receive}) = \frac{Z_{open}}{Z_{measure}}(Z_{probe} + Z_{receive}) - Z_{open} \quad (C.3)$$

$$(Z_{probe} + Z_{receive})\left(\frac{Z_{open}}{Z_{measure}} - 1\right) = Z_{open} \quad (C.4)$$

$$(Z_{probe} + Z_{receive})(Z_{open} - Z_{measure}) = Z_{open}Z_{measure} \quad (C.5)$$

$$Z_{probe} + Z_{receive} = \frac{Z_{open}Z_{measure}}{Z_{open} - Z_{measure}} \quad (C.6)$$

This rewritten relation as provided in equation C.6, provides the manner in which the open calibration was applied to the measurement data before attempting the fit of the probe impedance. The receiver port impedance was determined numerically, as the difference in impedance remaining after the fitted parameters of the probe model have been applied and subtracted. It is represented by the yellow line in the calibration figures and suggests a significant contribution from 1 MHz onward inline with the measurement devices datasheet [43].

In table C.2 the resulting estimates are provided, with the probe inductance being provided a range of 10 nH up to 1 μ H and the probe resistance being allowed values from 0.1 Ω up to 10 Ω . Following from the observation that the attached short on top of the circuit board would also behave as a wire inductor, for which the inductance increases per unit length, it can be derived that this inductance is approximately equal to 1.2 nH mm⁻¹. This additional compensated induction was left in the calibration, to account for the same effect occurring in the polymer sample.

	Low bound	Estimate	High bound	Fit 5mm	Fit 10mm	Fit 15mm
L_{probe}	10 nH	100 nH	1 μ H	133.78 nH	139.35 nH	145.51 nH
R_{probe}	0.1 Ω	1 Ω	10 Ω	0.78978 Ω	0.81746 Ω	0.81064 Ω

Table C.2: Fitted shorted calibration values

C.2.3 Gold: reference load circuit

The third measurement configuration for the gold coated PCB consisted of a Agilent 85033-60010 reference load [3] that was moved across the sample board. This was achieved by resoldering an interfacing coaxial cable to the different contact spacings as shown in figure C.28. The calibrated measurement for the 5 mm, 10 mm and 15 mm contact spacings are shown in figures C.25, C.26 and C.27 respectively.

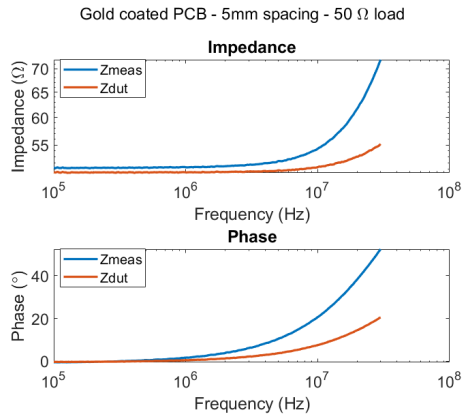


Figure C.25: 5 mm Gold loaded circuit

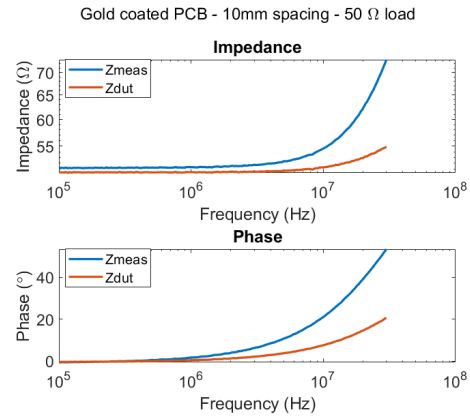


Figure C.26: 10 mm Gold loaded circuit

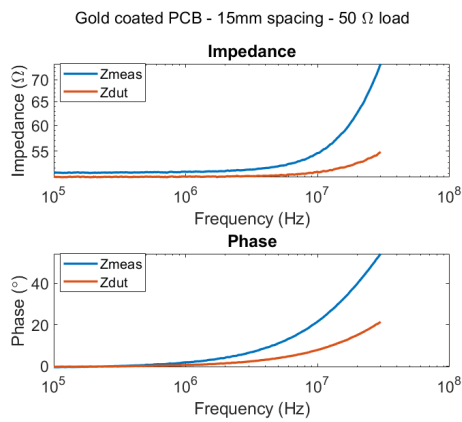


Figure C.27: 15 mm Gold loaded circuit

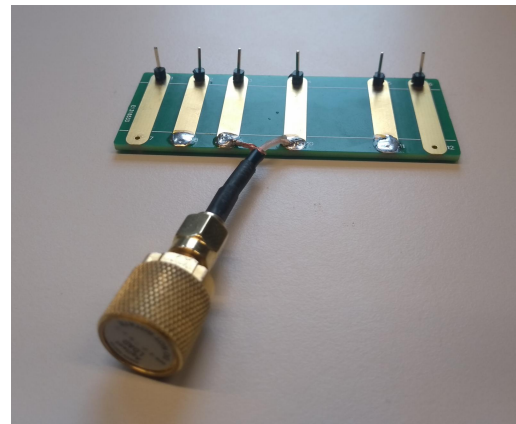


Figure C.28: Gold load circuit configuration

Like before a little rewriting is require to result in the value of Z_{dut} as compensated with the calibration impedances as derived on the basis of the loaded equivalent circuit model:

$$Z_{measure} = Z_{open} // (Z_{probe} + Z_{receive} + Z_{dut}) \quad (C.7)$$

$$Z_{measure} = \frac{Z_{open}(Z_{probe} + Z_{receive} + Z_{dut})}{Z_{open} + (Z_{probe} + Z_{receive} + Z_{dut})} \quad (C.8)$$

$$(Z_{probe} + Z_{receive} + Z_{dut}) = \frac{Z_{open}}{Z_{measure}} (Z_{probe} + Z_{receive} + Z_{dut}) - Z_{open} \quad (C.9)$$

$$(Z_{probe} + Z_{receive} + Z_{dut}) \left(\frac{Z_{open}}{Z_{measure}} - 1 \right) = Z_{open} \quad (C.10)$$

$$(Z_{probe} + Z_{receive} + Z_{dut})(Z_{open} - Z_{measure}) = Z_{open} Z_{measure} \quad (C.11)$$

$$Z_{probe} + Z_{receive} + Z_{dut} = \frac{Z_{open} Z_{measure}}{Z_{open} - Z_{measure}} \quad (C.12)$$

$$Z_{dut} = \frac{Z_{open} Z_{measure}}{Z_{open} - Z_{measure}} - Z_{probe} - Z_{receive} \quad (C.13)$$

With the use of equation C.13 the impedance of the device under test could then be determined whilst being compensated for the contribution of the probes and measurement equipment. In the figures the effect of the compensation can clearly be observed, although a inductive contribution is still observed. This contribution is believed to be the result of the adapting coax cable. The reference of 50Ω can however be observed to be correctly measured, with the contact and probe resistance being compensated as observed by the slightly lower DUT resistance in comparison to the measurement.

C.2.4 Tin: open circuit

Continuing from the gold coated samples, the calibration of the Tin coated samples will be provided. The first calibration being the open circuit calibration upon a bare PCB as shown in figure C.32. The calibrations for the 5 mm, 10 mm and 15 mm contact spacings are shown in figures C.29, C.30 and C.31 respectively.

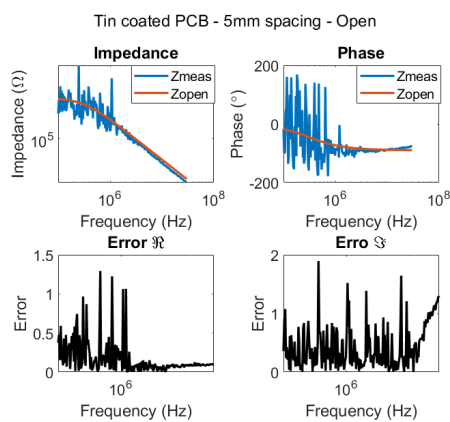


Figure C.29: 5 mm Tin open circuit

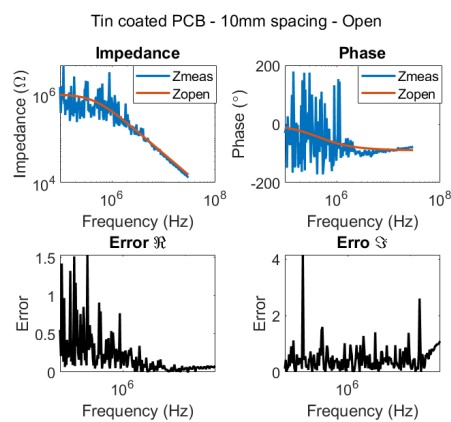


Figure C.30: 10 mm Tin open circuit

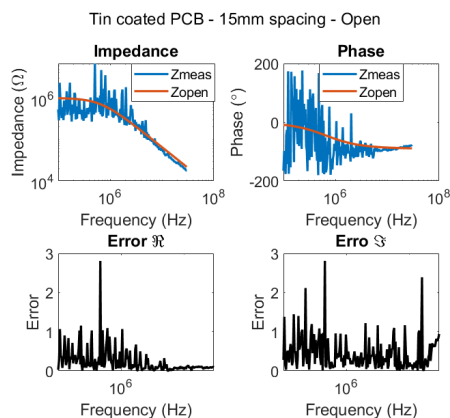


Figure C.31: 15 mm Tin open circuit

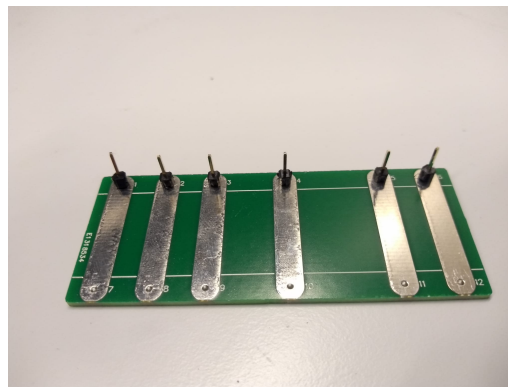


Figure C.32: Tin open circuit configuration

The resulting estimates are provided in table C.3, where the measurement resistance was fixed to the $1\text{M}\Omega$ of the used network analyzer. The capacitance was allowed an 0.1pF to 10pF estimation range. In correspondence with expectations the observed capacitance decreased as contact spacing increased for these measurements as well.

	Low bound	Estimate	High bound	Fit 5mm	Fit 10mm	Fit 15mm
$R_{measure}$	1 M Ω	1 M Ω	1 M Ω	1 M Ω	1 M Ω	1 M Ω
C_{stray}	0.1 pF	1 pF	10 pF	0.513 pF	0.351 pF	0.242 pF

Table C.3: Fitted open calibration values

C.2.5 Tin: short circuit

The shorted calibration samples for the Tin PCBs were also created by soldering a copper braid across the contacts as shown in figure C.36. With the 5 mm, 10 mm and 15 mm contact spacings being shown in figures C.33, C.34 and C.35 respectively.

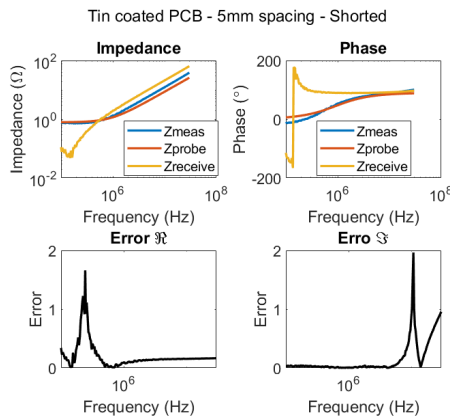


Figure C.33: 5 mm Tin shorted circuit

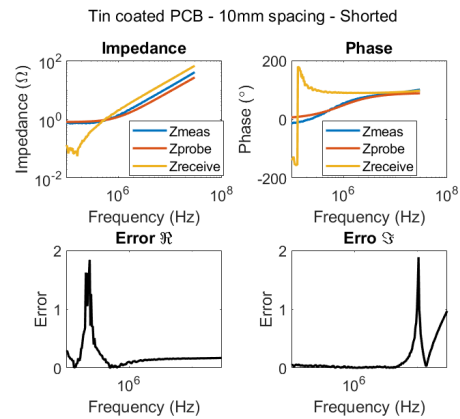


Figure C.34: 10 mm Tin shorted circuit

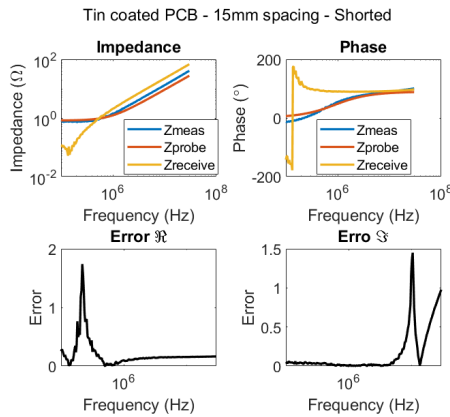


Figure C.35: 15 mm Tin shorted circuit

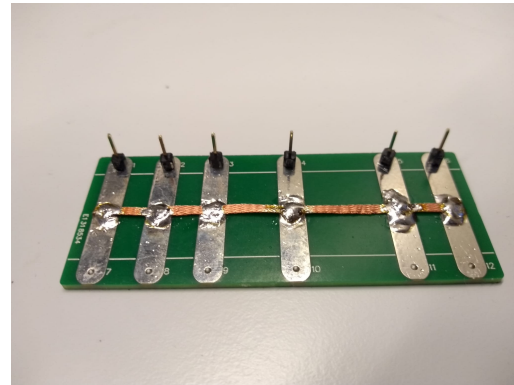


Figure C.36: Tin shorted circuit configuration

In table C.4 the resulting estimates are provided, with the probe inductance being provided a range of 10 nH up to 1 μ H and the probe resistance being allowed values from 0.1 Ω up to 10 Ω . Following the same conclusion as obtained for the gold coated samples, it can be derived that the inductance due to the shorting wire length is approximately equal to 1 nH mm⁻¹. This additional compensated induction once more left in the calibration, to account for the same effect occurring in the polymer sample.

	Low bound	Estimate	High bound	Fit 5mm	Fit 10mm	Fit 15mm
L_{Probe}	10 nH	100 nH	1 μ H	137.07 nH	140.63 nH	145.99 nH
R_{Probe}	0.1 Ω	1 Ω	10 Ω	0.78805 Ω	0.80365 Ω	0.81918 Ω

Table C.4: Fitted shorted calibration values

C.2.6 Tin: reference load circuit

The last measurement to be performed was as before the use of a 50 Ω reference load that was soldered in between the contacts as shown in figure C.40. With the 5 mm, 10 mm and 15 mm contact spacings being shown in figures C.37, C.38 and C.39 respectively.

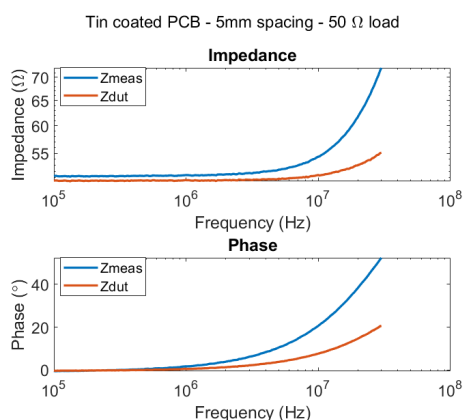


Figure C.37: 5 mm Tin loaded circuit

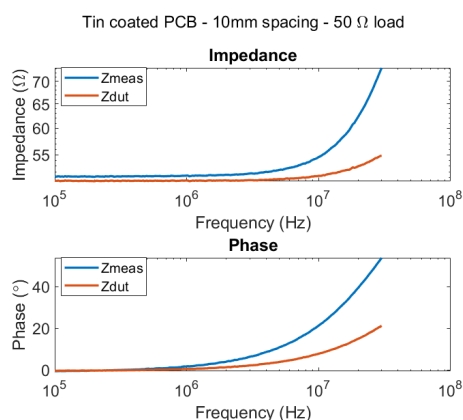


Figure C.38: 10 mm Gold loaded circuit

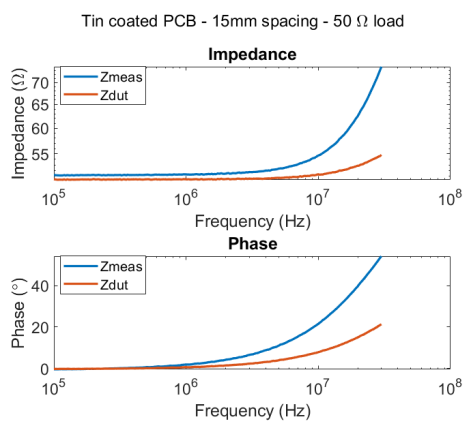


Figure C.39: 15 mm Gold loaded circuit

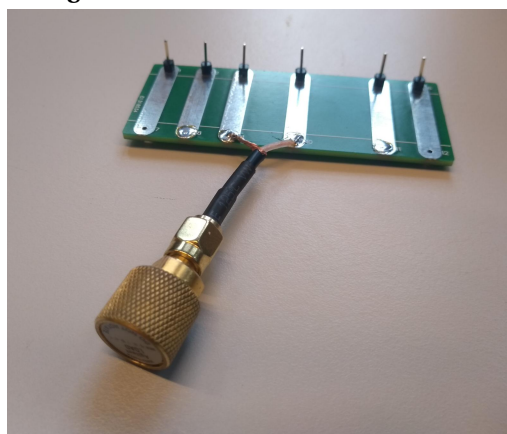


Figure C.40: Tin load circuit configuration

From the resulting calibration the effect of calibration can be observed to be comparable to that for the gold coated PCBs. The inductive contribution of the coaxial adapter cable is once more observed, as well as the compensation for the contact and probe resistances. The reference resistance of 50 Ω is also once more correctly derived.

D Silicon Wafer Experiment

Given the quantity of samples produced and tested during the silicon wafer experiment, detailed before and after pictures of the samples when clamped in the pressure testing jig are provided in this section of the appendix.

D.1 Control Sample

The first sample created for the wafer test is the control sample with only a 11 mm Polyimide film adhesive circle plugging the hole in the silicon wafer. As can be observed in figure D.1 that the manner wherein the circles adhere is slightly inconsistent. This is also observed in figure D.2 as this is reflected in the orientation of failure.



Figure D.1: Control sample before test

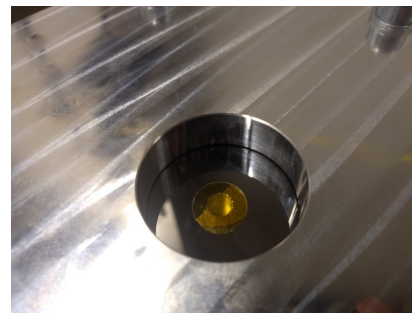


Figure D.2: Control sample after test

D.2 Protopasta Sample

The pressure test of the non-completed protopasta print as provided in figure D.3 resulted in a quick release of the printed plug from the underlying film and wafer. The released plug and still partially attached film can be observed in figure D.4.

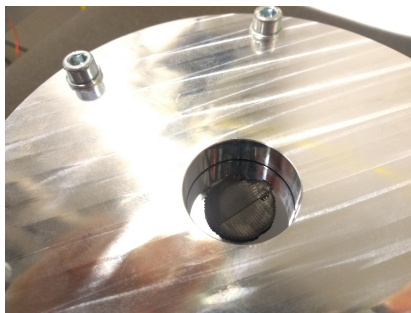


Figure D.3: Protopasta sample before test



Figure D.4: Protopasta sample after test

D.3 Electrifi Sample

As with the Protopasta sample, the non-completed Electrifi print is shown in figure D.5 where the lack of adhesion and material warping can clearly be observed. In figure D.6 the sample is shown after the pressure experiment with the sample being released from the wafer and the Polyimide film being partly detached.



Figure D.5: Electrifi sample before test

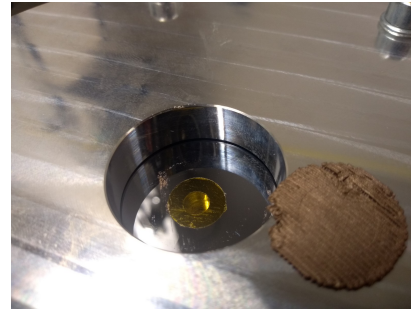


Figure D.6: Electrifi sample after test

D.4 Ninjatek Samples

Given that the Ninjatek samples were able to be fully printed, three samples were created and subsequently tested. The first sample as shown in figures D.7 and D.8 detached as one piece and was observed to float upon the gas flow being released at its point of detachment.

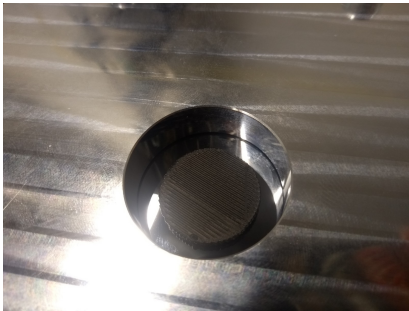


Figure D.7: Ninjatek #1 sample before test

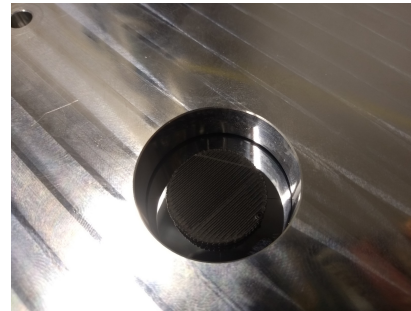


Figure D.8: Ninjatek #1 sample after test

The second Ninjatek sample as shown in figures D.9 and D.10 resulted in a more destructive result with the wafer fracturing. It could also be observed that despite the wafer disintegrating that the pieces of wafer remained attached to the printed plug.

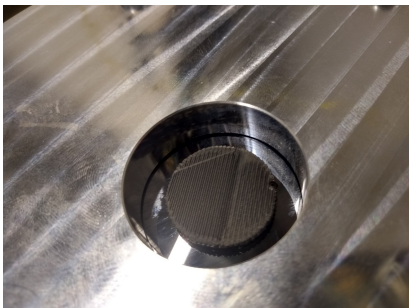


Figure D.9: Ninjatek #2 sample before test

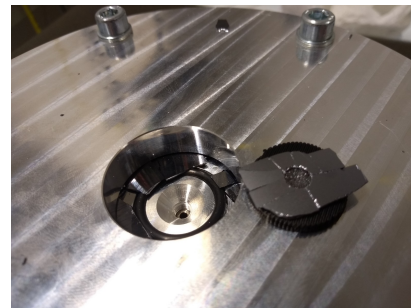


Figure D.10: Ninjatek #2 sample after test

The third Ninjatek sample detached partly in a similar manner as shown in figures D.9 and D.12. It can also be observed that the adhesion of the Polyimide film to the polymer might have been greater than that of the polymer to the wafer, as the remaining parts appear stuck to the film instead of the polymer.

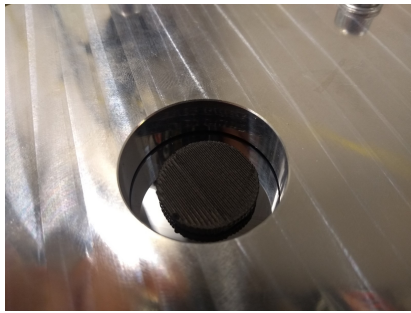


Figure D.11: Ninjatek #3 sample before test



Figure D.12: Ninjatek #3 sample after test

D.5 Palmiga Samples

Provided that the Palmiga filament is also a flexible TPU material able to adhere to the silicon wafer, three samples were also created. The first of which is shown in figures D.13 and D.14, with the note that unfortunately no before picture was taken of this sample. As with the Ninjatek samples, the wafer disintegrated before the sample was able to detach and pieces of silicon remained attached to the polymer and the polyimide film.

Sample Image
not recorded



Figure D.13: Palmiga #1 sample before test

Figure D.14: Palmiga #1 sample after test

The second Palmiga sample is shown in figure D.15 and D.16 where a similar disintegration of the wafer was once more achieved.



Figure D.15: Palmiga #2 sample before test



Figure D.16: Palmiga #2 sample after test

The third and last Palmiga sample did show detachment from the wafer surface leaving a clear mark of where it initially attached, as shown in figures D.17 and D.18. It can also be observed that the Polyimide film only detached on one of the two sides suggesting a levering action across the adhesion interface by the provided gas pressure, starting at a initial point of detachment.

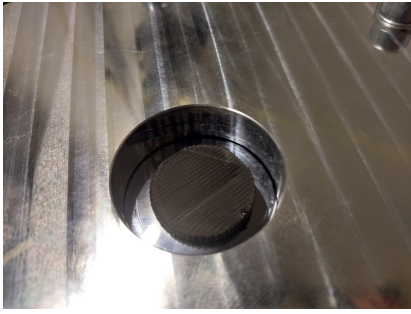


Figure D.17: Palmiga #3 sample before test

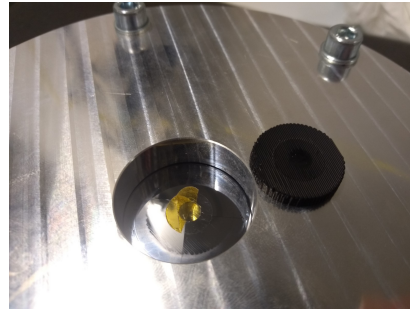


Figure D.18: Palmiga #3 sample after test

E Resistors

Given the several samples created for the infill based resistor design, the detailed description of the samples as printed by means of an image of each sample and a brief description will be provided below.

E.1 0° infill orientation samples

The first set of samples to discuss is that of the 0° infill orientation, with respect to the current path across the silver paint coated contact pads. In figure E.1 the 'lines'-type sample is shown, where the sample was ideally created by a set of continuous traxels, not connected at each end. It should be noted that due to the 2.0 mm width of the center track that 5 infill lines were created, which is one more than the second sample for this infill orientation as noted by the sample resistance that was observed.

The sample with 4 tracks and a meandering infill pattern, where the ends of the traxels are connected by a curve as the printer continues its path without halting material extrusion, is shown in figure E.2. Interestingly it can already be noted that although the infill pattern chosen is different between both samples, the formation of excess extrusion at the ends of the traxels is clearly observed. The lines infill resulted in more circular blobs as the printhead stops at each traxel end, whereas the meandering pattern results in more controlled curves.



Figure E.1: 0 Degree - lines

Figure E.2: 0 Degree - meander

E.2 15° infill orientation samples

As we start to rotate the infill pattern across the sample, these differences become even more pronounced, with the circular blobs as a result of the stopping of the printhead at the end of each traxel being clearly visible in the lines infill shown in figure E.3. A slight bloating of the print is also observed, which might have been resulted from accidental removal from the printbed before complete cooling of the sample.

The continuation of the lines as created the meandering pattern is also more clearly defined in the center section as shown in figure E.4, with the lines clearly continuing straight before returning to the printing path. The roughness at the sample edges as a result of this pattern is also different between the lines and the meandering pattern.



Figure E.3: 15 Degree - lines

Figure E.4: 15 Degree - meander

E.3 30° infill orientation samples

These trends continue when observing the differences between the samples shown in figures E.5 and E.6. As the infill pattern is rotated further, the blobs created with the lines pattern appear to fuse together into a straight line section. The meandering pattern clearly shows some more slope, and it also starts to become apparent that the continuous flow of material helps with preventing gaps in between traxels, as voids are starting to become observable in the lines sample.



Figure E.5: 30 Degree - lines



Figure E.6: 30 Degree - meander

E.4 45° infill orientation samples

Arriving at the halfway point of infill pattern rotation, the effect of stopping and continuing extrusion in comparison to continuous extrusion becomes very clear, with the fused sections of the meandering print being much longer than those of the lines based print. The wider center section as shown in figure E.7 in comparison to E.8 also results from the additional material extruded at the end of each print line, pointing to a limitation of the printers ability to prevent material oozing by retraction, not required for the meandering traxel.



Figure E.7: 45 Degree - lines



Figure E.8: 45 Degree - meander

E.5 60° infill orientation samples

The 60° samples show little difference from the previous 45° samples as shown in figures E.9 and E.10. The lines infill pattern once more shows clearly that less fusion occurs due to the traxel being stopped and then continuing, with the edges for both methods showing a comparable fusion.



Figure E.9: 60 Degree - lines



Figure E.10: 60 Degree - meander

E.6 75° infill orientation samples

For the 75° sample an interesting change is observed, as the meandering traxels as shown in figure E.12 start to fuse almost completely, in contrast to the line infill sample with appears to worsen in terms of the gaps in between the traxels as observed in figure E.12.



Figure E.11: 75 Degree - lines



Figure E.12: 75 Degree - meander

E.7 90° infill orientation samples

The last infill orientation is at 90° where the traxels are perfectly perpendicular to the current across the silver paint coated contact pads. In figures E.13 and E.14 it can be observed that both samples are very similar, with the additional fusion in the meandering sample being barely distinguishable.



Figure E.13: 90 Degree - lines



Figure E.14: 90 Degree - meander

F Capacitors and Inductors

Given the many capacitor and inductor samples created, sample images along with a brief description of each component will be provided below. This will be followed by a section detailing the calibrations performed for the impedance measurements performed upon these samples

F.1 Capacitor samples

To start off below pictures of the samples are provided with 2.54 mm pins attached through means of silver conductive epoxy [66].

F.1.1 Five plate capacitor stack

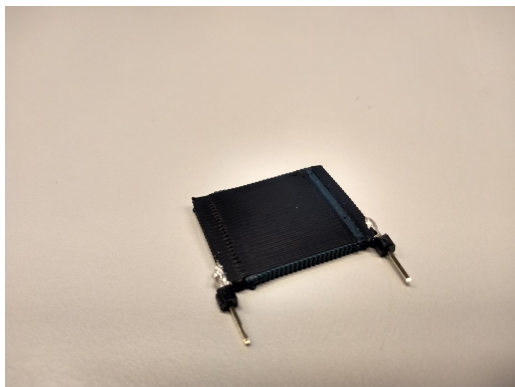


Figure F.1: Five plates - PLA dielectric

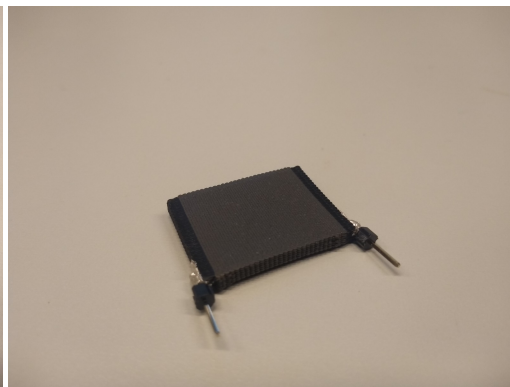


Figure F.2: Five plates - Iron dielectric

The first two capacitors shown are both constructed from three stacks of the designed plate pairs, to form a total of 5 pair with dielectric material in between. The plates were created from the conductive Protopasta PLA material, with neat PLA or iron filled PLA as a dielectric material. The neat PLA dielectric capacitor is shown in figure F.1, the iron filled PLA dielectric capacitor is shown in figure F.2. Slight warping can also be observed as an effect of the thermal anneal performed at a temperature of 115 °C for a period of 12 h.

F.1.2 Seven plate capacitor stack

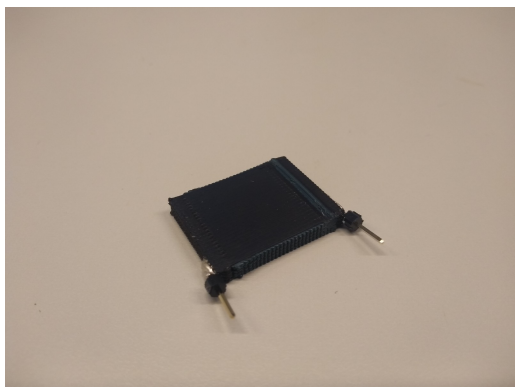


Figure F.3: Seven plates - PLA dielectric

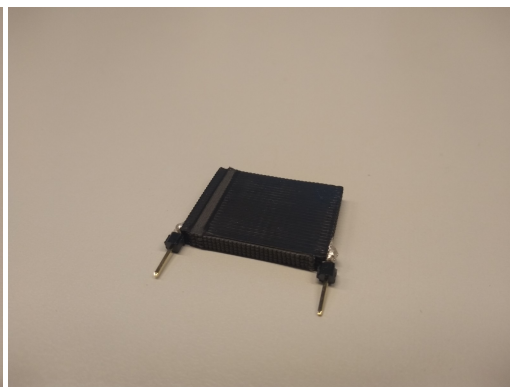


Figure F.4: Seven plates - Iron dielectric

The next set of capacitors were constructed from four stacks of designed stackable plate pairs, resulting in a total of 7 pairs of plates contributing to the capacitance. The capacitor with neat

PLA as a dielectric material is shown in figure E3 and the Iron filled PLA dielectric material capacitor is shown in figure F4.

F.1.3 Nine plate capacitor stack

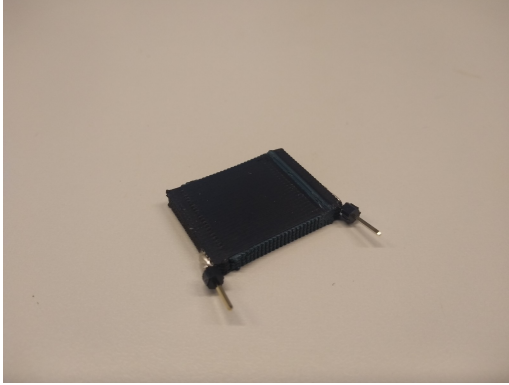


Figure F.5: Nine plates - PLA dielectric



Figure F.6: Nine plates - Iron dielectric

The last set of capacitors consisted of five stacks of plate pairs, resulting in a total of 9 pairs of contributing plates to the total capacitance. The neat PLA dielectric capacitor is shown in figure F5

F.2 Inductor samples

Likewise for the inductor samples, 2.54 mm pins were attached through means of silver conductive epoxy [66]. The four samples selected for measurement are shown below.

F.2.1 Solenoid inductors



Figure F.7: Three windings - Air core

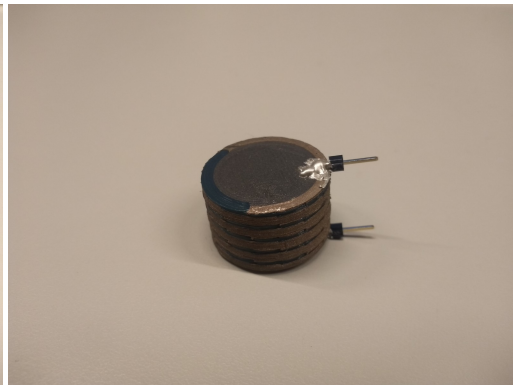


Figure F.8: Five windings - Iron PLA core

The first two inductors created consisted of a solenoid winding of square Electrifi filament wire, separated by a neat PLA dielectric, with two types of core material, air and iron filled PLA. Both coils were intended to have an equal set of windings, but due to difficulty during printing, the air core resulted with two less windings. The air cored, three winding inductor is shown in figure F.7 and the iron filled PLA core, five winding inductor is shown in figure F.8.

F.2.2 Planar inductors

In order to allow for a comparison in inductor performance to two dimensional designs, a set of four winding planar inductors were also created, with only neat PLA as a surrounding material. Two identical inductor designs were created, with one using air as a separator in between

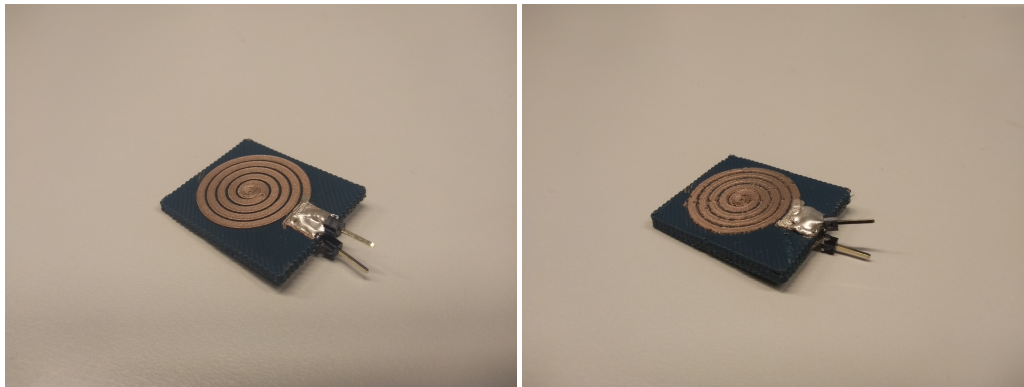


Figure F.9: Four windings - Coil embedded in air
Figure F.10: Four windings - Coil embedded in PLA

windings, and the other making use of the neat PLA as a separator, embedding the coil fully. In figure F.9 in air embedded inductor is shown, printed on top of the neat PLA, with figure F.9 providing the in PLA embedded inductor. It should be mentioned that from to the PLA embedding a rougher appearance resulted, with less apparent spacing between the coil wire.

E.3 LCR calibration

In order to compensate for the contribution of the measurement probes and the equipment a calibration was performed on the basis of the method as described in section 5.3.2

E.3.1 Open circuit calibration

The first calibration performed was an open circuit calibration, where the internal measurement impedance was fixed and the stray capacitance was estimated on the basis of a fit from 1 MHz to 30 MHz. This initial limiting of the bandwidth for estimation was performed to allow the algorithm to more accurately derive the slope resulting from the capacitance, given the contribution of the measurement resistance was fixed and equally weighted by the fitting algorithm. In figure F.11 the resulting calibration measurements along with the fitted equivalent circuit model as shown in figure F.12 are provided.

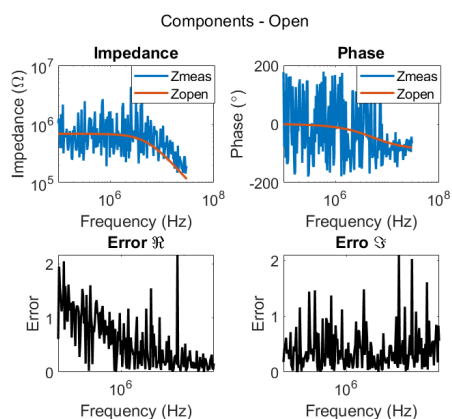


Figure F.11: Open circuit calibration

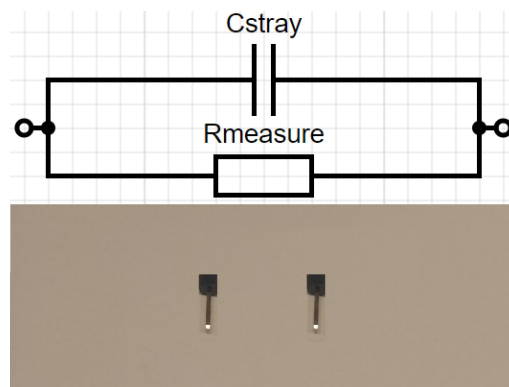


Figure F.12: Open circuit sample

The resulting derived equivalent circuit parameters are shown in table E.1. The measurement resistance $R_{measure}$ was fixed to the for the equipment specified $1\text{ M}\Omega$. The stray capacitance was found to have a very low value in comparison the previously derived pF capacitance for the PCB samples.

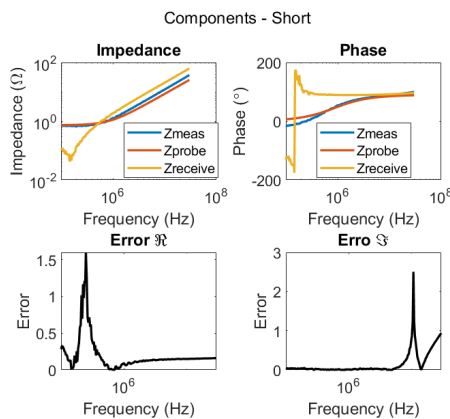
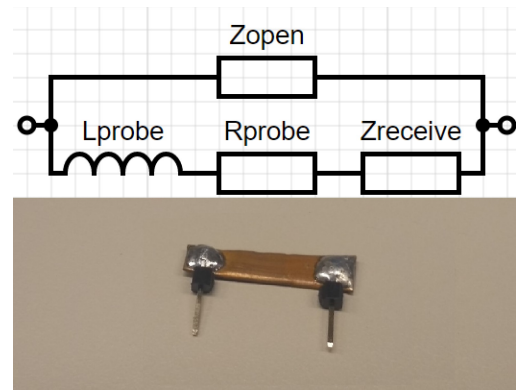
	Estimate	lb	hb	Fit
Measurement resistance	1 M Ω	1 M Ω	1 M Ω	1 M Ω
Stray capacitance	1 pF	1 fF	1 nF	41.445 fF

Table F.1: Fitted open calibration values

F.3.2 Short circuit calibration

The second calibration step involved shorting the probes, by means of the copper strip as shown in figure F.14. This results in an equivalent circuit where the previously derived open circuit impedances are placed in parallel with the series resistance and inductance of the measurement probes as well as the contribution of the receiver port.

With the use of rewritten equivalent shorted circuit model equation C.6 from appendix C.2 describing the calibration for the PCB samples, the probe and receiver port contributions were isolated. Maintaining the same methodology applied there, the probe impedance was fitted to a complex impedance model consisting of its inductance and its resistance. The remaining deviation from the observed impedance was captured numerically by the receiver port impedance. The calibration results are provided in figure F.13.

**Figure F.13:** Short circuit calibration**Figure F.14:** Short circuit sample

In figure F.13 the resulting fit obtained from the measurements and the measurements themselves are provided, where it should be noted that the initial and final deviation in the measurement of the phase are not captured by the component model for the probe. These remaining effects are suggested to result from a contribution from the measurement devices receiver port, for which it is noted in the manual that a parasitic capacitance at the receiver port will degrade accuracy [43] from 1 MHz onward. This is inline with the observation of the impedance of the receiver contribution becoming significant in comparison to the measurements at that frequency, as captured and to be compensated numerically in the $Z_{receive}$ impedance.

In table F.2 the resulting derived parameters for the probe impedances are provided. The probe resistance is slightly higher than what would be expected for the 0.6 mm copper conductor of the measurement probes, but could be explained by the several contact resistances present in between the equipment and the sample. The nH probe inductance was found to be inline with expectations for a 15 cm long set of coaxial probes with a 0.6 mm center conductor and a 3 mm outer conductor constructed with a Polyethylene dielectric [117].

	Estimate	lb	hb	Fit
Probe inductance	100 nH	10 nH	1 μ H	135.08 nH
Probe resistance	1 Ω	0.1 Ω	10 Ω	0.73763 Ω

Table F.2: Fitted shorted calibration values

F.3.3 Loaded circuit calibration

Providing a sanity check the last calibration that was performed was to make use of a 50 Ω standard load [3] to confirm the accuracy of the derived parasitic compensation model. In figure F.16 the equivalent circuit for the calibration and the reference load as connected through a SMA to 2.54 mm pin adapter is shown.

The derivation of the contribution of the device under test to the measured impedance was derived with the use of equation C.13 as provided from the PCB sample calibrations in appendix C.2. In figure F.15 the resulting measurement and fit can be observed.

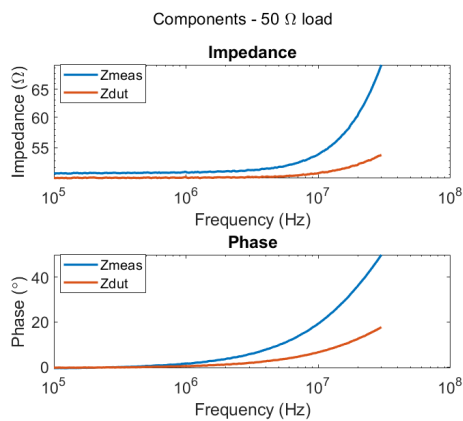


Figure F.15: Loaded circuit calibration

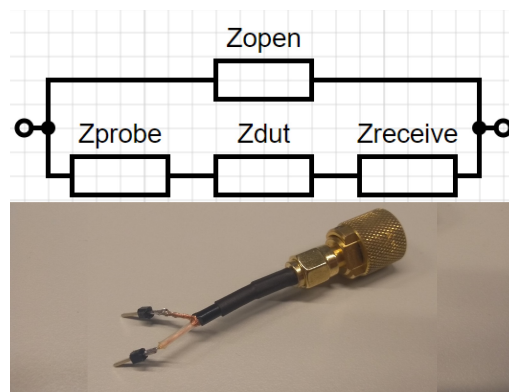


Figure F.16: Loaded circuit sample

From the compensated measurement a 50 Ω impedance for the connected reference was derived as would be expected. The slight inductance still observed is believed to have resulted from the short section of coaxial cable applied to adapt the load to the unconventional pin format of the probe, with the major probe inductance contribution having been compensated. The probe contact and probe wire resistance can also be observed to have been accounted for, given that the measurement impedance is slightly larger than the resulting device impedance.

Bibliography

- [1] 3DSourced (2021), *Material Jetting (PolyJet) 3D Printing: Everything You Need To Know*, Sourced Digital Ltd., 71 - 75 Shelton Street, London, United Kingdom, WC2H 9JQ.
<https://www.3dsourced.com/guides/polyjet>
- [2] AddNorth (2019), *Koltron TDS*, Add:North, Ulricehamnsvägen 11514 62; Ölsremma.
www.filament2print.com/gb/graphene/1175-koltron-g1.html
- [3] Agilent Technologies (2002), *Agilent Technologies 85033D 3.5 mm Calibration Kit*, Agilent Technologies Inc., 5301, Stevens Creek Blvd. Santa Clara, CA 95051, United States.
www.keysight.com/en/product/85033D/calibration-kit-35-mm.html
- [4] Agilent Technologies (2007), *E3631A Triple Output DC Power Supply*, Agilent Technologies Inc., 550 Clark Drive, Suite 101, Budd Lake, New Jersey, 07828, USA.
www.keysight.com/nl/en/product/E3631A/80w-triple-output-power-supply-6v-5a--25v-1a.html
- [5] All3DP (2021), *The Types of 3D Printing Technology*, All3DP GmbH, Ridlerstraße 31A, 80339 München, Germany.
www.all3dp.com/1/types-of-3d-printers-3d-printing-technology
- [6] AMFG (2020), *A Comprehensive Guide to Material Jetting 3D Printing*, Autonomous Manufacturing, Rosebery Ave 14, London, United Kingdom, EC1R 4TD.
www.amfg.ai/2018/06/29/material-jetting-3d-printing-guide
- [7] AMRG (2021), *Directed Energy Deposition*, Additive Manufacturing Research Group, Epinal Way, Loughborough Leicestershire, UK LE11 3TU.
www.lboro.ac.uk/research/amrg/about/the7categoriesofadditivemanufacturing/directedenergydeposition
- [8] AMRG (2021), *Powder Bed Fusion*, Additive Manufacturing Research Group, Epinal Way, Loughborough Leicestershire, UK LE11 3TU.
www.lboro.ac.uk/research/amrg/about/the7categoriesofadditivemanufacturing/powderbedfusion
- [9] AMRG (2021), *Sheet Lamination*, Additive Manufacturing Research Group, Epinal Way, Loughborough Leicestershire, UK LE11 3TU.
www.lboro.ac.uk/research/amrg/about/the7categoriesofadditivemanufacturing/sheetlamination
- [10] Analog Devices (2009), *Thermal Design Basic, Tutorial*, Analog Devices Inc., One Analog Way, Wilmington, Massachusetts, United States, 01887.
www.analog.com/media/en/training-seminars/tutorials/mt-093.pdf
- [11] Aoki, M., K. Hozawa and K. Takeda (2010), Wafer-level hybrid bonding technology with copper/polymer co-planarization, in *2010 IEEE International 3D Systems Integration Conference (3DIC)*, pp. 1–4, doi:10.1109/3DIC.2010.5751471.
www.doi.org/10.1109/3DIC.2010.5751471
- [12] ASTM (2017), *Standard Test Method for Peel or Stripping Strength of Adhesive Bonds*, Astm d903-98(2017), ASTM International, 100 Barr Harbor Drive, West Conshohocken, PA, USA, 19428-2959.
www.astm.org/d0903-98r17.html

- [13] ASTM (2017), Standard Test Method for Pull-Off Strength of Coatings Using Portable Adhesion Testers, Astm d4541-17, ASTM International, 100 Barr Harbor Drive, West Conshohocken, PA, USA, 19428-2959.
www.astm.org/d4541-17.html
- [14] ASTM (2020), Standard Test Methods for Measuring Resistance of Electrical Connections (Static Contacts), Astm b539-20, ASTM International, 100 Barr Harbor Drive, West Conshohocken, PA, USA, 19428-2959.
www.astm.org/b0539-20.html
- [15] Baran, D., D. Corzo and G. Blazquez (2020), Flexible Electronics: Status, Challenges and Opportunities, *Frontiers in Electronics*, vol. 1, p. 2, ISSN 2673-5857, doi:10.3389/felec.2020.594003.
www.doi.org/10.3389/felec.2020.594003
- [16] Bird, R. B., W. E. Stewart and E. N. Lighfoot (1960), *Transport phenomena*, John Wiley, second edition, ISBN 0-471-07392-X.
www.worldcat.org/title/transport-phenomena/oclc/964824
- [17] BlackMagic3D (2017), *Conductive graphene PLA filament*, Graphene Laboratories Inc., 760 Koehler Avenue - Suite 2, Ronkonkoma, United States, NY 11779.
www.web.archive.org/web/20170610125904/http://www.blackmagic3d.com/Conductive-p/grphn-pla.htm
- [18] BlackMagic3D (2017), *Ferro-Magnetic PLA filament*, Graphene Laboratories Inc., 760 Koehler Avenue - Suite 2, Ronkonkoma, United States, NY 11779.
www.web.archive.org/web/20170619072404/http://www.blackmagic3d.com/Magnetic-PLA-Filament-p/bm3d-175-mag.htm
- [19] Daniel, F., N. H. Patoary, A. L. Moore, L. Weiss and A. D. Radadia (2018), Temperature-dependent electrical resistance of conductive polylactic acid filament for fused deposition modeling, *The International Journal of Advanced Manufacturing Technology*, vol. 99, pp. 1215–1224, ISSN 1433-3015, doi:10.1007/s00170-018-2490-z.
www.doi.org/10.1007/s00170-018-2490-z
- [20] Diabase Engineering (2018), *Diabase h5*, Diabase Engineering LLC., 824 S, Lincoln Street, Longmont, CO 80501, United States of America.
www.diasemachines.com/hseries
- [21] Dijkshoorn, A. and G. Krijnen (2019), *Characterizing the Anisotropic Electrical Properties of 3D Printed Conductive Sheets*, Master's thesis, University of Twente, Drienerlolaan 5, Enschede, The Netherlands, 7522NB.
www.essay.utwente.nl/78084
- [22] Dima 3D (2019), *DimaFIX*, DIMA 3D s.l., Paseo de Belén 9, Valladolid, Spain, 47011.
www.dima3d.com/en/home/dimafix
- [23] Electrolube (2015), *Silver Conductive Paint TDS*, Electrolube Ltd., Unit 2 Genesis Business Park, Albert Drive, Sheerwater, Woking, Surrey, GU21 5RW, United Kingdom.
www.electrolube.com/product/scpsilver-conductive-paint
- [24] Engineers Edge (2000), *Thermal Diffusivity*, Engineers Edge LLC., 510 N Crosslane Road, Monroe, Georgia, 30656, United States.
www.engineersedge.com/heat_transfer/thermal_diffusivity_table_13953.htm
- [25] Eurocircuits (2021), *Selecting the Right Surface Finish for your PCB*, Eurocircuits N.V., Antwerpsesteenweg 66, 2800, Mechelen, Belgium.
www.eurocircuits.com/blog/which-surface-finish-fits-your-design

- [26] Fabbrix (2019), *CNT filament TDS*, Crea3D, via Don Primo Mazzolari, snc 70037, Ruvo di Puglia, BA, Italy.
www.fabbrix.com/it/materiali-fabbrix
- [27] Festo (2021), *Pressure regulator MS4-LR-1/4-D6-AS-Z*, Festo AG und Co. KG, Rüter Straße 82, 73734, Esslingen, Germany.
www.festo.com/us/en/a/download-document/datasheet/529418
- [28] Fiberology (2018), *Fiberology ESD ABS TDS*, Fiberlab S.A., Brzezie 387, 32-014, Brzezie, Poland.
www.fiberlogy.com/wp-content/uploads/2021/12/FIBERLOGY_ESD_PET-G_TDS.pdf
- [29] Filo Alpha (2019), *AlphaOhm PLA filament TDS*, Filo Alpha, Via Galvani 13, 20080, Ozzero (MI), Italy.
www.filoalfa3d.com/gb/content/20-alfaohm
- [30] Fjelstad, J. (2009), Retrospective on electronics technology and prospective methods for co-design of IC packaging and manufacturing improvements, in *2009 10th International Symposium on Quality Electronic Design*, pp. 559–564, doi:10.1109/ISQED.2009.4810355.
www.doi.org/10.1109/ISQED.2009.4810355
- [31] Flowers, P. F., C. Reyes, S. Ye, M. J. Kim and B. J. Wiley (2017), 3D printing electronic components and circuits with conductive thermoplastic filament, *Additive Manufacturing*, vol. 18, pp. 156–163, ISSN 2214-8604, doi:10.1016/j.addma.2017.10.002.
www.doi.org/10.1016/j.addma.2017.10.002
- [32] Gao, X., S. Qi, X. Kuang, Y. Su, J. Li and D. Wang (2021), Fused filament fabrication of polymer materials: A review of interlayer bond, *Additive Manufacturing*, vol. 37, p. 101658, ISSN 2214-8604, doi:10.1016/j.addma.2020.101658.
www.doi.org/10.1016/j.addma.2020.101658
- [33] GEMS (2011), *3300 Series Compact Low Pressure OEM Pressure Transmitters*, Gems Sensors and Controls Inc., 1 Cowles Road, Plainville, Connecticut, 06062, USA.
www.docs.rs-online.com/cd39/0900766b811c8806.pdf
- [34] Glier, T. E., L. Akinsinde, M. Paufler, F. Otto, M. Hashemi, L. Grote, L. Daams, G. Neuber, B. Grimm-Lebsanft, F. Biebl, D. Rukser, M. Lippmann, W. Ohm, M. Schwartzkopf, C. J. Brett, T. Matsuyama, S. V. Roth and M. Rübhausen (2019), Functional Printing of Conductive Silver-Nanowire Photopolymer Composites, *Scientific Reports*, vol. 9, p. 6465, ISSN 2045-2322, doi:10.1038/s41598-019-42841-3.
www.doi.org/10.1038/s41598-019-42841-3
- [35] Gregurić, L. (2021), *How Much Does a Metal 3D Printer Cost?*, All3DP GmbH, Ridlerstraße 31A, 80339 München, Germany.
www.all3dp.com/2/how-much-does-a-metal-3d-printer-cost
- [36] Grigson, A. (1994), Soldering on: the importance of surface-mount technology, *IEE Review*, vol. 40, pp. SUPL2–SUPL4, doi:10.1049/ir:19940615.
www.doi.org/10.1049/ir:19940615
- [37] Hirt, L., S. Ihle, Z. Pan, L. Dorwling-Carter, A. Reiser, J. M. Wheeler, R. Spolenak, J. Vörös and T. Zambelli (2016), Template-Free 3D Microprinting of Metals Using a Force-Controlled Nanopipette for Layer-by-Layer Electrodeposition, *Advanced Materials*, vol. 28, pp. 2311–2315, doi:10.1002/adma.201504967.
www.doi.org/10.1002/adma.201504967
- [38] ISO (2015), Additive manufacturing — General principles — Terminology, Iso/astm 52900:2015, International Organization for Standardization, Chemin de Blandonnet 8, Vernier, Geneva, Switzerland, CP 401 - 1214.

- www.iso.org/standard/69669.html
- [39] Ivanov, E., R. Kotsilkova, H. Xia, Y. Chen, R. K. Donato, K. Donato, A. P. Godoy, R. Di Maio, C. Silvestre, S. Cimmino and V. Angelov (2019), PLA/Graphene/MWCNT Composites with Improved Electrical and Thermal Properties Suitable for FDM 3D Printing Applications, *Applied Sciences*, **vol. 9**, ISSN 2076-3417, doi:10.3390/app9061209.
www.doi.org/10.3390/app9061209
- [40] Karl, W. J., M. Schikowski, J. Thon and R. Knechtel (2019), Adhesive Wafer Bonding for CMOS based Lab-on-a-Chip Devices, in *2019 6th International Workshop on Low Temperature Bonding for 3D Integration (LTB-3D)*, pp. 29–29, doi:10.23919/LTB-3D.2019.8735114.
www.doi.org/10.23919/LTB-3D.2019.8735114
- [41] Keithley Instruments (2010), *Model 2000 Multimeter User manual*, Keithley Instruments, Inc., Cleveland, Ohio, U.S.A., 2000-900-01 Rev. J.
www.download.tek.com/manual/2000-900_J-Aug2010_User.pdf
- [42] KEMET (2019), *Capacitor and Inductor Fundamentals*, KEMET Corporation, One East Broward Blvd., Fort Lauderdale, Florida, United States, FL 33301.
www.ec.kemet.com/wp-content/uploads/sites/4/2019/10/202-FY19-Apps-Capacitor-Inductor-Fundamentals-Final-v2.pdf
- [43] Keysight Technologies (2019), *E5061B Network Analyzer*, Keysight Technologies Inc., 1400, Fountaingrove Parkway Santa Rosa, CA 95403-1738.
[www.https://www.keysight.com/nl/en/product/E5061B/e5061b-ena-vector-network-analyzer.html](https://www.keysight.com/nl/en/product/E5061B/e5061b-ena-vector-network-analyzer.html)
- [44] Kim, M.-S., W.-S. Chu, Y.-M. Kim, A. P. G. Avila and S.-H. Ahn (2009), Direct metal printing of 3D electrical circuit using rapid prototyping, *International Journal of Precision Engineering and Manufacturing*, **vol. 10**, pp. 147–150, ISSN 2005-4602, doi:10.1007/s12541-009-0106-0.
www.doi.org/10.1007/s12541-009-0106-0
- [45] Kluger, R. and K. Rinortner (2021), *The History of Printed Circuit Boards*, Eurocircuits N.V., Antwerpsesteenweg 66, 2800, Mechelen, Belgium.
www.eurocircuits.com/blog/the-history-of-printed-circuit-boards
- [46] Kwok, S. W., K. H. H. Goh, Z. D. Tan, S. T. M. Tan, W. W. Tjiu, J. Y. Soh, Z. J. G. Ng, Y. Z. Chan, H. K. Hui and K. E. J. Goh (2017), Electrically conductive filament for 3D-printed circuits and sensors, *Applied Materials Today*, **vol. 9**, pp. 167–175, ISSN 2352-9407, doi:10.1016/j.apmt.2017.07.001.
www.doi.org/10.1016/j.apmt.2017.07.001
- [47] Laboratorios 3D (2021), *3Dlac*, Laboratorios 3D print s.l., C. los Aragonés, 549690 San Cristóbal de Entreviñas, Zamora, Spain.
www.3dlac.com
- [48] Latouche, M. (2021), *SLA 3D printing materials compared*, 3D Hubs, Danzigerkade 23A, 1013AP, Amsterdam, The Netherlands.
www.3dhubs.com/knowledge-base/sla-3d-printing-materials-compared
- [49] Lazarus, N. and S. S. Bedair (2020), Creating 3D printed sensor systems with conductive composites, *Smart Materials and Structures*, **vol. 30**, p. 015020, doi:10.1088/1361-665x/abcbe2.
www.doi.org/10.1088/1361-665x/abcbe2
- [50] Lazarus, N. and H. H. Tsang (2020), 3-D Printing Structural Electronics With Conductive Filaments, *IEEE Transactions on Components, Packaging and Manufacturing*

- Technology*, **vol. 10**, pp. 1965–1972, doi:10.1109/TCPMT.2020.3038563.
www.doi.org/10.1109/TCPMT.2020.3038563
- [51] Lei, Z., Z. Chen, Y. Zhou, Y. Liu, J. Xu, D. Wang, Y. Shen, W. Feng, Z. Zhang and H. Chen (2019), Novel electrically conductive composite filaments based on Ag/saturated polyester/polyvinyl butyral for 3D-printing circuits, *Composites Science and Technology*, **vol. 180**, pp. 44–50, ISSN 0266-3538, doi:10.1016/j.compscitech.2019.05.003.
www.doi.org/10.1016/j.compscitech.2019.05.003
- [52] Lu, C. (2013), Review on silver wire bonding, in *2013 8th International Microsystems, Packaging, Assembly and Circuits Technology Conference (IMPACT)*, pp. 226–229, doi:10.1109/IMPACT.2013.6706647.
www.doi.org/10.1109/IMPACT.2013.6706647
- [53] Lu, C., Y. Kho, C. Cheng, Y. Huang and K. Chen (2017), Polymer for wafer-level hybrid bonding and its adhesion to passivation layer in 3D integration, in *2017 International Conference on Electronics Packaging (ICEP)*, pp. 519–521, doi:10.23919/ICEP.2017.7939437.
www.doi.org/10.23919/ICEP.2017.7939437
- [54] Luanpitpong, S., L. Wang and Y. Rojanasakul (2014), The effects of carbon nanotubes on lung and dermal cellular behaviors, *Nanomedicine*, **vol. 9**, pp. 895–912, doi:10.2217/nnm.14.42.
www.doi.org/10.2217/nnm.14.42
- [55] Magdassi, S., M. Grouchko and A. Kamyshny (2010), Copper Nanoparticles for Printed Electronics: Routes Towards Achieving Oxidation Stability, *Materials*, **vol. 3**, pp. 4626–4638, ISSN 1996-1944, doi:10.3390/ma3094626.
www.doi.org/10.3390/ma3094626
- [56] MathWorks (2020), *MATLAB R2020b*, The MathWorks Inc., 1 Apple Hill Drive, Natick, Massachusetts, 01760-2098, USA.
www.mathworks.com/products/matlab.html
- [57] MatterHackers (2016), *Bed Surfaces: Applying Kapton Tape*, MatterHackers Inc., 20321 Valencia Cir, Lake Forest, California, 92630, United States.
www.matterhackers.com/articles/bed-surfaces-applying-kapton-tape
- [58] Meindl, J. (1997), A history of low power electronics: how it began and where it's headed, in *Proceedings of 1997 International Symposium on Low Power Electronics and Design*, pp. 149–151, doi:10.1109/LPE.1997.621267.
www.doi.org/10.1109/LPE.1997.621267
- [59] Meindl, J., A. Naeemi, M. Bakir and R. Murali (2010), Nanoelectronics in retrospect, prospect and principle, in *2010 IEEE International Solid-State Circuits Conference - (ISSCC)*, pp. 31–35, doi:10.1109/ISSCC.2010.5434062.
www.doi.org/10.1109/ISSCC.2010.5434062
- [60] Memmert (2021), *Universal oven UF30*, Memmert GmbH + Co. KG, Aeussere Rittersbacher, Strasse 38, D-91126 Schwabach, Germany.
www.memmert.com/products/heating-drying-ovens/universal-oven/UF30
- [61] Meng, S., H. He, Y. Jia, P. Yu, B. Huang and J. Chen (2017), Effect of nanoparticles on the mechanical properties of acrylonitrile–butadiene–styrene specimens fabricated by fused deposition modeling, *Journal of Applied Polymer Science*, **vol. 134**, doi:10.1002/app.44470.
<https://doi.org/10.1002/app.44470>

- [62] Mensley, M. (2021), *Best Budget Resin 3D Printers 2021 (April Update)*, All3DP GmbH, Ridlerstraße 31A, 80339 München, Germany.
www.all3dp.com/1/best-resin-dlp-sla-3d-printer-kit-stereolithography
- [63] Moschytz, G. S. (2010), From printed circuit boards to systems-on-a-chip, *IEEE Circuits and Systems Magazine*, vol. 10, pp. 19–29, doi:10.1109/MCAS.2010.936783.
www.doi.org/10.1109/MCAS.2010.936783
- [64] Multi3D (2016), *MSDS Electrifi Conductive 3D Printer Filament*, Multi3D LLC., 101-U Woodwinds Industrial Court, Cary, North Carolina, 27511, USA.
www.multi3dllc.com/wp-content/uploads/2016/09/Electrifi_MSDS.pdf
- [65] Multi3D (2021), *Electrifi conductive filament faqs*, Multi3D LLC., 101-U Woodwinds Industrial Court, Cary, North Carolina, 27511, USA.
www.multi3dllc.com/faqs
- [66] Multicomp (2018), *Silver Conductive Epoxy Adhesive, Moderate Cure / High Conductivity*, Newark Electronics Corporation, 300 South Riverside Plaza Suite, 2200, Chicago, Illinois, 60606, United States.
www.farnell.com/datasheets/2686273.pdf
- [67] Multicomp Pro (2021), *Equipment Wire: Defence Standard 61-12 Part 6 and BS 4808 Part 2*, Newark Electronics Corporation, 300 South Riverside Plaza Suite, 2200, Chicago, Illinois, 60606, United States.
www.farnell.com/datasheets/3217056.pdf
- [68] Nano Dimension (2020), *DragonFly LDM*, Nano Dimension Ltd., 13798 NW 4th Street, Suite 315 Sunrise, FL 33325, United States.
www.nano-di.com/ame-dragonfly-ldm-2-0
- [69] Nassar, H. and R. Dahiya (2021), Fused Deposition Modeling-Based 3D-Printed Electrical Interconnects and Circuits, *Advanced Intelligent Systems*, p. 2100102, doi:10.1002/aisy.202100102.
www.doi.org/10.1002/aisy.202100102
- [70] Nathan, A., A. Ahnood, M. T. Cole, S. Lee, Y. Suzuki, P. Hiralal, F. Bonaccorso, T. Hasan, L. Garcia-Gancedo, A. Dyadyusha, S. Haque, P. Andrew, S. Hofmann, J. Moultrie, D. Chu, A. J. Flewitt, A. C. Ferrari, M. J. Kelly, J. Robertson, G. A. J. Amaratunga and W. I. Milne (2012), Flexible Electronics: The Next Ubiquitous Platform, *Proceedings of the IEEE*, vol. 100, doi:10.1109/JPROC.2012.2190168.
www.doi.org/10.1109/JPROC.2012.2190168
- [71] National Instruments (2016), *NI myDAQ User Guide*, National Instruments Corporation, 11500 N Mopac Expwy, Austin, TX 78759-3504.
www.ni.com/pdf/manuals/373060g.pdf
- [72] Nave, C. R. (2017), *Cylindrical Capacitor*, Georgia State University, Department of Physics and Astronomy, 25 Park Place, Atlanta, Georgia, 30303, United States.
www.hyperphysics.phy-astr.gsu.edu/hbase/electric/capcyl.html
- [73] Nave, C. R. (2017), *Dielectric Constants at 20°C*, Georgia State University, Department of Physics and Astronomy, 25 Park Place, Atlanta, Georgia, 30303, United States.
www.hyperphysics.phy-astr.gsu.edu/hbase/Tables/diel.html
- [74] Nave, C. R. (2017), *Inductance of a Coil*, Georgia State University, Department of Physics and Astronomy, 25 Park Place, Atlanta, Georgia, 30303, United States.
www.hyperphysics.phy-astr.gsu.edu/hbase/magnetic/indcur.html

- [75] Nave, C. R. (2017), *Parallel Plate Capacitor*, Georgia State University, Department of Physics and Astronomy, 25 Park Place, Atlanta, Georgia, 30303, United States.
www.hyperphysics.phy-astr.gsu.edu/hbase/electric/pplate.html
- [76] Nave, C. R. (2017), *Resistance: Temperature Coefficient*, Georgia State University, Department of Physics and Astronomy, 25 Park Place, Atlanta, Georgia, 30303, United States.
www.hyperphysics.phy-astr.gsu.edu/hbase/electric/restmp.html
- [77] Nave, C. R. (2017), *Resistivity and Conductivity*, Georgia State University, Department of Physics and Astronomy, 25 Park Place, Atlanta, Georgia, 30303, United States.
www.hyperphysics.phy-astr.gsu.edu/hbase/electric/resis.html
- [78] Neuvel, P. (2020), Developing a reliable method to connect conductors to 3d printed conducting structures, Bachelor's thesis, Robotics and Mechatronics group, University of Twente, Drienerlolaan 5, Enschede, The Netherlands, 7522NB.
www.essay.utwente.nl/83047
- [79] NinjaTek (2018), *MSDS NinjaTek EEL 3D Filament*, Fenner Inc., 311 W Stiegel Street, Manheim, Pennsylvania, 17545, USA.
www.ninjatek.com/wp-content/uploads/SDS_EEL.pdf
- [80] NinjaTek (2021), *NinjaTek Eel 3D Printing Filament TDS*, Fenner Inc., 311 W Stiegel Street, Manheim, Pennsylvania, 17545, USA.
www.ninjatek.com/eel
- [81] Ostfeld, A. E., I. Deckman, A. M. Gaikwad, C. M. Lochner and A. C. Arias (2015), Screen printed passive components for flexible power electronics, *Scientific Reports*, **vol. 5**, p. 15959, ISSN 2045-2322, doi:10.1038/srep15959.
www.doi.org/10.1038/srep15959
- [82] Palm, P., J. Moisala, A. Kivikero, R. Tuominen and A. Iihola (2005), Embedding active components inside printed circuit board (PCB) - a solution for miniaturization of electronics, in *Proceedings. International Symposium on Advanced Packaging Materials: Processes, Properties and Interfaces, 2005.*, pp. 1–4, doi:10.1109/ISAPM.2005.1432034.
www.doi.org/10.1109/ISAPM.2005.1432034
- [83] Palmiga Innovations (2016), *ETPU-95 Carbon Black*, Palmiga Innovations, Fläderbärsvägen 4, 263 71, Jonstorp, Sweden.
www.rubber3dprinting.com/pi-etpu-95-250-carbon-black/
- [84] Palmiga Innovations (2016), *MSDS PI-ETPU 95-250 Carbon Black*, Palmiga Innovations, Fläderbärsvägen 4, 263 71, Jonstorp, Sweden.
www.rubber3dprinting.com/MSDS_PI-ETPU_95-250_Carbon_Black_Eng.pdf
- [85] Paolo, F. D. (2000), *Networks and Devices Using Planar Transmission Lines*, CRC Press, ISBN 978-0849318351.
www.books.google.com/books?id=tV9uu2Bq2X0C
- [86] Postiglione, G., G. Natale, G. Griffini, M. Levi and S. Turri (2015), Conductive 3D microstructures by direct 3D printing of polymer/carbon nanotube nanocomposites via liquid deposition modeling, *Composites Part A: Applied Science and Manufacturing*, **vol. 76**, pp. 110–114, ISSN 1359-835X, doi:10.1016/j.compositesa.2015.05.014.
www.doi.org/10.1016/j.compositesa.2015.05.014
- [87] Potter, P. M., S. R. Al-Abed, D. Lay and S. M. Lomnicki (2019), VOC Emissions and Formation Mechanisms from Carbon Nanotube Composites during 3D Printing, *Environmental Science & Technology*, **vol. 53**, pp. 4364–4370, doi:10.1021/acs.est.9b00765.
www.doi.org/10.1021/acs.est.9b00765

- [88] ProtoPasta (2018), *MSDS Composite Conductive Fiber PLA*, Protoplant Inc., 12001 NE 60th Way B2, Vancouver, Washington, 98682, United States.
www.proto-pasta.com/pages/technical-data-sheets
- [89] ProtoPasta (2021), *Conductive PLA TDS*, Protoplant Inc., 12001 NE 60th Way B2, Vancouver, Washington, 98682, United States.
www.proto-pasta.com/pages/technical-data-sheets
- [90] ProtoPasta (2021), *Magnetic Iron PLA TDS*, Protoplant Inc., 12001 NE 60th Way B2, Vancouver, Washington, 98682, United States.
www.proto-pasta.com/pages/technical-data-sheets
- [91] Riegel, J., W. Mayer and Y. van Havre (2021), FreeCAD (Version 0.18).
www.freecadweb.org
- [92] RS Pro (2014), *PTFE Insulated Equipment Wire (Type B)*, RS Components Ltd., Birchington Road Northants, Corby, NN17 9RS, United Kingdom.
www.docs.rs-online.com/265a/0900766b8135dba8.pdf
- [93] Sampson, K. L., B. Deore, A. Go, M. A. Nayak, A. Orth, M. Gallerneault, P. R. L. Malenfant and C. Paquet (2021), Multimaterial Vat Polymerization Additive Manufacturing, *ACS Applied Polymer Materials*, pp. 4304–4324, doi:10.1021/acsapm.1c00262.
www.doi.org/10.1021/acsapm.1c00262
- [94] Schouten, M. (2017), *Towards additively manufactured complex robotic systems*, Master's thesis, University of Twente, Drienerlolaan 5, Enschede, The Netherlands, 7522NB.
www.essay.utwente.nl/74355
- [95] Scordo, G., V. Bertana, L. Scaltrito, S. Ferrero, M. Cocuzza, S. L. Marasso, S. Romano, R. Sesana, F. Catania and C. F. Pirri (2019), A novel highly electrically conductive composite resin for stereolithography, *Materials Today Communications*, vol. 19, pp. 12–17, ISSN 2352-4928, doi:10.1016/j.mtcomm.2018.12.017.
www.doi.org/10.1016/j.mtcomm.2018.12.017
- [96] Shepheard, S. (2021), *Directed Energy Deposition (DED): A Complete Guide*, Sourced Digital Ltd., 71 - 75 Shelton Street, London, United Kingdom, WC2H 9JQ.
www.3dsourced.com/3d-printing-technologies/directed-energy-deposition
- [97] Simpson, T. W. (2018), *Why Does My 3D-Printed Part Cost So Much?*, Gardner Business Media, Inc., 6915 Valley Ave, Cincinnati, Ohio, 45244, United States.
www.additivemanufacturing.media/articles/why-does-my-3d-printed-part-cost-so-much
- [98] Singh, R., G. S. Sandhu, R. Penna and I. Farina (2017), Investigations for Thermal and Electrical Conductivity of ABS-Graphene Blended Prototypes, *Materials*, vol. 10, ISSN 1996-1944, doi:10.3390/ma10080881.
www.doi.org/10.3390/ma10080881
- [99] Stano, G., A. Di Nisio, A. M. Lanzolla, M. Ragolia and G. Percoco (2020), Fused filament fabrication of commercial conductive filaments: experimental study on the process parameters aimed at the minimization, repeatability and thermal characterization of electrical resistance, *The International Journal of Advanced Manufacturing Technology*, vol. 111, pp. 2971–2986, ISSN 1433-3015, doi:10.1007/s00170-020-06318-2.
www.doi.org/10.1007/s00170-020-06318-2
- [100] T, S., S. Ponnusamy and P. C. (2019), Application of 3D printed PLA-carbon black conductive polymer composite in solvent sensing, *Materials Research Express*, vol. 6, doi:10.1088/2053-1591/ab5040.
www.doi.org/10.1088/2053-1591/ab5040

- [101] Tan, J. and H. Low (2018), Embedded electrical tracks in 3D printed objects by fused filament fabrication of highly conductive composites, *Additive Manufacturing*, **vol. 23**, pp. 294–302, ISSN 2214-8604, doi:10.1016/j.addma.2018.06.009.
www.doi.org/10.1016/j.addma.2018.06.009
- [102] Temna Test Equipment (2004), *Model 72-7740/72-7745 Operating manual*, Newark Electronics Corporation, 300 South Riverside Plaza Suite, 2200, Chicago, Illinois, 60606, United States.
www.farnell.com/datasheets/1490819.pdf
- [103] Treed Filaments (2021), *The filament must be dry*, SA2P di Dario Negrelli Pizzigoni, Via Messina, 101, 20831, Seregno MB, Italy.
www.treedfilaments.com/wp-content/uploads/2021/05/Dry_3d_filaments.pdf
- [104] Tuttle, G. (2021), *EE 432 : TLM measurements*, Iowa State University, Ames, IA 50011, United States.
www.tuttle.merc.iastate.edu/ee432/homepage.htm
- [105] Ultimaker (2021), *Ultimaker Cura*, Ultimaker B.V., Stationsplein 32, 3511 ED, Utrecht, The Netherlands.
www.ultimaker.com/software/ultimaker-cura
- [106] Valentine, A. D., T. A. Busbee, J. W. Boley, J. R. Raney, A. Chortos, A. Kotikian, J. D. Berrigan, M. F. Durstock and J. A. Lewis (2017), Hybrid 3D Printing of Soft Electronics, *Advanced Materials*, **vol. 29**, doi:10.1002/adma.201703817.
www.doi.org/10.1002/adma.201703817
- [107] Varotsis, A. B. (2021), *Introduction to binder jetting 3D printing*, 3D Hubs, Danzigerkade 23A, 1013AP, Amsterdam, The Netherlands.
www.3dhubs.com/knowledge-base/introduction-binder-jetting-3d-printing
- [108] Wheeler, H. (1928), Simple Inductance Formulas for Radio Coils, *Proceedings of the Institute of Radio Engineers*, **vol. 16**, pp. 1398–1400, doi:10.1109/JRPROC.1928.221309.
www.doi.org/10.1109/JRPROC.1928.221309
- [109] Wiklund, J., A. Karakoç, T. Palko, H. Yiğitler, K. Ruttik, R. Jäntti and J. Paltakari (2021), A Review on Printed Electronics: Fabrication Methods, Inks, Substrates, Applications and Environmental Impacts, *Journal of Manufacturing and Materials Processing*, **vol. 5**, ISSN 2504-4494, doi:10.3390/jmmp5030089.
www.doi.org/10.3390/jmmp5030089
- [110] Wolterink, G., R. Sanders and G. Krijnen (2018), Thin, Flexible, Capacitive Force Sensors Based on Anisotropy in 3D-Printed Structures, in *2018 IEEE SENSORS*, pp. 1–4, doi:10.1109/ICSENS.2018.8589584.
www.doi.org/10.1109/ICSENS.2018.8589584
- [111] Wolterink, G., A. Umrani, M. Schouten, R. Sanders and G. Krijnen (2020), 3D-Printed Calorimetric Flow Sensor, in *2020 IEEE SENSORS*, pp. 1–4, doi:10.1109/SENSORS47125.2020.9278640.
www.doi.org/10.1109/SENSORS47125.2020.9278640
- [112] Wu, S.-Y., C. Yang, W. Hsu and L. Lin (2015), 3D-printed microelectronics for integrated circuitry and passive wireless sensors, *Microsystems & Nanoengineering*, **vol. 1**, p. 15013, ISSN 2055-7434, doi:10.1038/micronano.2015.13.
www.doi.org/10.1038/micronano.2015.13
- [113] Xiang, D., X. Zhang, E. Harkin-Jones, W. Zhu, Z. Zhou, Y. Shen, Y. Li, C. Zhao and P. Wang (2020), Synergistic effects of hybrid conductive nanofillers on the performance of 3D printed highly elastic strain sensors, *Composites Part A: Applied Science and*

- Manufacturing*, vol. 129, p. 105730, ISSN 1359-835X,
doi:10.1016/j.compositesa.2019.105730.
www.doi.org/10.1016/j.compositesa.2019.105730
- [114] Yoo, J. J. and E. Meng (2019), Fine-Pitch Bonding Methods for Integrating Asics with Flexible Polymer Memes, in *2019 20th International Conference on Solid-State Sensors, Actuators and Microsystems Eurosensors XXXIII (TRANSDUCERS EUROSENSORS XXXIII)*, pp. 1623–1626, doi:10.1109/TRANSDUCERS.2019.8808219.
www.doi.org/10.1109/TRANSDUCERS.2019.8808219
- [115] Yoon, D., S. H. Lee and K. Paik (2018), A Study on the Anchoring Polymer Layer (APL) Solder Anisotropic Conductive Films (ACFs) for Ultra Fine Pitch Flex-on-Flex (FOF) Assembly Using an Ultrasonic Bonding Method, in *2018 IEEE 68th Electronic Components and Technology Conference (ECTC)*, pp. 15–20, doi:10.1109/ECTC.2018.00010.
www.doi.org/10.1109/ECTC.2018.00010
- [116] Zakel, E., J. Gwiasda, J. Kloeser, J. Eldring, G. Engelmann and H. Reichl (1994), Fluxless flip chip assembly on rigid and flexible polymer substrates using the Au-Sn metallurgy, in *Proceedings of 16th IEEE/CPMT International Electronic Manufacturing Technology Symposium*, pp. 177–184 vol.1, doi:10.1109/IEMT.1994.404670.
www.doi.org/10.1109/IEMT.1994.404670
- [117] Zolotkov, A. (2002), *Coaxial Cable Calculator*, ANVICA Software Development, 1425 Bodmin Rd., Suite 407, Mississauga, Ontario, Canada.
www.translatorscafe.com/unit-converter/en-US/calculator/coaxial-cable

List of Figures

2.1	Filament fusion process	8
2.2	Illustration of extrusion calibration	8
2.3	Part components	8
2.4	Infill concept	8
3.1	Alongside Infill pattern	15
3.2	Perpendicular Infill pattern	15
3.3	Mask Creation	16
3.4	Pattern Application	16
3.5	Pad Creation	17
3.6	Wire Addition	17
3.7	4-wire measurement concept	17
3.8	Resistivity extrapolation example	18
3.9	Real Time measurement setup	18
3.10	Example of room recorded room sample resistivity over time	19
3.11	Example of recorded oven sample resistivity over time	20
3.12	Example of anneal and exposure curves	21
3.13	Example of thermal resistance of oven samples	23
3.14	Ninjatek	25
3.15	Palmiga85	25
3.16	Protopasta	25
3.17	Electrifi	25
4.1	2D sketch of sample geometry used	30
4.2	Traxel layout for 1x1mm, 2x2mm, 3x3mm, 5x5mm, 8x8mm samples	30
4.3	Samples after printing	31
4.4	Silver paint coated samples	31
4.5	Measurement setup used for current density experiment	32
4.6	Voltage profile programmed during current measurements	33
4.7	Example of marked current and temperature plots	34
5.1	Traxel conduction model	40
5.2	Design of printed circuit board	41
5.3	Alongside Infill pattern	41
5.4	Perpendicular Infill pattern	41
5.5	PCB locating jig	42
5.6	PCB after print	42

5.7	Transfer Length Visualized	43
5.8	Transfer length derivation	43
5.9	GP series measurement configuration for E5061B Network analyzer	44
5.10	Overview of calibrated measurement system	45
5.11	Open probes	45
5.12	Shorted probes	45
5.13	Loaded probes	45
5.14	Ninjatek Gold print	47
5.15	Ninjatek Tin print	47
5.16	Palmiga Gold print	47
5.17	Palmiga Tin print	47
5.18	Protopasta Gold print	47
5.19	Protopasta Tin print	47
5.20	Electrifi Gold print	48
5.21	Ninjatek Gold Alongside	48
5.22	Ninjatek Gold Perpendicular	48
5.23	Ninjatek Tin Alongside	49
5.24	Ninjatek Tin Perpendicular	49
5.25	Palmiga Gold Alongside	50
5.26	Palmiga Gold Perpendicular	50
5.27	Palmiga Tin Alongside	51
5.28	Palmiga Tin Perpendicular	51
5.29	Gold contact behaviour	52
5.30	Tin contact behaviour	53
6.1	centering shim infill	56
6.2	Plug infill	56
6.3	5mm drilled wafer	57
6.4	PVA shim infill	57
6.5	Sample printing	57
6.6	Wafer experiment concept	57
6.7	Wafer clamping jig	58
6.8	Experimental pressure testing setup	59
6.9	Ninjatek printing result	60
6.10	Palmiga printing result	60
6.11	Protopasta waferprint top	60
6.12	Electrifi waferprint botom	60
6.13	Pressure graphs observed for polyimide film, electrifi and protopasta samples	61
6.14	Pressure graphs for ninjatek samples	61

6.15 Pressure graphs for palmiga samples	62
7.1 Sample dimensions	66
7.2 Sample infill orientations	66
7.3 Resistor slice type A - Lines	67
7.4 Resistor slice type B - Meander	67
7.5 Resistor samples with silver painted contacts	68
7.6 Resistances measured	70
7.7 Line printing effects	70
7.8 Meander printing effects	70
8.1 Capacitor dimensions	73
8.2 Sliced capacitor design for a single stack	74
8.3 Annealed capacitors	75
8.4 Plate capacitor	75
8.5 Material resistance	76
8.6 Capacitor equivalent model	77
8.7 Five plates - PLA dielectric	79
8.8 Seven plates - PLA dielectric	79
8.9 Nine plates - PLA dielectric	79
8.10 Five plates - Iron dielectric	80
8.11 Seven plates - Iron dielectric	80
9.1 Solenoid inductor dimensions	83
9.2 Sliced air core solenoid design	84
9.3 Sliced iron core solenoid design	84
9.4 Planar inductor design	85
9.5 Sliced on top planar design	85
9.6 Sliced embedded planar design	85
9.7 Solenoid with core material	86
9.8 Solenoid winding capacitance	87
9.9 Solenoid with air core	88
9.10 Planar with air core	88
9.11 Planar inductor winding resistance	89
9.12 Planar inductor winding capacitance	89
9.13 Inductor equivalent model	90
9.14 Three windings - Air core	93
9.15 Five windings - Iron PLA core	93
9.16 Four windings - Coil in air	94
9.17 Four windings - Coil in PLA	94

A.1	Ninjatek samples used for real time experiment	102
A.2	Palmiga samples used for real time experiment	103
A.3	Protopasta samples used for real time experiment	103
A.4	Electrifi samples used for real time experiment	104
A.5	Resistivity derived for Ninjatek samples during room measurement	105
A.6	Resistivity derived for Palmiga samples during room measurement	106
A.7	Resistivity derived for Protopasta samples during room measurement	106
A.8	Resistivity derived for Electrifi samples during room measurement	107
A.9	A comparison of 2- and 4-wire resistance measurements	108
A.10	Resistances observed for Ninjatek samples during oven measurement	109
A.11	Resistances observed for Palmiga samples during oven measurement	110
A.12	Resistances observed for Protopasta samples during oven measurement	110
A.13	Resistances observed for Electrifi samples during oven measurement	111
A.14	Resistivity derived for Ninjatek samples during oven measurement	111
A.15	Resistivity derived for Palmiga samples during oven measurement	112
A.16	Resistivity derived for Protopasta samples during oven measurement	113
A.17	Resistivity derived for Electrifi samples during oven measurement	114
A.18	Labeled anneal curves for Ninjatek alongside traxel samples	115
A.19	Labeled anneal curves for Ninjatek perpendicular traxel samples	115
A.20	Labeled anneal curves for Palmiga alongside traxel samples	116
A.21	Labeled anneal curves for Palmiga perpendicular traxel samples	117
A.22	Labeled anneal curves for Protopasta alongside traxel samples	118
A.23	Labeled anneal curves for Protopasta perpendicular traxel samples	118
A.24	Labeled anneal curves for Electrifi alongside traxel samples	119
A.25	Labeled anneal curves for Electrifi perpendicular traxel samples	120
A.26	Thermal response of Ninjatek samples during exposure	121
A.27	Thermal response of Palmiga samples during exposure	122
A.28	Thermal response of Protopasta samples during exposure	123
A.29	Thermal response of Electrifi samples during exposure	124
B.1	Current and temperature measurements for Ninjatek current density experiment	125
B.2	Ninjatek samples post current density experiment	126
B.3	Ninjatek current density limitation on the basis of surface area to volume ratio .	127
B.4	Current and temperature measurements for Palmiga current density experiment	127
B.5	Palmiga samples post current density experiment	129
B.6	Palmiga current density limitation on the basis of surface area to volume ratio . .	129
B.7	Current and temperature measurements for Protopasta current density experiment	130
B.8	Protopasta samples post current density experiment	131
B.9	Protopasta current density limitation on the basis of surface area to volume ratio	132

C.1 Ninjatek Alongside Gold	133
C.2 Ninjatek Perpendicular Gold	133
C.3 Ninjatek Alongside Tin	133
C.4 Ninjatek Perpendicular Tin	133
C.5 Palmiga Alongside Gold	134
C.6 Palmiga Perpendicular Gold	134
C.7 Palmiga Alongside Tin	134
C.8 Palmiga Perpendicular Tin	134
C.9 Ninjatek & Protopasta Alongside Gold	135
C.10 Ninjatek & Protopasta Perpendicular Gold	135
C.11 Ninjatek & Protopasta Alongside Tin	135
C.12 Ninjatek & Protopasta Perpendicular Tin	135
C.13 Palmiga & Protopasta Alongside Gold	135
C.14 Palmiga & Protopasta Perpendicular Gold	135
C.15 Palmiga & Protopasta Alongside Tin	135
C.16 Palmiga & Protopasta Perpendicular Tin	135
C.17 5 mm Gold open circuit	136
C.18 10 mm Gold open circuit	136
C.19 15 mm Gold open circuit	136
C.20 Gold open circuit configuration	136
C.21 5 mm Gold shorted circuit	137
C.22 10 mm Gold shorted circuit	137
C.23 15 mm Gold shorted circuit	137
C.24 Gold shorted circuit configuration	137
C.25 5 mm Gold loaded circuit	139
C.26 10 mm Gold loaded circuit	139
C.27 15 mm Gold loaded circuit	139
C.28 Gold load circuit configuration	139
C.29 5 mm Tin open circuit	140
C.30 10 mm Tin open circuit	140
C.31 15 mm Tin open circuit	140
C.32 Tin open circuit configuration	140
C.33 5 mm Tin shorted circuit	141
C.34 10 mm Tin shorted circuit	141
C.35 15 mm Tin shorted circuit	141
C.36 Tin shorted circuit configuration	141
C.37 5 mm Tin loaded circuit	142
C.38 10 mm Gold loaded circuit	142
C.39 15 mm Gold loaded circuit	142

C.40 Tin load circuit configuration	142
D.1 Control sample before test	143
D.2 Control sample after test	143
D.3 Protopasta sample before test	143
D.4 Protopasta sample after test	143
D.5 Electrifi sample before test	144
D.6 Electrifi sample after test	144
D.7 Ninjatek #1 sample before test	144
D.8 Ninjatek #1 sample after test	144
D.9 Ninjatek #2 sample before test	144
D.10 Ninjatek #2 sample after test	144
D.11 Ninjatek #3 sample before test	145
D.12 Ninjatek #3 sample after test	145
D.13 Palmiga #1 sample before test	145
D.14 Palmiga #1 sample after test	145
D.15 Palmiga #2 sample before test	145
D.16 Palmiga #2 sample after test	145
D.17 Palmiga #3 sample before test	146
D.18 Palmiga #3 sample after test	146
E.1 0 Degree - lines	147
E.2 0 Degree - meander	147
E.3 15 Degree - lines	147
E.4 15 Degree - meander	147
E.5 30 Degree - lines	148
E.6 30 Degree - meander	148
E.7 45 Degree - lines	148
E.8 45 Degree - meander	148
E.9 60 Degree - lines	148
E.10 60 Degree - meander	148
E.11 75 Degree - lines	149
E.12 75 Degree - meander	149
E.13 90 Degree - lines	149
E.14 90 Degree - meander	149
F1 Five plates - PLA dielectric	150
F2 Five plates - Iron dielectric	150
F3 Seven plates - PLA dielectric	150
F4 Seven plates - Iron dielectric	150

E5	Nine plates - PLA dielectric	151
E6	Nine plates - Iron dielectric	151
E7	Three windings - Air core	151
E8	Five windings - Iron PLA core	151
E9	Four windings - Coil embedded in air	152
E10	Four windings - Coil embedded in PLA	152
E11	Open circuit calibration	152
E12	Open circuit sample	152
E13	Short circuit calibration	153
E14	Short circuit sample	153
E15	Loaded circuit calibration	154
E16	Loaded circuit sample	154

List of Tables

2.1 Binder Jetting characteristics [107]	4
2.2 Directed energy deposition characteristics [96]	4
2.3 Vat Polymerisation [48, 62]	5
2.4 Material Jetting characteristics [6, 1]	5
2.5 Powder Bed Fusion characteristics [5]	6
2.6 Sheet Lamination characteristics [9]	6
2.7 Material extrusion characteristics [5]	7
3.1 Custom Cura Slicer profiles for sample creation	16
3.2 Resistivity reduction derived from measured resistivities	20
3.3 Resistivity reduction derived from measured resistivities	20
3.4 Anisotropy ratio derived from measured resistivities	21
3.5 Resistance changes due to Annealing and Exposure for Alongside samples	22
3.6 Resistance changes due to Annealing and Exposure for Perpendicular samples	22
3.7 Derived temperature coefficients by linear fit	23
3.8 Final volume resistivities derived for non-annealed samples	24
3.9 Final volume resistivities derived for annealed samples	24
3.10 Thermal coefficients for filaments as found in literature	26
4.1 Filament polymer properties derived from medical safety data sheets [79, 84, 88, 64]	29
4.2 Custom Cura Slicer profiles for sample creation	31
4.3 Average sample resistances measured for ninjatek current density samples	33
4.4 Average sample resistances measured for palmiga current density samples	33
4.5 Average sample resistances measured for protopasta current density samples	34
4.6 Derived current densities from measurement current and cross sectional area	35
5.1 Custom Cura Slicer profiles for sample creation	42
5.2 Complex impedance modelling	46
5.3 Determined resistivities of Ninjatek Gold samples	49
5.4 Determined resistivities of Ninjatek Tin samples	49
5.5 Determined resistivities of Palmiga Gold samples	50
5.6 Determined resistivities of Palmiga Tin samples	51
6.1 Custom Cura Slicer profiles for sample creation	56
6.2 Recorded polymer-wafer separation pressures	62
7.1 Custom Cura Slicer profiles for sample creation	67
7.2 Calculated estimates of sample resistivity and resistance	69

7.3	Measured resistances for varying traxel orientations	69
8.1	Custom Cura Slicer profiles for capacitor creation	74
8.2	Calculation parameters used to derive plate capacitance	77
8.3	Calculation parameters used to derive plate resistance	78
8.4	Calculation parameters used to derive interconnect resistance	78
8.5	Capacitance and series resistance as calculated for neat PLA dielectric capacitors	78
8.6	Fitted capacitor model for Neat filled PLA dielectric	79
8.7	Fitted capacitor model for Iron filled PLA dielectric	80
9.1	Custom Cura Slicer profiles for solenoid inductor creation	84
9.2	Custom Cura Slicer profiles for planar inductor creation	86
9.3	Calculation parameters used to solenoid inductance	90
9.4	Calculation parameters used to derive solenoid inductance	91
9.5	Calculation parameters used to derive solenoid winding resistance	91
9.6	Calculation parameters used to derive solenoid winding capacitance	91
9.7	Calculation parameters used to derive planar coil inductance	92
9.8	Calculation parameters used to derive planar coil winding resistance	92
9.9	Calculation parameters used to derive planar coil winding capacitance	92
9.10	Derived concentric circle capacitances for planar coil winding resistance estimate	92
9.11	Fitted inductor model for solenoid inductors	93
9.12	Fitted inductor model for solenoid inductors	94
A.1	Resistivity reduction and ratio derived for Ninjatek samples during room measurement	105
A.2	Resistivity reduction and ratio derived for Palmiga samples during room measurement	106
A.3	Resistivity reduction and ratio derived for Protopasta samples during room measurement	107
A.4	Resistivity reduction and ratio derived for Electrifi samples during room measurement	108
A.5	Resistivity reduction and ratio derived for Ninjatek samples during oven measurement	112
A.6	Resistivity reduction and ratio derived for Palmiga samples during oven measurement	112
A.7	Resistivity reduction and ratio derived for Protopasta samples during oven measurement	113
A.8	Resistivity reduction and ratio derived for Electrifi samples during room measurement (*measured to end of first resting period)	114
A.9	Resistance changes due to Annealing and Exposure for Ninjatek filament	116
A.10	Resistance changes due to Annealing and Exposure for Palmiga filament	117
A.11	Resistance changes due to Annealing and Exposure for Protopasta filament	119

A.12	Resistance changes due to Annealing and Exposure for Electrifi filament	120
A.13	Estimated thermal coefficient for Ninjatek filament	121
A.14	Estimated thermal coefficient for Palmiga filament	122
A.15	Estimated thermal coefficient for Protopasta filament	123
B.1	Current flow achieved at marked points in current measurements for Ninjatek samples	125
B.2	Temperatures achieved at marked points in temperature measurements for ninjatek samples	126
B.3	Ninjatek sample resistances recorded recorded pre and post current density experiment	126
B.4	Current flow achieved at marked points in current measurements for Palmiga samples	128
B.5	Temperatures achieved at marked points in temperature measurements for Palmiga samples	128
B.6	Palmiga sample resistances recorded pre and post current density experiment	128
B.7	Current flow achieved at marked points in current measurements for Protopasta samples	130
B.8	Temperatures achieved at marked points in temperature measurements for Protopasta samples	130
B.9	Protopasta sample resistances recorded pre and post current density experiment	131
C.1	Fitted open calibration values	137
C.2	Fitted shorted calibration values	138
C.3	Fitted open calibration values	141
C.4	Fitted shorted calibration values	142
E.1	Fitted open calibration values	153
E.2	Fitted shorted calibration values	154